UC Riverside

UC Riverside Electronic Theses and Dissertations

Title

Non-Thermal Plasmas and Material Synthesis: Applications in Quantum Dots, Lithium-Ion Batteries, and Pathogen Decontamination

Permalink

https://escholarship.org/uc/item/7dz1f3d3

Author

Schwan, Joseph

Publication Date

2022

Supplemental Material

https://escholarship.org/uc/item/7dz1f3d3#supplemental

Copyright Information

This work is made available under the terms of a Creative Commons Attribution-NoDerivatives License, availalbe at https://creativecommons.org/licenses/by-nd/4.0/

Peer reviewed|Thesis/dissertation

eScholarship.org Powered by the California Digital Library
University of California

UNIVERSITY OF CALIFORNIA
RIVERSIDE

Non-Thermal Plasmas and Material Synthesis: Applications in Quantum Dots, Lithium-Ion Batteries, and Pathogen Decontamination

A Dissertation submitted in partial satisfaction
of the requirements for the degree of

Doctor of Philosophy

in

Mechanical Engineering

by

Joseph Schwan

March 2023

Dissertation Committee
Dr Lorenzo Mangolini, Chairperson
Dr. Chen Li
Dr. Richard Wilson

Copyright by
Joseph Schwan
2023

The Dissertation of Joseph Schwan is approved:

_____

_____

_____
Committee Chairperson

University of California, Riverside

Acknowledgements:

I would like to thank:

My family and friends for getting me to graduate school,

Giorgio Nava for keeping me in graduate school,

and my labmates, collaborators, & advisor for getting me through graduate school.

Acknowledgement of Previously Published Materials and Funding Sources:

The text of this dissertation contains works, in part or in full, reprinted from the following materials:

Interaction between a Low-Temperature Plasma and Graphene: An in situ Raman Thermometry Study published in *2021* within *Physical Review Applied*, volume *15*. The co-authors of this publication: *Carla Berrospe-Rodriguez, Giorgio Nava, Fariborz Kargar, Alexandar A. Balandin, and Lorenzo Mangolini*; conducted, directed, and supervised the research which has been partially reprinted within this dissertation as Section 1.2. [1]

Controlled growth of silicon particles via plasma pulsing and their application as battery material published in *2022* within *Journal of Physics D: Applied Physics*, volume *55*. I am the primary contributor in this article. The co-authors of this publication: *Brandon Wagner, Minseok Kim, and Lorenzo Mangolini*; conducted, directed, and supervised the research which has been entirely reprinted within this dissertation as Section 1.4. [2]

Bidirectional triplet exciton transfer between silicon nanocrystals and perylene published in *2021* within *Chemical Science*, volume *12*. The co-authors of this publication: *Tingting Huang, Timothy T. Koh, Tiffany T.-T. Tran, Pan Xia, Kefu Wang, Lorenzo Mangolini, Ming Lee Tang, and Sean Roberts*; conducted, directed, and supervised the research which has been partially reprinted within this dissertation as Section 2.2. [3]

Air-Stable Silicon Nanocrystal-Based Photon Upconversion published in *2021* within *Advanced Optical Materials,* volume *9*. The co-authors of this publication: *Pan Xia, Thomas W. Dugger, Lorenzo Mangolini, and Ming Lee Tang*; conducted, directed, and supervised the research which has been partially reprinted within this dissertation as Section 2.3. [4]

Gas-Phase Grafting for the Multifunctional Surface Modification of Silicon Quantum Dots published in *November 2022* within *Nanoscale*. I am a co-primary contributor in this article with *Kefu Wang*. The co-authors of this publication: *Ming Lee Tang and Lorenzo Mangolini*; conducted, directed, and supervised the research which has been entirely reprinted within this dissertation as Section 2.4.[5]

Silicon-Core-Carbon-Shell Nanoparticles for Lithium-Ion Batteries: Rational Comparison between Amorphous and Graphitic Carbon Coatings published in *2019* within *Nano Letters,* volume *19*. The co-authors of this publication: *Giorgio Nava, Matthew G. Boebinger, Matthew T. McDowell, and Lorenzo Mangolini*; conducted, directed, and supervised the research which has been partially reprinted within this dissertation as Section 3.2. [6]

Critical barriers to the large scale commercialization of silicon-containing batteries published in *2020* within *Nanoscale Advances,* volume *2*. The co-authors of this

publication: *Giorgio Nava and Lorenzo Mangolini*; conducted, directed, and supervised the research which has been partially reprinted within this dissertation as Section 3.3. [7]

Efficient facemask decontamination via forced ozone convection published in *2021* within *Scientific Reports*, volume *11*. I am a co-primary contributor in this article with *Troy R. Alva*. The co-authors of this publication: *Giorgio Nava, Carla Berrospe-Rodriguez, Spencer Dunn, Justin W. Chartron, Joshua Morgan, Pin Wang, and Lorenzo Mangolini*; conducted, directed, and supervised the research which has been entirely reprinted within this dissertation as Section 4.1. [8]

I acknowledge the financial support of the Graduate Assistance in Areas of National Need (GAANN) Program, The National Science Foundation under grant number 1940952, The Department of Energy through the Office of Science Graduate Student Research (SCGSR) Fellowship, and Dissertation Year Program (DYP) Award via The University of California at Riverside.

ABSTRACT OF THE DISSERTATION

Non-Thermal Plasmas and Material Synthesis:
Applications in Quantum Dots, Lithium-Ion Batteries, and Pathogen Decontamination

by

Joseph Schwan

Doctor of Philosophy, Graduate Program in Mechanical Engineering
University of California, Riverside, March 2023
Dr. Mangolini, Lorenzo, Chairperson

Plasma is the state of matter produced when molecules and atoms are energized to a point where their electrons escape and the constituent material becomes ionized. It is described as the fourth state of matter making up the vast majority of the observable universe, and over the past century has been studied and developed into usable human-scale applications. As a category, plasma exists in a thermal spectrum as ionization and unbound electrons are the defining characteristics. Thus, non-thermal plasmas made up of near room temperature ionized gasses formed through strong alternating electromagnetic fields make up one side of the spectrum and thermal plasmas that have heated materials to the point of ionizing constitute the other. This dissertation focuses on the application of non-thermal plasmas for reactive gas generation and nanomaterial synthesis, in addition to more fundamental studies of how the plasma interacts with solid interfaces or forms nanomaterials. The studies that this work is composed of are broken down into sections, the first of which is fundamental investigations of non-thermal plasma properties, such as in-situ monitoring of plasma-induced surface-heating via Raman-thermometry and

investigations into nanomaterial growth mechanics when exposed to discontinuous (pulsing) plasma conditions. The second section puts the silicon nanomaterials produced via plasma to use in quantum dots, where the silicon nanocrystal is combined with non-toxic organic molecules to achieve record setting photon upconversion and investigates the fundamental mechanisms impacting this method of light conversion. Next, plasma-grown and commercial silicon nanomaterials are applied as a next generation lithium-ion battery anode material, where unanswered questions about carbon shell structure and solid electrolyte interphase growth are investigated with novel techniques of material production and analysis. Finally, the reactive gas output of a plasma is put to work as a cheap and efficient method of pathogen decontamination for face-piece-respirators, demonstrating the wide breadth of applications for non-thermal plasmas and the materials it can produce.

Table of Contents:

ACKNOWLEDGEMENTS: ..... **IV**

ACKNOWLEDGEMENT OF PREVIOUSLY PUBLISHED MATERIALS AND FUNDING SOURCES: ..... **V**

TABLE OF CONTENTS: ..... **X**

LIST OF FIGURES: ..... **XIV**

LIST OF TABLES: ..... **XXIV**

LIST OF EQUATIONS: ..... **XXV**

SECTION 1: NON-THERMAL PLASMA (BACKGROUND AND FUNDAMENTAL RESEARCH) **1**

1.1 – BACKGROUND IN NON-THERMAL PLASMA 1

1.1.1 – Introduction to Plasma: *1*

1.1.2 – Types of Plasma: *2*

1.1.3 – Plasma-Surface Interactions: *8*

1.2 – NON-THERMAL PLASMA-INDUCED SURFACE-HEATING VIA IN-SITU RAMAN THERMOMETRY[1] 16

1.2.1 – In-situ Raman Plasma Setup: *18*

1.2.2 – Raman Thermometry: *21*

1.2.3 – Thermal Convection Modeling: *23*

1.2.4 – Gas Composition Plasma-Induced Surface-Heating Influence: *24*

1.2.5 – Summary: *27*

1.3 – NON-THERMAL PLASMAS MATERIAL SYNTHESIS 28

1.3.1 – Gas-Precursor Plasma Synthesis: *28*

1.3.2 – Standard Experimental Synthesis and Collection: *31*

1.4 – EFFECTS OF DISCONTINUOUS PLASMA EXPOSURE ON PARTICLE GROWTH[2] 36

1.4.1 – Particle Production, Analysis, and Battery Testing: *38*

1.4.2 – Coagulation Modeling and Calculations: *42*

1.4.3 – Silicon Nanoparticle Growth and Impacts on Battery Cycling: *48*

1.4.4 – Modeling Variables Impacting Nanoparticle Growth and Charging: *55*

1.4.5 – Summary: *65*

SECTION 2: HYBRID ORGANIC-INORGANIC QUANTUM DOTS 67

2.1 – BACKGROUND IN SILICON QUANTUM DOTS 67

2.1.1 – Introduction to Quantum Dots: *67*

2.1.2 – Section Shorthand: *69*

2.1.3 – Silicon QD Properties: *70*

2.1.4 – TTA Upconversion: *72*

2.1.5 – SiQD Synthesis: *77*

2.1.6 – Standard Measurement Used: *83*

2.2 – TRIPLET EXCITON TRANSFER BACK AND FORTH BETWEEN SILICON AND PERYLENE[3] 93

2.2.1 – 3EP Upconverting System: *95*

2.2.2 – Investigating Quenching with TA: *98*

2.2.3 – Relaxation Rate Modeling: *102*

2.2.4 – UCQY Reduction Causes: *108*

2.2.5 – Summary: *112*

2.3 – AIR-STABILIZATION OF UPCONVERTING SILICON QUANTUM DOTS[4] 114

2.3.1 – Solvent Comparison: *115*

2.3.2 – Polymers as Oxygen Barriers: *118*

2.3.3 – Micelles for Water Based Applications: *123*

2.3.4 – Summary: *125*

2.4 – IN-FLIGHT PARTIAL FUNCTIONALIZATION, SURFACE COVERAGE, AND SILICON QUANTUM DOT SIZE EFFECTS[5] 127

2.4.1 – Synthesis and Characterization: *129*

2.4.2 – Ligand Saturation Effects: *133*

2.4.3 – Size Effects: *140*

2.4.4 – Alkyl Chain Ligand:UCQY Relation: *143*

2.4.5 – Summary: *146*

SECTION 3: BATTERY MATERIALS AND INVESTIGATIONS 147

3.1 – BACKGROUND ON LITHIUM-ION BATTERIES 147

3.1.1 – History of Batteries *147*

3.1.2 – Why Silicon is Interesting: *150*

3.1.3 – Electrochemical Testing: *153*

3.1.4 – Battery Construction: *158*

3.2 – CORE-SHELL GRAPHITIZATION STUDY[6] 164

3.2.1 – Two-Step CVD for Graphitized Carbon-Shells: *166*

3.2.2 – Carbon-Coated Silicon Material Properties: *168*

3.2.3 – Carbon-Shell Silicon-Core Electrochemical Performance: *173*

3.2.4 – Silicon as a Drop-In Additive: *178*

3.2.5 – Summary: *181*

3.3 – SILICON SYNTHESIS METHODS AND COMMERCIAL MATERIAL EFFECTS[7] 182

3.3.1 – Mechanical Synthesis: *183*

3.3.2 – Reactive Synthesis: *185*

3.3.3 – Plasma Synthesis: *187*

3.3.4 – Thermal Synthesis: *192*

3.3.5 – Effects of Size and Purity: *196*

3.3.6 – Summary: *200*

3.4 – ANODE MATERIAL SURFACE CHEMISTRY EFFECTS ON SEI 202

3.4.1 – Intro to SEI: *202*

3.4.2 – Carbon Shell Effects on SEI: *205*

3.4.3 – Carbon Shell Lithiation: *215*

3.4.4 – Summary: *218*

SECTION 4: MASK DECONTAMINATION AND ENERGETIC MATERIALS 219

4.1 – FACEMASK DECONTAMINATION VIA PLASMA-PRODUCED FORCED OZONE CONVECTION[8] 219

4.1.1 – Motivation and Method: *220*

4.1.2 – DBD Plasma Reactor for FPR Decontamination: *223*

4.1.3 – Low-Cost Plasma Reactor for FPR Disinfection: *224*

4.1.4 – Gas Composition and Characterization: *226*

4.1.5 – Quantifying Decontamination Efficacy: *228*

4.1.6 – Results and Discussion: *232*

4.1.7 – Summary: *241*

FINAL CONCLUSIONS: 242

BIBLIOGRAPHY: 247

APPENDIXES: 276

APPENDIX A: PULSED PLASMA MODELING CODE (PYTHON) 276

List of Figures:

Figure 1: Illustration showing the general difference between thermal and non-thermal plasmas. 6

Figure 2: Examples of plasma formation from either electron emission or E-field ionization. 7

Figure 3: Illustration of the development of a Debye sheath. 10

Figure 4: Cartoon of plasma etching mechanisms and effects with a) a pristine initial state, then the effects of b) sputter etching, c) gas-phase pure chemical etching, d) ion-enhanced energy-driven etching, and e) ion-enhanced inhibitor etching. 14

Figure 5: a) Illustration of the in-situ Raman plasma reactor chamber concept. b) Raman spectrum of multilayered graphene film and c) Stokes and anti-Stokes signal and fittings of the same graphene sample when heated to 600 ºC under a 12 W plasma. 18

Figure 6: a) Diagram of the optical path for the in-situ Raman and b) a labeled image of the plasma reactor and chamber setup. 20

Figure 7: a) Stokes and anti-Stokes for the graphene G peak as substrate temperature is increased from 200-600 C without plasma impingement and b) the in-situ Raman determined surface temperature to sample stage temperature with and without plasma impingement. 22

Figure 8: a) COMSOL MULTIPHYSICS heat transfer model to determine convection effects of the potential hot plasma gasses and b) the resulting substrate temperatures upon exposure to differing flow rates and gas temperatures. 24

Figure 9: a) Collapsed plasma emission spectra (748-966 nm) for a 10 W Ar plasma with increasing H_2 dilution, and b) substrate temperature with relation to plasma power and gas composition using the same color scheme. c) Integrated area of OES peaks as a function of H_2 dilution. 25

Figure 10: a) SEM images of the graphene sample before and after Ar or Ar:H_2 (80:20) plasma treatment with b) corresponding normalized Raman spectra. 26

Figure 11: Illustration of particle nucleation and growth within a plasma (yellow indicates electrons and negative charge, red indicates positive charge, green as reactive species, and blue as neutral species). 31

Figure 12: a) Image of a vertically mounted standard silicon synthesis plasma system (used in Section 1.4) and b) corresponding schematic. 34

Figure 13: (a) Average particle diameter as a function of reactor pressure for a continuous plasma. (b) Average particle diameter at various pressure, as a function of number of plasma pulses per residence time. The duty cycle is 50% for all these measurements. The diameters reported in this figure are based on XRD measurements and Scherrer's analysis..... 49

Figure 14: (a) Particle size distributions for the continuous and pulsed cases, as obtained by analysing several TEM micrographs. (b-e) Representative TEM micrographs for particles produced with a continuous plasma, or with 3, 12.5 and 25 pulses per residence time, respectively. 51

Figure 15: TEM micrographs of silicon particles produced using a continuous (left) or pulsed (right) mode, after coating with a graphitized carbon shell..... 52

Figure 16: (a) Gravimetric capacity vs. cycle number for the samples produced with a continuous plasma and at varying pulsing frequencies. The charging rate is kept at 0.1C for the first 5 formation cycles, then increased to 0.5C. (b) Same as (a) but showing the Coulombic efficiency vs. cycle number. In the inset we summarize the first cycle efficiency for the samples. 54

Figure 17: (a) Time variation of ion, electron and nanoparticle densities, together with the average particle charge, during the 'plasma on' phase. (b) Time variation of ion, electron and metastable densities in the plasma afterglow. (c) Same as (b), but showing the nanoparticle density, the electron temperature and the average particle charge. Please note that the x-axis is on a logarithmic scale for plots (b) and (c)..... 55

Figure 18: (a) Evolution of total particle densities in the afterglow for initial metastable densities of 10^8 cm^{-3} and 10^{13} cm^{-3}. (b) Corresponding particle charge distributions in the afterglow, after the initial charge relaxation transient. (c) Dependence of the Q_{+1}/Q_{-1} and Q_{+1}/Q_0 parameters on the initial metastable density. (d) Dependence of particle size and density on the initial metastable density. (e) Evolution of total particle density in the afterglow for gas temperature of 300 K and 1000 K. (f) Corresponding particle charge distributions in the afterglow, after the initial charge relaxation transient. (g) Dependence of the Q_{+1}/Q_{-1} and Q_{+1}/Q_0 parameters on the gas temperature. (h) Dependence of particle size and density on the gas temperature..... 59

Figure 19: (a) Calculated cumulative effect of 10 plasma pulses on the total particle density, compared to the case of a continuous plasma and the case of free-molecular agglomeration, without any electrostatic effects. (b)(c) 2 dimensional plots of particle densities as a function of size and charge after the last 'plasma on' pulse and after the last afterglow, based on the computational approached described in this manuscript..... 63

Figure 20: Exciton formation via a) cartoon and b) energy level diagram. 73

Figure 21: Primary active components of TTA based upconverting SiQDs. 74

Figure 22: TTA upconversion Jablonski energy diagram with cartoon represenatation. . 76

Figure 23: Silicon nanocrystal synthesis, inflight functionalization, and material collection schematic. 77

Figure 24: Images of the a) plasma reactor and b) bubbler system used for SiQD synthesis. 79

Figure 25: Subcritical (left) and critical/supercritical (right) alkyl chain ligand loading of partially functionalized SiQDs in mesitylene at room temperature. 83

Figure 26: PL spectra of Si:9EA:DPA (d=3.1nm, critical dodecane loading, the sample with best UCQY), black solid line, 5.2 mM DPA as emitter, excited at 488 nm) and low-concentration DPA (red dashed line, excited at 365 nm). 85

Figure 27: Example of XRD based sizing through Scherrer's analysis with TEM inset for comparison. 87

Figure 28: TA spectra of a) Si-dodecyl without 9EA and b) Si-dodecyl with 9EA (d = 3.1 nm, 3 9EA molecules per SiQD) in toluene excited at 532 nm. (TA measurements were conducted using an enVISion spectrometer from Magnitude Instruments that employed a 532 nm excitation laser with a 10 kHz repetition rate and a pump fluence of 150 $\mu J/cm^2$. The instrument response function for these measurements was found to give a time resolution of 4.2 ns.) 92

Figure 29: Perylene-SiQD schematic. 95

Figure 30: (A) 3EP|C18|SiQD absorption spectra in toluene with increasing 3EP surface coverage. (A inset) observation that the 3EP absorption spectra appears as a 53 meV bathochromically shifted version of tBu_4perylene. (B) 3EP|C18|SiQD emission spectra in toluene with 532 nm excitation corresponding to the samples in (A) with * designating Raman scattering peaks. (B inset) Increasing 3EP quenching of the SiQD appears to shift and narrow the bandedge PL signal. 96

Figure 31:Transient absorption spectra of (A) C18|SiQDs and (B) 3EP|C18|SiQDs. Transitions indicate excited carriers while the accelerated decay of SiNC induced absorption bands demonstrate features of the 3EP T_1 state. 99

Figure 32: (A) Appearance of new 3VP T_1 features between 400 and 520 nm in TA spectra of a 3VP|C18|PtOEP system following 532 nm excitation. (B) Spectral comparison of 3VP's T_1 state and the SiNC to 3EP triplet energy transfer. 100

Figure 33: (A) Time absorption of the 3EP T_1 state in 3EP|C18|SiQD sample from 532 nm photoexcitation and kinetic model fittings. (B) Energy level schematic of the kinetic model fits with and without triplet energy back transfer from 3EP to the SiNC, demonstrating a greatly improved fit with energy back transfer (dashed black line). (C) Exciton populations of SiNC and 3EP estimated using best fit values of forward and backward TET rates and removing energy relaxation effects. This predicts a 40% of excitations will exist within the 3EP in the 3EP|C18|SiQD system. 101

Figure 34: Kinetics demonstrating the relaxation rate of C18|SiQD photogenerated excitons in toluene measured via TA with a 1000 nm probe following 532 nm excitation and its fitting. 107

Figure 35: (A) Jablonski diagram illustrating the upconversion energy transfer pathway for TTA and (B) the emission spectra demonstrating upconversion in the 3EP|C18|SiQD system in a 0.5 mM tBu_4perylene in toluene solution undergoing 532 nm photoexcitation (upconverted emission is shaded in blue while SiQD emission is shaded in grey). (C) Excitation flux to upconversion emission intensity under either 532 nm (green circles) or 640 nm (red squares) illumination, demonstrating a linear increase over the range examined. Illumination with 730nm (inset) demonstrates the emission intensity scales with a slope between 1 and 2. 110

Figure 36: (A) XRD and Scherrer's Analysis fitting of the 111 peak showing nm crystal size with TEM demonstrating a larger size (inset). (B) Absorption spectra and emission spectra under 488 nm excitation for the C18|SiQD system. 112

Figure 37: Emission spectra over time of air-exposed 9EA|C18|SiQD with DPA and 3.2 nm SiNC cores in solvents of a) toluene, b) octadecene, c) oleic acid, and d) methyl oleate. 116

Figure 38: a) Energy diagram and molecular cartoon of photon upconversion with 9EA|C18|SiQD in a DPA solution utilizing toluene, mesitylene, methyl oleate, oleic acid, or octadecene as the solvent with O_2 as a quenching agent. b) Air exposure time vs normalized UCQY relative to initial values for each solvent. 117

Figure 39: DLS measurements of 9EA|C18|SiQD samples in toluene and DCM with thermal hydrosilylation times of a) 3 hours and b) 15 hours. Multiple scans were performed for each sample and are represented with different colors. 119

Figure 40: a) Elugram of SiNC and SiQD samples with different thermal hydrosilylation times and solutions, with peaks at 30-35 minutes correspond to ODE. b) Molecular weight as calculated from retention time in DLS with exceptionally low peaks being attributed to dimers of ODE. 120

Figure 41: a) DLS measurements demonstrating incorporation of 3 nm 9EA|C18|SiQDs into polymeric matrices that grow with extended exposure of ODE and 9VA in

mesitylene at 175 ºC for 3 hours and 15 hours. b) GPC of the same samples confirming polymerization. c) UCQY and d) bandedge PLQY of 9EA||SiQD samples with differing length alkyne ligands (C8, C12, C16, and C18) in toluene normalized to their initial values to demonstrate the effects of air exposure. 122

Figure 42: a) 9EA|C18|SiQDs with DPA suspended in methyl oleate micelles stabilized by P188 triblock copolymer to form photon upconverting oil-in-water micelles and b) the possible mechanisms for air stability during photon upconversion while in methyl oleate. c) Photon upconversion of 9EA|C18|SiQD samples using a 3.2 nm in methyl oleate exposed to air. d) Normalized changes in UCQY (black squares) and bandedge PLQY (red circles) corresponding to the spectra in (c). e-f) the same test as in (c-d) except with the micelles suspended in water with P188. 124

Figure 43: a) Illustrations of functionalized SiQD with 9EA transmitter ligands and critically loaded alkyl chain ligands to maintain solubility, in addition to b) an energy level diagram illustrating photon upconversion process utilizing TET of the SiQD's photoexcited excitons, through the 9EA, and on to the DPA where they undergo TTA resulting in upconverted photon emission. 129

Figure 44: Simplified diagram of gas-phase SiQD synthesis and in-flight functionalization system using standard electrical and process flow diagram symbols. 130

Figure 45: Three different flow rates of hydrogen gas saturated with 1-dodecene fed to the plasma afterglow alter the SiQD solubility and photon upconversion quantum yield (UCQY). a) Illustrative cartoons of the QD surfaces, b) normalized FTIR spectra for the pristine SiQDs terminated with hydride groups, as well as SiQDs with a critical or high amount of Si-dodecyl ligands. c) The Si-dodecyl chain surface coverage on 3.1 nm diameter SiQDs and their UCQYs plotted against the hydrogen flow rate in the bubbler. 132

Figure 46: a) Fitting of the absorption cross section at 2922 cm^{-1} for alkyl groups with respect to carbon chain length and b) predicted ligand surface coverage using the silylidyne and dodecane absorption cross sections for samples produced with differing amounts of 1-dodecene flow. 136

Figure 47: Prior to affixing the 9EA transmitter ligands to the SiQDs, the minimum amount of aliphatic ligands required to maintain solubility in toluene (critical loading) is investigated with 1-dodecene, 1-octene, or 1-hexene. a) Normalized FTIR scans of the partially functionalized SiQDs, which provide the b) Alkyl chain surface coverage on the SiQDs vs. the average number of surface-bound 9EA per SiQD after 9VA hydrosilylation. c) UV-Vis absorption spectra showing 9EA is bound to the SiQD surface. 139

Figure 48: Photoluminescence (PL) of 488 nm irradiated, Si-dodecyl functionalized 3.1 nm diameter SiQDs with 745 nm PL maxima. These QDs have differing amounts of 9VA

added during hydrosilylation to optimize the upconversion quantum yield (QY). (b) The bandedge PL QYs of SiQDs of varying diameter are compared to their optimized upconversion quantum yields. All measurements are performed in toluene at room temperature. 143

Figure 49: a) The bandedge photoluminescence and upconversion quantum yields for 3.1 nm diameter SiQDs functionalized with critical surface density of Si-hexyl, Si-octyl and Si-dodecyl, i.e. the minimum amount of aliphatic ligands required for colloidal stability. b) Comparison between ligand surface coverage and UCQY showing similar rates of surface coverage produce similar UCQY. 145

Figure 50: Electrochemical cell in a salt bridge configuration (top) and an illustrative cartoon demonstrating equivalencies in modern batteries (bottom). 148

Figure 51: Illustration of pulverization, electrode collapse and uncontrolled SEI growth that happens due to silicon expansion during cycling. 152

Figure 52: Example battery data comparing commercial silicon nanoparticles to silicon nanoparticles made at the University of California Riverside within the Mangolini lab. a) Cycle life testing with different C-rates demonstrating differing capacities and b) resulting coulombic efficiencies. Note that CE exceeds 100% during rapid cycling with reduced capacity, this is likely due to slower discharging ions working their way to the surface of materials enabling discharges of lithium ions present within the material bulk. 158

Figure 53: Slurry casting tools. 160

Figure 54: Cell assembly and electrochemical stages as (left) half-cell components needed for assembly, (center) coin-cell crimping tool, and c) Arbin potentiostat battery testing station. 163

Figure 55: a) Cartoon scheme of the 2-step CVD process and b) image of the actual CVD system used. 168

Figure 56: Carbon shell thickness measured via TEM of a) AC-SNP and b) GC-SNP. c) Chemical composition of the materials via EDS. 169

Figure 57: TEM images of a) AC-SNP and b) GC-SNP displaying the silicon core and highly uniform carbon shell for both samples, with graphitic fringing visible on the carbon shell in b). Raman spectra taken with 532 nm laser light in addition to D and G peak fittings for c) AC-SNP and d) GC-SNP. e) shows the I_D/I_G peak ratio for both AC-SNP and GC-SNP demonstrating a change, while f) shows BET analysis of all three SNP, AC-SNP, and GC-SNP samples. 171

Figure 58: STEM images of GC-SNP in a) bright-field, b) dark-field, and c-f)STEM-EDS chemical highlighting..... 172

Figure 59: a) Charge/discharge curves and b) concurrent CE for SNP, AC-SNP, and GC-SNP in 85% active material 15% CMC binder configuration. c) shows an example EIS curve with the circuit fitting used to find the relevant variables including R_{SEI} and R_{CT} whose values over the first 10 cycles are plotted in d). TEM analysis of SNP size population provided e) a size distribution and cumulative volume fraction with material above the 150 nm lithiation fracture radius shaded in a red background. 176

Figure 60: In-situ TEM of AC-SNP and GC-SNP lithiation. a) shows pristine AC-SNP while e) shows the same material after 480 seconds of lithiation. b-d) highlight the lithiation of specific particles with relevant timestamps. Similarly, f) shows pristine GC-SNP while g) shows the same material after 636 seconds of lithiation. h-j) highlight the lithiation of specific particles with relevant timestamps..... 178

Figure 61: a) Charge/discharge curves and b) CE of a graphite control anode and 10% wt. drop in additives of SNP, AC-SNP, and GC-SNP in a graphite anode mixture. c-e) Show CV curves of the graphite anode, the GC-SNP anode, and the GC-SNP being used as a 10% wt. drop in additive, displaying characteristics of both active components. 180

Figure 62: a) Thermal inductively coupled plasma reactor schematic for conversion of silicon microparticles to silicon nanoparticles with TEM images and size distribution of the resulting materials. b) Schematic of a similar silicon nanoparticle synthesis system with additional carbon-coating abilities also with output material TEM. Reproduced with permission from [296,297] in [7]. 190

Figure 63: a) Silane-laser pyrolysis process using SF_6 as a photosensitizer to react SiH_4 and b) a two-step laser pyrolysis system for silicon nanoparticle production and carbon-shell application. Reproduced with permission from [306,309] in [7]. 194

Figure 64: Photographs of a) pilot-scale hot-walled reactor and b) the related plant. Reproduced with permission from [310] in [7]. 194

Figure 65: Comparison of a) cycling performance, b) first cycle coulombic efficiency, and c) chemical content via EDS of four identically marketed “100 nm Silicon Nanopowders” from Sigma Aldrich (Sigma), Nanostructured and Amorphous Materials (NanoAmor), Tekna, and GetNanoMaterials (GNM).[7] 198

Figure 66: Size distribution and resultant volume distributions for “100 nm silicon” materials from multiple suppliers (Tekna, Sigma Aldrich, Nanostructured and Amorphous Materials, GetNanoMaterials).[7] 199

Figure 67: Non-thermal capacitive plasma and sintering induced growth of branch structures system cartoon (top) and branch size-distribution to annealing temperature relation (bottom). 200

Figure 68: Illustration of the cyclical formation of additional SEI species due to volumetric expansion and contraction. 205

Figure 69: Size distribution and TEM of a-b) “20 nm” lab-synthesized material and c-d) commercially purchased Nanostructured and Amorphous “100 nm” material. 208

Figure 70: Electrochemical cycling data silicon nanoparticles with varying coating thicknesses and structures of a-b) commercial particles sold as 100 nm in average diameter, and c-d) 20 nm lab-made silicon nanoparticles. 210

Figure 71: FTIR data of 100 nm commercial silicon with differing carbon-coating thicknesses after 5 charge/discharge cycles at 0.1 C to develop an SEI, with scans taken while a) still coated in electrolyte, b) after the electrolyte had dried, and c) while the electrolyte was drying (green dashed line indicates relative signal increase with time with red line indicating decrease). 211

Figure 72: a) FTIR spectra of washed anodes composed of 100 nm silicon particles with varying coating thicknesses and structures, with peak magnitudes normalized to the Si-O-Si peak at 1073 cm^{-1} relative to a low at 1173 cm^{-1}. Using this normalization minimal differences are observed between the samples. b) Cycled anode FTIR spectra compared to its constituent parts and c) peak location noting. 212

Figure 73: Comparison of XPS anode signals for DMC washed 20 nm silicon-based anodes. 213

Figure 74: Comparison of in-situ Raman spectra and the associated charge/discharge curves for a-b) 20 nm uncoated silicon and e-f) 36% Graphite (20 nm). Spectra for the 36% Graphite (20 nm) particles are highlighted at the c) fully charged state and d) fully discharged state, illustrating the growing fluorescent signal and constant changing nature of the spectra. 215

Figure 75: a) Stratified in-situ Raman spectra during lithiation and delithiation of the graphite shell and b) the charge/discharge curve with relevant times marked, illustrating the deformation of the carbon via the shifting D and G peak ratios in the Raman spectra. 216

Figure 76: a) XRD scan of uncycled anodes with active material of 20 nm silicon containing differing shell thicknesses and structures. Using the sample with the strongest graphite signal at 25 degrees a comparison of b) XRD spectra of DMC washed anodes after a discharge and charge cycle and c) TEM images of the 72% Graphite (20 nm) material scanned. 217

Figure 77: (a) Picture and (b) schematic of the DBD reactor used in the mask sterilization experiments. 224

Figure 78: Schematic of cost-effective plasma reactor build by using a commercial toy plasma-ball (top), its simplified circuit diagram (bottom left), and a picture of the system (bottom right). 225

Figure 79: The same system was used to characterize the chemical composition (FTIR spectrometer and IR source) and the ozone concentration (V-INR monochromator and UV lamp) after the plasma discharge. 227

Figure 80: (a) Lissajous Figure as a function of applied voltage, (b) coupled power and (c) FTIR measured downstream of the reactor as a function of applied voltage. (d) FTIR measurement downstream of the plasma reactor in plasm-on condition, right after switching off the plasma, after 2 minutes and after 4 minutes. 234

Figure 81: (a) Ozone concentration as a function of DBD plasma discharge voltage. (b) Ozone concentration as a function of time (maximum disinfection time) for 7 kV applied voltage. 235

Figure 82: Bacterial sterilization of surgical masks over time. (a) Fluorescent images of colony growth on agar after varying decontamination times are portrayed on the left. The image at 64 minutes (bottom) is overexposed as only a single colony was observed (red). In the scatter plot, each point represents the mean and S.E.M. from three technical replicates that were normalized by their respective control's mean CFU (mean of control's CFU was $10^{3.42}$). Relative CFU were modelled as the sum of two exponential decays. The gray ribbon represents a 95% confidence interval calculated using a parametric bootstrap. After 64 minutes, a $10^{2.78}$ reduction in CFU is observed as illustrated in the inlayed plot. (b) Optical microscope image of mask before decontamination. (c) Optical microscope image of mask after 64 minutes of O_3 sterilization. Major discrepancies in strand formation were not observed. 236

Figure 83: (a) Voltage signal produced by the power supply of the plasma globe. (b) Lissajous Figure of the plasma globe reactor. (c) FTIR analysis of the gas composition produced by the Plasma Globe Reactor and (d) corresponding O_3 concentration produced by the plasma globe reactor as a function of time. An average of 1010 ± 5 ppm along the stability period (4 to 32 minutes). 238

Figure 84: Sterilization efficacy using different sterilization configurations. The left inset shows fluorescent images of colony growth on agar after 32 minutes of sterilization using different configurations. Right graph shows CFU values of different configurations relative to the negative control. 239

Figure 85: VSV sterilization results (a) VSV sterilization of surgical masks over time. Each point represents the mean and S.E.M. from three biological replicates that were

normalized by the control's mean TU (mean of control TU was $10^{5.68}$). Relative TU were modelled as the sum of two exponential decays. The gray ribbon represents a 95% confidence interval calculated using a parametric bootstrap. After 64 minutes, a $10^{2.13}$ reduction in TU is observed as illustrated in the inlayed plot. (b) Sterilization efficacy after 30 minutes using low-cost sterilization system on different mask types. (c) Filtration efficiency of KN95 masks as a function of sterilization time. No significant change in filtration was observed. 240

List of Tables:

Table 1: 3EP|C18|SiQD functionalization molar ratios and corresponding emission properties for the samples in Figure 30. λ_{3EP} is the absorption maxima wavelength for surface bound 3EP while λ_{MAX} referrs to the emission maxima wavelength from 532 nm stimulated emission. The PLQY was then calculated using R6G as a standard. 98

Table 2: Kinetic model best-fit parameters to match the data in Figure 33A. 106

Table 3: Dynamic viscosity and diffusivity of oxygen in different solvents. 118

Table 4: Estimation of molecular weights of 9EA|C18|SiQD with a SiNC of 3.0 nm ... 120

Table 5: Absorption Cross sections at a given wavenumber. 135

Table 6: Standard mixtures used for optimizing 9EA||SiQDs via in-solution thermal hydrosilylation. 141

List of Equations:

Equation 1: Plasma parameter definition. 3

Equation 2: Fractional ionization equation. 4

Equation 3: Debye length. 10

Equation 4: Raman thermometry Stokes:anti-Stokes signal intensity relation. 21

Equation 5: Coagulation of charged aerosols in the absence of electrostatic dispersion. . 42

Equation 6: Coagulation coefficient of charged particles. 43

Equation 7: Frequency of coagulation between two particles of volume v_i and v_j. 43

Equation 8: Charge coefficient for particle interactions. 43

Equation 9: Radius of newly formed particles. 44

Equation 10: Rate of change for nanoparticles of size i and charge p. 44

Equation 11: Electron-particle collision frequency. 44

Equation 12: Ion-particle collision frequency. 45

Equation 13: Metastable-particle collision frequency. 45

Equation 14: Change in the fraction of net-zero charge particles. 59

Equation 15: Ratio of positively particles with a +1 to zero net charge. 60

Equation 16: Charging frequency relation. 60

Equation 17: Temperature dependent sintering time of particles. 64

Equation 18: Upconversion quantum yield without reabsorption correction. 84

Equation 19: Scherrer Equation 86

Equation 20: SiNC diameter to PL peak relation. 87

Equation 21: Atoms in a nanocrystal based on material density. 89

Equation 22: Internal nanocrystal diameter. 89

Equation 23: Surface atoms in a nanocrystal based on material density. 89

Equation 24: Atoms in a nanocrystal based on the crystal unit cell. 90

Equation 25: Nanocrystal surface atoms based on the crystal unit cell. 90

Equation 26: 9EA per SiQD based on absorption data. 91

Equation 27: Differential equation describing rate of SiNC exciton change over time. 103

Equation 28: Differential equation describing rate of 3EP exciton change over time.... 103

Equation 29: Miller-Abrahams rate expression for SiNC to 3EP exciton transfer. 104

Equation 30: Miller-Abrahams rate expression for 3EP to SiNC exciton back transfer. 104

Equation 31: Time dependent population of excitons within SiNC after a pulse of laser exposure. 104

Equation 32: Time dependent population of excitons within the 3EP after a pulse of laser exposure. 104

Equation 33: Absorption compensated ratio between ligand covered surface and hydrogen terminated silicon. 135

Equation 34: Estimated alkyne ligand surface coverage fraction. 136

Equation 35: Magnesiothermic reduction of silica example reaction. 186

Equation 36: Removal of partially reacted magnesium in magnesiothermic reduction. 186

Equation 37: Absorption based ozone concentration calculation. 228

Equation 38: Transducing units calculation for E. coli quantification. 231

Equation 39: Power consumption via Lissajous figure calculation 233

Equation 40: Dissociation of O_2 via electron collision. 233

Equation 41: Ozone formation via third-body collision. 233

Equation 42: Production of NO via oxygen radicals. 235

Equation 43: Destruction of ozone via NO. 235

Section 1: Non-Thermal Plasma (Background and Fundamental Research)

1.1 – Background in Non-Thermal Plasma

Note to the reader: This and the other explanatory subsections (1.1, 1.3, 2.1, 3.1) are intended as a quick overview to allow a fuller understanding of the following sections and their studies. Each subsection could be a book of their own (some books were referenced in writing), so the purpose of these subsections is not to educate on an entire field of study, but instead provide a general understanding of the topics covered within the dissertation and give references to useful resources.

1.1.1 – Introduction to Plasma:

If you have solid ice and add energy it melts and forms liquid water. If you have liquid water and add energy it vaporizes and becomes gaseous steam. If you take gaseous steam and add energy it ionizes and you have a plasma. Naturally there are the caveats of pressure and phase changes that keep these transitions from being simple, but the ionization of a material through energy input is the basis of what defines a plasma. More technically a plasma is "an electrically conducting medium made up of an ionized gas".[9] It makes up over 99% of the observable universe and can take forms as various and benign as wound sterilization cold plasmas[10] or as intense as the surface of the sun itself.[11] On a human scale we have learned and developed plasmas as a scientific field from its first documented intentional sparks by Irving Langmuir and Lewi Tonks in the 1920s to the fusion efforts at

the International Thermonuclear Experimental Reactor (ITER) that continue to this day.[12] Over the past century our understanding of plasma has enabled societal growth and development, enabling technologies ranging from: plasma welding,[13] to fluorescent lamps,[14] to integrated circuits,[15] to plasma screen TVs,[16] to rocket thrusters (Hall thrusters),[17] to sewage sterilization,[18] and the list goes on and on.[19] This subsection will act as a quick introduction to the plasma science concepts that will be useful in understanding the rest of this dissertation and will be added to in Section 1.3 regarding material synthesis. To be upfront, if the reader intends to get deeper into the topic of non-thermal plasma processing I would recommend getting a copy of *Principles of Plasma Discharges and Materials Processing* by M.A. Lieberman and A.J. Lichtenberg,[20] while if they are looking to have a basis in general plasma physics I would promote *Introduction to Plasma Physics and Controlled Fusion* by F.F. Chen.[11]

1.1.2 – Types of Plasma:

Typical plasmas can be described as quasi-neutral gasses of charged particles capable of demonstrating a collective behavior. The term "quasi-neutral" refers to the fact that even though a plasma is composed of charged ions and free electrons, the overall charge density of a bulk plasma region is neutral as the ions and electrons balance each other's net charge. The "collective behavior" part is in reference to the fact that macroscopic field effects tend to dominate when compared to smaller fluctuations allowing for the manipulation of an entire plasma region more easily than single charges. Due to the charged nature of plasma, a key variable when describing it is its electron or ion-density.

Being that most plasmas exhibit quasi-neutrality the ion density is sometimes used as a proxy and described as "plasma density" (n). Naturally, the spatial density of ions will be dependent on the amount of material in a region as well as the amount of power causing ionization as more power will tend to ionize more of the material and raise the average electron temperature (T_e). As a result plasmas can attain densities of ~10^{26} cm^{-3} with electron temperatures of ~10^3 eV within stars or fusion devices,[21] while lab-scale non-thermal capacitive plasmas exist closer to $n_e \approx 10^{11}$ cm^{-3} and $T_e \approx 4$ eV.[22] Differences in plasma density impact different things like mean-free-path (l), the average distance a particle can travel before experiencing a collision event, and the Debye length (λ_D), the distance required for electronic shielding to occur (more on that later). These variables can be combined to describe the plasma more simply with a "plasma parameter" (g) where a value below one implies that collective effects are more dominant than inter-particle effects.

$$g \equiv \frac{1}{n_e \lambda_D^3}$$

Equation 1: Plasma parameter definition.

As can be seen within the equation, collective effects tend to be more dominant at higher electron densities and longer Debye lengths which are typically inversely related. Here it amounts to more-dense higher-power plasmas tend to have more collective effects. A final variable to be aware of is known as fractional ionization (x_{iz}) which is as the name suggests the comparative proportion of the ionized gas density to the total gas density (n_g = neutral density):

$$x_{iz} = \frac{n_i}{n_g + n_i}$$

Equation 2: Fractional ionization equation.

Full ionization is denoted as 1 while less ionized plasmas are much lower, with standard plasma conditions used in microchip manufacturing (and within this document) being estimated at 10^{-6}-10^{-3}.[20] This implies that less than a percent of the gas is ionized at any given moment, however due to the short timescales recombination and ionization deals in an entire volume will be ionized in rapidly (eg. full silane precursor consumption by a non-thermal RF plasma occurs within 50 milliseconds despite expected low fractional ionization).[23]

Thermal vs. Non-thermal:

As noted above, plasma density can vary greatly so that "plasma" can refer to the bulk inside of a star ($n_e \approx 10^{26}$ cm^{-3}) as well as the wisps of an aurora ($n_e \approx 10^{6}$ cm^{-3}).[21] Somehow, the definition of plasma gets even more broad when the focus is brought to the technology developed for industrial processes. To make sense of all of the human scale plasmas they have been broken down into two primary categories:[24,25]

- *Thermal plasmas* – Plasmas existing at thermal equilibrium, meaning that the plasma's ions and electrons have an average of the same thermal energy. These plasmas are able to form in environments of comparatively high pressures (>10 kPa) and power a small yet hot volume. As a result, the hot ions are able to

effectively transfer heat leading to applications in plasma torches and experimental fusion reactors.

- *Non-thermal plasmas (also known as "cold plasmas")* – Plasmas not existing at thermal equilibrium, characterized by their ions having much lower temperatures than the electron population. This is more commonly done in small volumes (microplasmas) or at low pressures via strong electromagnetic fields that restrict ion kinetic energy accumulation.

The difference in ion motion is illustrated in Figure 1. It should be noted that thermal equilibrium does not mean ions and electrons move at the same speed, as thermal energy when equated to kinetic energy creates a relation of: $KE = \frac{1}{2}mv^2 = \frac{3}{2}k_B T_e$ and $m_i \geq 1836m_e$. This difference in mass and possession of the same energy implies that the ions, despite carrying the same energy are travelling much slower, which leads to the common mathematical approximation that they are stationary in comparison to the fast-moving electrons. The comparatively slow ions of non-thermal plasmas only compound this perceived stationary motion.[21]

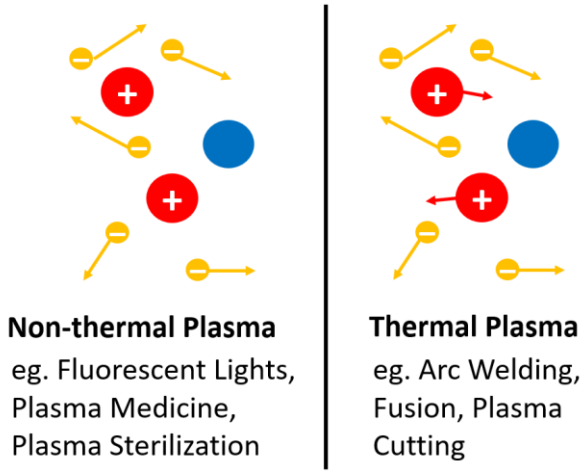

Figure 1: Illustration showing the general difference between thermal and non-thermal plasmas.

Methods of Forming Plasmas:

The numerous forms of plasma discussed above are not all formed and maintained by the same mechanism. There are in fact a wide variety of methods for inducing a charge cascade/avalanche/breakdown/ignition, ranging even more than the terms for staring a plasma. All plasmas are based on ionization, so the method of forming a plasma are essentially the methods of rending electrons from ions. This can be done through collisions of fast particles with atoms (such as electrons emitted from a filament), high-energy photoionization (using laser light or microwaves), electrical breakdown from a strong electromagnetic field (RF or DC), electrical breakdown from a strong magnetic field (inductively induced magnetic fields), and thermal excitation (as with high-energy chemical reactions).[21] The many terms for starting a plasma are all based on the fact that highly energized electrons will collide with a neutral species can free an additional

electron. If these electrons have the high initial energy maintained, it causes a cascade effect growing the ion and free electron populations as show in Figure 2.

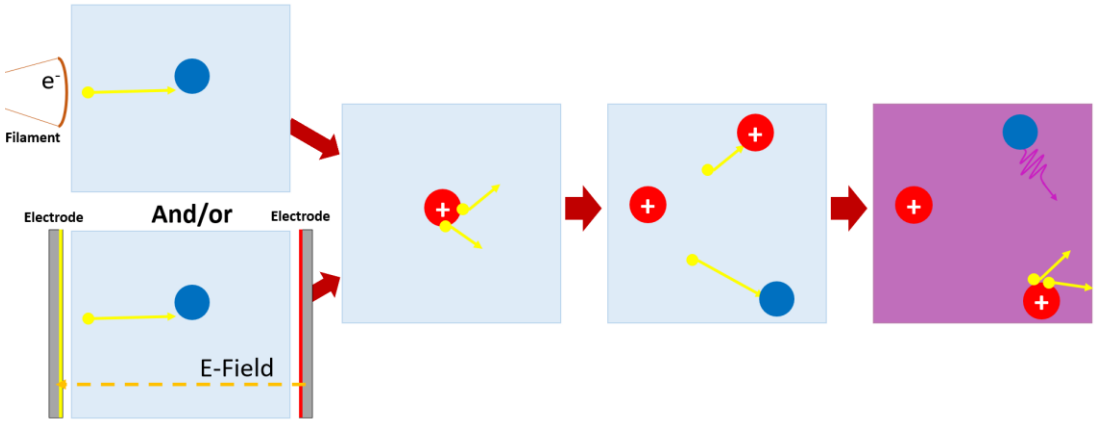

Figure 2: Examples of plasma formation from either electron emission or E-field ionization.

The work in this dissertation is based on capacitively coupled plasmas (CCP) which are non-thermal in nature. As mentioned above, this implies that the ions are unable to gain sufficient kinetic energy to exist in thermal equilibrium with the electrons. For CCPs there are several different electrode geometries, but the idea is the same with all of them. Grounding or applying a constant bias to one electrode, the other electrode (called the cathode for some reason) has high voltages oscillating back and forth at a high frequency. The high voltage enables field ionization of the gas while the rapid oscillating nature of the electric field prevents the ions from gaining large levels of momentum before being redirected in the opposite way with the changing E-field. A form of this is used in semiconducting manufacturing, plasma sterilization, and lab-scale experiments alike. However, despite the fact that this method can work with different frequencies, a select

few have been designated ISM (Industrial, Scientific and Medical) bands have been set aside by the International Telecommunications Union radio regulations for use without the potential of interfering with communications.[26] As a result, most RF power supplies available serve these bands with the most common band used being 13.56 MHz. Matching networks, systems that ease the input power into plasma by mirroring its electronic properties (resistance, inductance, and capacitance), have been developed to maximize the energy efficiency of these CCP systems.

1.1.3 – Plasma-Surface Interactions:

When created and being put to use by humans it is inevitable that a plasma will in some way interact with a solid, whether it be a material that the plasma formed or simply the chamber that the plasma formed in. Depending on the type and power of said plasma a long list of potential effects can be seen, ranging from material etching to film deposition, from emission of secondary electrons to electron surface charging.[27] These seemingly contradictory effects are dependent on both the plasma and the container material as well as the plasma conditions itself, to not even mention magnetic guiding effects. Below is a simplified overview of a couple relevant plasma-surface interactions, continued into material formation within Section 1.3.

Debye Sheath:

As plasmas are defined by the energetic ionization of their materials it is almost inevitable that charge will play a defining role in plasma physics. Indeed, the concept of

the Debye sheath spans all types of plasma, thermal to non-thermal, low to high pressure, and is needed to understand everything from nuclear fusion technologies to the comparatively low-pressure plasmas this text focuses on. Consider the wall of a glass tube with a plasma inside of it. Regardless of whether the plasma is thermal or non-thermal, the average electron speed will be faster than the average ion speed due to the mass imbalance ($KE = \frac{1}{2}mv^2 = \frac{3}{2}k_B T_e$ and $m_i \geq 1836 m_e$, with non-thermal having even slower ions). As a result, the electrons are likely to collide/interact with more things more quickly than the ions, which includes solid surfaces like the walls of the reactor. Electrons colliding with the chamber wall can induce secondary electron emission (incident electrons hit an atom with enough energy to escape and knock off a second electron), but tend to be absorbed into the comparatively un-energetic surface developing a net negative surface charge. Net charges have the effect of repelling like charges and attracting opposite charges, but due to the difference in speed many electrons will be able to overcome the repulsive force and continue charging the surface until it reaches a "sheath potential" (aka. "floating potential") before ion attraction can balance their effect. More-slowly, but still occurring at the same time, ions are attracted to the net negative region creating a proportionally large cloud of positive charges. It is proportional as with the presence of each positive ion the apparent net charge to a more distant observer is slightly reduced in magnitude. This charge shielding will continue until there is no apparent net charge at which point, the non-uniform region becomes the quasi-neutral bulk plasma once more. This process is defined by the Debye length (λ_D), which is the distance from the charge collecting surface until bulk plasma characteristics are restored and follows the definition:

$$\lambda_D \equiv \sqrt{\frac{\epsilon_0 K T_e}{n q_e^2}}$$

Equation 3: Debye length.

where ε_0 is vacuum permittivity, K is the Boltzmann constant, T_e is the electron temperature, n is the electron density, and q_e refers to electron charge. It should be noted that this equation is an approximation based on the assumption that ion move on a timescale that is negligibly slowly. An illustration of sheath development is shown in Figure 3.

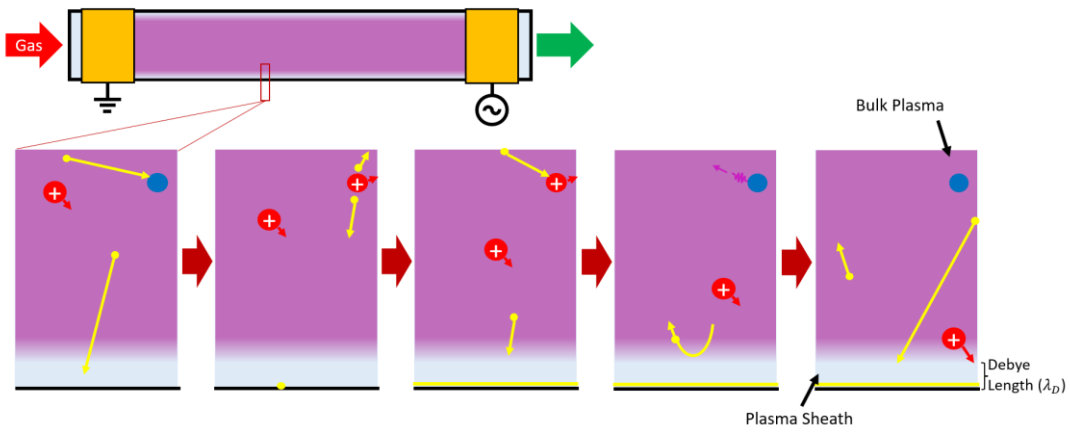

Figure 3: Illustration of the development of a Debye sheath.

This surface-charging and net-charge shielding phenomenon can even occur when intentionally biasing a surface with a voltage leading to the alternate name of "shielding distance" and is generally used as a characteristic length-scale.[11]

Plasma-Induced Surface-Heating:

Not to be confused with "plasma heating" which refers to the increase in temperature of the plasma itself,[28] plasma-induced surface-heating is the phenomenon where a plasma through interactions with a solid induces non-uniform highly-localized surface heating.[29] Plasmas create highly reactive ions and generally induce a kinetic energy above ambient temperature. This implies that a surface in contact with a plasma will experience both increased photon, ion, and electron bombardment causing the transfer of kinetic and thermal energy, in addition to potential surface reactions (either with the surface or while adsorbed onto it) imparting chemical energy transfer. Both of these phenomena are surface localized and occur very quickly (estimated at 2.5 nm deep within 10^{-12} seconds),[30] so the surface in contact with a plasma is heated faster than the bulk of the material can draw it away. As a result, the surface interacting with the plasma can attain temperatures differing from the bulk only a few atoms away. This topic will be directly explored and measured within the next subsection.

Plasma Etching:

Etching is the process of cutting into unprotected parts of a material (often a metal) to create a design. It is commonly done with aqueous corrosive chemicals such as acids being exposed to a non-reactive patterned surface layered on top of a reactive substrate (commonly called a "resist") so as to etch the pattern into the substrate. Unfortunately, this method of chemical etching acts isotropically (if done well) and will eat away all reactive surfaces expanding the etching pattern like ink on wet paper. Plasma etching (also known

as “dry etching”) is a method capable of bypassing undesired spreading of a pattern through anisotropic material removal. In other words, it can etch a pattern vertically into a substrate with limited to no spread. This means that plasma etching is capable of creating patterns of incredibly fine detail, which enables its near ubiquity in the manufacture of integrated circuit manufacturing.[31] Plasma etching operates in one of four ways:[32]

1. *Sputtering* – The ejection of atoms from a surface due to energetic ion bombardment. It can be enhanced by magnetic fields creating a region of high plasma density, but in essence the plasma supplies energetic ions which collide into a surface (generally a sputtering substrate acting as an electrode for a DC or RF system) with enough force to knock off substrate atoms. These ejected atoms can be directed to form a thin coating on another material, but also leave behind an unselective etching region as sputtering is non-selective and can destroy both the substrate and any protective films.

2. *Pure-chemical* – Gas-phase etching chemicals are excited to ionization, becoming energetically capable of chemically reacting with the substrate and forming a gas-phase product that can easily be removed. As this method is based on chemical reactions the process can be chemically selective allowing for resists to function, but without additional electric or magnetic field manipulation the method acts isotropically in a way mirroring its aqueous chemical etching counterparts.

3. *Ion-enhanced energy-driven* – This method is effectively a combination of both sputtering and pure-chemical etching by using gas-phase etchant chemicals and directing the energized ions to the substrate surface. The chemical etching will predominantly collide with the unprotected substrate and reacted molecules are more easily released due to ion induced collisions. As it is dependent on both the chemicals used and the directed collisional nature of sputtering, the effects appear to be chemical etching that is rate controlled proportional to ion energy (above a minimum threshold). As the chemical etching is directed through the electric field enabling sputtering the pattern becomes much less isotropic, creating wells instead of bowls. It should be noted that the resist layer will also be etched, though not at the rate of the intended substrate.

4. *Ion-enhanced inhibitor* – Adding precursor molecules into the gas composition can induce the deposition of a thin film on the surfaces of the substrate and resist. This film is described as an "inhibitor layer" and protects the surface from the etchant but cannot protect against ion bombardment. The ions remove the inhibitor layer tangential to their direction of travel, that allows for selective etching in only the direction of ion bombardment. As a result, the inhibitor layer will be more effective at protecting surfaces angled away from the electrically induced ion bombardment direction like the walls of a well, creating precise vertical etching patterns.

Pictorial representations of these methods can be found in Figure 4. Etching is a complex process that can be enhanced, slowed, and directed by factors as minor as the angle of the substrate's crystal structure. It is also a process that is constantly evolving to enable greater precision and efficiency,[33] so it should be expected that when plasma etching is intentionally applied to produce a result, as in making integrated circuits, a combination of these methods and potentially others will be employed. Even in the following section, multiple forms of etching were observed despite a lack of intent.[1]

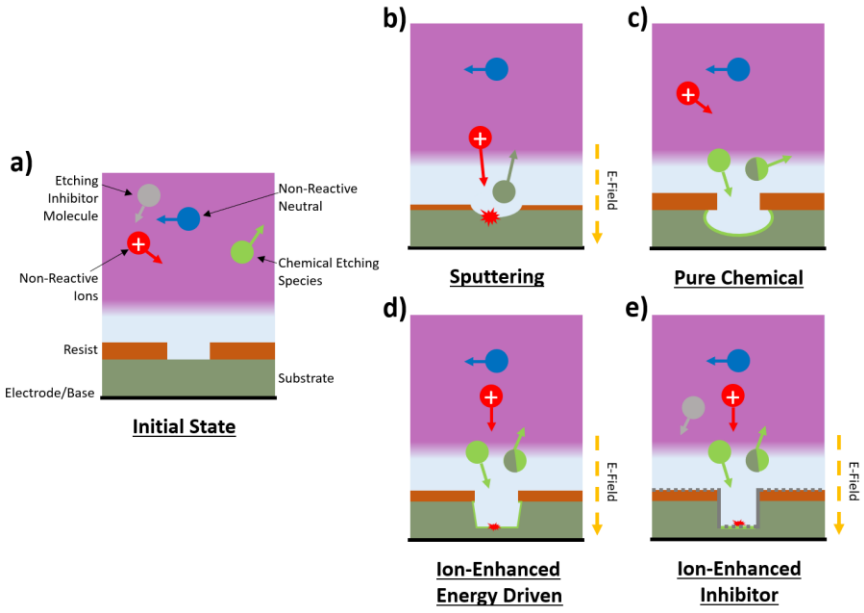

Figure 4: Cartoon of plasma etching mechanisms and effects with a) a pristine initial state, then the effects of b) sputter etching, c) gas-phase pure chemical etching, d) ion-enhanced energy-driven etching, and e) ion-enhanced inhibitor etching.

Potentially relevant to the following study, but not technically a method of etching is charged particle ejection due to patched charging. When a material is exposed to an ionizing beam whether consisting of photons or electrons, secondary charge emission will

produce adjacent regions with similar charges that experience a repulsive force. This has been put forward as a plasma induced effect causing dust lofting in air-free environments such as the moon's surface and may be a contributing factor to surface material loss when loosely bound and capable of charging.[34]

1.2 – Non-Thermal Plasma-Induced Surface-Heating via In-Situ Raman Thermometry[1]

Non-thermal plasmas have found an extremely large base of applications from ozone production,[8] to nanomaterial synthesis for quantum dots and batteries,[2–4,6] to surface etching and surface modification through atomic layer deposition (ALD),[35–38] to plasma catalysis,[39,40] and even 2-D material processing.[41–45] Within this subsection we will be examining plasma-solid interactions with a focus on surface effects like accelerated kinetics using non-thermal radio-frequency capacitive plasmas. Plasma enhanced surface reactions can be attributed to multiple kinetic factors, with a key component being the excitation of gas-phase molecules that are then able to transfer energy via momentum in ion bombardment to a material. Plasma induced reactive or metastable species (atomic or molecular species energized into a long-lived excited state capable of transferring energy or disassociating upon collision) are also able to react at or near plasma exposed surfaces, transferring heat through chemical reactions to demonstrate a phenomenon known as "plasma-induced surface-heating". For instance, recombination of atomic hydrogen on the surfaces of nanoparticles within dusty plasmas is known to produce substantial levels of heating, even enabling the processing of refractory materials.[22,46,47] Direct measurement of nanoparticle temperatures has also confirmed the effects of plasma-induced surface-heating, though it should be noted that these experiments are performed in vacuum which enhances particle heat retention.[48–50] Plasma-induced surface-heating of particles has been well documented at this point, while large area surface heating effects are under debate and generally lack quantitative characterization. Attempts to understand semi-infinite substrate

heating like this have been performed by Walton et al. through time-domain thermoreflectance measurements on metallic films exposed to atmospheric non-thermal plasma jets.[29] This study was able to demonstrate plasma-induced surface-heating and showed that the surface itself was not in thermal equilibrium with the bulk material, but due to the complex specialized equipment the method itself would be difficult to implement in other experimental settings.

The study described within this subsection investigates plasma-induced surface heating quantitatively through the use of Raman thermometry. To enable this method graphene was used as the surface being heated due to its relatively high Raman cross-section and distinctive Raman signature while still being atomically thin, allowing for measurement of surface phenomena. Raman thermometry is a strategy that takes advantage of the difference in strength of the Stokes (downshifted photon frequency from energizing a rovibronic state) and anti-Stokes (upshifted photon frequency via collecting energy from a rovibronic state) signals. Measuring with this method requires calibration by heating the substrate to different temperatures and measuring the trend in the Stokes:anti-Stokes ratio, but when performed with the setup used for experimenting convolving factors will be nullified. As a result, this method offers a no-contact spatially resolved temperature measurement leading to increasing adoption.[51,52] As noted, this experiment relies on graphene as the substrate for plasma-surface interactions and will focus on the G band ($\pm$1598 cm^{-1}) due to its clarity of signal. The graphene is deposited via CVD on a copper foil substrate and all measurements take place within a small vacuum chamber see Figure 5a. Raman signal calibration was performed by heating the graphene substrate within the

chamber in 100 ºC increments between 200-600 ºC while under vacuum conditions and flowing 30 sccm of a 90% Ar 10% H_2 mixture. This provided a linear relation between the Stokes:anti-Stokes ratio, enabling simple calculation of the substrate temperatures observed within the experiment.

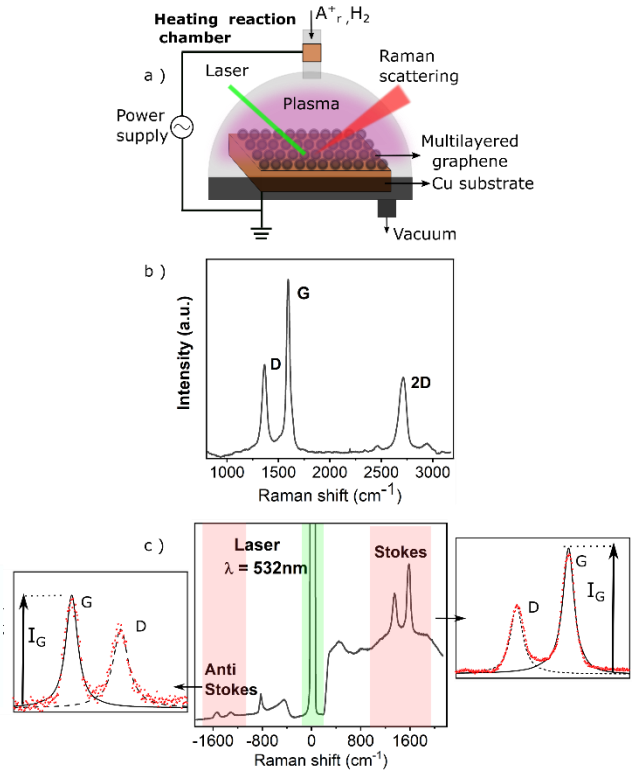

Figure 5: a) Illustration of the in-situ Raman plasma reactor chamber concept. b) Raman spectrum of multilayered graphene film and c) Stokes and anti-Stokes signal and fittings of the same graphene sample when heated to 600 ºC under a 12 W plasma.

1.2.1 – In-situ Raman Plasma Setup:

In order to both heat the sample and attain the vacuum conditions required for the non-thermal plasma, a modified HVC-DRM-5 chamber from Harrick Scientific was used, having one of its windows replaced with a flared-end borosilicate tube so as to fit in the

window mounting and act as the plasma reactor. The chamber itself has a raised stage in the center where the sample rests, with three symmetrically spaced 15 mm diameter windows angled at ~40 degrees to focus on the stage. One of these windows is replaced by the borosilicate plasma reactor, acting as a gas inlet so as to impinge plasma onto the substrate. As such the plasma reactor was 7.5 cm in length with an outer diameter of 10 mm and an inner diameter of 5.16 mm, with a PLA structure to assist in weight distribution of attached vacuum and power connections. RF power was supplied to the plasma at 13.56 MHz via a RFPP-RF5S radio frequency generator, running signal through an MFJ-989D matching network to minimize reflected signal, before powering the plasma via a copper ring electrode as live with the substrate and its chamber acting as ground. Gas enters the chamber via the reactor and exits through a tube at the base of the chamber, while an identical tube connects to a MKS 626D12TBE pressure transducer allowing for monitoring of reactor pressure conditions.

Raman measurements were performed using a continuous wave (CW) laser supplying 532 nm light and a visible to near-infrared (Vis-NIR) Acton Spectra Pro monochromator. The laser was focused to supply 1 W with a spot size of 500 μm (4×10^5 mW/cm^2) through a chamber window on the graphene substrate. Scattered light from the substrate is collected and focused through a notch filter, removing the laser light and allowing the shifted Raman signal into the monochromator where it is spread and imaged by a CCD camera so that intensity along a vertical band corresponds to intensity at a specific wavelength. As graphene is being used within these experiments the D and G peaks will be the most prominent features at 1332 cm^{-1} and 1598 cm^{-1} followed by the second

harmonic 2D peak at ~2600 cm^{-1}, respectively when disregarding the laser intensity as shown in Figure 5b. Unfortunately, the plasma impinging onto the substrate also has spectral lines that can interfere with the signal. In order to account for this, the in-situ Raman measurement implemented a chopper operating at 0.5 Hz while synchronized signals are sent to the CCD so that alternating every second a scan of the plasma would be taken or a scan of both the plasma and Raman signal would be taken. With this data, the plasma only signal can be actively subtracted from the plasma and Raman, leaving an in-situ Raman spectra demonstrating plasma-graphene interactions. A diagram of this setup and image of the system can be seen in Figure 6.

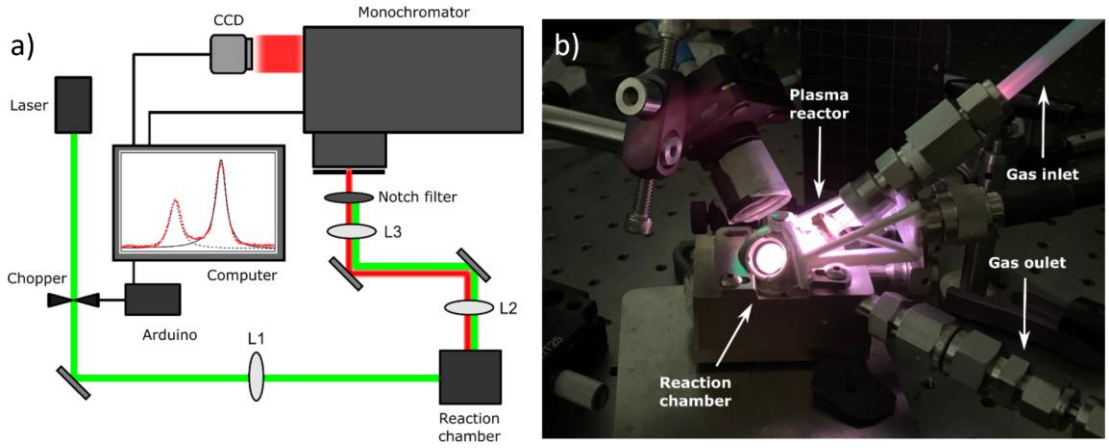

Figure 6: a) Diagram of the optical path for the in-situ Raman and b) a labeled image of the plasma reactor and chamber setup.

Growth of the graphene itself was done through heating the copper foil to 1030 ºC in a low-pressure environment and exposing it to a hydrogen methane mixture, then over the course of 10 hours returning to room temperature as outlined in the following references.[53,54] The result is termed a "multilayer graphene film" (MGF) and is simply

mounted in the center of the stage within the vacuum chamber for measurement. Impinging gasses ranging in composition from pure argon to argon with 20% hydrogen are used throughout the experiment with flow rates between 15-40 sccm while maintaining approximately 13 Torr of pressure.

1.2.2 – Raman Thermometry:

After data collection a spectral deconvolution is performed to separate and fit the D and G peaks with a Lorentzian and a Breit Wigner Fano function respectively as shown in Figure 5c.[55] From there the temperature of each sample is determined through the following equation:

$$\frac{I_s}{I_{as}} = \left(\frac{\lambda_s}{\lambda_{as}}\right)^4 \mathrm{e}^{-\frac{h\nu}{kT}}$$

Equation 4: Raman thermometry Stokes:anti-Stokes signal intensity relation.

where h is Planck's constant, k is the Boltzmann constant, v is the Raman frequency, T is the substrate temperature, I_s and λ_s are the Stokes signal intensity and precise wavelength, while I_{as} and λ_{as} are the anti-Stokes signal intensity and precise wavelength. As a result, the substrate temperature can be calculated based off of the temperature-dependent population of vibrational modes. Although the D and G peaks are a result of resonance, it is worth noting that Equation 4 is valid for non-resonant Raman scattering.[56] Being that MGF lacks singularities in its electronic structure,[57] this resonant effect is negligible allowing for its accurate implementation.

Thermal calibration without plasma conditions increased observed the anti-Stoke vibrational modes as predicted, providing a clear signal increase as shown in Figure 7a while demonstrating an obvious linear trend as shown in Figure 7b. When applying plasma conditions by inputting 12 W of power to the same gas mixture, note an estimated 9% of this power is used by the plasma while the remainder is radiated away,[58] a step of 68±5 ºC is observed for all initial temperature conditions (also shown in Figure 7b). Such a stable increase in temperature is highly indicative of plasma-heating, however additional efforts were performed to determine if there is any convection-heating effects from the plasma.

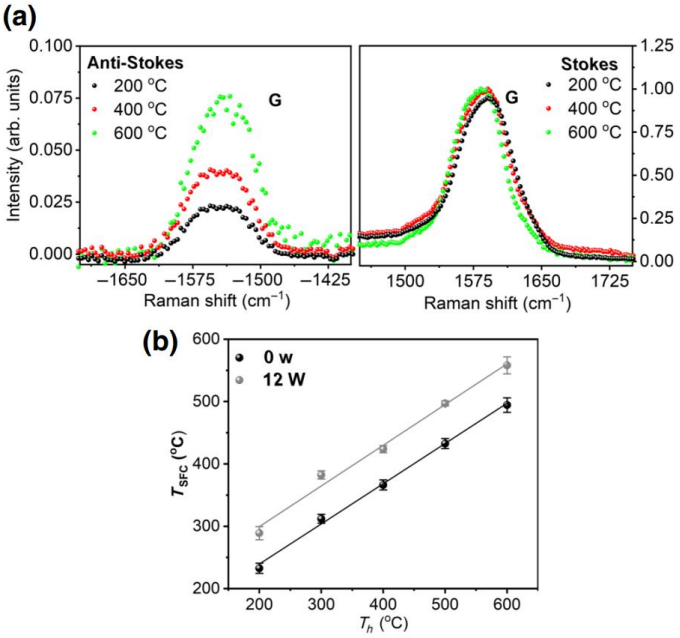

Figure 7: a) Stokes and anti-Stokes for the graphene G peak as substrate temperature is increased from 200-600 C without plasma impingement and b) the in-situ Raman determined surface temperature to sample stage temperature with and without plasma impingement.

1.2.3 – Thermal Convection Modeling:

For this COMSOL MULTIPHYSICS was employed to model heat transfer within the chamber. A simplified 2D model was made with an initial temperature of 200 ºC for the sample stage (Note: the sample is not set at the stage temperature as it is merely placed atop it). Argon gas was added to the model through the top inlet and removed through outlet on the bottom-right as shown in Figure 8a. Within the simulation, the injected gas temperature and flow rate is increased from 24-900 ºC and 0-40 sccm while the substrate temperature (T_{SFC}) is measured as shown in Figure 8b. Due to vacuum conditions minimizing convection and thermally conductive substrate draining energy through conduction, only minor deviations in substrate temperature is observed with a maximum potential increase of ~12 ºC. Gas-heating would also become less effective as the substrate temperature was increased, thus reducing the thermal gap between prospective hot plasma gasses and the substrate, while a stable thermal gap is observed instead. This is to say, if the inlet gas were to be 600 ºC and the sample stage was held at 600 ºC, the gas-heating thermal gradient would be null and there would be no increase in temperature as opposed to the ~70 ºC observed. It should also be noted that borosilicate begins to deform at ~550 ºC, and as the plasma reactor remains optically unchanged gas temperatures exceeding that is highly unlikely.

In order to confirm that the gas temperature is not significantly higher than 600 ºC the rate of gas heating via free electron collisions was modeled via BOLSIG+. Using a 90% Ar and 10% H_2 composition with plasma density of 10^{10} particles/cm^3 and electron temperature of 2 eV, an increase in outlet gas temperature of ~50 ºC is found. This clearly

demonstrates that plasma-heating as localized releases of chemical energy and not kinetic gas-heating is the primary factor in the substrate temperature increase seen in Figure 8b.

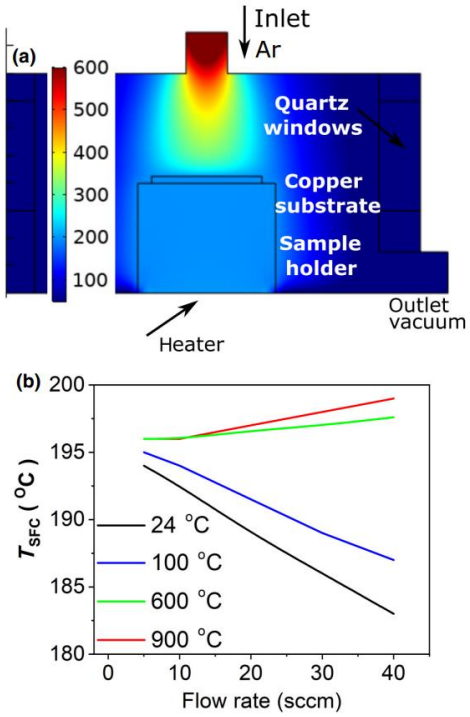

Figure 8: a) COMSOL MULTIPHYSICS heat transfer model to determine convection effects of the potential hot plasma gasses and b) the resulting substrate temperatures upon exposure to differing flow rates and gas temperatures.

1.2.4 – Gas Composition Plasma-Induced Surface-Heating Influence:

As plasma-heating has been shown to be the primary method of substrate heating, a question arises, "what influence does gas composition have over the plasma-heating phenomenon?" To answer this, different Ar:H_2 ratios ranging from 0-20% H_2 are tested. Optical Emission Spectroscopy (OES) was performed on each of these gas-conditions with 10 W input power sustaining the plasma (see Figure 9a). Peak intensities between 640-970

nm are reduced as hydrogen content increases as shown in Figure 9b, demonstrating a general reduction in plasma intensity with hydrogen addition. Following these tests, pristine MGF samples on a 200 ºC stage were exposed to these gas conditions under multiple plasma powering conditions, demonstrating a stratification of plasma-induced surface-heating resulting from changes in gas composition (see Figure 9c). Hydrogen appears to reduce the effects of plasma-induced surface-heating, even preventing gas breakdown at low input powers when making up a large portion of the gas-composition. This difference in general plasma characteristics and observed thermal effects raises the question of whether the presence of hydrogen alters the substrate itself.

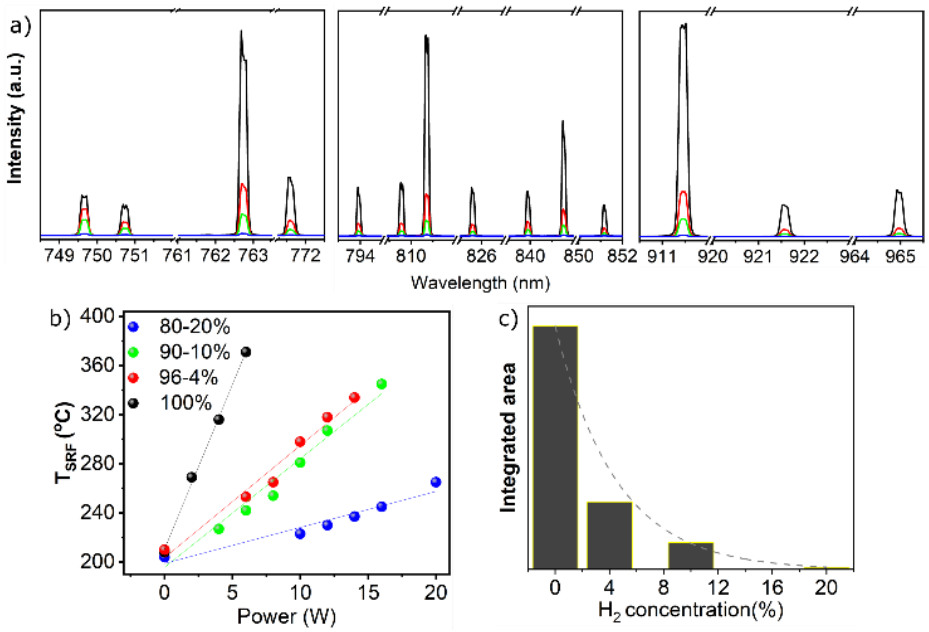

Figure 9: a) Collapsed plasma emission spectra (748-966 nm) for a 10 W Ar plasma with increasing H_2 dilution, and b) substrate temperature with relation to plasma power and gas composition using the same color scheme. c) Integrated area of OES peaks as a function of H_2 dilution.

To answer this Scanning Electron Microscopy (SEM) is performed on the MGF samples before and after exposure to the plasma conditions. Based on the double fitting of the 2D peak method provided by Bellani et al., the estimated number of graphene layers is ~10.[59] After 5 minutes of a 4 W pure argon plasma, continuous films peeled off leaving smaller graphene structures with no apparent change in the I_D:I_G ratio, thus suggesting no major crystal changes (see Figure 10a,b). When altering gas composition to be 20% H_2 and increasing power to 10 W the structure observably changed within SEM images and the I_D:I_G ratio changed from ~0.5 to ~0.9 indicating an increased density of structural defects.[60] This phenomenon is consistent with hydrogen exacerbated anisotropic plasma etching at point defects, which has been previously reported by Xie et al. overall demonstrating gas-composition producing significant impacts on plasma properties and surface interaction effects.[61]

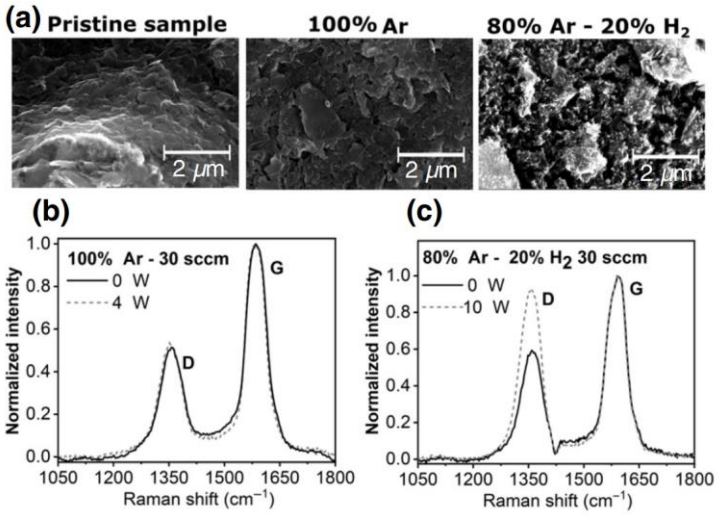

Figure 10: a) SEM images of the graphene sample before and after Ar or Ar:H_2 (80:20) plasma treatment with b) corresponding normalized Raman spectra.

1.2.5 – Summary:

Using multilayer graphene films, we were able to probe the plasma-surface interactions of a non-thermal capacitive RF plasma. In-situ Raman thermometry was able to demonstrate that plasma-heating consistently increased substrate temperatures 68±5 ºC irrespective of the initial temperature of the substrate. The conclusion that plasma-heating and thermal convection from hot gas heated by the plasma was supported through modeling of thermal convection effects in COMSOL MULTIPHYSICS and gas temperature predictions done in BOLSIG+. The uniform temperature increase experienced from plasma exposure also indicated plasma-heating as the thermal gradient convection would experience would reduce in effect as the substrate increases in temperature while near surface reactions would not. Additional testing demonstrated that plasma density, substrate temperature, and substrate etching effects are all dependent on gas-composition and input power. Increasing hydrogen content effectively reducing plasma power and thus substrate temperature effects, while simultaneously increasing etching and altering the graphitic structure. Overall, this study acts as a clear demonstration that this method of in-situ Raman thermometry can non-destructively observe plasma's thermal and structural interactions enabling further studies.

1.3 – Non-thermal Plasmas Material Synthesis

1.3.1 – Gas-Precursor Plasma Synthesis:

Plasmas can form using a variety of precursors. Gasses like helium, hydrogen, or argon are interesting, but unable to form solid material outputs. If adding gasses that contain an atomic species capable of bonding to itself or others and form a solid (eg. carbon, silicon, etc.) the ionization process experienced in plasmas enables chemical reactions or physical adsorption which can result in the formation of materials. This subsection provides a quick introduction into material synthesis via plasma and introduces the standard flow-through reactor geometry used for silicon material synthesis.

Plasma Deposition:

Use of plasmas to grow films or layers of materials on other materials is termed plasma deposition and can be the result of chemical decomposition as with Plasma Enhanced Chemical Vapor Deposition (PECVD) or cross-linking organic materials as for Plasma Polymerization (PP).[62] In comparison to standard thermal Chemical Vapor Deposition (CVD) where the precursor gas is broken down through exposure to heat, PECVD causes feedstock dissociation through electron impact and keeps the temperature comparatively low. As a result, PECVD is regularly used in semiconductor manufacturing as reduced thermal effects enables the use of a wider variety of materials and techniques. Reactor pressures for PECVD film growth are generally within the 0.1-10 Torr range which as shown in later sections is the same regime as PECVD for nanomaterial synthesis and

considerably higher than in etching processes (0.005-0.1 Torr).[20,63] Nanoparticle formation does happen even during designed film growth, but film growth appears to be more dominant when the substrate acts as an electrode. As a method of CVD, PECVD makes the precursor gas reactive or "activated" through ionization or removal of a terminal bond enabling ready reactions to a surface (eg. $SiH_4 + e^- \rightarrow SiH_3^+ + H + 2e^-$).[64] These processes tend to be done at low powers with low fractional ionization (10^{-7}-10^{-4}), sometimes in areas entirely separated from the substrate as with remote PECVD,[65] with the intention of creating reactive compounds that make their way to the substrate.[20] This tends to produce amorphous materials, but heating the substrate several hundred degrees or increasing the power or changing the precursor composition are all methods of inducing increased crystallinity.

Particle Formation:

Within non-thermal and thermal plasmas there are different dominant forces in the formation of nanoparticles.[66,67] An updated review paper by Kortshagen et al. from 2016 is a fantastic introduction to these concepts,[67] while the following is a simplification for clarity of subsequent studies. Current understanding of plasma-based particle formation and growth has been simplified into three stages:[68]

1. *Nucleation* – Formation of neutral or singly charged clusters via anion collisions with small molecules (eg. $Si_nH_{2n}^- + SiH_4 \rightarrow Si_{n+1}H_{2n+2}^- + H_2$) until around 100 core atoms per cluster.[69]

2. *Coagulation* – Due to charging, coagulation between the clusters is fairly imbalanced occurring primarily between small clusters with neutral or opposite net charges.[70] As particles grow their charge is no longer determined primarily by reaction chemistry, but by the accumulation of surface charge as with the Debye sheath.

3. *Surface Growth* – Upon reaching a size where the nanoparticles have attained a net negative charge and are seldom interacting with each other, particle growth is dominated by surface growth through Physical Vapor Deposition (PVD) or Chemical Vapor Deposition (CVD). In this way CVD has reactive molecules react with the nanoparticle surface through heterogeneous reactions, while PVD simply has supersaturated vapor collide and stick to the nanoparticle.[67]

A simple cartoon of these stages is illustrated in Figure 11, clearly defining separate stages of growth despite the fuzzy overlapping nature of reality. As Lopez et al. described, initial particle growth appears to occur rapidly (<50 milliseconds) in diluted mixtures of precursors, allowing for additional plasma exposure to induce crystallization via ionized gas exposure.[23] In effect, amorphous particle formation can be done relatively quickly at lower powers, but more crystalline materials require longer plasma exposure or higher input powers. Additionally, plasma density plays a key role in controlled particle growth as it heavily influences nucleated particle collision probabilities, thus reactor pressure

heavily influencing the average material diameter of synthesized particles as shown in Figure 13 from Section 1.4. It has recently been theorized that particle size limitations may be in part an effect of particle drag overcoming electronic trapping within the E-field.[71,72] Overall, these amount to increased plasma power leading to increased material crystallinity and increased pressure (while maintaining stable non-filamentary plasmas) leading to larger particles.

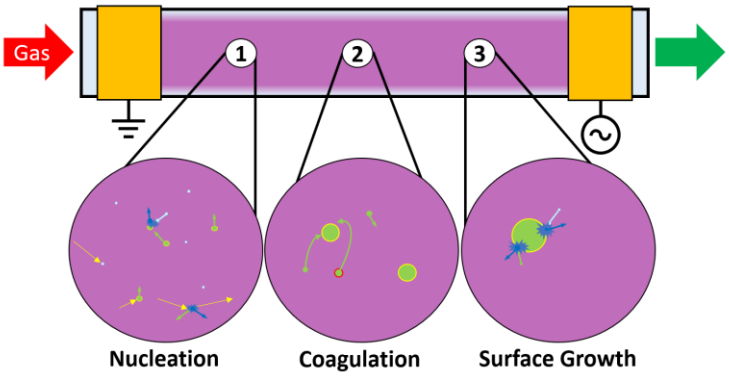

Figure 11: Illustration of particle nucleation and growth within a plasma (yellow indicates electrons and negative charge, red indicates positive charge, green as reactive species, and blue as neutral species).

1.3.2 – Standard Experimental Synthesis and Collection:

As mentioned above, pressure and power influence plasma density which influences particle growth and crystallization. To enable consistent material synthesis these variables need to be controlled with the same high precision as the precursor gas composition and flowrate. Within this text there are several references to plasma reactors used for material synthesis to achieve the described application. Unless specified they follow the same layout with similar if not the same components of construction.

Beginning with the precursor, each system is hooked up to a manifold allowing access to the desired gasses with several layers of Swagelok quarter-turn valves to prevent accidental source contamination. The gasses are supplied primarily through stainless-steel 1/4 inch tubing connected through MKS 1179C Mass Flow Controllers (MFCs) to precursor gasses of Ultrahigh Purity Argon (UHP Ar, Airgas), Ultrahigh Purity Hydrogen (UHP H_2, Airgas), 1.37% SiH4 diluted in Argon (Airgas), and other precursors for differing applications such as Acetylene. The MFCs operate on the principle of thermal conduction, measuring the amount of gas that passes through them via the heat convection from a filament to a thermocouple inside the system, after being calibrated for the gas's thermal characteristics. With an accurate gas flow measurement, it then restricts or enables the flow to the desired quantity by partially opening or closing an internal valve.[??] In this way the MFCs can output within ±1% of their maximum rated flow and enable precise gas mixtures by programming the MKS 247D Four Channel Flow Controller Power Supply and Readout. The selected gas mixture flow through the gas lines and enter the first stage of the reactor. Generally, this is where the pressure is monitored through the use of a 100 Torr MKS 626D12TBE absolute pressure transducer. Pressure readings are sent to an external MKS 651CD2S2N digital/analog pressure controller working in concert with an MKS 253B-1-40-a exhaust throttle valve downstream of the plasma and material collection stages to control the reactor pressure. Gasses then enter the next stage of the reactor which generally consists of a quartz tube ringed by a copper electrode. This quartz tube acts as an electrically insulative reactor wall allowing for the copper ring to supply strong E-fields between it and the electrically grounded ultratorr flanges that the tube is connected to

without shorting. The E-field supplies the gas with enough plasma to ionize and maintain a plasma state, but generally operates at low energy efficiency (10 mm diameter reactors experience ~10% plasma power consumption)[1] due to the electrode geometry radiating away a majority of the power. Power is supplied to the electrode by a RFPP-RF5S radio frequency generator (or equivalent) through an MFJ-989D matching network that acts to ease the electrical signal into the reactor and prevent signal reflection (discontinuous electrical impedances can reflect a portion of RF signals like light travelling from air to water).[73] The input RF signal travels through N-type plug high-voltage coaxial cables to a soldered/crimped connection port on the electrode, supplying the 13.56 MHz signal powering the system. Exiting the plasma section, the material has been synthesized and needs to be collected. The plasma reactor not consisting of ¼ inch tubing or quartz is held together via clamped KF (Kleinflansch – German for "Small Flange") connections that use O-rings to maintain a vacuum seal and metal centering rings to keep the O-rings in place. After the plasma section one of these metal centering rings has a piece of 400 grade stainless-steel mesh clipped to it with a spring-clip. This obstructs the nano-particle laden gas flow with a non-reactive electrically conductive membrane, which collects the nanoparticles with high efficiency despite holes being many orders of magnitude larger, likely through a combination of image charge effects (grounded materials exhibiting charge mirroring to match electric fields), static forces, and van der walls effects as with glitter. Following the collection section is the aforementioned exhaust throttle valve, which is simply a disk that turns to enable or restrict gas flow to induce a desired pressure change. After that is the pump which has its exhaust connected to a fumehood or equivalent air

separation/scrubbing system. Images and simplified cartoon schematics of a standard setup can be seen in Figure 12.

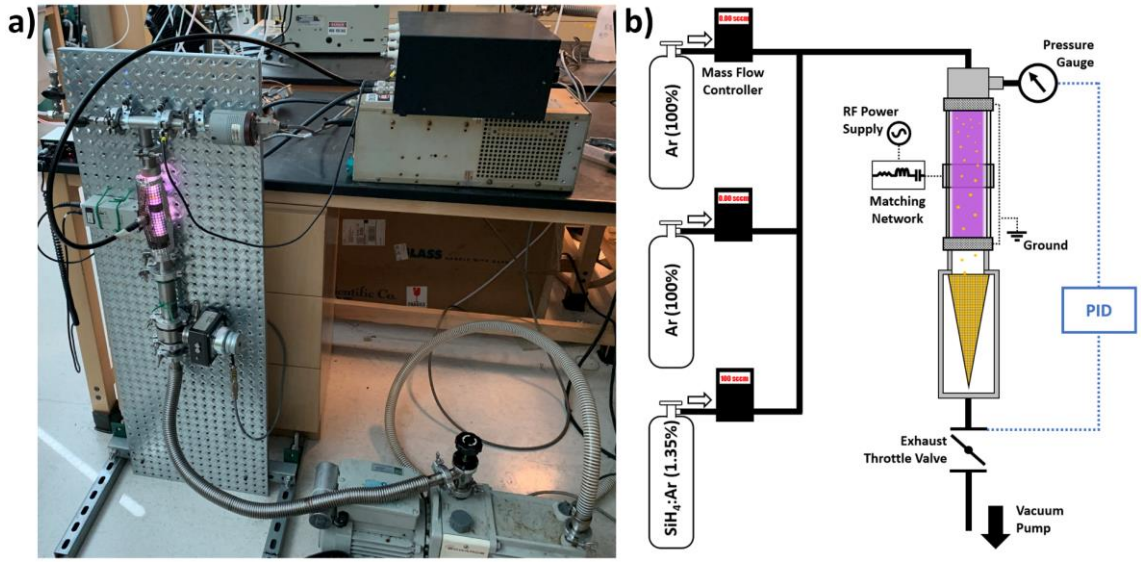

Figure 12: a) Image of a vertically mounted standard silicon synthesis plasma system (used in Section 1.4) and b) corresponding schematic.

Before operating any system, it is "leak-tested" by evacuating the reactor and all connected gas lines, recording the lowest pressure achieved, then closing the pump and timing how long it takes to increase 0.01 Torr. For the sake of consistency, a minimum of a 20 second "leak-rate" was required for all described vacuum experiments (whether or not they used plasma). For experiments requiring higher purities of material (less oxygen contamination) or better size control as with the quantum dot experiments, minimum leak-rates of 90 seconds were used. To achieve these times, air needed to be desorbed/outgassed from the reactor walls and gas lines, which was done by leaving the reactor in a static vacuum state (apply the vacuum and then turn the pump off) overnight. Actively inducing outgassing can also be done through flowing a carrier-gasses or inducing a cleaning plasma with a gas incapable of material synthesis (eg. argon or hydrogen) in a process known as

"sputter cleaning" or "ion scrubbing".[62] When adequate vacuum conditions are achieved, the appropriate gas mixture is flowed, reactor pressure is achieved, and power is supplied to induce the desired material synthesis.

1.4 – Effects of Discontinuous Plasma Exposure on Particle Growth[2]

Flow-through low-temperature plasma reactors provide a simple and effective approach for the synthesis of nanoscale silicon particles.[67,74] These reactors can rapidly consume the chemical precursors such as silane gas and convert it into sub-10 nm unagglomerated particles. The capability of producing small particles with a narrow size range makes this process particularly interesting for the synthesis of next-generation battery materials. Silicon has received considerable attention in this area, because of its high lithiation capacity.[6,75–77] Still, this application is sensitive to the size distribution of the utilized silicon particles, as our group has recently shown by comparing the performance of commercial silicon particles of nominally the same size.[7] Particles in the large size tail of the distribution, with diameters above the generally accepted critical size of ~150 nm,[78] are more likely to fail during repeated lithiation-delithiation cycles. Even though commercial silicon samples may have a small fraction of particles above the critical size, these particles occupy a significant volume fraction of the overall sample. Their mechanical failure due to swelling upon lithiation induces significant loss in anode capacity. It would be highly desirable to have access to silicon particles with a narrow size distribution, without particles at or above the critical size range. On the other hand, the reduction in particle size and the corresponding increase in specific surface area has drawbacks in terms of low first cycle Coulombic efficiency. This is a consequence of electrolyte decomposition at the surface of the active material during the first charging cycles, which results in an irreversible loss of lithium to form a shell known as the solid

electrolyte interphase (SEI). This is highly detrimental for the battery stability, particularly when the anode is interfaced with a real-life cathode material (like lithium iron phosphate or lithium nickel manganese cobalt oxide), as opposed to the lithium metal which is broadly used by the scientific community, but that is not compatible with commercial applications.

These considerations motivate this investigation, which aims at producing silicon powders with a narrow size distribution, but in sizes that are larger than the sub-10 nm particles typically produced by low-temperature plasma reactors. We have found that by operating the radio frequency-driven plasma in a square wave "pulsed mode" it is possible to significanlty increase the average nanoparticle size, from ~8 nm for the case of a continuous plasma to ~20 nm for a pulsed plasma, all while maintaining a fairly narrow size distribution and with no particles above 100 nm in size. We have verified the electrochemical performance of the material and found that the particles produced via the pulsed-plasma indeed show significantly larger first cycle Coulombic efficiency compared to the continuous plasma case.

Our choice of exploring pulsed operation as a mean to tune the particle size is motivated by recent reports discussing the particle charge dynamics in spatial afterglows, i.e. immediately downstream of the plasma volume,[79,80] confirming that the particle charge relaxes in the afterglow and can even become positive depending on process condition, leading to an electrostatically-enhanced agglomeration rate. The complex plasma and dust dynamics in afterglows have attracted the interest of several groups, with the majority of these investigations being of a theorethical nature.[81–86] With this work, we explore the use of pulsed plasma operation to leverage the enhanced particle agglomeration rate in the

afterglow, provide an additional mean to tune particle size, and ultimately realize materials with improved functionality for applications in energy storage.

Given the potential of plasma pulsing for improving material functionality, we have developed a zero-dimensional plasma aerosol model to both investigate the dynamics of particle charge relaxation in the afterglow and to provide a tool that can aid in the choice of process parameters, thus enabling further improvements in the material functionality. Results from this model show good qualitative agreement with the experimental observation in term of particle growth rate, confirming that the systems switches from a configuration in which electrostatic effects slow down agglomeration while the plasma is on, to a configuration in which electrostatic effects actually increase the particle agglomeration rate in the afterglow because of the presence of both negatively and positively charged particles. Still, our model predict a smaller degree of particle growth in the afterglow compared to the experimental observation. This underscores the need for better characterization of these systems in terms of parameters, such as argon metastable density, gas temperature, and kinetics of electron cooling in the afterglow. We have found that all of these parameters affect the particle charge distribution in the afterglow, which in turn affects the kinetics of particle growth via coagulation.

1.4.1 – Particle Production, Analysis, and Battery Testing:

This silicon synthesis system consists of a 2.54 cm (1”) diameter quartz tube fed with a precursor of 1.37% silane (SiH_4)-argon mixture at a 100 standard cubic centimeters per minute (sccm) volume flow rate. SiH_4 is a common precursor for this type of processes,

and low-temperature plasmas rapidly initiate the particle nucleation process in silane-containing mixtures.[23] In addition, the cost of anode materials amounts to only a small fraction of the total battery cost, alleviating concerns related to the cost of silane as precursor for silicon nanoparticle synthesis.[87] The precursor gas is excited into a non-thermal plasma state within the quartz tube through the use of a 13.56 MHz electrical signal supplied by a 2.54 cm thick copper ring electrode. The electrode is wrapped around the outside of the reactor chamber and placed equidistant from the grounded metal flanges on each end of the reactor so as to fill the entire chamber volume with plasma. This setup corresponds to a capacitively coupled plasma, with the RF-biased electrode coupling to the grounded flanges. The flow rate is maintained by an MKS 1179C mass flow controller, while the electrode is powered by an RFPP RF-5S Advanced Energy power supply matched to the reactor's electrical impedance using an MFJ-989D matching network. Both constant and pulsed plasmas are supplied with 100 W of power, with both high time and duty cycle controlled through the power supply. Reactor pressure is controlled through the use of an MKS Digital/Analogue pressure control system with a capacitive pressure gauge. The reactor is evacuated with a roughing pump to a base pressure of ~1 Pa. The leakage rate is tested before each nanoparticle production run, which does not proceed unless the leakage rate is as low as ~2.5 Pa/min or less. Moreover, a cleaning plasma in an argon-hydrogen mixture is ignited before any production run to remove any contaminants potentially absorbed onto the reactor walls. Synthesized material is caught on 5 μm stainless steel mesh, held downstream of the reactor at a sufficient distance to avoid any

coupling between the plasma and the collection mesh. Vacuum is maintained by an Edwards 28 E2M28 rotary vane pump.

The average diameter of the pure silicon material is analyzed through Scherrer's analysis performed on X-Ray Diffraction (XRD) spectra collected on a PANalytical Empyrean Series 2. Transmission Electron Microscopy (TEM) is carried out on a Tecnai T12 to verify the size predicted by the XRD data and to gather size distributions through direct measurement of imaged particles. These TEM grids are prepared by temporarily directing the reactor output through the TEM grid while under vacuum conditions.

For the experiments discussed in this manuscript, the reactor length is 10.1 cm. This gives a residence, based on the flow velocity, of 100 ms for a flow rate of 100 sccm, at a pressure of 526 Pa (4 Torr). The system has been characterized over a wide range of pressures, varying from ~65 Pa to ~4200 Pa (0.5 Torr and 32 Torr). The effect of pulsing has been investigated at 131.5, 263, 526, and 1052 Pa (1, 2, 4, and 8 Torr) with a minimum plasma-on time of 2 ms (corresponding to a frequency of 250 Hz) as limited by the capability of our RF power supply.

For successful cycling of silicon in a lithium-ion (Li-ion) half-cell, a conductive matrix of non-reactive carbon is generally used. Recent advances in chemical vapor deposition (CVD) particle coating techniques have allowed for the controlled deposition of conformal graphitic carbon shells around each particle.[6] After silicon synthesis, the pure silicon material is collected and exposed to 40 sccm of acetylene at a pressure of 50,000 Pa and at a temperature of 650 ^{o}C for 30 minutes to achieve carbon coating, then placed under 20 sccm of argon at 1000 ^{o}C at 263 Pa (2 Torr) for 10 minutes to promote the carbon

shell graphitization. The CVD reaction took place in a 2.54 cm quartz tube with the pure silicon material held in an alumina boat placed in the center of the tube furnace's heating region.

For anode production, the CVD processed materials are mixed in deionized water with carboxymethyl-cellulose (CMC, Sigma Aldrich), which acts as a binder, and spread across 90 mm by 30 mm copper foil with a doctor blade coater. The anode is then vacuum dried at 90 ^{o}C for 12 hours. Circular anodes 12.5 mm in diameter are then punched out of the foil and measured to learn the precise anode weight loading per coin-cell. Coin-cell assembly takes place within an argon filled glovebox, using 2032 stainless steel coin-cell components from MTI. The acting cathode is a 1 mm thick 12.4 mm diameter disk of metallic lithium from Alpha Aesar, with a 25 μm trilayer polypropylene-polyethylene-polypropylene membrane separator, and a 9:1 volume composition of lithium hexafluorophosphate ($LiPF_6$):fluoroethylene carbonate (FEC) as the acting electrolyte.

Chemical analysis is performed on the active anode materials through an FEI NNS450 Scanning Electron Microscope (SEM) and Energy Dispersive X-Ray Spectrometer (EDS). The elemental analysis provided by the EDS measurements and the measured coin-cell weight loading is then used to calculate the theoretical capacity of these batteries and their respective "C rate", i.e. the current required to fully charge or discharge the anode within an hour. The coin-cells are tested on a Neware BTS 4000, set to perform 5 cycles at 0.1 C from 1.5 V to 0.05 V for anode "formation", a standard industry process allowing for slow development of a solid electrolyte interphase that will permit cycling

stability. Upon completing the formation cycles the battery testing system then cycles the half-cells at 0.5 C until adequate data is collected.

Four silicon synthesis conditions are chosen for a direct comparison of their electrochemical performance. The tested samples were all prepared at a pressure of 526 Pa (4 Torr), 100 sccm of precursor mixture, and a 50% pulsing duty cycle. One of the samples is produced under continuous conditions, while the others are produced with 3, 12.5, and 25 pulses per residence time (corresponding to 30, 125, and 250 Hz pulsing frequency). All the samples undergo the same CVD coating, anode production, battery assembly, and half-cell testing processes described above. The anode weight loading is consistently between 1.0 and 1.21 mg/cm^2 for all the tested samples.

1.4.2 – Coagulation Modeling and Calculations:

The coagulation of nanoparticles in both the plasma and its afterglow is modelled using the governing equation from *Coagulation of symmetric and asymmetric bipolar aerosols* by S. Vemury et al.:[88]

$$\frac{dN_i^p}{dt} = \frac{1}{2}\sum_{q=-\infty}^{\infty}\sum_{j=1}^{i-1}\beta_{i-j,j}^{p-q,q}N_{i-j}^{p-q}N_j^q - \sum_{q=-\infty}^{\infty}\sum_{j=1}^{i-1}\beta_{i,j}^{p,q}N_i^pN_j^q$$

Equation 5: Coagulation of charged aerosols in the absence of electrostatic dispersion.

Where N_i^p is the number density of particles with volume v_i and charge p. The indexes i and j refer to the particle volume, which is assumed to be an integer multiple of the primary particle volume. For the results discussed here, the primary volume is the one corresponding to a particle with a diameter of 8 nm. This choice is motivated by

experimental measurements, which suggest that the particle average diameter is 8 nm with a narrow size distribution for a continuous plasma operating at a pressure of 526 Pa (4 Torr). The indexes *p* and *q* refer to the number of elementary charges on each particle. The coeficient β accounts for the rate of coagulation as a function of both size and charge of the collision partners. It can be written as:

$$\beta_{i,j}^{p,q} = Q_{i,j}^{p,q} \beta'_{i,j}$$

Equation 6: Coagulation coefficient of charged particles.

Where $\beta'_{i,j}$ is the coagulation coeficient for neutral particles of volumes v_i and v_j, in the free molecular regime:[89]

$$\beta'_{i,j} = \left(\frac{3}{4\pi}\right)^{\frac{1}{6}} \left(\frac{6k_B T_{gas}}{\rho}\right)^{\frac{1}{2}} \left(\frac{1}{v_i} + \frac{1}{v_j}\right)^{\frac{1}{2}} \left(v_i^{1/3} + v_j^{1/3}\right)^2$$

Equation 7: Frequency of coagulation between two particles of volume v_i and v_j.

Here ρ is the particle material density (2330 kg/m^3 for silicon), k_B is the Boltzmann constant and T_{gas} is the gas temperature. The term $Q_{i,j}^{p,q}$ accounts for the electrostatic interaction between colliding nanoparticles and it is written as:[89]

$$Q_{i,j}^{p,q} = \begin{cases} exp\left(-\dfrac{pqe^2}{4\pi\epsilon_0 R_{s,ij} k_B T_{gas}}\right) if\ p \cdot q > 0 \\ -\dfrac{pqe^2}{4\pi\epsilon_0 R_{s,ij} k_B T_{gas}} \qquad if\ p \cdot q \leq 0 \end{cases}$$

Equation 8: Charge coefficient for particle interactions.

Where e is the elementary charge and ε_0 is vacuum permittivity. This term induces an increase in the agglomeration rate for particles of opposite charge, and a reduction in agglomeration rate for particles of the same charge. $R_{s,ij}$ has the following expression:

$$R_{S,ij} = \left(\frac{3}{4\pi}\right)^{1/3}\left(v_i^{1/3} + v_j^{1/3}\right)$$

Equation 9: Radius of newly formed particles.

Equation 5 is coupled to the following equation that accounts for the charging of nanoparticles, both in the plasma and in the afterglow, because of collision with electrons, ions and metastables:

$$\frac{dN_i^p}{dt} = -\left(\nu_e^{i,p} + \nu_i^{i,p} + \nu_M^i\right)N_i^p + \nu_e^{i,p+1}N_i^{p+1} + \left(\nu_i^{i,p-1} + \nu_M^i\right)N_i^{p-1}$$

Equation 10: Rate of change for nanoparticles of size *i* and charge *p*.

Where $\nu_e^{i,p}$ is the collision frequency between electrons and a particle with volume v_i and charge *p*, $\nu_i^{i,p}$ is the collision frequency between ions and a particle with volume v_i and charge *p*, and ν_M^i is the collision frequency between argon metastables and a particle with volume v_i. For electrons, the rate of nanoparticle charging is determined using the orbital motion limited (OML) theory:[90–92]

$$\nu_e^{i,p} = \begin{cases} n_e \pi R_{p,i}^2 \upsilon_{e,th} exp\left(\dfrac{eV_{p,i}}{k_B T_e}\right) & if\ V_p < 0 \\ n_e \pi R_{p,i}^2 \upsilon_{e,th}\left(1 + \dfrac{eV_{p,i}}{k_B T_e}\right) & if\ V_p \geq 0 \end{cases}$$

Equation 11: Electron-particle collision frequency.

Where n_e is the electron density, $R_{p,i}$ is the radius of a particle with volume v_i, $\upsilon_{e,th}$ is the electron thermal velocity, T_e is the electron temperature and $V_{p,i}$ is the particle floating potential, equal to $ke/4\pi\epsilon_0 R_{p,i}$ with *k* being the number of elementary charges carried by the particle. For ions, we use the expression from Gatti and Kortshagen to account from deviations from the OML theory due to ion collisions with the backgroun gas:[93]

$$\nu_i^p = \begin{cases} n_i \pi R_p^2 \upsilon_{i,th} exp\left(-\frac{eV_p}{k_B T_i}\right) & if\ V_p \geq 0 \\ P_0 \nu^{OML} + P_1 \nu^{CE} + P_2 \nu^{HY} & if\ V_p < 0 \end{cases}$$

Equation 12: Ion-particle collision frequency.

Where n_i is the ion density, $\upsilon_{i,th}$ is the ion thermal velocity, and T_i is the ion temperature. ν^{OML}, ν^{CE}, ν^{HY} are the ion-nanoparticle collision frequency in the OML (collisionless) limit, for the collision-enhanced regime, and for the hydrodynamic limit, respectively. P_0, P_1 and P_2 are weights that depend on the particle Knudsen number. For the exact expression of these terms, we refer the reader to *Analytial model of particle charging in plasmas over a wide range of collisionality* by M. Gatti et al.[93] We have found that utilizing this expression for the ion collection frequency makes a significant difference in the average particle charge for a given plasma condition, reducing by roughly 50%. This is to be expected, given the relatively high pressure at which the experiments are performed and the calculations are run (526 Pa). We calculate the Knudsen number λ_i/R_p (with λ_i being the ion mean free path) to be ~1000 for a 8 nm particle, sufficiently small to lead to a deviation from OML theory. The ion mean free path is estimated to be 4.7 μm at 526 Pa (4 Torr), based on the ion mobility data from *Mobilities and Reactions of Ions in Argon* by K.B. McAfee et al.[94] We assume the dominant ion to be H_3^+.[95,96] At 526 Pa, the ion mobility is 1038.8 $cm^2/(V \cdot s)$ and the ion diffusion coefficient is 26.84 cm^2/s.

The charging frequency due to collisions between a particle with volume v_i and metastable argon atoms is equal to:

$$\nu_M^i = n_M \pi R_{p,i}^2 \upsilon_{M,th}$$

Equation 13: Metastable-particle collision frequency.

With n_M equal to the argon metastable density and $\upsilon_{M,th}$ being the metastable thermal velocity. n_M is the sum density of the $1s_5$ and $1s_3$ metastable states (in Paschen notation) at energies of 11.548 eV and 11.723 eV respectively. The metastable translational temperature is assumed to be equal to the gas temperature.

This basic set of equations is solved in two different ways depending on whether the 'plasma on' or the 'afterglow' phase is modelled. For the 'plasma on' phase, the ion density, metastable density and electron temperature are kept constant and equal to values obtained from the literature. The ion density is $n_i = 10^{11}$ cm^{-3} and the electron temperature T_e is equal to 4 eV.[22] The metastable density is has been reported to be as high as $2x10^{11}$ cm^{-3} for the case of a low-temperature dusty plasma with carbon particles dispersed within it.[86] Interestingly, the metastable density has not been measured for the case of a flow-through, silicon nanoparticle-producing plasma such as the one used here. In the model, we have varied the metastable density between 10^8 cm^{-3} and 10^{13} cm^{-3} to investigate its role on the charging dynamics. The electron density is calculated by assuming quasineutrality, i.e. $n_i = n_e + k \cdot n_p$ with n_p being the total nanoparticle density equal to $\sum_{p=-\infty}^{\infty} \sum_{i=0}^{\infty} N_i^p$.

In the 'afterglow' phase, the electron, ion and metastable densities decay in time with a rate calculated using the collection frequencies in equations (7), (8), and (9). Quasineutrality is not strictly applied in the afterglow. In addition, diffusional losses of charge carriers to the reactor walls are accounted for by using effective electron and ion diffusion coefficients. These are calculated using the approach outlined in the works of L. Couëdel et al. and R.A. Gerber et al.[82,97] In short, the electron and ion diffusion coeficients are equal to the ambipolar diffusion coefficient, $D_i \cdot (1 + T_e/T_i)$ with D_i being the ion diffusion

coefficient, in the early phase of the afterglow. Later in the afterglow, the electron and ion diffusion coefficients diverge following the trend shown in figure 1 of L. Couëdel's *Influence of the ambipolar-to-free diffusion transition on dust particle charge in a complex plasma afterglow*.[82] The critical parameter that controls the transition is the ratio between the electron debye length and the system characteristic diffusion length, equal to R/2.404 for a cylindrical system, with R being the inner reactor radius (10 mm in our case). This approach allows to transition smoothly from an ambipolar diffusion regime early in the afterglow, to a free diffusion regime late in the afterglow when electrons cool and the debye length increases.

We make the reasonable assumption that ion and metastable temperature are in equilibrium with the gas temperature. The electron temperature is calculated by assuming that each electron lost to either the reactor wall or to the nanoparticles carries with it an average energy of $2k_BT_e$.[32] We assume that the electron temperature cannot decay below the gas temperature in the afterglow, i.e. T_e has a floor value equal to T_{gas}.

This set of equations is discretized and integrated in time using an explicit scheme with an adaptive time step. The initial time step is set to 10 ns, and its value can increase by up to a factor of 5 depending on the rate of change in the electron density value. This captures the need for a shorter computational time step earlier in the 'plasma on' phase when particles are charging and the electron density is decaying, as well as earlier in the 'afterglow' phase when the particle charge is neutralizing and the plasma density is decaying.

As initial conditions, we use monodispersed particles with a diameter of 8 nm and without charge. First, the 'plasma on' phase is calculated until a steady state in average particle charge and in electron density is reached. This occurs within 10 μs. The plasma is then turned off and the model switches to the 'afterglow' case.

For the results discussed in this manuscript, we used a total of 14 charge bins (from -8 to +5 charges per particle) and 12 volume bins (from a 8 nm particle to a 18.315 nm particle). See Apendix A for the full python code.

1.4.3 – Silicon Nanoparticle Growth and Impacts on Battery Cycling:

Figure 13a summarizes the dependence of the average particle diameter on the reactor pressure, for the case of a continuous plasma. The total flow rate is constant and equal to 100 sccm (1.37% silane in argon). An increase in reactor pressure induces an increase in particle size, going from <5 nm at 131.5 Pa (1 Torr) to 16 nm at 4210 Pa (32 Torr). Unfortunately, we have also reproducibly observed a significant drop in particle yield at higher operating pressures, going from ~50 mg/hour at 526 Pa (4 Torr), corresponding to a 50% silane-to-particle conversion rate, to ~5 mg/hour at 4210 Pa (32 Torr), making this approach challenging for applications requiring large yields. In Figure 13b, we show the variation in particle diameter at different reactor pressures, but comparing the continuous mode (0 pulses) to pulsed mode with varying number of pulses per residence time. The duty cycle was 50% for all of these samples. Given the residence time of 100 ms, based on flow velocity, the 3, 12.5 and 25 pulses per residence time correspond to pulsing frequencies of 30 Hz, 125 Hz and 250 Hz respectively.

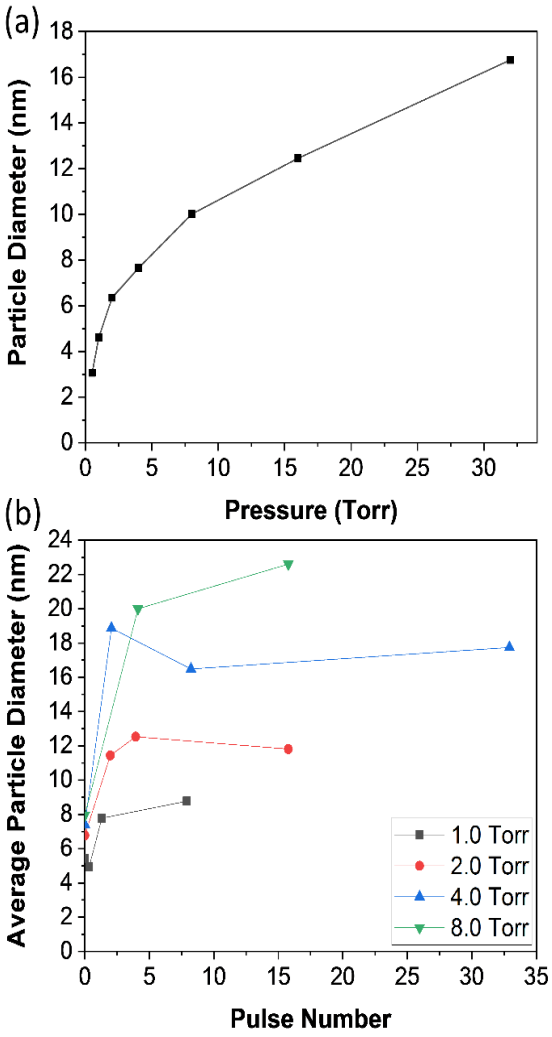

Figure 13: (a) Average particle diameter as a function of reactor pressure for a continuous plasma. (b) Average particle diameter at various pressure, as a function of number of plasma pulses per residence time. The duty cycle is 50% for all these measurements. The diameters reported in this figure are based on XRD measurements and Scherrer's analysis.

We should point out that we have also observed a decrease in mass yield for the pulsed case compared to the continuous case, although that drop is less severe (from ~50 mg/hour to ~30 mg/hour). The average particle diameters for Figure 13 have been obtained by X-ray diffraction measurements, using Scherrer analysis to estimate the crystal size. From Figure 13b, it is clear that operating the plasma in pulsing mode has important

consequences on the particle size, with even 3 pulses inducing a significant increase in diameter. Figure 14a shows the particle size distribution for the continuous and for the pulsed cases, with Figure 14b-e showing some representative TEM micrographs. The TEM analysis is in good agreement with the average particle diameters obtained by XRD and shown in Figure 13. For the continuous case, the average particle diameter is 8 nm and the size distribution is narrow, in agreement with previous reports suggesting that electrostatic stabilization while in the plasma prevents particle agglomeration.[23] Even with 3 pulses per residence time, the average particle size increaseses significantly to almost 20 nm. The size distributions for the pulsed cases is still relatively narrow, with very few particles in the 50-100 nm range and no particles above 100 nm in size.

After silicon production we have proceeded to investigate the effect of pulsing on the electrochemical performance of the materials when used as anodes for lithium-ion

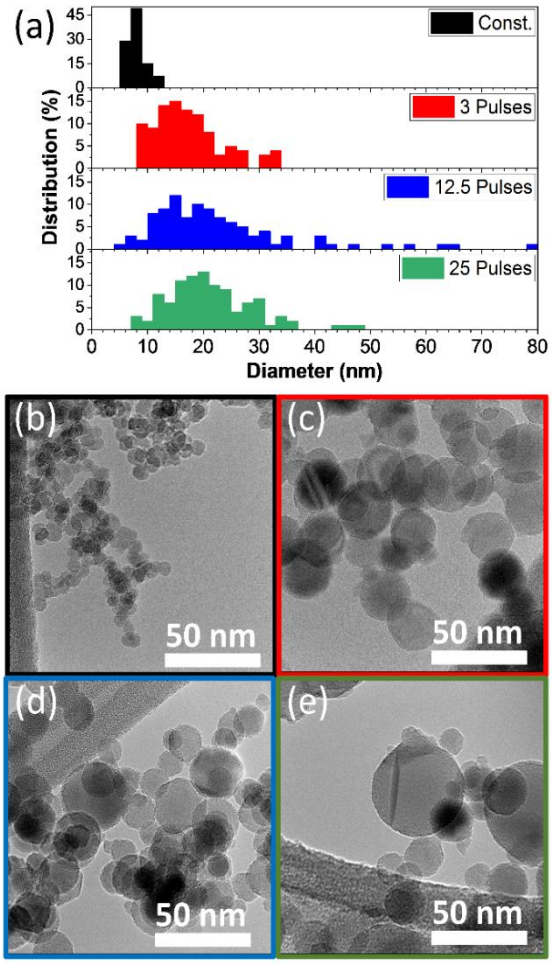

Figure 14: (a) Particle size distributions for the continuous and pulsed cases, as obtained by analysing several TEM micrographs. (b-e) Representative TEM micrographs for particles produced with a continuous plasma, or with 3, 12.5 and 25 pulses per residence time, respectively.

batteries. The samples shown in Figure 14 were processed according to the procedure outline in the experimental details section of this manuscript. In short, it is important to coat the silicon with a carbon protective layer to enhance their electrochemical performance. Moreover, it is preferrable to achieve a high degree of graphitization of the

carbon shell to improve the electrical transport properties of the anode.[6] This can be achieved by the two-steps chemical vapor deposition and graphitization process that our group has previously described in details.[6] The same technique is used to process the silicon particles discussed here. TEM micrographs for particles produced in continuous and pulsed modes, after carbon coating, are shown in Figure 15. The silicon cores appear enclosed in a conformal carbon layer. Elemental analysis perform via SEM suggest that the silicon-to-carbon ratio is between 0.6 and 0.7 for the pulsed samples, by weight. The ratio is significantly smaller (0.24) for the particles produced with a continuous plasma. All the samples are processed using identical CVD parameters in terms of process time, temperature and pressure. The fact that a comparatively thicker carbon layer is grown on the smallest particles, with the same processing condition, hints at a curvature dependence on the carbon growth kinetics.

The sample electrochemical characterization is summarized in Figure 16. Figure 16a shows the cycling data for the 4 samples shown in Figure 14. The sample produced

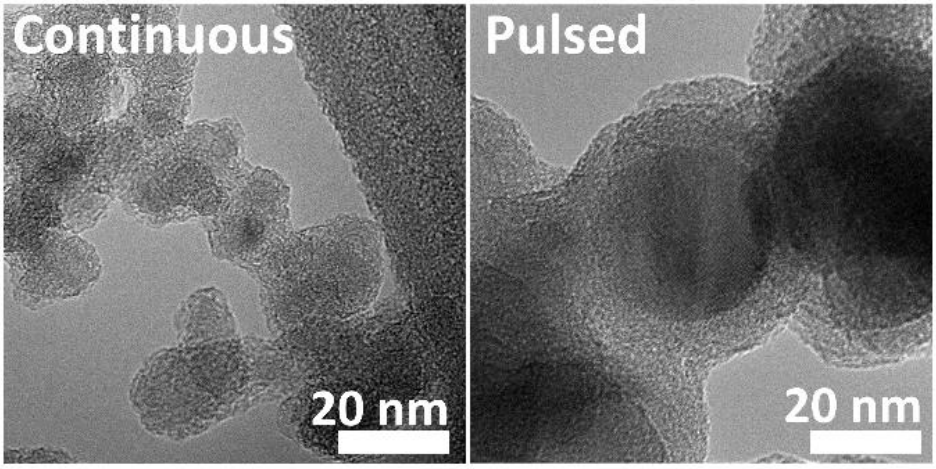

Figure 15: TEM micrographs of silicon particles produced using a continuous (left) or pulsed (right) mode, after coating with a graphitized carbon shell.

with a pulsing plasma have a gravimetric capacity of between 1000 and 1400 mAh/g. They show reasonable stability, with <10% capacity loss over the first 60 charge-discharge cycles. The sample produced with a continuous plasma has significantly lower capacity, around 400 mAh/g. This is expected given the significantly lower content of silicon in the sample. The cycling stability for this sample is very good. Figure 16b shows the variation in Coulombic efficiency over number of cycles for the 4 samples. The samples produced with a pulsing plasma have a first cycle efficiency of ~74%, while the sample produced with a continuous plasma has a significantly lower first cycle efficiency (<50%). This confirms that even a relatively small change in particle size (from 8 nm to 20 nm) has profound effects on the anode performance, and that this application is particualrly sensitive to particle size. All samples show good stability, likely because there are no large particles (close to 150 nm or above) in these samples.

Overall, these data confirm that it is desirable to achieve a precise control on the size distribution of silicon particles, as their performance as anode material in lithium-ion batteries is strongly affected by it. A simple approach such as pulsing of the RF power has important consequences on the particle size, even at seemingly low pulse rates.

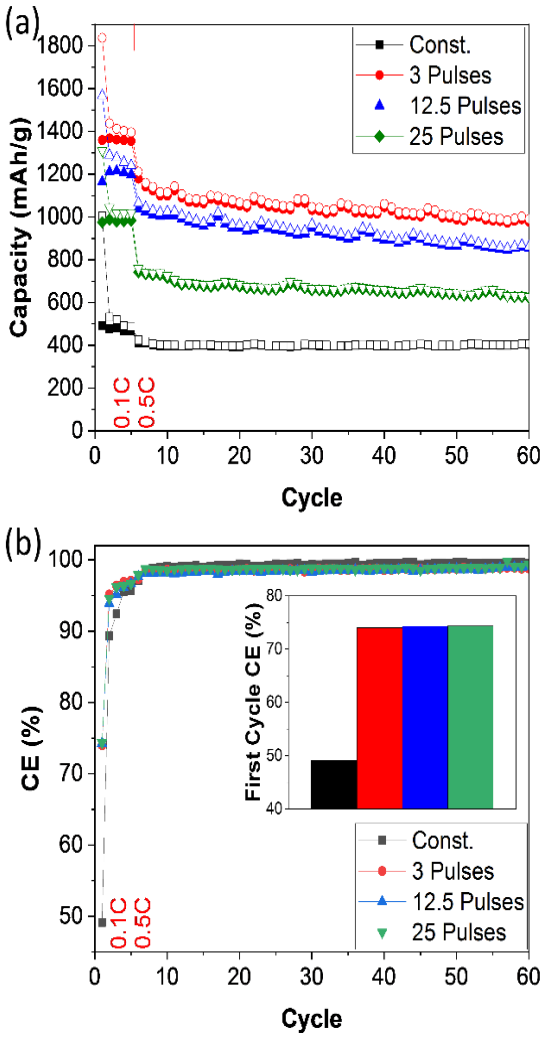

Figure 16: (a) Gravimetric capacity vs. cycle number for the samples produced with a continuous plasma and at varying pulsing frequencies. The charging rate is kept at 0.1C for the first 5 formation cycles, then increased to 0.5C. (b) Same as (a) but showing the Coulombic efficiency vs. cycle number. In the inset we summarize the first cycle efficiency for the samples.

1.4.4 – Modeling Variables Impacting Nanoparticle Growth and Charging:

To better understand how pulsing affects the kinetics of coagulation in this system, we have performed a series of computational experiments using the modelling approach outlined earlier in the computational details section. Figure 17 shows the modelled variation in critical parameters during the 'plasma on' and 'afterglow' phases of the process. During the 'plasma on' phase (Figure 17a), the initially neutral aerosol is charged and acquires an average negative charge of ~ -1.45. The ion density is kept constant during this phase. The electron density rapidly decays as more negative charge is carried by the particles. The nanoparticle density remains stable and close to its initial value. This value is calculated using the experimentally measured mass production rate (~ 50 mg/hour) for the case of 8 nm particles produced in the continous plasma. The system reaches steady

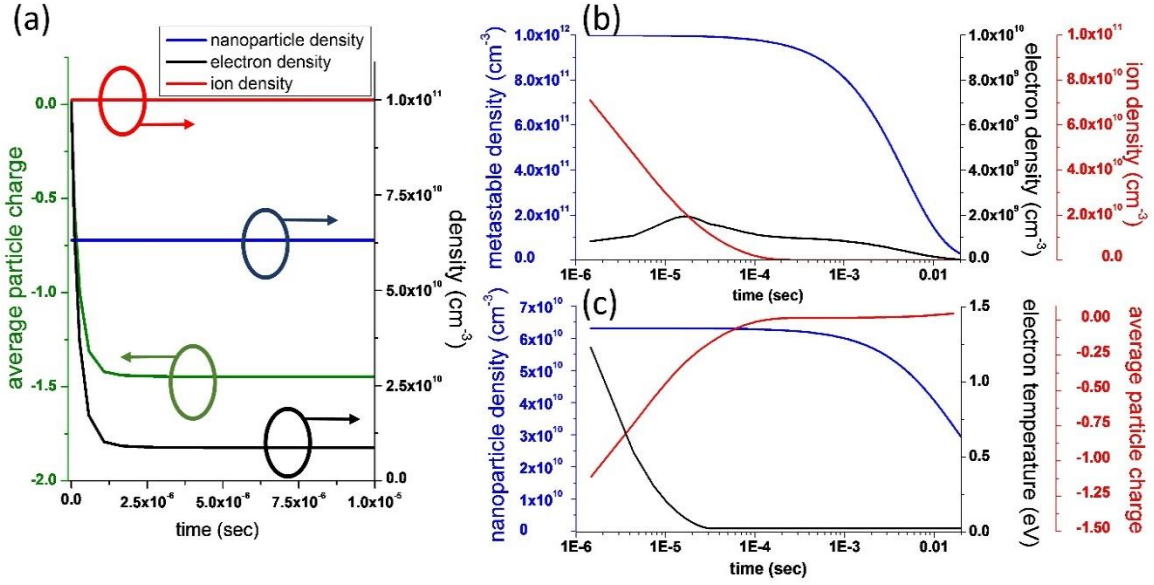

Figure 17: (a) Time variation of ion, electron and nanoparticle densities, together with the average particle charge, during the 'plasma on' phase. (b) Time variation of ion, electron and metastable densities in the plasma afterglow. (c) Same as (b), but showing the nanoparticle density, the electron temperature and the average particle charge. Please note that the x-axis is on a logarithmic scale for plots (b) and (c).

state rapidly, well within 10 μs. After steady state is reached, the model switches to the 'afterglow' phase, with results summarized in Figure 17b-c. For this plot, a single afterglow with a total duration of 20 ms is considered. The metastable density is assumed to be 10^{12} cm^{-3} for these plots. Figure 17b shows the decay of charge carriers and argon metastables as a function of time. It should be noted that the electron and ion densities are plotted on two different y-axes, for clarity. The ion density drop considerably with 100 μs. The electron density has a more complex time dependance. This is due to the presence of long-lived argon metastables, which continuously supply electrons to the reaction volume by ionizing collisions with the nanoparticles. These trends are in good agreement with previous modelling results and measurements of metastable lifetime in afterglows, which are well know to be several microseconds.[80,85,86] Measurement of the electron density decays in dusty plasma afterglows are also consistent with these computational result.[98] The electron temperature decays from its initial value of 4 eV to its floor value, equal to the gas temperature, within 50 μs. It should be mentioned that we assume that the electrons supplied late in the afterglow because of nanoparticle-metastable collisions are assumed to be "cold", meaning at a temperature equal to the gas temperature. We also neglect metastable pooling effects, which could both induce a more rapid decay in the metastable density but also result in electron heating due to the formation of energetic electrons after metastable-metastable collisions. This assumption is justified by the relatively slow kinetic of the metastable pooling reaction compared to quenching at the nanoparticle surfaces, which we estimate to be the dominant quenching mechanism even for metastable densities as high as 10^{12} cm^{-3} when using the pooling reaction rate from *A global model for the*

afterglow of pure argon and of argon with negatively charged dust particles by I. Denysenko et al. (6.2×10^{-10} cm^3/s).[83] Also shown in Figure 17c are the nanoparticle density and average nanoparticle charge. The density drops by roughly a factor of 2 within 20 ms, while the average charge relaxes from the negative value acquired in the plasma to zero in less than a millisecond. After this relaxation phase, the charge becomes quasi-steady-state, with a visible increase to a small positive value around 10 ms of afterglow time. This is likely due to the transition from ambipolar to free diffusion regime, which induces a loss of electrons at the reactor walls.

We have found that electrostatic effects enhance the agglomeration of particles in the afterglow. These effects are dependent on the shape of the charge distribution in the quasi-steady-state phase of the afterglow (after ~1 ms), which in turn is dependent on various process parameters. Here in particular we discuss the importance of metastable density and gas temperature on the coagulation dynamics in the afterglow. The dependece on the metastable density is summarized first in Figure 18a-d. For these computation experiments, the gas temperature is kept at 300 K, and the ion density and electron temperature are kept at the same values specified before (10^{11} cm^{-3} and 4 eV respectively). The metastable density is varied between 10^8 cm^{-3} and 10^{13} cm^{-3}. Admittedly, the 10^{13} cm^{-3} value is probably unrealistic, although values exceeding 10^{11} cm^{-3} have been reported for the case of an argon plasma with carbon nanodust dispersed within it.[86] Figure 6a shows the variation in nanoparticle density in the afterglow for the two limiting values of metastable density. The higher metastable density leads to a faster decrease in nanoparticle density. The charge distributions after 2 ms in the afterglow are shown in Figure 18b. The

higher metastable density leads to a broader charge distribution, in particular with a higher fraction of positive particles. We choose to use two quantities to describe the shape of the particle charge distribution: the ratio between the densities of particles with charge +1 and charge -1 (Q_{+1}/Q_{-1}) and the ratio between the particles with charge +1 and the non-charged particles (Q_{+1}/Q_0). The first parameter describes how symmetric is the distribution, and the second provides information on its width. As shown in Figure 18c, Q_{+1}/Q_{-1} remains close to 1 over the range of considered metastable densities, although it increases to 2.5 for the maximum density value. Q_{+1}/Q_0 progressively increases as the metastable density increases.

These two descriptors correlate well with the dependece of nanoparticle density and size with the metastable density, as shown in Figure 18d. This is reasonable, as a broader charge distribution is expected to lead to a more significant electrostatic enhancement of the coagulation rate in the afterglow. Interestingly, the gas temperature also has an effect the charge distribution in the afterglow, as summarized in Figure 18e-h. Increasing the gas temperature from 300 K to 1000 K leads to an increase in the agglomeration rate and a faster drop in nanoparticle density (see Figure 18e). The charge distribution at 1000 K appears to be wider than at 300 K, as shown in Figure 18f and as confirmed by the variation of the Q_{+1}/Q_{-1} and Q_{+1}/Q_0 parameters (Figure 18g). Figure 18h indeed shows how the

increase in temperate progressively increases the particle size and decreases the particle density after 20 ms in the afterglow.

This dependence can be theorethically predicted by writing an expression for the fraction of particles with zero charge, F_0:

$$\frac{dF_0}{dt} = -(\nu_M + \nu_e^0)F_0 + \nu_M F_{-1} + \nu_e^{+1} F_{+1}$$

Equation 14: Change in the fraction of net-zero charge particles.

Where ν_M is the charging frequency due to metastable collisions, ν_e^0 and ν_e^{+1} are the electron collection frequencies for a neutral and a positive particle respectively, and F_{-1} and F_{+1} are the fraction of particles with charges -1 and +1 respectively. Here we neglect the role of positive ions, since we are considering the later stage of the afterglow after the ion

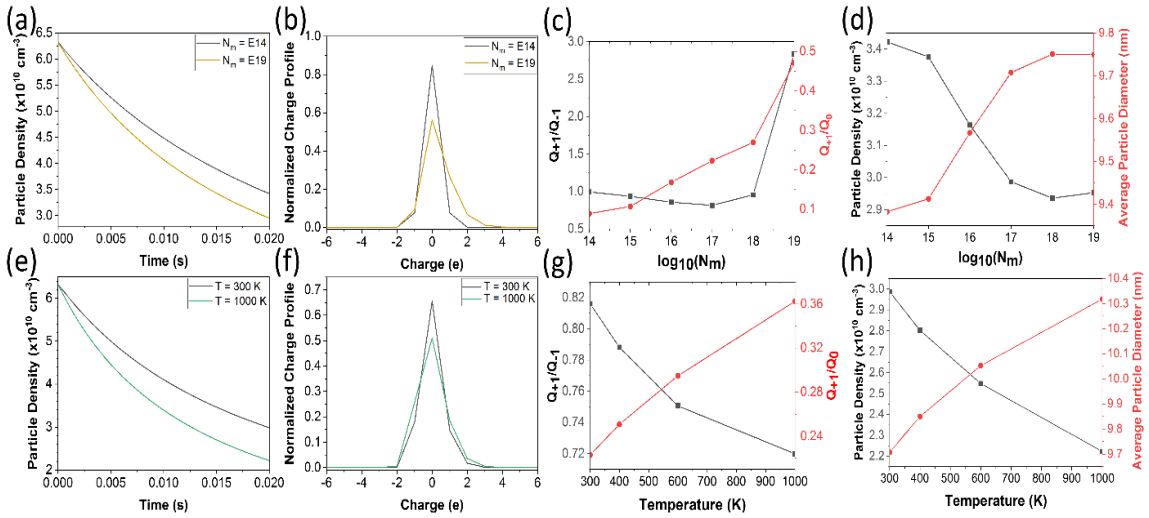

Figure 18: (a) Evolution of total particle densities in the afterglow for initial metastable densities of 10^8 cm^{-3} and 10^{13} cm^{-3}. (b) Corresponding particle charge distributions in the afterglow, after the initial charge relaxation transient. (c) Dependence of the Q_{+1}/Q_{-1} and Q_{+1}/Q_0 parameters on the initial metastable density. (d) Dependence of particle size and density on the initial metastable density. (e) Evolution of total particle density in the afterglow for gas temperature of 300 K and 1000 K. (f) Corresponding particle charge distributions in the afterglow, after the initial charge relaxation transient. (g) Dependence of the Q_{+1}/Q_{-1} and Q_{+1}/Q_0 parameters on the gas temperature. (h) Dependence of particle size and density on the gas temperature.

density has decayed. Since the charge distribution is near steady state after the initial transient, and approximating its shape to be symmetric (meaning $F_{+1} \approx F_{-1}$), we then find:

$$\frac{F_{+1}}{F_0} = \frac{\nu_M + \nu_e^0}{\nu_M + \nu_e^{+1}}$$

Equation 15: Ratio of positively particles with a +1 to zero net charge.

This relation explains why an increase in the metastable density leads to a broadening of the particle charge distribution in the afterglow, since this leads to an increase in ν_M. In addition, and increase in temperature also leads to a broadening of the charge distribution because the charging frequencies ν_e^0 and ν_e^{+1} are related by the following, according to OML theory:

$$\nu_e^{+1} = \nu_e^0 \left(1 + \frac{eV_p}{k_B T_e}\right)$$

Equation 16: Charging frequency relation.

This implies that an increase in electron temperature in the afterglow brings their ratio closer to one, widening the particle charge distribution and enhancing the particle coagulation rate. We remind the reader that for simplicity we assume that the electron temperature has a floor value equal to the gas temperature. Therefore, varying the gas temperature also affect the electron temperature late in the afterglow. We assume that electrons emitted from particles after collision with a metastable are "cold" (i.e. 300 K). A more precise description of the electron temperature and of the degree of non-thermal equilibrium in the late afterglow is needed to model the coagulation dynamics with greater precision. Indeed more refined simulations have shown that the electron temperature can exceed the gas temperature by more than one order of magnitude even after 1 ms in the

afterglow, because of long-lived metastables.[81,84] With respect of gas (neutral) temperature, a value of 1000 K is probably excessively high for this system, although it is also well-known that the assumption that the gas temperature stays at 300 K is simplistic.[85] There is a need of more precise experimental measurements of both the metastable density and the gas temperature in this system, as they affect the particle agglomeration dynamics.

Finally, in Figure 19 we show the result of a computational experiment in which the system is pulsed 10 times. While in the experiment we use a 50% duty cycle (meaning the plasma on time is equal to the afterglow time), for the sake of reducing computational time the plasma is kept on only for 10 μs per pulse, as this is more than sufficient for the system to reach steady state. Figure 19a shows the evolution of particle density over the sum of 10 afterglows, each with a 2 ms duration. The result is compared to the case in which the plasma is kept on for 20 ms (continuous case) and for the case of a neutral aerosol with same initial average size and density as for the plasma cases. Pulsing of the plasma leads to a clear decrease in nanoparticle density compared to the continuous plasma case, consistent with the experimental result. Moreover, pulsing leads to an enhanced particle agglomeration compared to the neutral case in which any electrostatic enhancement of the agglomeration rate is absent. Figure 19b-c show a 2 dimensional plot of the particle density as a function of size (x-axis) and charge (y-axis) after the last plasma on phase and after the last afterglow, confirming that the charge relaxes to zero in the afterglow and the density at large particle sizes increases.

While the data discussed so far suggests that the bipolar charge distribution in the afterglow enhances the agglomeration kinetics compared to the neutral case, our modelling

results are still only in qualitative agreement with the experimental data. Given a 100 ms residence time in the experiment, the 25 pulses case at 50% duty cycle corresponds to a duration of 2 ms for the plasma on and afterglow phases. In the total afterglow time (50 ms) the size grows from 8 nm to 20 nm, leading to a drop in nanoparticle density by a factor of more than 15. Various reasons may contribute to the quantitative disagreement between our model results and the experimental data. As recently shown by Chen and Hogan,[80] the thermal desorption of negative charges from the particles may have an important effect on both the average particle charge in the plasma and on the charge distribution in the afterglow. The reduced heat loss to the background gas at lower pressure leads to an increase in particle temperature, making electron desorption more likely. There is also siginificant uncertainty on the value of energy barrier that should be used to estimate the emission current. In our previous work, the emission current was estimated via the Richardson Dushman equation using the material work function in the exponential term, reduced by the coulombic potential of the charges present on the particle.[99] This value is typically a few eVs. Chen and Hogan use signicantly lower energy barriers,[80] with values of either 0.6 eV as derived in *Physisorption kinetics of electrons at plasma boundaries* by F.X. Bronold et al.,[100] or 1 eV based on the measurements reported in *Tandem IMS-MS study of ion evaporaition from ionic liquid-acetonitrile nanodrops* by C.J. Hogan Jr and Fernandez de la Mora.[101] In addition, there is also uncertainty in the temperature that nanoparticles attain in these systems, while in the plasma.

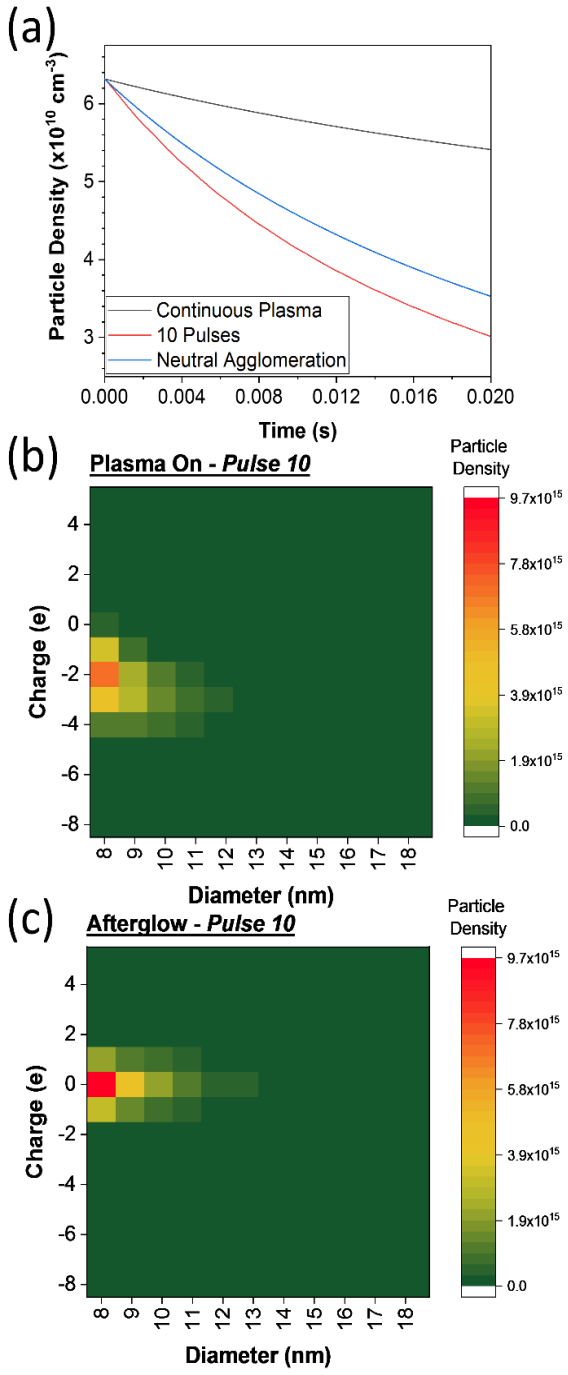

Figure 19: (a) Calculated cumulative effect of 10 plasma pulses on the total particle density, compared to the case of a continuous plasma and the case of free-molecular agglomeration, without any electrostatic effects. (b)(c) 2 dimensional plots of particle densities as a function of size and charge after the last 'plasma on' pulse and after the last afterglow, based on the computational approached described in this manuscript.

Theorethical predictions suggest that the particle temperature can be few hundreds of degrees higher than the gas temperature while in the plasma,[22,102] although these models have not been applied to the afterglow case and do not include any heating from interaction with argon metastables. Finally, plasma-induced heating effects and cooling to the background gas both scale like the particle surface area, making the steady-state temperature size-independent. On the other hand, under unsteady conditions the particle cooling rate is proportional to the particle surface-to-volume ratio, i.e. they scale like $1/R_p$. This indicates that particles of different sizes will cool and desorb negative charges at different rates in the plasma afterglow, leading to a potential coupling between particle charge and size distributions. A more in depth investigation of these aspects is left for a future study.

We should also point out that we have only observed spherical, single-crystal nanoparticles in our TEM analysis of the samples produced via plasma pulsing. This suggests that the particles agglomerates, formed during the afterglow, most likely experience rapid sintering in the subsequent 'plasma on' phase. An estimate of the temperature needed to achieve complete sintering within the duration of the plasma pulse can be obtained using the following formula:[103–105]

$$\boldsymbol{\tau_{sinter} = \frac{3k_B T_P N}{64\pi D(T_P)\sigma}}$$

Equation 17: Temperature dependent sintering time of particles.

Where τ_{sinter} is the sintering time, T_P is the particle temperature, N is the number of atoms in the particle, $D(T_P)$ is the self-diffusion coefficient and σ is the surface tension. Using a surface tension value of 0.826 J/m^2,[103] and a self-diffusion coeficient of $4.69\times10^{-7}\exp(-$

7562/T) m^2/s,[104] we find that two ~16 nm particles can sinter into a ~20 nm particle within 2 ms at a temperature τ_{sinter} of 470K. This temperature increase to 575K for two ~40 nm particles to give a ~50 nm particle. These temperature values are reasonable given the theorethical estimates of particle temperatures in plasmas that can be found in the literature,[22,102] and in agreement with our observation of single-crystal spherical particles.

1.4.5 – Summary:

While low-temperature plasmas are capable of producing ultra-fine particles with excellent precursor utilization, excessively small nanoparticle are actually detrimental for applications such as for lithium-ion battery materials. For the case of silicon, very small particles have too large of a surface area, reducing the first cycle Coulombic efficiency upon lithiation. This manuscript demonstrates that operation in a pulsed mode is a simple approach to significantly increase the average particle size (from ~8 to ~20 nm) and improve the electrochemical performance in anodes for lithium-ion batteries. The zero-dimensional model described here predicts that electrostatic effects enhance the particle coagulation rate in the afterglow due to the transition from a dominantly negative to a bipolar nanoparticle charge distribution. The width of the charge distribution, and in turn the coagulation rate in the afterglow, depends on parameters such as metastable density in the plasma, gas temperature, and electron temperature in the afterglow. All of these parameters are still poorly characterized for the case of flow-through reactor, in argon-silane mixtures. Advances in both the experimental characterization of these systems and

in their modelling is needed to achieve a better agreement between plasma aerosol models and measured growth of particle size during pulsed operation.

Section 2: Hybrid Organic-Inorganic Quantum Dots

2.1 – Background in Silicon Quantum Dots

2.1.1 – Introduction to Quantum Dots:

In the 1970s there was a scientific effort to understand "quantum wells", a method to restrict the motion of excited electrons by confining them within a material possessing low energy levels sandwiched between materials possessing high energy levels. When the electron decayed to a ground state it emitted a photon with a frequency corresponding to the thickness of the quantum well, allowing for tunable photon emission.[106] This led to quantum well based lasers, but these layered structures naturally brought up the question of "what if the electron well confined in all directions?" In the early 1980s this concept was tested by Alexi Ekimov via CdS and CuCl microcrystals in glass matrixes[107] and Louis Brus by CdS colloids in an aqueous solution.[108] At the same time Alexander Efros was working on physical theories for what would happen in these cases.[109] For Ekimov and Brus, these materials demonstrated controllable absorption peaks indicating controllable exciton energies. A few years later in 1985 the first scientific use of the term "Quantum Dot" (QD) was made to describe these energy confining semiconductors that were so small they had "zero degrees of freedom".[110] Similarly to the development of transistors these materials were studied and implemented in niche applications until their true potential was understood. Now the research field is rapidly expanding into biological,[111] photocatalyst,[112] and energy collecting applications[113] while successfully jumping the gap to be implemented in commercial products ranging from LEDs[114] to display technologies.[115]

These applications rely on QD materials to be excited either electrically or through photoexcitation, whereby the energy can be put to use emitting light, inducing chemical reactions, or potentially as a qubit.[116] Within this section we will be focusing on photoexcitation and photoemission, more specifically bandedge photoluminescence and photon upconversion.

Initial studies focused on bandedge photoemission, which is effectively shining a higher frequency light source on the QD to excite an electron into the lowest conduction band so that when it decays it will emit a lower-frequency photon (eg. shining UV light on a QD that emits green light).[117] Triplet-fusion is a process with the opposite goal of increasing output photon frequency by taking 2 lower frequency photons and fusing their energy to form 1 higher frequency photon.[118] This effort of converting low-frequency input light up into higher frequency output is termed photon upconversion and is the primary focus of the studies within this section.

Methods of producing QDs has become almost as diverse as their applications, ranging from viral assembly[119] to classical colloidal synthesis.[108] Aqueous synthesis is still a preferred method of QD formation, with colloidal synthesis being robust and implemented even in the original studies with roots going back to 1857 via Michael Faraday.[120] In essence the classical method of forming nanoscale semiconducting crystals is performed simply by injecting precursor reagents (generally ligands containing some group II-VI elements) into a hot and continuously mixing solution to maximize nucleation points and thereby limit Ostwald ripening (large particles growing larger). Additional steps to precipitate out larger particles and narrow the size distribution have made this method

very powerful for precise nanocrystal formation. However, advances made by Mangolini et al. in 2005 enabled the rapid formation of relatively monodisperse materials use of gas-phase precursors and non-thermal plasmas.[121] Previous work with non-thermal plasmas were also able to produce QD materials via etching, however the method was costly and time consuming compared to the more recent flow-through methods.[122] The science behind why the material is small and monodisperse is described in detail within Section 1. This method gas-phase (more accurately plasma-phase) QD synthesis is used as the basis of QD formation within this section, focusing on controlled production of silicon nanocrystals to investigate key variables and operational principles in QDs.

2.1.2 – Section Shorthand:

Within this section SiNC will refer to the unfunctionalized (silicon without any ligand attachments) hydrogen terminated silicon nanocrystal that acts as the QD core and upconversion system sensitizer. SiQD will be an all-encompassing term referring to SiNCs that have undergone a form of functionalization resulting in colloidal stability, whether functionalized with only alkyne groups or with additional transmitter ligands to enable upconversion. When referring to samples functionalized with a specific alkyne ligand the SiQD will be supplemented so that a sample functionalized with only octadecane (ODA) is C18|SiQD with the C18 referring to the length of the carbon chain. Finally, when referring to specific QD samples containing both alkyl groups such as ODA and transmitter ligands such as 9-ethylanthracene (9EA), this text will denote them as 9EA|C18|SiQD.

2.1.3 – Silicon QD Properties:

Silicon is a cheap and abundant material with semiconducting properties that make it incredibly useful and interesting to study on its own. When shaped into QDs silicon becomes even more interesting, opening new potential applications due to its reasonably harmless nature while simultaneously being easily tunable allowing optimization for a given application. Within the studies outlined in this section it is even demonstrated that photon upconversion systems using SiQDs can achieve efficiencies of 17.17%, (see Section 2.4) essentially fusing light wavelengths as low as 730 nm near infrared (NIR) light to form 488 nm violet light.[3] The rapidly developing method of gas-phase synthesis also indicates that SiQD materials could be produced quickly and affordably through a scalable system, enabling prospective commercial applications beyond research.

Toxicity:

Unlike traditionally used QD materials like CdS and PbS, silicon is a non-toxic inorganic semiconducting material. When reduced in size to form SiQDs there is minor concern of "silicosis", a condition similar to asbestos exposure where lung tissue is torn and cut by the presence of sharp silica dust fragments inducing edema, poor oxygen uptake, and sometimes inducing cancer. However, this condition is only really present in glass blowers, miners, and construction workers, generally after decades of high levels of dust exposure. Additionally, the nanoscale nature of SiNCs alters their potential effects from micro lacerations to cellular uptake, but with non-pulmonary applications done in small doses and harboring no toxic

products, use of SiNC for biological applications generally described as safe.[123] Thus, SiNCs as a QD material or QD system scaffolding is a very rare non-toxic alternative to traditional QD materials. This expands the potential applications for SiQD systems beyond applications in solar energy harvesting[124] and electronics[125] to bioimaging,[126,127] phototherapy,[111,128] and optogenetics[129,130] (as long as the other components of the SiQD system are also non-toxic). Biological applications are particularly interesting as the human body is more transparent to infrared (IR) wavelengths, allowing QDs capable of photon upconversion to have a light source external to the body while emitting visible light internally, hence the newly accessible applications.

Exciton Tunability:

Silicon is a naturally semiconducting material, which lends it some useful optical, electrical, and even magnetic properties when formed into nanomaterials.[131] It has been observed that for semiconducting materials of a size beneath its exciton Bohr radius, the apparent energy gap and auger rate are heavily influenced by the precise material size.[132] The exciton Bohr radius is simply defined as the distance between the excited electron and its hole pair, which for silicon appears to be ~5 nm.[133–136] As the semiconducting material size is now a dominant influence on the effective energy gap with smaller diameter particles expressing higher energy levels, the average exciton energy resulting from photoexcitation (when incoming photons are high enough in energy to photoexcite) will be tunable simply by changing the material size.[137,138] This tunability enables absorption for applications

ranging from NIR to ultraviolet (UV) wavelengths. [139,140] For the studies outlined in this section the SiNCs are synthesized using a non-thermal plasma with relatively simple reactor-pressure to SiNC-size relations. This allows for a simple way to tune exciton size to maximize a desired optoelectronic effect. However, the reduction of QD size directly influences exciton confinement with smaller QDs having less space for excitons to exist, increasing exciton recombination probability.[141] Recombination generally can be viewed as a waste of energy, but increasing QD size to reduce recombination probability would also reduce the average exciton energy. Less energy provides less of a "driving force" or diffusion potential of an exciton population embodied as its ability to overcome energy barriers or bandgaps in order to achieve an intended result.[3,142]

As a result, transferring excitons from a SiNC core to a molecule would impose molecular energy level that requires a SiQD sample to be a maximum of a certain size in order to produce excitons capable of transitioning into a molecule. However, smaller SiNCs would produce a greater driving force as the excitons would have a higher energy and higher probability of making the transfer. This would need to be balanced with the increased confinement increasing recombination potential, thus producing an optimization curve which is explored directly in Section 2.4.3.

2.1.4 – TTA Upconversion:

Within this section, the described photon upconversion is achieved through a process known as triplet-triplet annihilation (TTA). In this case we are dealing with "excitons" or electron-hole pairs, where an electron is excited to the point of leaving the

valence band to exist in the conduction band of a material allowing for transportation while dragging around the hole it was excited from. As a result, there is no net charge transfer as excitons move, but the electron's ability to recombine with the hole allows for chargeless energy transfer. From there exciton types are described by the sum of their electron-hole spin states (see Figure 20 for simplified illustration). Thus a "triplet" is referring to the electron-hole pair being in an unpaired spin state so that it has a net spin, while "singlet" refers to the lowest excited state with no unpaired electrons or net spin. The triplet state has a forbidden optical transition, preventing anything but the singlet state to emit a photon instead of radiating energy away.

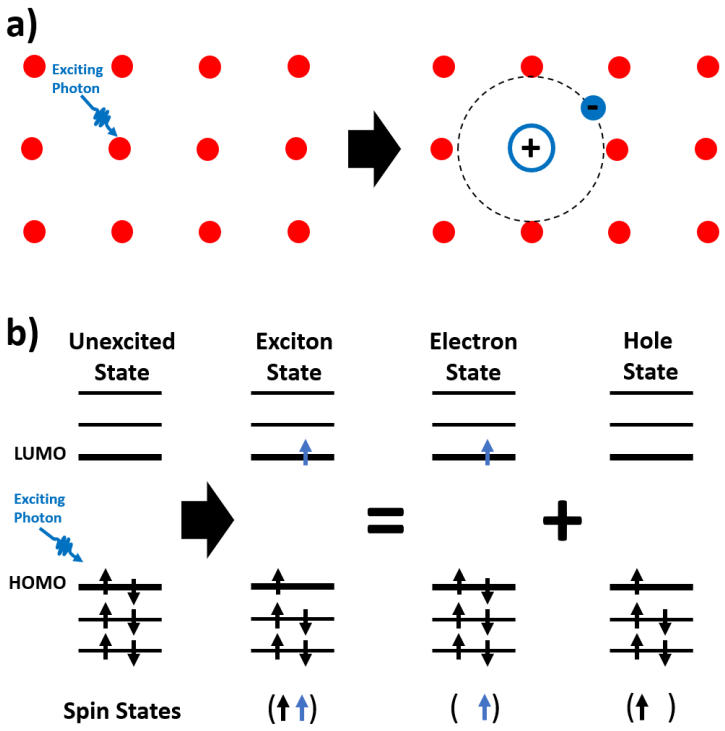

Figure 20: Exciton formation via a) cartoon and b) energy level diagram.

The hybrid inorganic-organic system of SiQDs used is composed of 4 active components, only 3 of which are optoelectronically active (see section 2.4 for how the alkyl

ligands indirectly impact upconversion). These 4 components are described in Figure 21 where:

1. The SiNC acts as a *sensitizer* to absorb the energy of incoming photons, allowing the energy to exist as an exciton.
2. *Alkyl chains* grafted to the surface of the SiNC maintain solubility of the SiQD system in the desired solution.
3. The *transmitter ligand* also grafted to the SiNC, depicted as 9-ethylanthracene (9EA), enables Triplet Energy Transfer (TET) from the sensitizer to the emitter molecule.
4. The *emitter molecule* depicted as 9,10-diphenylanthracene (DPA) accepts the triplet excitons and undergoes TTA upon interacting with a second excited DPA molecule.

Upconversion via TTA requires the interaction of two emitter molecules each excited with a triplet exciton, so that when they get close enough for the molecules' wave functions to

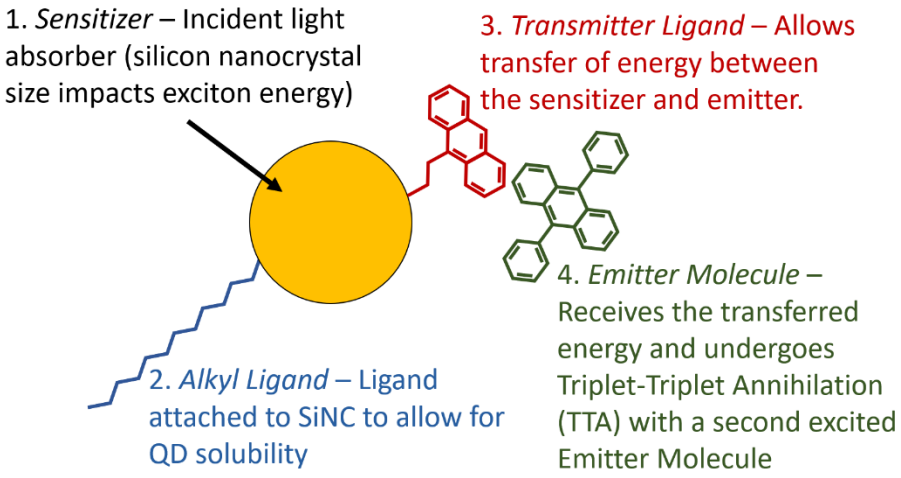

Figure 21: Primary active components of TTA based upconverting SiQDs.

interact, one molecule's triplet energy is transferred to the other molecule causing it to drop into a ground state while the other molecule is excited into a singlet state (note: the summed energy of two triplet excitons will generally not equal that of a stable singlet, requiring the high energy state to radiate energy until it reaches a more stable state). This singlet will eventually fluoresce to a ground state emitting a photon of light as shown in Figure 22.

In the case where the sensitizer is excited by low frequency photons and the TTA process emits higher frequency photons the incoming light is effectively converted up from a lower to a higher frequency (upconverted). As 2 photons are required to excite 2 excitons the maximum conversion of light would be 2 low frequency photons become 2 excitons which become 1 high frequency photon. A perfect conversion rate of 2 low frequency photons to 1 high frequency photon will be described as 100% efficiency throughout this section.

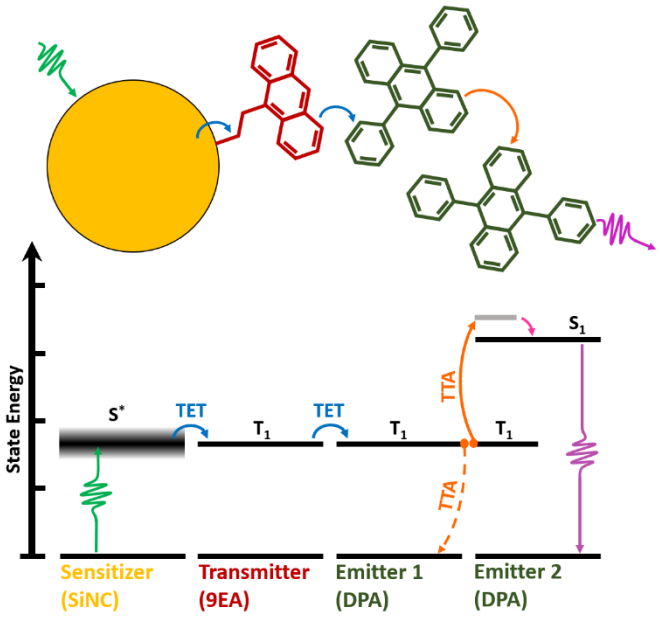

Figure 22: TTA upconversion Jablonski energy diagram with cartoon represenatation.

Energy transfer between the transmitter ligand and the emitter molecule takes the form of Dexter energy transfer. Also known as Dexter electron transfer, the energy transfer takes the form of moving an excited electron (and hole) non-radiatively from one molecule to another over a short gap (generally < 1 nm) due to overlapping molecular wavefunctions.

This method is not necessarily new and TTA has been implemented with more toxic chemistries such as PbS and CdS with sensitizers gathering wavelengths from the near infrared (NIR)[139] to within the UV range.[140] When SiNC began their use in TTA upconversion with Xia et al. a functional chemical system was found and has operated as the standard system. For much of this section the SiNCs will be sized to ~3.1 nm to maximize formation of excitons at or near the energy of the T_1 state for the transmitter ligand (generally 9EA at 1.8 eV).[143,144] As an anthracene molecule it will be compatible to

do Dexter energy transfer with DPA, an anthracene based emitter. Upon TTA and singlet decay a 432 nm photon will be emitted regardless or incident light wavelength.[4,145]

2.1.5 – SiQD Synthesis:

SiNC via Plasma:

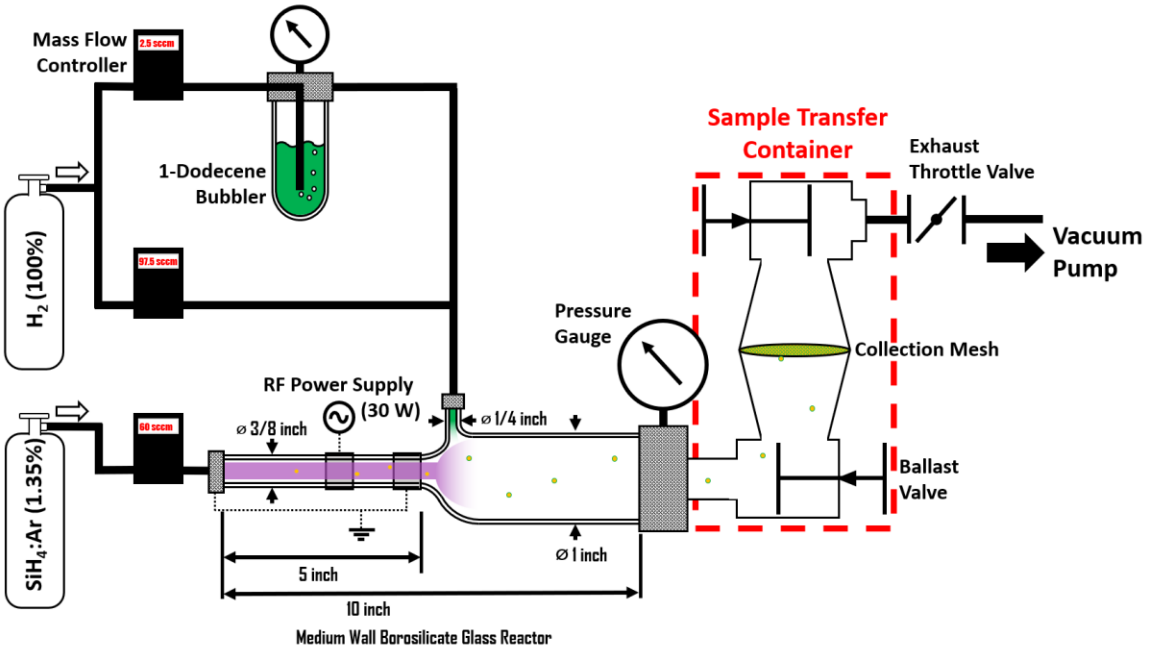

Figure 23: Silicon nanocrystal synthesis, inflight functionalization, and material collection schematic.

For the studies in this section, SiNC synthesis is performed through the use of a low-pressure non-thermal capacitive plasma. This plasma contained in a borosilicate reactor with a 5.4 mm internal diameter (3/8" outer diameter) with energy being provided in the form of strong RF electric fields supplied through 12 mm wide copper loop electrodes. These electrodes are oriented so that the upstream flange is grounded, the live electrode is in the reactor center and downstream is grounded to contain the plasma. The

live electrode is powered by a RFPP-RF5S radio frequency (13.56 MHz) generator coupled to the reactor by an MFJ-989D matching network. The reactor pressure is adjusted to tune particle size through the use of an MKS 253B-1-40-1 Exhaust Throttle Valve placed downstream of both the reactor and the MKS 626D12TBE Absolute Pressure Transducer. Readings from the pressure transducer are processed by an MKS 651CD2S2N Digital/Analog Pressure Controller, which sends instructions to the exhaust throttle valve to either close slightly to increase pressure through increased flow restriction or slightly open for the opposite effect, thus allowing for dynamic pressure control. After SiNC synthesis the reactor expands into a 21 mm internal diameter (1" outer diameter) section with a side inlet (1/4" outer diameter) for hydrogen or ligand saturated hydrogen addition. As the gas has exits the powered region it relaxes into a grounded state forming an afterglow within the larger section where hydrogen saturation or ligand grafting occurs. The material then flows out of the reactor to be caught via triboelectric forces (static electricity) on a stainless-steel mesh (grade 400). This mesh is held in place with a spring clip on a centering ring in a sealable area so as to allow for air-free transfer into a glovebox for further processing. The system can be seen as a schematic in Figure 23 or in photos as Figure 24.

For all of the studies in this section the SiNCs were formed by flowing 60 sccm of an 1.37% SiH_4:Ar mixture axially through the 3/8" diameter reactor tube while supplying 30 W of power to the ~5" long region. When exiting the plasma and entering the 1" diameter portion of the reactor, the side inlet flowed 100 sccm of hydrogen (either pure hydrogen or intentionally laden with alkyl ligands). This ensured a rapid reduction in the

afterglow power and saturated the SiNC surface with hydrogen or a hydrogen alkyl ligand combination (note: other ligand structures like allylbenzene have been successfully attached, but the subsequent studies were a dead-end, so they are not mentioned). Pressures for these studies were held constant for each synthesis batch, but batch pressures ranged from 0.6-2.5 Torr depending on the desired PL peak position.

When flowing pure hydrogen, the gas system would bypass the ligand bubbler. However, in the cases using in-flight functionalization to form SiQDs a portion of the hydrogen flow was put through the bubbler. The reason for only a portion of the hydrogen

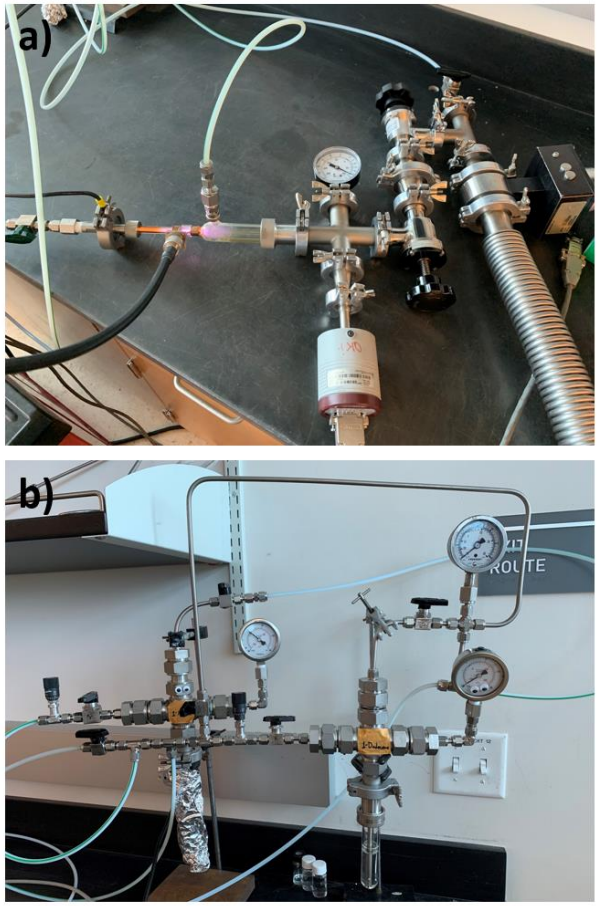

Figure 24: Images of the a) plasma reactor and b) bubbler system used for SiQD synthesis.

being subjected to the bubbler is explored in detail within Section 2.4.1, but in short: less hydrogen flowing through a bubbler means less ligand being carried to the reactor via saturated hydrogen. Altering the pressure within the bubbler is another method of diluting the ligand vapor pressure with hydrogen, so the combination of the two acts as a fine and course tuning of the amount of ligand entering the reactor's plasma afterglow. Due to different ligands having different vapor pressures, control of the carrier gas flow is essential to SiQD surface-composition control. The alkyl chain ligands used with the bubbler were 1-hexene (Sigma Aldrich 95%), 1-octene (Sigma Aldrich 98%), or 1-dodecene (Sigma Aldrich 99%). As these compounds differ in length, their vapor pressures vary under standard conditions (25 ºC, 1 atm), with 1-dodecene at 19.27 Pa, 1-octene at 2317.19 Pa, and 1-hexene at 24794.58 Pa, as found using the Antoine equation and constants determined by A. Forziati et. al.[146] The three orders of magnitude in vapor pressure variation requires the ligand vapors within the bubbler to be diluted with differing levels of hydrogen to attain similar ligand flow rates.

Controlling flow through MFCs is simple, but to ensure a bubbler is flowing the correct amount of a ligand when held at a pressure above the plasma reactor there are a couple of tricks. When flowing precursor gasses the reactor pressure will increase, so 60 sccm of the SiH_4:Ar mixture + 100 sccm of H_2 may result in a "flow pressure," pressure above the zeroed value resultant of unimpeded flow, of 0.33 Torr before using the exhaust throttle valve to control the pressure. When a bubbler is filled with hydrogen so that it is at a higher pressure than the reactor, fully opening the connection to the reactor will flow a high uncontrolled amount of gas causing

the bubbler pressure to drop and the conditions within the reactor to constantly change. To control the bubbler output so as to operate at the desired steady state, simply record the flow pressure with all gasses bypassing the bubbler, then when using the bubbler slightly open its output to match the previously recorded flow pressure (this should ensure the MFC controlled flow into the bubbler matches the flow out). From there increase the reactor pressure using the exhaust throttle valve, ignite the plasma, and collect the material.

In-Solution Thermal Hydrosilylation and Sample Preparation:

Thermal hydrosilylation is the attachment of a ligand to the surface of a hydrogen terminated silicon material by breaking the hydrogen bond via heat and exposing the bond site to ligands for attachment. In the liquid phase this is accomplished by dispersing SiNCs or partially functionalized SiQDs in mesitylene as it has a relatively high atmospheric boiling point of 164.7 ºC. To maintain uniformity and help suspend the insoluble SiNCs a stir-bar keeps the solution well mixed. When optimizing transmitter molecule loadings on a SiQD sample the optical density of a sample is used as a proxy for precise SiQD number as more QDs produce a more optically dense sample. For consistency in transmitter functionalization all samples are made to have the same optical density at 488 nm of 1.2 while in a 10 mm cuvette as measured via UV-Vis absorption on an Agilent Technologies Cary 5000 spectrometer. As the samples are consistent with each

other, adjusting the amount of transmitter molecules is simply done by adding more or less of the chemical to the vial undergoing thermal hydrosilylation.

Thus, a standard sample might be 2 mL of mesitylene and C12|SiQD with an optical density of 1.2 mixed with 125 μg of 9-vinylanthracene (9VA, TCI America 97%) by a stir-bar and held at 180 ºC in a sealed Teflon capped glass vial for 1.5 hours. This simple heating of a mixed solution on a hotplate functionalizes the SiQD, but they still need to be removed from the mesitylene for testing. To accomplish this, methanol will be added in a 2:1 ratio to the sample which is mixed and then centrifuged at 12,000 rpm for 30 minutes. The SiQDs precipitate out due to the alkynes being slightly less soluble in methanol, and are then redispersed in 4.5 mL of a 2:1 ratio of methanol and toluene. This solution will again be mixed and centrifuged with the methanol-toluene mixing and centrifuging steps being repeated 2 more times. Finally, after a total of 4 centrifuging steps the sedimented material is dispersed in toluene (or the desired solvent) and diluted until it has an optical density of 0.1 at 488 nm in a 10 mm cuvette. For upconversion this solution will need to have an emitter molecule, so for our example 9,10-diphenylanthracene (DPA, TCI America 98%) will be added to the solution until it reaches a final concentration of 5.2 mM. At this point the sample is ready to test and is put into a cuvette sealed with a Teflon cap for optical characterization.

In the case that the alkyl chain used for solubility does not have a high enough surface loading per SiQD, material will simply fall out of solution. If it is near the critical point where it can maintain solubility this will take a while, however it will

still be apparent that the material is not ready as it will appear “cloudy” and opaque as opposed to transparent as shown in Figure 25. This cloudiness also appears when the SiNC is not fully crystalline and in essence is an indicator that the sample will not work as desired.

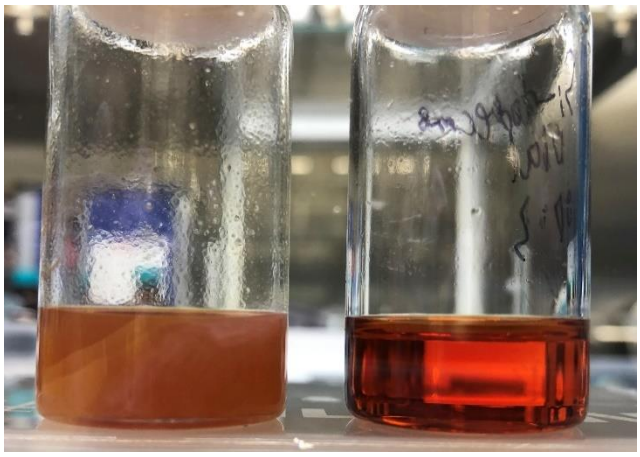

Figure 25: Subcritical (left) and critical/supercritical (right) alkyl chain ligand loading of partially functionalized SiQDs in mesitylene at room temperature.

2.1.6 – Standard Measurement Used:

Corrected Upconversion Values:

All photon upconversion measurements in this section are performed using a laser array for excitation (either a 405 nm OBIS LX 50 mW, 488 nm OBIS LS 60 mW, 532 nm Sapphire SF 532, 640 nm OBIS LX 40 mW, or 730 nm OBIS LX 30 mW coherent laser) followed by an Ocean Optics Maya 2000 Pro spectrometer for detection. A ThorLabs notch filter of the same wavelength as the laser used is placed before the spectrometer to remove

the laser contribution. A chemical with a known emission quantum yield is then used to measure the response of the system, generally Rhodamine 6G (R6G) dissolved in ethanol. R6G has a fluorescence quantum yield of 95%, so the received emission quantum yield (QY) is calibrated to be equal to 95%. This calibration is used to determine the QY of the SiQD photoluminescence and UCQY. The quantum yield for photon upconversion is given by following equation:

$$\Phi_{UC} = 2\,\Phi_{reference}\frac{photons\ absorbed\ by\ reference}{photons\ absorbed\ by\ upconversion}\frac{PL\ of\ upconversion}{PL\ of\ reference} =$$

$$2\,\Phi_{R6G}\frac{n_{DPA}^2}{n_{R6G}^2}\frac{[Area]_{DPA}}{[Area]_{R6G}}\frac{1-10^{-OD_{R6G}}}{1-10^{-OD_{SiQD}}}$$

Equation 18: Upconversion quantum yield without reabsorption correction.

Where $\phi_{reference}$ is the fluorescence quantum yield of R6G, n_{DPA} and n_{R6G} refer to the refractive indices of the solvents for the DPA and R6G, which are toluene and ethanol, respectively. $[Area]_{DPA}$ and $[Area]_{R6G}$ are the integrated areas of the fluorescence peaks of DPA and R6G, while OD_{R6G} and OD_{SiQD} denote the absorbance of the R6G and the SiQD at the laser excitation wavelength. The same method can be used with alternate standards if the wavelength range allows.

For photon upconversion, strong reabsorption of the upconverted light by emitter molecules in solution (the inner filter effect) will happen, thereby lowering the apparent upconversion efficiency. To evaluate the real UCQY values, upconverted emission spectra are matched with those measured by exciting the emitters directly in low concentration

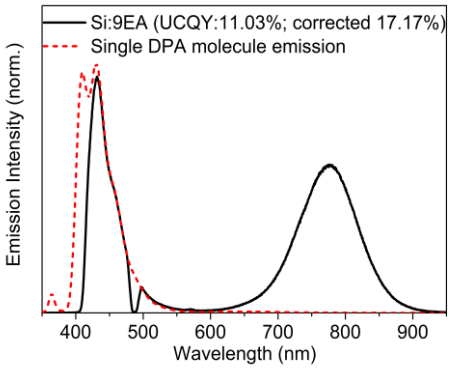

Figure 26: PL spectra of Si:9EA:DPA (d=3.1nm, critical dodecane loading, the sample with best UCQY), black solid line, 5.2 mM DPA as emitter, excited at 488 nm) and low-concentration DPA (red dashed line, excited at 365 nm).

solutions wherein negligible reabsorption of emitted light occurs (see Figure 26). Negligible reabsorption in low concentration reference solutions is confirmed by observation of an unchanged emission line-shape with decreasing emitter concentration. Emission spectra measured from upconversion samples were normalized to those of the low-concentration references by matching spectra along their long-wavelength edges wherein emitters show no appreciable light reabsorption. Using this, the ratio of the integrated area of the photon upconversion line-shape and the intrinsic emission line-shape of the emitter and scale measured UCQYs to account for the reabsorption of emitted light can be computed. After considering this inner filter effect, UCQY of the highest performing sample thus far, critically loaded 3.1 nm diameter 9EA|C12|SiQD, reaches 17.17% while

the uncorrected value would produce 11.03%. All values in this section account for reabsorption in this way.

Size:

XRD:

X-Ray Diffraction (XRD) spectrometry can also be used to determine the size of nanocrystalline domains through a technique known as Scherrer Analysis. As each SiNC will become a separate SiQD the determined nanocrystalline domain is effectively the SiNC size. It should be noted that this technique only works for crystalline materials, so the oxide layer that forms on silicon nanoparticles will reduce the internal crystal size and skew the data so the SiNC seems smaller than it actually is. To perform Scherrer analysis an XRD scan of the powder is taken and one of the observed peaks should be fit (any peak will work after removing any background signal). When the full width half max (FWHM) in units of 2θ is known the crystal size can be found through the following equation:

$$\tau = \frac{K\lambda}{\beta \cos\theta}$$

Equation 19: Scherrer Equation

where λ is the X-ray wavelength, β is the line broadening FWHM value, θ is the Bragg angle (the center of the selected peak), K is a dimensionless shape factor dependent on the crystal shape and instrument used, and τ is the average size of the crystal. For the scan shown in Figure 27, spherical nanoparticles being analyzed with a PANalytical Empyrean Series 2 the values were λ = 15.4 pm, β = 0.06257 radians, θ = 28.61409 radians, and K = 0.96 giving τ = 2.44 nm.

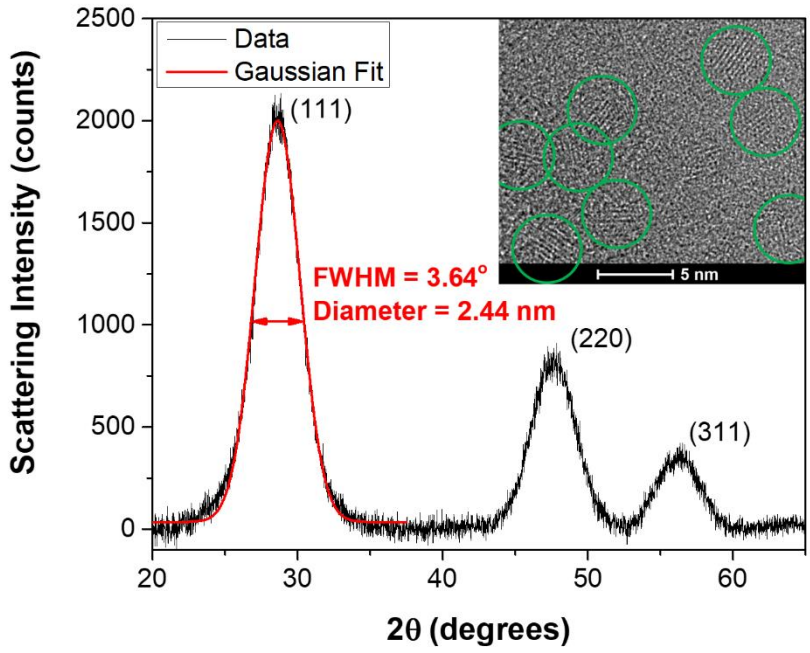

Figure 27: Example of XRD based sizing through Scherrer's analysis with TEM inset for comparison.

\PL Peak Position:

Using SiQDs that only have alkyl functionalization, exposure to photoexciting laser light will result in the observation of a photoluminescent peak. It was noted that this peak shifts as the SiNC size changes, which can be expected due to the effect size has on exciton energy as described in Section 2.1.3. This change was quantified and fitted for SiQDs by Wheeler et al. resulting in an equation relating SiNC size to the peak PL emission in eV.[136] Converting from eV to photon wavelength in nm via $E = \frac{hc}{\lambda}$ the relation becomes:

$$\lambda = \frac{1239.8}{1.12 + 3.73d^{-1.69}} \quad \text{or} \quad d = \left(\frac{332.39}{\lambda} - 0.30027\right)^{-0.592}$$

Equation 20: SiNC diameter to PL peak relation.

where d is SiNC diameter and λ is the average PL emission wavelength. As a result, a SiNC of diameter 3.12 nm would produce a wavelength of 745 nm, so observation of a PL peak at 745 nm would imply a 3.12 nm size. This technique is heavily employed within the following section as it does not require the QDs be exposed to air, which alters the crystalline structure. As a result, though emission measurement and Equation 20 is indirect as a method of observing size it is a reliable and nondestructive method of analysis.

Surface Atom Calculation:

There are multiple commonly used methods for approximating the total number of atoms or number of surface atoms on a spherical nanoparticle. As crystal structures deform significantly when dealing with nanomaterials all methods can only be used as an approximation, so for accuracy two methods were employed in this study. Both of which required the SiNC diameter (d = 3.1 nm) as well as its associated surface area (S = 30.6 nm^2) and volume (V = 15.9 nm^3) as determined through basic geometry.

Density Method

The first method appears to be the most common and utilizes readily available information such as silicon's atomic mass (A_Γ = 28.085 g/mol), density (σ = 2.329 g/cm^3), and covalent bond length (r_A = 0.111 nm). From there the total number of atoms is determined by dividing the volume of the nanoparticle by an approximate atomic volume as found through the density and atomic mass, where N_A is Avogadro's constant.

$$\boldsymbol{Atoms_{Total} = V\frac{\sigma}{A_\Gamma}N_A = 779.4\ \text{atoms}}$$

Equation 21: Atoms in a nanocrystal based on material density.

To determine the number of surface atoms the approach is simply to reduce the radius of the particle by 1 fully bonded atomic layer or 2 covalent bond lengths. Repeat the process with the reduced particle diameter and subtract the number of atoms in this reduced particle from the original diameter.

$$\boldsymbol{d_{core} = d - 4r_A = 2.656\ \text{nm}}$$

Equation 22: Internal nanocrystal diameter.

$$\boldsymbol{Atoms_{Surface} = Atoms_{Total} - \left(\frac{1}{6}\pi d_{core}^3\right)\frac{\sigma}{A_\Gamma}N_A = 289.1\ \text{atoms}}$$

Equation 23: Surface atoms in a nanocrystal based on material density.

Unit Cell Method

The second method is based on the silicon unit cell and its key features. Silicon has a diamond structure which means that it contains $N_V = 8$ atoms per cell with $N_S = 2$ bisected atoms on each cell face, which is $a = 0.0543$ nm in length.

$$\boldsymbol{Atoms_{Total} = \frac{V}{a^3} N_V = 779.4 \text{ atoms}}$$

Equation 24: Atoms in a nanocrystal based on the crystal unit cell.

$$\boldsymbol{Atoms_{Surface} = \frac{S}{a^2} N_S = 204.8 \text{ atoms}}$$

Equation 25: Nanocrystal surface atoms based on the crystal unit cell.

As can be seen, both methods give approximately the same number of atoms within the nanoparticle total volume ~795 atoms but differ in the number of surface bound atoms leaving the possible range for the 3.1 nm silicon nanoparticle as likely being between 207 and 294 atoms.

9EA Per SiQD:

The average number of 9EA groups per quantum dot is estimated by the following procedure. First, the absorption spectra of the SiQDs with alkyl chains but without 9EA groups and then with both alkyl chains and 9EA groups are dissolved in toluene are measured separately. Then, the contribution from the SiQD with only the alkyl chain is subtracted to isolate the absorbance from the 9EA groups:

$$\langle N_{9EA} \rangle = \frac{[9EA]}{[SiQD]} = \frac{\left(abs_{F:SiQD,395nm} - abs_{SiQD,395nm} \frac{\langle abs_{F:SiQD} \rangle}{\langle abs_{SiQD} \rangle} \right)}{\epsilon_{9VA,389nm}} \frac{\epsilon_{SiQD,488nm}}{abs_{F:SiQD,488nm}}$$

Equation 26: 9EA per SiQD based on absorption data.

Here, $\langle abs_{F:SiQD} \rangle / \langle abs_{SiQD} \rangle$ is the ratio between the absorbance of the fully functionalized and partially functionalized quantum dots in the 550-700 nm region. The extinction coefficient of 9MA at 389 nm ($\varepsilon_{9MA,389nm}$) in toluene is 8413 $M^{-1}cm^{-1}$, while the extinction coefficient of SiQD with size approximately 3.1 nm at 488 nm is 10000 $M^{-1}cm^{-1}$.[145,147,148]

Transient Absorption:

Standard transient absorption with excitation at 532 nm, is used to demonstrate triplet energy transfer from the SiNC to an attached transmitter molecule (generally 9EA). In Figure 28 below, C12|SiQD and 9EA|C12|SiQD are shown, demonstrating the 9EA peak resonance at 435 nm present only for SiQDs functionalized with the 9EA transmitter. As laser light at 532nm is unable to excite 9EA directly and can only excite SiNC, this triplet signal of 9EA must be a result of the triplet transfer from SiQD, demonstrating the energy transfer between the SiQD sensitizer and the 9EA transmitter molecule.

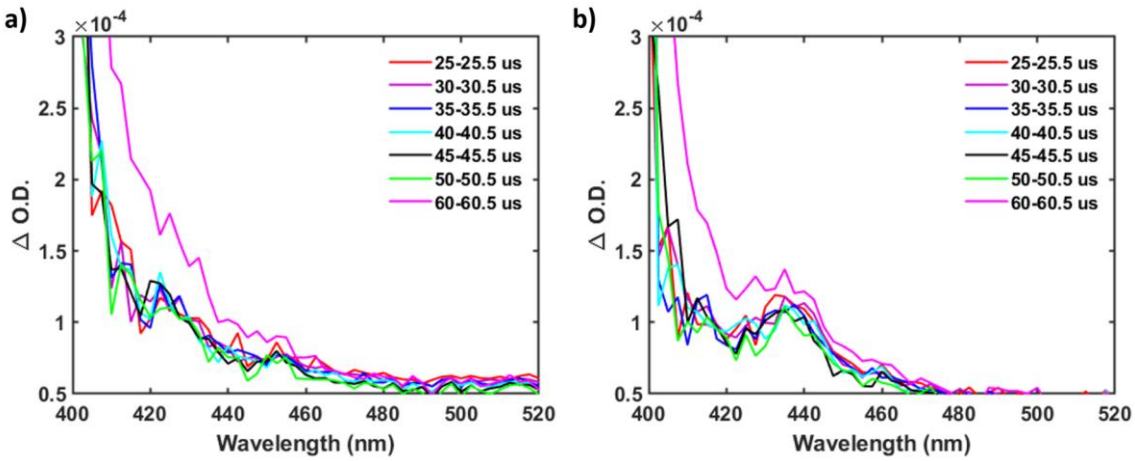

Figure 28: TA spectra of a) Si-dodecyl without 9EA and b) Si-dodecyl with 9EA (d = 3.1 nm, 3 9EA molecules per SiQD) in toluene excited at 532 nm. (TA measurements were conducted using an enVISion spectrometer from Magnitude Instruments that employed a 532 nm excitation laser with a 10 kHz repetition rate and a pump fluence of 150 μJ/cm^2. The instrument response function for these measurements was found to give a time resolution of 4.2 ns.)

2.2 – Triplet Exciton Transfer Back and Forth Between Silicon and Perylene[3]

Hybrid organically functionalized inorganic SiQDs have displayed promise for conversion of near-IR to visible light,[149–151] acting as sensitizer to collect longer wavelength photons and convert them via the aforementioned upconversion process (see Section 2.1.4) into a shorter wavelength counterpart.[137,152–155] The relatively long-lived (microsecond to millisecond range) molecular triplet excitons are able to operate at low photon fluxes enabling use for solar applications[141,156] while simultaneously limiting heat radiation, thus enabling use in phototherapy and bio-imaging.[138,157–160] Upconversion systems using QDs has been performed before, however these efforts have focused on using toxic elements such as Cadmium[152,154,161] or Lead[153,155,162,163] which limits their use in biological applications. Organically functionalized silicon does not face this same issue of biotoxicity, expanding potential uses and reducing risk of environmental contamination.

The triplet-fusion upconversion process can also be run in reverse as singlet-fission, with applications like in photovoltaics focusing on conversion of high frequency light into the cell's more sensitive wavelengths as a means to increase performance,[156,164–169] generally by interfacing singlet-fission materials in the back-contact of a semiconductor solar cell.[170–172] Silicon already dominates as the semiconductor of choice in the photovoltaic market,[163,173] which indicates that improving the understanding of organic-Silicon interface energy transfer could demonstrate broad utility.[166,167,170]

Organically functionalized SiQDs are uniquely positioned to allow the study of organic-inorganic junctions and their ability to permit triplet exciton cross-junction

movement. Previously we demonstrated a 7% UCQY with TET across SiNC to surface bound anthracene, however the inverse process, which is needed for singlet fission, was not observed or measured.[145] This section demonstrates molecule to SiNC triplet energy transfer through a perylene functionalized SiQD system by placing spin-triplet excitons in dynamic equilibrium between the perylene and SiNC via photoexcitation. Similar experiments have been done for other molecule-QD systems,[174–176] however this is the first effort on characterizing SiQD based systems.

Beginning with transient absorption (TA) spectroscopy we find the timescale for TET from the SiNC to surface-bound perylene to be 4.2 microseconds and from perylene to SiNC to be 22 nanoseconds. Such a difference in the rates of energy transfer can be ascribed to the differences in triplet excitation state density within perylene and the SiNC. A photon upconversion scheme interfacing the perylene-functionalized SiQD with a perylene-based triplet fusion annihilator is also developed, upconverting photons from as low energy as 730 nm to up to 475 nm (far red to blue). Using 532 nm (green) illumination at fluxes as low as 80 mW/cm^2 the system is able to achieve an UCQY of 1.5%, comparable to use of the same perylene annihilator in a Pd-porphyrin system.[177] In effect, this system demonstrates that short chemical links between molecules and silicon enables triplet exciton exchange, providing new opportunities in system design for upconversion and energy transfer applications.

2.2.1 – 3EP Upconverting System:

As described above, the SiQD system contains four primary components. In this case a 3.4 nm SiNC acts as the scaffold and primary absorber for upconversion, octadecane (ODA) maintains solubility in the toluene solution, 3-ethylperylene (3EP) grafted to the SiNC acts as the energy transmitting molecule, and tuB$_4$perylene acts as the emitter molecule dissolved within the solution. A schematic of this can be seen in Figure 29. The SiNC is synthesized through a non-thermal plasma with a geometry described in Section 2.1, at 23-30 W with a reactor pressure of 1.32-1.50 Torr and a 1.37% SiH_4:Ar mixture flowing at 60 sccm.[142,178] Due to silicon's Bohr excitation radius being ~5 nm[133–136] while the SiNCs are ~3.4 nm the material demonstrate quantum confinement, while the SiNC's precise size forms an emission peak at 780 nm (1.59 eV) after hydrosilylation with octadecene. As the 1.59 eV radiatively emitted from the octadecene functionalized SiQD is above perylene's lowest energy triplet state of 1.53 eV and below the lowest excited singlet state of 2.6 eV, the only viable energy transfer pathway from the SiNC to the perylene is through TET.[143,179–182]

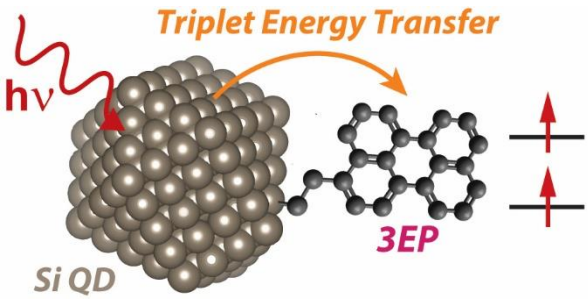

Figure 29: Perylene-SiQD schematic.

Initial efforts to functionalize SiQDs with perylene via thermal hydrosilylation as done with octadecene resulted in hybrid organo-silicon materials unable to perform photon upconversion, instead providing broad featureless photoluminescence from 550 nm to 900 nm suggesting an inhomogeneous mixture. To overcome this, lowering the hydrosilylation temperature from 180 ºC to 60 ºC and incorporating 2,2'-azobis(2-methylpropionitrile) (AIBN) as a radical initiator for the 3-vinylpyrelene (3VP) and the 1-octadecene (ODE) produces colloidally stable SiQDs. This process resulted in the covalent bonding of 3VP and ODE to the SiNC forming 3EP and ODA.

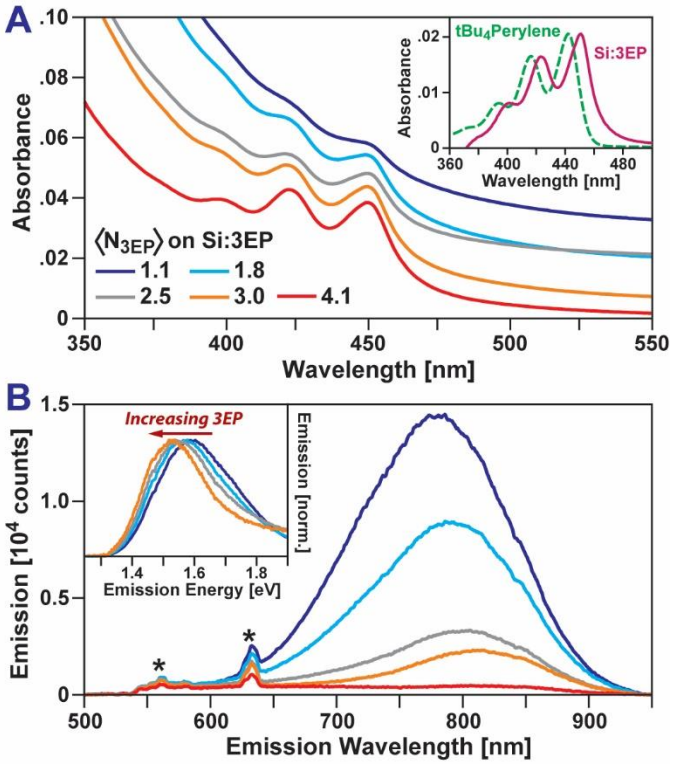

Figure 30: (A) 3EP|C18|SiQD absorption spectra in toluene with increasing 3EP surface coverage. (A inset) observation that the 3EP absorption spectra appears as a 53 meV bathochromically shifted version of tBu_4perylene. (B) 3EP|C18|SiQD emission spectra in toluene with 532 nm excitation corresponding to the samples in (A) with * designating Raman scattering peaks. (B inset) Increasing 3EP quenching of the SiQD appears to shift and narrow the bandedge PL signal.

The absorption and emission spectra of the 3EP-Si resulting from functionalization with differing 3VP and ODE ratios can be seen in Figure 30. Successful grafting of 3VP is seen through the appearance of a vibronic progression beginning at 450 nm which derives from the 3EP's S_1 state. Additionally, it is observed that increasing the ratio of 3VP to ODE from 0.02% to 0.5% increases the 3EP absorption features indicating a greater surface coverage of the transmitter ligand on the SiQD. Increased 3EP attachment does appear to increase 3EP's absorption signal, but does not induce any spectral shifting as shown in Table 1, suggesting spatial separation between surface bound 3EPs. When observing the 3EP it is notable that the primary absorption features appear as a version of tert-butyl perylene (tBu_4perylene) that has been redshifted 53 meV. In past studies a similar absorption shift was observed for 9EA functionalized SiQDs[145] which indicates a degree of electronic coupling between transmitter molecules and the SiNC they are bonded to. With regards to photoluminescence, increased presence of surface bound 3EP appears to induce quenching within the SiQD resulting in lower PLQY and strongly indicating energy transfer from the SiNC to the 3EP. A consequent bathochromic shift and narrowing of the SiQD emission peak with increased 3EP is reminiscent of the narrowing and shifting observed in similar experiments with 9EA|C18|SiQD systems.[145] In that case the effect was ascribed to the preferential quenching of smaller SiQDs with bandgaps matching the 9EA's triplet energy level.

Table 1: 3EP|C18|SiQD functionalization molar ratios and corresponding emission properties for the samples in *Figure 30*. λ_{3EP} is the absorption maxima wavelength for surface bound 3EP while λ_{MAX} referrs to the emission maxima wavelength from 532 nm stimulated emission. The PLQY was then calculated using R6G as a standard.

Sample	**3VP/ODE (%)**	**λ_{3EP} (nm)**	**λ_{MAX} (nm)**	**PLQY (%)**
C18|SiQD	0	N/A	774	8.6
3EP|C18|SiQD	0.02	449	775	10.5
3EP|C18|SiQD	0.05	449	781	6.2
3EP|C18|SiQD	0.10	449	784	5.5
3EP|C18|SiQD	0.20	450	792	2.6
3EP|C18|SiQD	0.50	451	-	1.0

2.2.2 – Investigating Quenching with TA:

In an effort to definitively determine the cause of PL quenching within the 3EP|C18|SiQD samples, nanosecond transient absorption (TA) experiments were performed. A comparison between samples functionalized with only ODA (C18|SiQD) or with both 3EP and ODA (3EP|C18|SiQD)was performed using a photoexcitation at 532 nm as shown in Figure 31. It is observed that QD photoexcitation induces a broad photoinduced absorption region spanning both the NIR and visible range, decaying over several hundred microseconds with transitions indicating photoexcited carriers.[145,183–186] An inability to fit the data with a single exponential function indicates the presence of multiple channels for quenching within the QD system. This particular decay can be fitted using a Poisson distribution as illustrated in Figure 34.[145,187]

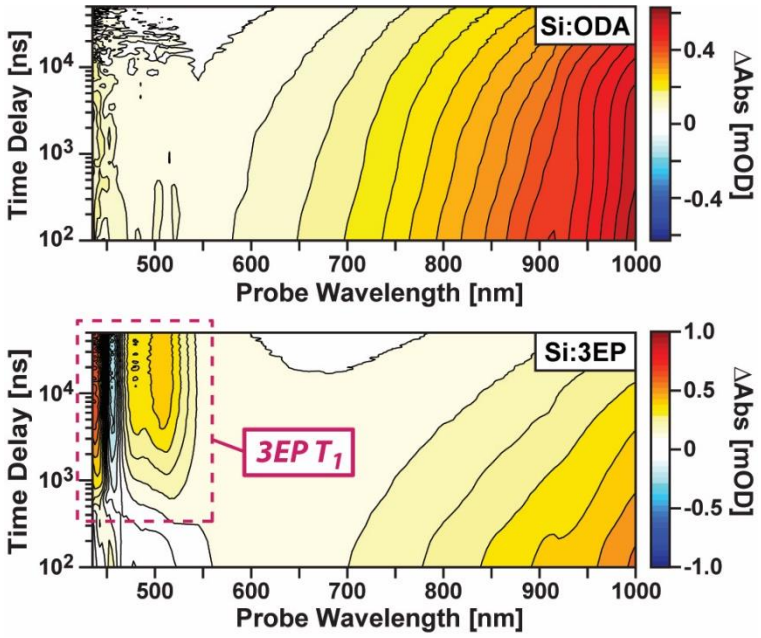

*Figure 31:*Transient absorption spectra of (A) C18|SiQDs and (B) 3EP|C18|SiQDs. Transitions indicate excited carriers while the accelerated decay of SiNC induced absorption bands demonstrate features of the 3EP T_1 state.

Within the SiQD systems, both are observed having the SiNCs photoinduce absorption at early delays over a few microseconds. For the 3EP|C18|SiQD sample a negative photobleach region at 455 nm and positive absorption features at 437 nm, 479 nm, and 508 nm mapping to the spectral positions of 3EP's 0-0 ground state absorption peak (see Figure 30A) and triplet exciton induced absorption bands.[188,189] Additional experiments using Pt-octaethylporphyrin (PtOEP) to sensitize tBu_4perylene triplet exciton formation confirm these features are a result of 3EP's T_1 state as shown in Figure 32. A clear inverse relation between 3EP triplet growth and the loss of SiQD absorption features exhibited by their same rate constants, substantiates the idea that direct energy transfer from the SiQD to the 3EP induces the 3EP excitons with no intermediate states.

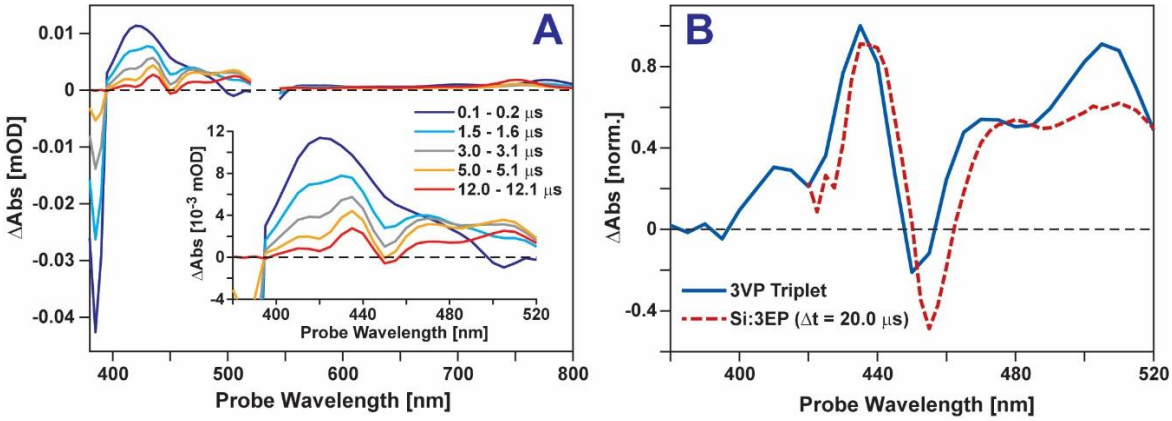

Figure 32: (A) Appearance of new 3VP T_1 features between 400 and 520 nm in TA spectra of a 3VP|C18|PtOEP system following 532 nm excitation. (B) Spectral comparison of 3VP's T_1 state and the SiNC to 3EP triplet energy transfer.

Temporal slices at a probe wavelength of 505 nm for the TA data from the 3EP|C18|SiQD samples demonstrate the growth and decay of the 3EP's T_1 state and can be seen in Figure 33A. When fitted using a kinetic model, the time constant for the 3EP T_1 state appears as $1/k_{TET}$ = 4.2 microseconds. When compared to past work with 9EA|C18|SiQD ($1/k_{TET}$ = 15 nanoseconds) this time constant seems slow, though it should be noted that these rate constants represent pre-exponential factors derived from a model accounting for energetic differences between SiQD and organic T_1 state acceptors. Thus, the difference in TET rate constants doesn't derive from differences in energy mismatch between the SiQD and its molecular exciton level or even the number of energy transfer ligands per QD operating as energy acceptors. Mismatches in energy level of this nature would in all likelihood accelerate energy transfer to 3EP over 9EA due to its lower triplet energy (1.53 eV vs. 1.8 eV) activation barrier.

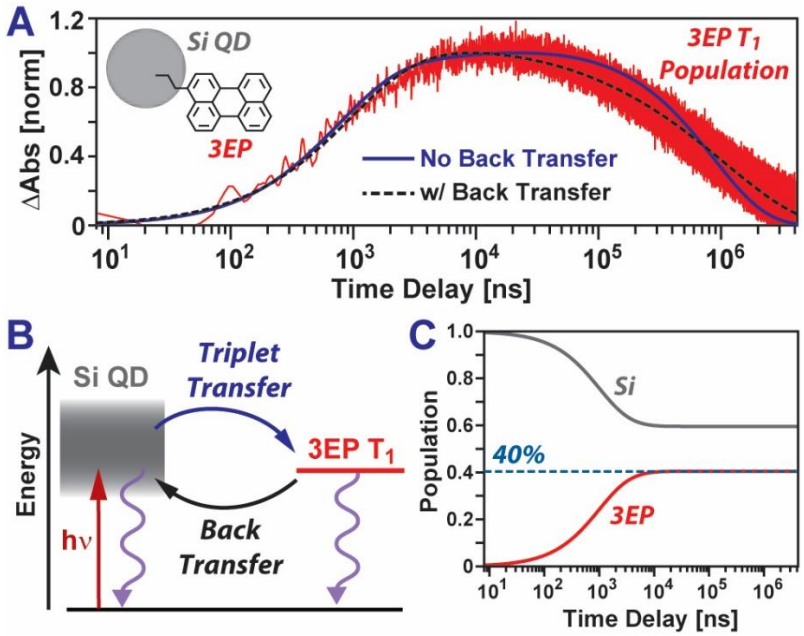

Figure 33: (A) Time absorption of the 3EP T_1 state in 3EP|C18|SiQD sample from 532 nm photoexcitation and kinetic model fittings. (B) Energy level schematic of the kinetic model fits with and without triplet energy back transfer from 3EP to the SiNC, demonstrating a greatly improved fit with energy back transfer (dashed black line). (C) Exciton populations of SiNC and 3EP estimated using best fit values of forward and backward TET rates and removing energy relaxation effects. This predicts a 40% of excitations will exist within the 3EP in the 3EP|C18|SiQD system.

Molar extinction estimates of SiQDs are relatively broad,[147,190] though when using reported values for SiQD and perylene derivatives an acceptable average number of surface bound 3EP (aka. $\langle N_{3EP} \rangle$) is estimated within the range of 0.9-4.6 3EP per SiQD for the samples undergoing TA measurement. This level of $\langle N_{3EP} \rangle$ uncertainty would not account for the k_{TET} to vary by more than a factor of 2, which clearly does not explain the more than 280 times difference between the rates of 3EP|C18|SiQD and 9EA|C18|SiQD. If instead the TET rate difference can be traced to electronic coupling between the energy transfer molecules and the SiNC and assuming the rate difference relates to the square of the

coupling as with Fermi's Golden Rule, a 17 times larger coupling between 9EA|C18|SiQD vs 3EP|C18|SiQD could be responsible.

As both 9EA and 3EP bond to the SiNC surface with 2-carbon chains, the molecules likely maintain similar distances from the SiQD surface. That said, the SiNC diameter of the 9EA|C18|SiQD was ~3.1 nm as opposed to the ~3.4 nm structure of the 3EP|C18|SiQD. Previous studies on perovskite QDs indicates that increased exciton confinement (via reduced QD size) can increase TET rate to pyrene by >3 orders of magnitude via spatial leakage of the QD exciton wavefunction past the surface to overlap with the pyrene wavefunction.[191] This phenomenon of stronger coupling stemming from wavefunction overlap could help explain the observed TET rate difference. Increased coupling could also be a result of super-exchange energy transfer pathways, involving second order coupling for high energy charge transfer configurations between the SiNC and the energy transfer molecule.[192–194] With the increase of potential electronic configurations due to increased density of states, more charge transfer configurations will be resonant between the SiNC with 9EA than 3EP. Unfortunately, all that can be conclusively said given the current data is that there is a >280 times increase in TET rate for 9EA|C18|SiQD systems when compared to 3EP|C18|SiQD systems that likely stems from increased surface coupling.

2.2.3 – Relaxation Rate Modeling:

Looking now at the decay function for the T_1 state of 3EP it is seen that a return to the ground state has a half-life of ~600 microseconds, roughly 7-10 times faster than reported lifetimes for perylene monomers in solution (4-6 milliseconds).[195–197] To explain

the accelerated decay a kinetic rate model is fitted to the absorption spectra (see Figure 33A), with the model assuming an ensemble of QDs that have differing exciton energies (see Figure 33B) based on the emission of C18|SiQD (see Figure 30B).

The standard kinetic model relies on the assumption that samples are comprised of an QDs with differing exciton energies as a result of the particle size distribution (see Sections 2.1.3 and 2.4.3 for why size matters). Additionally, SiQDs within a sample can have differing numbers of 3EP bound to them, and as the SiNC when photoexcited will either relax to its ground state or transfer the exciton to a 3EP we are left with the differential equation:

$$\frac{\mathrm{d}[Si^*]}{\mathrm{d}t} = -k_{Si}[Si^*] - k_{TET}(E_a^{TET})N_{3EP}[Si^*] + k_{TEBT}(E_a^{TEBT})[3EP^*]$$

Equation 27: Differential equation describing rate of SiNC exciton change over time.

where [Si^*] and [$3EP^*$] are the concentration of SiNC excitons and 3EP triplet excitons respectively, k_{Si} is the deactivation rate of SiNC excitons, k_{TET} and k_{TEBT} indicate the rates of TET from SiNC to 3EP and from 3EP to SiNC respectively, and N_{3EP} represents the number of 3EP molecules grafted to the SiNC surface. The recombination of SiNC excitons will be enhanced by carrier traps within the crystal and will be a contributing factor to the k_{Si} term. Similarly to SiNC exciton change rate above, the 3EP triplet exciton population is described as:

$$\frac{\mathrm{d}[3EP^*]}{\mathrm{d}t} = -k_{3EP}[3EP^*] + k_{TET}(E_a^{TET})N_{3EP}[Si^*] - k_{TEBT}(E_a^{TEBT})[3EP^*]$$

Equation 28: Differential equation describing rate of 3EP exciton change over time.

where k_{3EP} is the decay rate of 3EP triplet excitons. In order to keep track of differences in the triplet exciton energy of SiNCs and the 3EP molecules, a Miller-Abrahams rate expression is employed:[198,199]

$$k_{TET}(E_a^{TET}) = \begin{cases} k_{TET}^0 & , E_a^{TET} \leq 0 \\ k_{TET}^0 * exp(-E_a^{TET}/k_bT) & , E_a^{TET} > 0 \end{cases} \text{ where } E_a^{TET} = E_{3EP} - E_{Si}$$

Equation 29: Miller-Abrahams rate expression for SiNC to 3EP exciton transfer.

where E_{Si} and E_{3EP} are the exciton energies in the SiNC and 3EP respectively. Naturally this equation can be reversed for triplet energy back transfer as:

$$k_{TEBT}(E_a^{TEBT}) = \begin{cases} k_{TEBT}^0 * exp(-E_a^{TEBT}/k_bT) & , E_a^{TEBT} \leq 0 \\ k_{TEBT}^0 & , E_a^{TEBT} > 0 \end{cases} \text{ where } E_a^{TEBT} = E_{Si} - E_{3EP}$$

Equation 30: Miller-Abrahams rate expression for 3EP to SiNC exciton back transfer.

Being a coupled pair of linear first order differential equations, the system can be analytically solved (using the condition of only excitons being created in the SiNC by a laser impulse). Simplifying the equation as $\Delta = \frac{k_{Si}+k_{TET}-k_{3EP}-k_{TEBT}}{2}$, $\Omega = \sqrt{\Delta^2 + k_{TET}k_{TEBT}}$, and $\lambda_{\pm} = -\frac{k_{Si}+k_{TET}+k_{3EP}+k_{TEBT}}{2} \pm \Omega$, the exciton populations can be seen as:

$$[Si^*(t)] = \frac{[Si^*]_0}{2\Omega}\left((\Omega - \Delta)e^{\lambda_+ t} + (\Omega + \Delta)e^{\lambda_- t}\right)$$

Equation 31: Time dependent population of excitons within SiNC after a pulse of laser exposure.

$$[3EP^*(t)] = \frac{[Si^*]_0 k_{TET}}{2\Omega}\left(e^{\lambda_+ t} - e^{\lambda_- t}\right)$$

Equation 32: Time dependent population of excitons within the 3EP after a pulse of laser exposure.

The $[Si^*]_0$ term represents the SiNC exciton population excited by the laser at time $t = 0$. To get an accurate picture of the real-world system a set of solutions are found for varying: exciton energy values (E_{Si}), the amount of surface-bound 3EP (N_{3EP}), and exciton trap density via N_m in $k_{Si} = k_{Si}^0 + \sum_m N_m k_m$. Using the output, a weighted average of the populations is calculated to best fit the observed emission spectrum, with the number of traps in the SiNC and number of 3EP molecules distributed according to Poisson statistics. The best fit parameters can be seen below in Table 2.

Table 2: Kinetic model best-fit parameters to match the data in Figure 33A.

	Parameter	**Method of Determination**
$\langle N_{3EP} \rangle$	3.2	Range estimated from absorption spectra of Si:3EP
$1/k_{TET}^{0}$	4.22 ms	Floated to fit Si:3EP dynamics
$1/k_{TEBT}^{0}$	22.0 ns	Floated to fit Si:3EP dynamics
$1/k_{3EP}$	2.26 ms	Floated to fit Si:3EP dynamics
$1/k_{Si}^{0}$	210 μs	Constrained when fitting Si:3EP based on Si:ODA decay
$\langle N_1 \rangle$	0.17	Floated to fit Si:3EP dynamics
$1/k_1$	197 ns	Constrained when fitting Si:3EP based on Si:ODA decay
$\langle N_2 \rangle$	0.58	Floated to fit Si:3EP dynamics
$1/k_2$	57.4 ms	Constrained when fitting Si:3EP based on Si:ODA decay
E_{3EP}	1.53 eV	Estimated from Reference[143,179–182]

This fitting of the TA spectra produces Figure 33A's blue trace, which despite matching the 3EP triplet population rise does not match the population decay. It should also be noted that the model only obtained these results by using a $\langle N_{3EP} \rangle$ of 0.57, which is well below the calculated range of 0.9-4.6. Being unable to fully fit the 3EP T_1 population or do so with known system constraints implies unaccounted additional energy transfer

pathways. Being that the T_1 state of 3EP is close to the average exciton energy of the SiNC, the question of whether a more dynamic equilibrium existing between the 3EP and SiNC excited populations like in acene|PbS QD systems is raised as a potential explanation for the model's failings.[174,175] For previous 9EA|C18|SiQD systems an observed exciton lifetime of 1.16 microseconds, roughly 3 orders of magnitude smaller than anthracene in solution, allowed for reverse energy transfers to be ignored within models.[145,200,201] Recent efforts suggest that the shortened lifetime is a result of either the presence of oxygen which quenches 9EA triplets or a greater density of surface traps on the SiQDs as shown in Figure 34. Improvements in processing procedure have increased 9EA triplet lifetimes to greater than 10 microseconds and doubling upconversion efficiencies to 15%, suggesting that previous efforts didn't observe reverse energy transfers due to 9EA triplet quenching instead of the system being unable to reverse energy transfer.

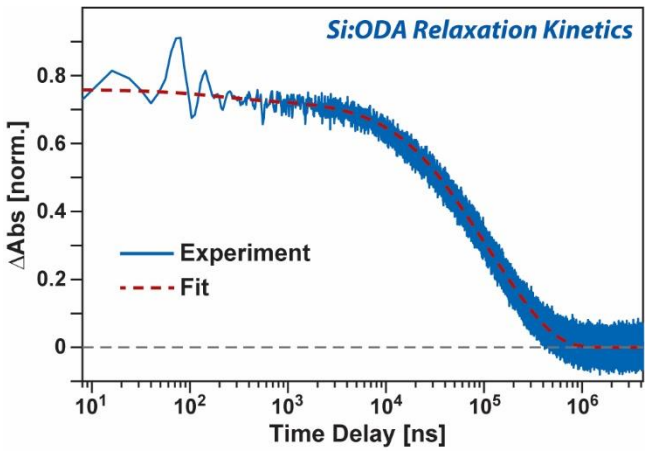

Figure 34: Kinetics demonstrating the relaxation rate of C18|SiQD photogenerated excitons in toluene measured via TA with a 1000 nm probe following 532 nm excitation and its fitting.

Upon allowing for triplet energy back transfer, from the 3EP to the SiNC, the model's fit regarding the 3EP T_1 population decay is greatly improved as seen in Figure

33A's dotted black line and conforms to the 0.9-4.6 $\langle N_{3EP} \rangle$ predicted range with an optimal fit at 3.2 3EP per SiQD.[147,190] Additionally the new fit provides a 3EP triplet lifetime of 2.3 milliseconds, matching reported values,[195–197] while also giving a back transfer time constant of $1/k_{BT}$ = 22 nanoseconds, approximately 190 times faster than standard TET from SiNC to the 3EP making exciton populations prefer SiNC for "storage" in absence of a driving force.

2.2.4 – UCQY Reduction Causes:

Dynamic equilibrium of excitons between the 3EP and SiNC will effectively reduce the available excitons within the 9EA available for Dexter transfer to the DPA emitter. Quickly looking at the TET rates between the SiNC and 3EP one would think the excitons would greatly skew to the SiNC. In the case where SiNC exciton energy exactly matches 3EP and there is only one surface bound transmitter ligand this may be the true; however, for the experimental conditions we find ourselves in with SiNCs that have larger exciton energies than the numerous surface bound 3EP molecules a skewed relative population of excitons in 3EP vs. SiNCs is possible. Estimation of the new equilibrium for the 3EP|C18|SiQD system is done using the model without allowing decay to ground state ($k_{Si} = k_{3EP} = 0$) while allowing for 3EP and SiNC populations to transfer freely, resulting in the Figure 33C plot. This demonstrates that after ~10 microseconds under conditions experimental conditions the 3EP|C18|SiQD system has ~40% of excitons populating the surface bound 3EPs.

Similar to the 9EA|C18|SiQD system transmitting excitons for TTA between DPA emitter molecules, an analogous system where the 3EP|C18|SiQD system transmits its lower energy excitons to 2,5,8,11-tetra-*tert*-butylperylene (tBu_4perylene) for TTA and upconversion was created and tested (see Figure 35A). This will allow for testing of exciton extraction from the 3EP|C18|SiQD system while also demonstrating the triplet fusion phenomenon, where one exciton is excited into a singlet state while the other is reduced to ground. The emission spectra upon illumination with 532 nm (green) or 640 nm (red) light of this new SiQD system can be seen in Figure 35B, where $\langle N_{3EP} \rangle$ was 1.2-6.5 per SiQD while the QDs were dispersed in a 0.5 mM tBu_4perylene in toluene solution. The lower wavelength violet light observed can be ascribed to the tBu4perylene emission resultant of TTA upconversion. Upconverted violet light from the tBu_4perylene photoluminescence demonstrates a linear dependence with both red (640 nm) and green (532 nm) incident light intensity between 25-800 mW/cm^2 as shown in Figure 35C. A linear as opposed to quadratic dependence implies that within these intensities exciton decay is primarily a result of TTA and photoemission.[202,203] This would only be possible if the sensitizer to emitter (SiQD to tBu_4perylene) triplet exciton transfer process through 3EP was efficient enough to not be rate limiting in TTA. It is also worth noting that the presence of surface-bound 3EP was required for upconversion (for this sample $\langle N_{3EP} \rangle = 6.5$), as C18|SiQD were unable to perform upconversion while in the presence of tBu_4perylene. Under 532 nm excitation an UCQY of 1.5% is attained, making it a comparable non-toxic alternative to analogous palladium(II) *meso*-tetraphenyl-tetrabenzoporphyrin (PdTPTBP) systems which also utilize tBu_4perylene to attain 0.1-7.6% UCQY.[177]

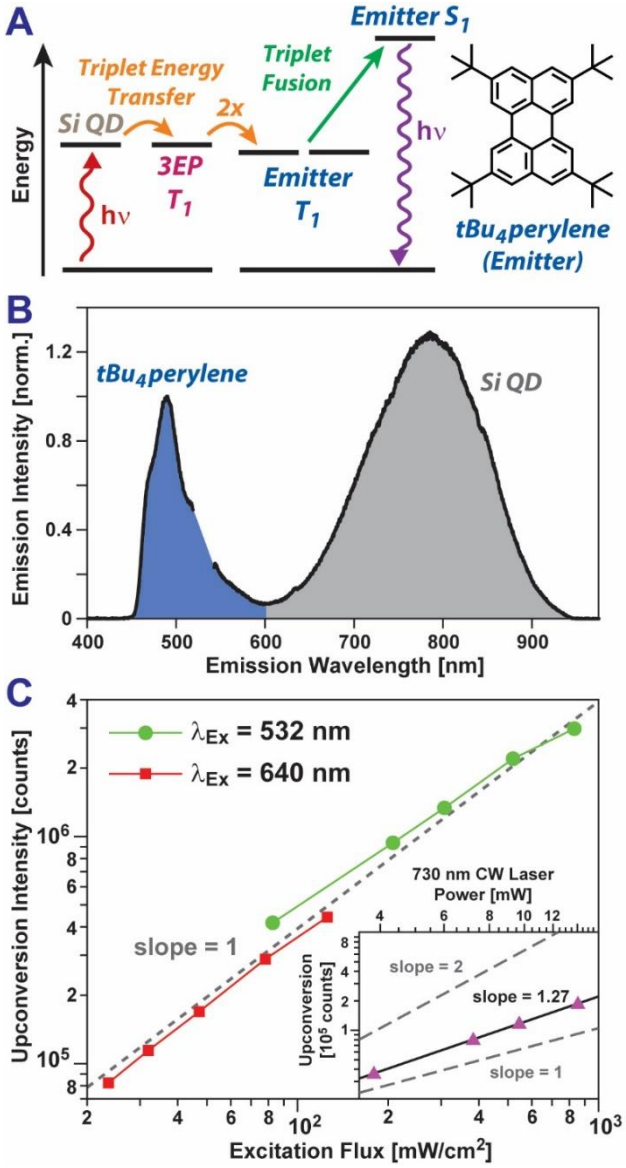

Figure 35: (A) Jablonski diagram illustrating the upconversion energy transfer pathway for TTA and (B) the emission spectra demonstrating upconversion in the 3EP|C18|SiQD system in a 0.5 mM tBu_4perylene in toluene solution undergoing 532 nm photoexcitation (upconverted emission is shaded in blue while SiQD emission is shaded in grey). (C) Excitation flux to upconversion emission intensity under either 532 nm (green circles) or 640 nm (red squares) illumination, demonstrating a linear increase over the range examined. Illumination with 730nm (inset) demonstrates the emission intensity scales with a slope between 1 and 2.

Using 730 nm Far Red/NIR as a source we pushed the system and attained upconversion, however intensity power measurements this time resulted in a slope of 1.27 (Figure 35C inset) suggesting the system is no longer operating in an exciton "saturated regime". A possible reason for reduced efficacy is that the SiQD's absorption cross-section relates directly to wavelength, with greater absorption coefficients at lower wavelengths. This relation is demonstrated as the same sample will produce a 1.5% UCQY under 532 nm light, and only 0.42% under 640 nm light, demonstrating a ~3 times difference in upconversion matching the extinction ratio between the wavelengths. Curiously, the 640 nm light has only ~2.5 times stronger absorbance than 730 nm and likely does not fully account for the reduced performance in the Far Red/NIR.

The SiNC size distribution is likely a secondary explanation for reduced UCQY with longer wavelength inputs. Despite 730 nm photons (1.70 eV) falling within the middle of the 3EP emission band, the observed average PL of the ensemble falls at 1.6 eV with a FWHM of 0.29 meV implying that the 730 nm light would likely not be able to excite all of the SiQDs. This can be traced primarily to the broad energy levels resulting from in imperfect SiNC size distribution. Broadness of the SiNC population can be inferred from the TEM and XRD analysis seen in Figure 36A, while its effects can effectively be seen with the broad emission spectra of C18|SiQD in Figure 36B.

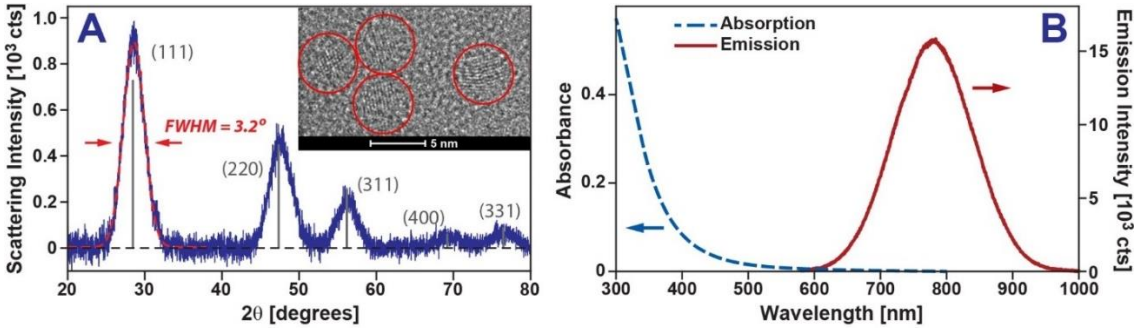

Figure 36: (A) XRD and Scherrer's Analysis fitting of the 111 peak showing nm crystal size with TEM demonstrating a larger size (inset). (B) Absorption spectra and emission spectra under 488 nm excitation for the C18|SiQD system.

Adjusting the model to limit exciton energies beneath 1.70 eV the 3EP only maintains ~20% of the exciton population as opposed to ~40%, which would necessarily reduce TET to the tBu_4perylene, TTA, and UCQY. If this is truly a contributing factor a simple correction method would be to either create a more monodisperse SiNC population or reduce the SiNC size to increase average exciton energy levels. Alternatively replacing the transmitter with a molecule containing lower energy levels would skew the excitons to populate the transmitter molecules more. If for instance, the surface-bound perylene was replaced with tetracene (E_T = 1.25 eV),[204–206] our model predicts the exciton population would reside primarily (>94%) within the tetracene. Rao et al. have also come to a similar conclusion with their work on tetracene||PbS,[175] highlighting the importance of exciton population equilibriums.

2.2.5 – Summary:

This study has demonstrated that SiQD systems establish a energetic quasi-equilibrium state with triplet excitons dynamically moving back and forth between the SiNC and the

transmitter molecule bound to its surface. Physical experiments were performed on 3EP functionalized SiNCs, with transient absorption experiments indicating a 4.2 microsecond equilibrium timescale and emission spectroscopic measurements demonstrating 1.5% UCQY at low photon fluxes. Using different wavelengths of light, the ligand-bound excitation population was able to be altered as observed through a changing UCQY and incident-flux to upconversion relations, with longer wavelengths reducing energy transfer efficiency. Taken together, in organic-to-silicon junctions a system can be designed move energy in a desired direction through manipulation of the incident light and relative relation of the silicon and organic compounds energy levels.

2.3 – Air-Stabilization of Upconverting Silicon Quantum Dots[4]

When considering QD use in biological applications there are two key problems that need to be addressed: 1) toxicity of the QD material, and 2) the quenching effect of oxygen on quantum yield. Addressing the toxicity of QDs by changing them from cadmium and lead based cores to silicon with surface-bound organics is the foundation of this chapter and has had multiple publications demonstrating viability.[137,207,208] Issues with this non-toxic alternative become apparent when considering the effect of oxygen exposure via air. The triplet excited states used in TTA are "quenched" by oxygen, a process where the oxygen is excited by or instead of the transmitter ligand or emitter molecule, thus preventing effective energy transfer to desired SiQD system components. This study is one of the first investigating air-stability of nanocrystal based photon upconversion, though there have been several attempting to solve the problem in molecular systems by creating oxygen barriers with polymers, microcapsules,[209,210] supramolecular self-assembly systems,[211,212] and even porous silica.[39] In these cases oxygen scavenging molecules like soybean oil[213] or oleic acid[39] or poly(phosphoesters)[214] have been used, spanning natural to hyperbranched unsaturated lipids.

Using this as a basis, a one-step thermal hydrosilylation is performed to attach both the transmitter ligand and a terminal alkene to the surface of SiNCs for energy transmission and solubility purposes respectively. The long-chain nature and hydrogen saturated nature will also allow for the formation of polymer barriers with the terminal alkene, slowing the diffusion of oxygen into the SiQD system and thus extending the usable photon

upconversion time. As discussed before TTA as a method of upconversion relies on multiple energy transfer steps which are illustrated in Figure 38a for this study. This system relies on a SiNC core as a sensitizer, while surface-bound 9-ethylanthracene (9EA) acts as the transmitter ligand passing excitons to 9, 10-diphenylanthracene (DPA) in a toluene solution. These DPA when excited interact with other excited DPA, inducing TTA and act as the emitter molecule in the system sending out 432 nm (violet) light. Hydrogen terminated SiNCs between 3.0-3.2 nm in diameter were used for this study, undergoing a 3 hour thermal hydrosilylation with 9-vinylanthracene (9VA) to become the surface bound 9EA transmitter ligand, in addition to linear terminal alkenes to enable colloidal stability.

2.3.1 – Solvent Comparison:

Compared to Cadmium Selenide/Lead Sulfide (CdSe/PbS) nanocrystal-based systems[137,215] 9EA|C18|SiQD already perform well in an oxygen rich environment, maintaining a detectable upconversion signal in an air exposed toluene solution for an hour as opposed to < 3 minutes. This resistance to oxygen was observed in solvents ranging from toluene, mesitylene, octadecene, oleic acid, and methyl oleate as shown in the spectra of Figure 37 and Figure 38b.

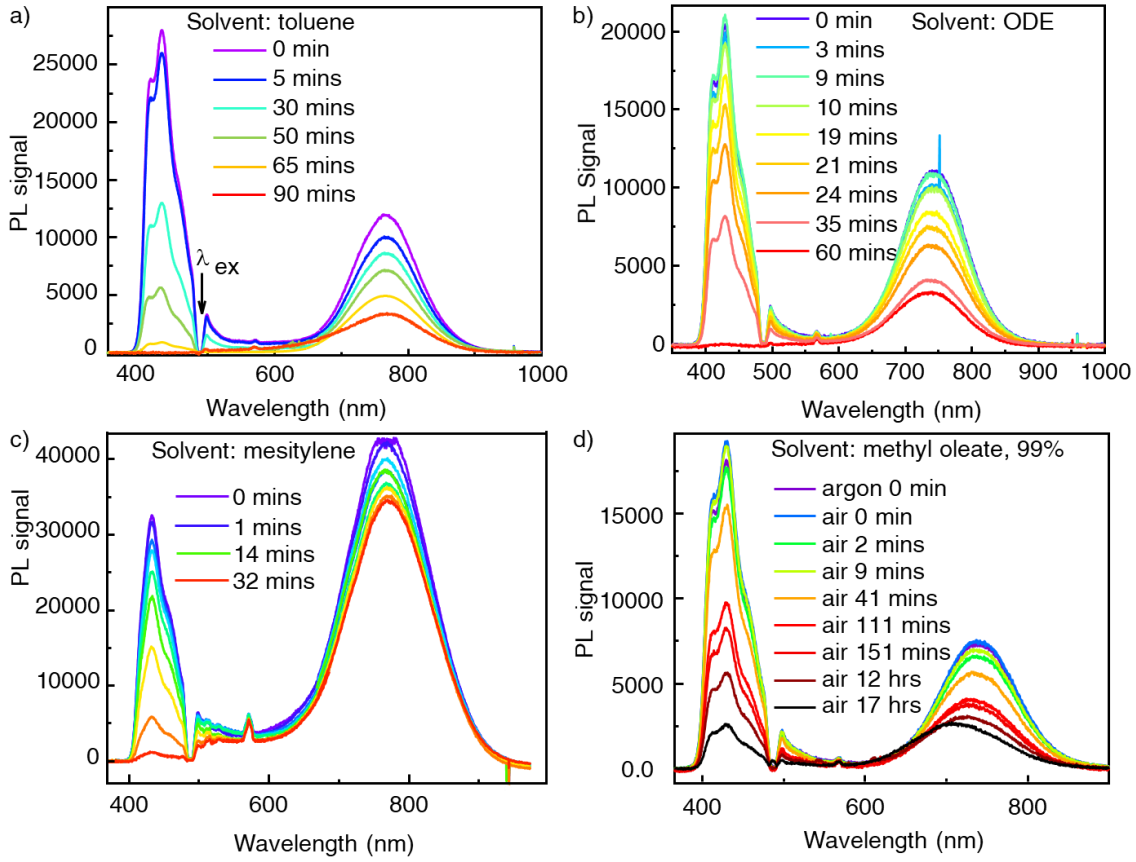

Figure 37: Emission spectra over time of air-exposed 9EA|C18|SiQD with DPA and 3.2 nm SiNC cores in solvents of a) toluene, b) octadecene, c) oleic acid, and d) methyl oleate.

(Methyl oleate and oleic acid were selected as they are natural or FDA approved food additives implying ready biocompatibility.) As shown in Figure 38b, methyl oleate and oleic acid greatly outperformed octadecene, mesitylene, and toluene in upconversion longevity, with upconversion signals lasting up to 4 days. Despite being a welcome result, it is unexpected as oxygen's ground triplet state ($^3O_2$) easily reacts with DPA molecules in their triplet state to form an oxygen singlet ($^1O_2$) of 0.98 eV.[216]

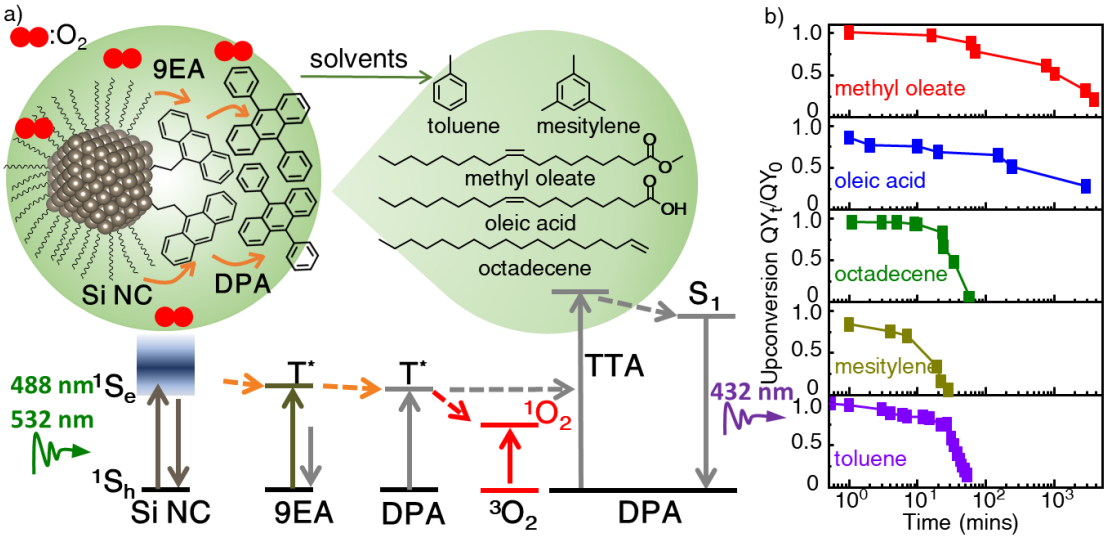

Figure 38: a) Energy diagram and molecular cartoon of photon upconversion with 9EA|C18|SiQD in a DPA solution utilizing toluene, mesitylene, methyl oleate, oleic acid, or octadecene as the solvent with O_2 as a quenching agent. b) Air exposure time vs normalized UCQY relative to initial values for each solvent.

Both GPC and DLS data indicate that 9EA|C18|SiQD are becoming embedded into polymer matrices that form due to thermal polymerization of alkenes during the thermal hydrosilylation step. Longer precursor alkenes appear to form better oxygen barriers for longer lasting air-exposed upconversion. Heat induced polymerization is to be expected[217] and long, close-packed aliphatic groups have already been shown as effective O_2 barriers for bimolecular TTA upconversion systems.[209,210,212,218] Yanai et al. have demonstrated ion-dipole interactions that promote long-chain aliphatic group stacking to form air-stable gels,[219,220] while Kouno et al. showed double-bonds are not necessary for long-chain terminal carboxylic acids to establish physical O_2 barriers.[221] Our observations that oleic acid and methyl oleate as polar solvents stabilize SiQD upconversion in air while toluene,

mesitylene, and octadecene did not demonstrates consistency with previous findings. The diffusion of O_2 can be seen to be slow in these solvents in Table 3.

Table 3: Dynamic viscosity and diffusivity of oxygen in different solvents.

Solvent	**Viscosity (mPa·s) at RT at 1 atm**	**Diffusivity(m^2/s)**	**Diffusivity estimated from viscosity**[222]
toluene	0.56	4.38×10^{-9} [222,223]	3.82786×10^{-9}
mesitylene	0.66-0.72 [224]		3.21654×10^{-9}
hexadecane	3 [225]	2.49×10^{-9} [226]	1.25019×10^{-9}
octadecane	3.57 [227]		1.11329×10^{-9}
methyl oleate	5.3 [228]		8.55458×10^{-10}
oleic acid	27.64		2.84446×10^{-10}

2.3.2 – Polymers as Oxygen Barriers:

Based on the aforementioned previous studies, reduction in oxygen diffusion mobility appears to be a good strategy for preserving upconversion efficiency in an oxygen rich environment. Using Dynamic Light Scattering (DLS) and Gel Permeation Chromatography (GPC) measurements demonstrate hydrocarbon polymer formation resulting from the thermal hydrosilylation process. After performing thermal hydrosilylation in mesitylene at 175 ºC for 3 hours, DLS measurements of 9EA|C18|SiQD showed two primary populations of diameter 9.5±0.9 nm (88% of the population) or 370±70 nm (12% of the population). As the SiNC is ~3 nm in diameter and the C18 (ODA) attached is ~2 nm, the 9.5 nm population can likely be attributed to single SiQDs.

Conversely the 370 nm peak can be ascribed to larger polymeric aggregates containing multiple SiNCs. Continued heating for a total of 12 hours produces another peak in DLS at 1400 nm, increasing the proportion of SiQDs within the polymer matrix from 12% to 73% as shown in

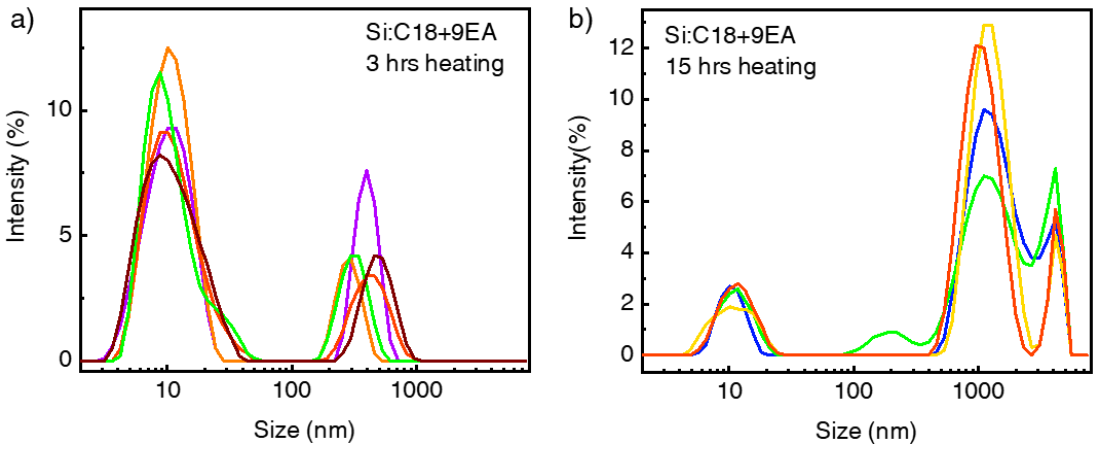

Figure 39 and Figure 41a.

GPC measurements on the same 9EA|C18|SiQD samples confirm the presence of polymers, especially those resulting from prolonged heat treatments. Heating SiNCs on

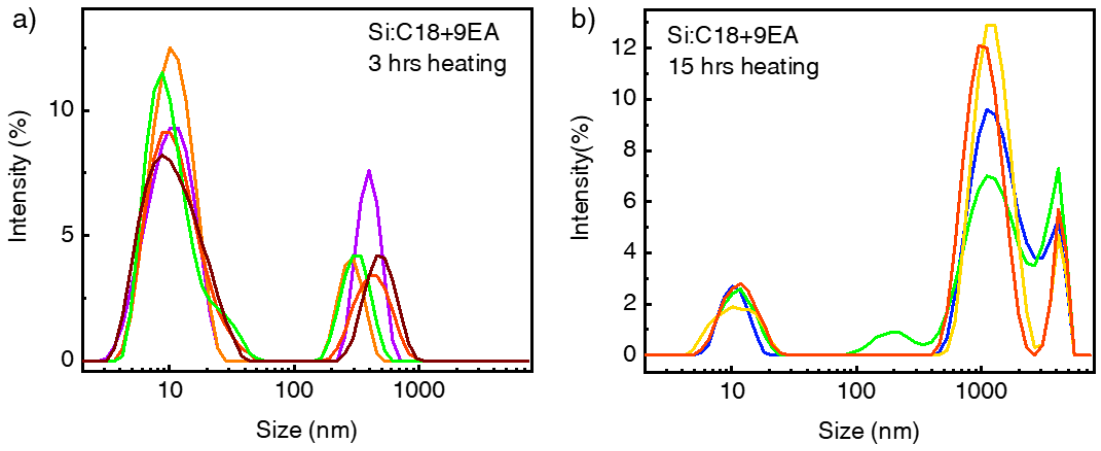

Figure 39: DLS measurements of 9EA|C18|SiQD samples in toluene and DCM with thermal hydrosilylation times of a) 3 hours and b) 15 hours. Multiple scans were performed for each sample and are represented with different colors.

their own produced no polymeric species as detected by GPC, however treatment with ODE for 3 hours shows species at 30,000-36,000 g/mol while 15 hours shows species at 305,000 g/mol (see Figure 41b). These numbers correspond to the molecular weight of isolated 9EA|C18|SiQDs as seen in Table 4.

Table 4: Estimation of molecular weights of 9EA|C18|SiQD with a SiNC of 3.0 nm

Diameter (nm)	**number of Si atoms per NC**	**Si NC weight (g/mol)**	**Molecular weight after adding surface ligands**
3.0	353.20	9889	35089-60289

The 10 times increase in GPC's observed molecular weight with an increase to 15 hours of thermal hydrosilylation corresponds with the increase to 1400 nm diameter observed with DLS, while single SiQD peaks are still observed by GPC as shown in Figure 40. Extending the thermal hydrosilylation process from 3 hours to 15 hours does not significantly impact the PLQY, however UCQY increases from 9.6% to 12.5%. More dense ligand coatings

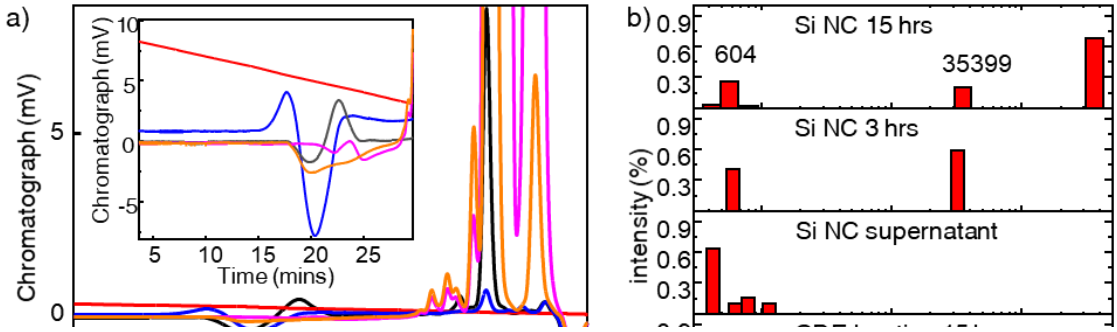

Figure 40: a) Elugram of SiNC and SiQD samples with different thermal hydrosilylation times and solutions, with peaks at 30-35 minutes correspond to ODE. b) Molecular weight as calculated from retention time in DLS with exceptionally low peaks being attributed to dimers of ODE.

appear to provide more effective oxygen barriers, as longer alkynes seem to provide greater air stability upon thermal hydrosilylation with 9VA. Exposure to air quenches upconversion and photoluminescence more generally as shown in Figure 41c-d. It should be noted that sacrificial oxidation of a solvent cannot be the primary factor for blocking oxidation as octadecene would have no impact if that was the case.

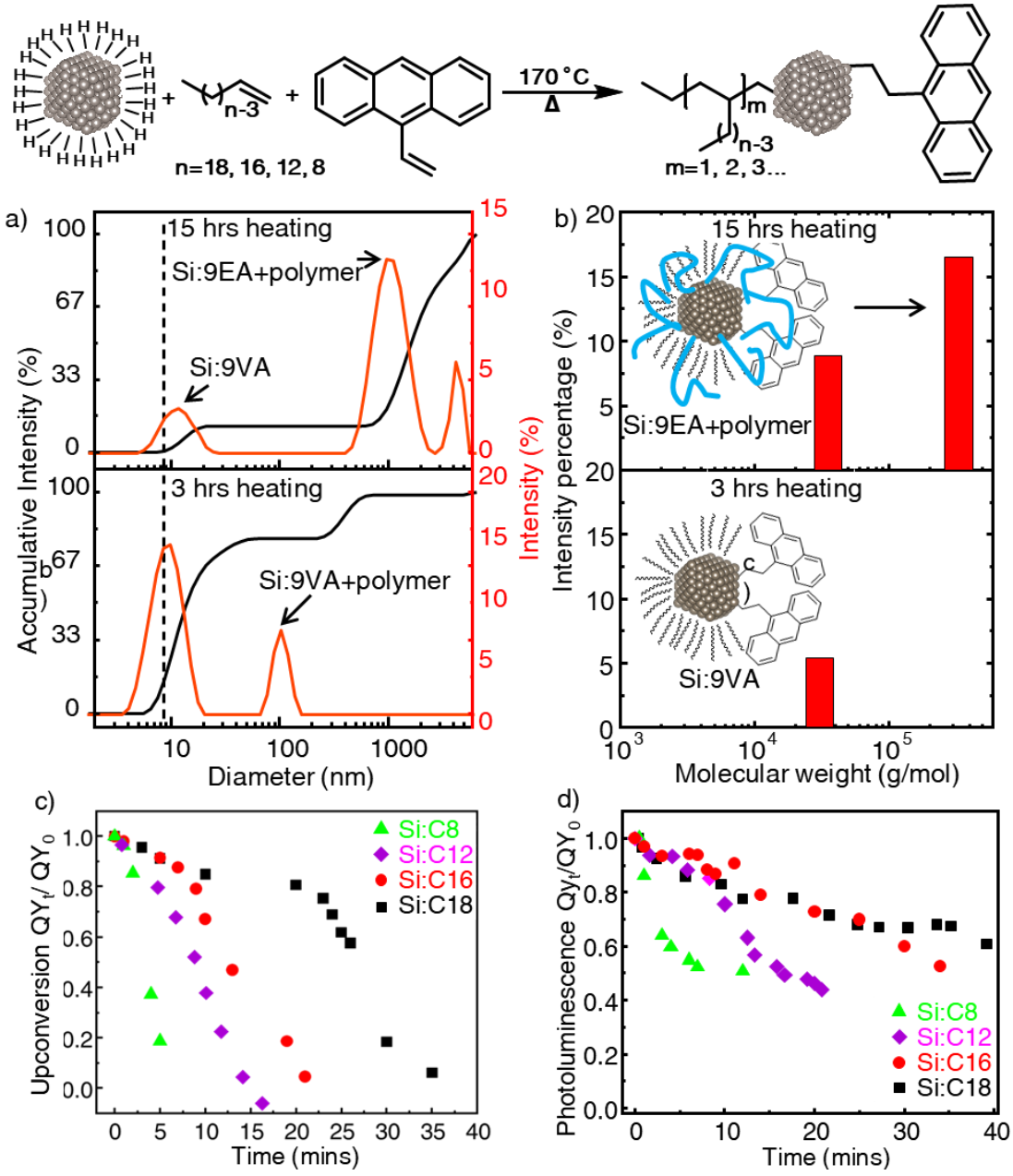

Figure 41: a) DLS measurements demonstrating incorporation of 3 nm 9EA|C18|SiQDs into polymeric matrices that grow with extended exposure of ODE and 9VA in mesitylene at 175 ºC for 3 hours and 15 hours. b) GPC of the same samples confirming polymerization. c) UCQY and d) bandedge PLQY of 9EA||SiQD samples with differing length alkyne ligands (C8, C12, C16, and C18) in toluene normalized to their initial values to demonstrate the effects of air exposure.

2.3.3 – Micelles for Water Based Applications:

In an attempt to provide functionality in water, 9EA|C18|SiQDs and DPA were encapsulated in water soluble methyl oleate micelles as shown in Figure 42a-b. While UCQY decreased dramatically in the presence of anhydrous oleic acid (90% purity), with methyl oleate (99% purity) the SiQD system was stable for over 4 days and halved in efficiency after 25 hours (see Figure 42c). There are two quenching phases observed from air exposure: the first is a fast initial quenching of both the UCQY and PLQY, while the second is ~10^2 times slower (see Figure 42d). Observation of a slight blue-shift and decrease in bandedge peak PL implies that oxygen is penetrating the polymer barrier and oxidizing the SiNC core, forming an oxide layer and reducing the active silicon nanocrystal size inside. Under initial air-free conditions UCQY reached as high as 15% with 488 nm incident light at 1.0 W/cm^2. The oil-in-water emulsions are 100-500 nm in diameter and were stabilized by a Poloxamer 188 triblock polymer, self-assembled using methyl oleate

and are shown in Figure 42e. Colloidal stability of the micelles degrades after 2 days in air, limiting the upconversion endurance as shown in Figure 42f.

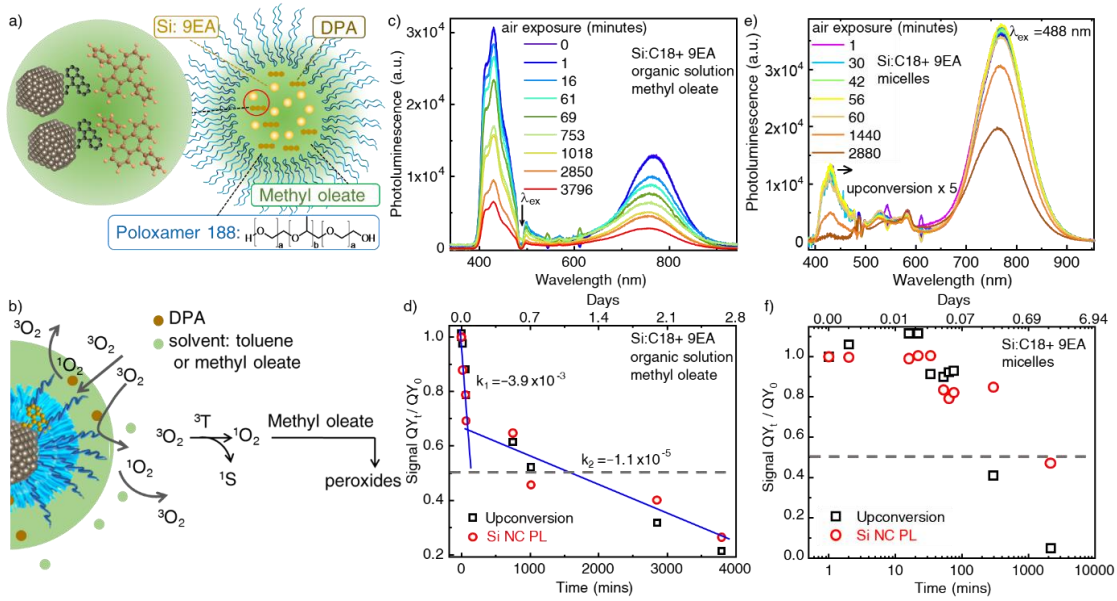

Figure 42: a) 9EA|C18|SiQDs with DPA suspended in methyl oleate micelles stabilized by P188 triblock copolymer to form photon upconverting oil-in-water micelles and b) the possible mechanisms for air stability during photon upconversion while in methyl oleate. c) Photon upconversion of 9EA|C18|SiQD samples using a 3.2 nm in methyl oleate exposed to air. d) Normalized changes in UCQY (black squares) and bandedge PLQY (red circles) corresponding to the spectra in (c). e-f) the same test as in (c-d) except with the micelles suspended in water with P188.

The two quenching regimes of air-exposed SiQDs can be explained by the oxygen forming a "sacrificial" oxidation layer on the SiNC and the internal double bonding of methyl oleate or oleic acid. At a minimum, the blueshift observed in the spectra overtime implies a shrinking of the crystalline silicon which would be accomplished through surface oxidation of the SiNC. However, even when the UCQY drops to zero the PLQY maintains 30-50% of its initial value. Stabilization of PLQY infers that the SiNC oxidation is self-limiting in

a manner similar to how bulk silicon will develop a ~1 nm surface oxide layer that prevents further oxidation.[229] As a result, the fast quenching phase can be attributed to formation of the SiNC oxide layer that acts as a tunneling barrier slowing TET, which reduces the concentration of excited DPA, and diminishes UCQY. The fact that upconversion occurs throughout this process implies that oxidation does not impact the surface-bound 9EA. Upon reaching the self-limiting oxide layer thickness oxidation of the SiNC slows to the point where oxygen reacting with the DPA becomes the dominant form of exciton quenching by forming singlet-oxygen and ground state DPA as shown in Figure 42b. As singlet oxygen is highly reactive it is able to form peroxides from carbon-carbon double bonds.[230–232] and as methyl oleate is in chemical excess when compared to DPA concentrations it may reduce the relative oxidation rate of DPA compared to other solvents.

2.3.4 – Summary:

The SiNC platform has performed well, being able to accomplish UCQY exceeding 15%. While the UCQY drops to 7% within a day of air exposure, the ability to upconvert light in environments containing oxygen for extended periods of time opens this technology to biological applications. Oxygen pressure within biological tissues present between 0.5-5 kPa[233,234] which is significantly lower to the 21 kPa experienced in direct air exposure. Improved air stability can be achieved through dense long-chain polymeric barriers formed through thermal hydrosilylation which creates local pockets in the SiNC for sacrificial oxidation reducing SiNC surface oxidation rates. Incorporating the 9EA|C18|SiQD into oil-in-water micelles with methyl oleate and P188 triblock polymers

resulted in initial UCQY up to 11% that were air-stable for more than 2 days, being limited primarily by the micelle stability instead of the SiQD system.

2.4 – In-Flight Partial Functionalization, Surface Coverage, and Silicon Quantum Dot Size Effects[5]

This subsection addresses this twin issues of slow processing and limited control over uniform surface functionalization in SiQDs by implementing a hybrid gas- and liquid-phase functionalization approach. The gas-phase grafting of SiQDs with various organic groups was first introduced by Mangolini and Kortshagen in 2007 as a way to provide soluble SiQDs immediately after synthesis.[235] Anthony et al. have shown that the same functionalization can be achieved by injecting a gas saturated with an organic ligand in the plasma afterglow, i.e. the region downstream of the powered electrodes where the plasma extinguishes.[236] In this study, alkyl chains are grafted onto the surface of SiQDs immediately after their synthesis in the gas-phase using a low-temperature plasma. Subsequent 9-vinylanthracene (9VA) is attached to the remaining surface sites via thermal hydrosilylation in mesitylene to form surface bound 9-ethylanthracene (9EA) groups. By carefully controlling the process parameters it is possible to realize partially functionalized SiQDs, i.e. nanoparticles with adequate solubility after in-flight grafting but with unreacted surface sites available for further modification. This approach allows for the investigation of how the length and surface density of alkyl chains affect the upconversion with SiQDs. It is found that the same solubility can be achieved by grafting roughly 24% of the SiQD's surface with 1-dodecene, in contrast to the 49% coverage of 1-hexene needed, as estimated from FTIR spectra. The partial coverage

with Si-dodecyl allows for a greater fraction of the surface to be available for 9EA, whose density can be optimized to maximize the upconversion quantum yield (UCQY). The UCQY is as high as 17.17% when 3 9EA molecules are attached on average per SiQD. On the other hand, only 1.5 9EA molecules can be grafted onto SiQDs with Si-hexyl groups, leading to a lower 5.16% UCQY (see Figure 43a for a cartoon representation). This is a new strategy towards achieving SiQDs with a multifunctional surface modification in a rapid, uniform, and tuneable way. The approach simplifies SiQD functionalization and reducing processing time, all while providing material with high upconversion quantum efficiencies.

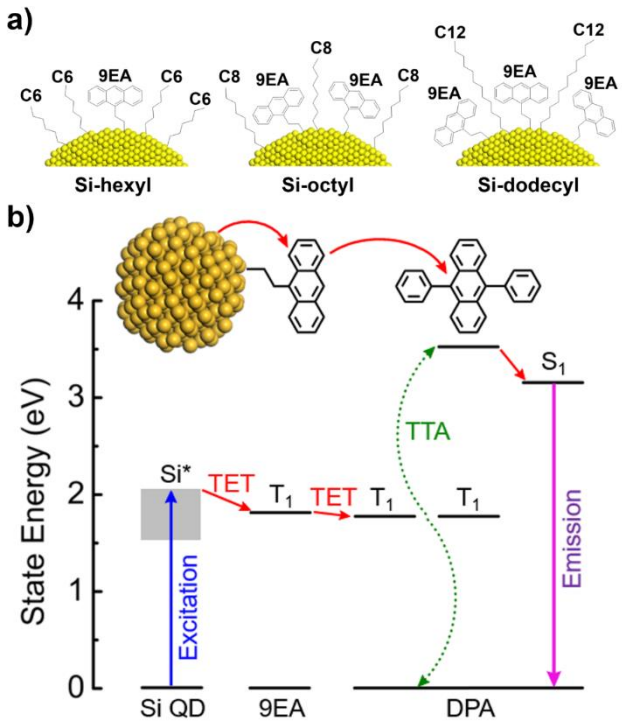

Figure 43: a) Illustrations of functionalized SiQD with 9EA transmitter ligands and critically loaded alkyl chain ligands to maintain solubility, in addition to b) an energy level diagram illustrating photon upconversion process utilizing TET of the SiQD's photoexcited excitons, through the 9EA, and on to the DPA where they undergo TTA resulting in upconverted photon emission.

2.4.1 – Synthesis and Characterization:

In-flight Synthesis and Functionalization:

As within previous sections, the first stage of SiQD in-flight synthesis consists of the SiNC formation. A diagram of the in-flight synthesis and partial functionalization system can be seen in Figure 44. Using the same reactor described in subsection 2.1, 30 W of power is applied to a precursor gas mixture of 1.37% (v:v) silane:argon at a flowrate of 60 sccm. Plasma within the 5.4 mm diameter tube breaks down the SiH_4 and forms the SiNCs, exiting into an unpowered plasma

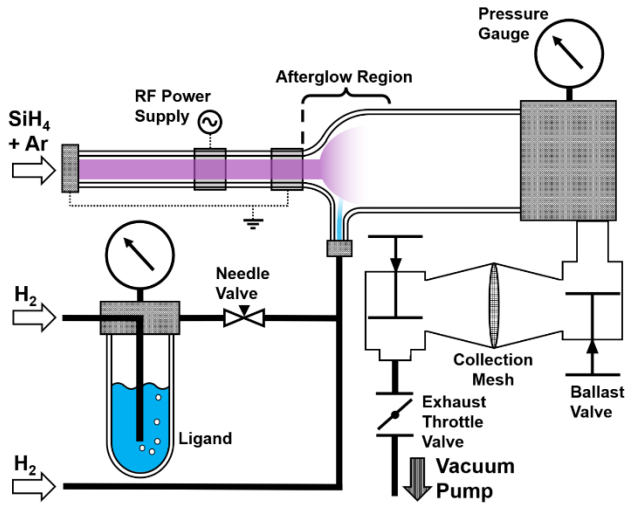

Figure 44: Simplified diagram of gas-phase SiQD synthesis and in-flight functionalization system using standard electrical and process flow diagram symbols.

afterglow that acts as the second stage of the in-flight functionalization process. Gas-phase ligand grafting is accomplished by flowing hydrogen gas saturated with the ligand into the plasma afterglow. The afterglow environment is sufficiently energetic to drive the grafting of the ligands onto the SiQD surfaces, while avoiding decomposition of the organic ligand which would occur in a powered plasma environment. To improve mixing and increase the reaction volume, the reactor is expanded to an inner diameter of 20.5 mm shortly after the downstream grounding electrode while simultaneously injecting the ligand-saturated hydrogen gas through a side inlet. The saturated gas is produced by passing hydrogen through a bubbler filled with the desired ligand. The absolute pressure in the bubbler is kept at 0.1 kPa, 20 kPa, and 100 kPa for the 1-dodecene, 1-octene, and 1-hexene respectively to provide a coarse adjustment of the ligand flow rate. The higher the pressure of hydrogen within the bubbler, the more dilute the ligand's vapor with the hydrogen carrier gas. As a method of fine control, the hydrogen flow through the bubbler is

varied between 2.5 and 10 sccm to adjust the flux of ligand molecules entering the plasma afterglow. For consistency in gas flow conditions between samples, additional hydrogen is added downstream of the bubbler so that the total hydrogen flow within the system is 100 sccm. The SiQDs partially functionalized in the gas-phase with aliphatic ligands and are transferred air-free into a nitrogen-filled glovebox for further processing.

Liquid Phase Hydrosilylation:

The SiQDs partially functionalized with alkyl chains are processed in the glovebox to complete their surface functionalization with transmitter molecules. Samples with no ligands or surface density lower than the critical loading do not disperse to form a clear solution, while materials with a "critical" surface density of alkyl chains form a stable colloidal dispersion in solution (see Figure 45a for ligand loading illustration and Figure 25 for sample images demonstrating colloidal stability). The thermal hydrosilylation process is then employed with 9VA using published methods as outlined in Section 2.1. Upon completion of the hydrosilylation process the functionalized samples are then diluted, placed in 10mm x 10mm path length quartz cuvettes and optically characterized with the same method described in Section 2.1 and by P. Xia et. al.[145]

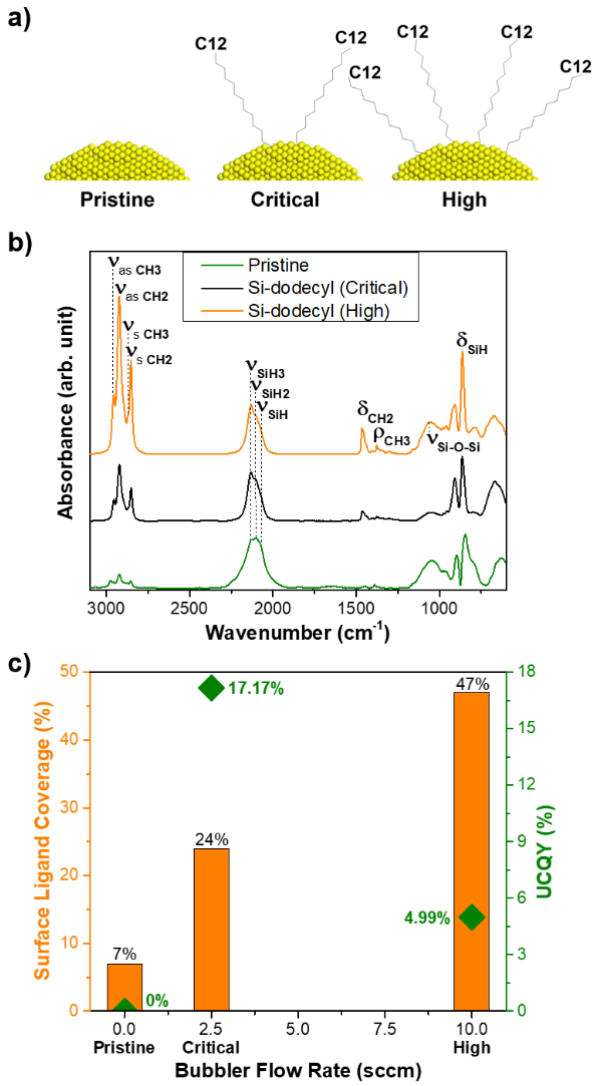

Figure 45: Three different flow rates of hydrogen gas saturated with 1-dodecene fed to the plasma afterglow alter the SiQD solubility and photon upconversion quantum yield (UCQY). a) Illustrative cartoons of the QD surfaces, b) normalized FTIR spectra for the pristine SiQDs terminated with hydride groups, as well as SiQDs with a critical or high amount of Si-dodecyl ligands. c) The Si-dodecyl chain surface coverage on 3.1 nm diameter SiQDs and their UCQYs plotted against the hydrogen flow rate in the bubbler.

Sample Characterization:

A Thermo Scientific Nicolet iS50 FTIR is used in conjunction with a Pike Technologies ZnSe attenuated total reflectance (ATR) crystal (Catalog #: 1605554)

for characterization of the surface chemistry. The material is dispersed in chloroform and dropcast on the ATR crystal. 50 scans are averaged for each measurement from 3100 to 600 cm^{-1} and OMNIC software is used to average the data, remove interference from air and subtract the baseline signal. Using this FTIR absorption spectra in conjunction with absorption cross sections for SiH and the utilized alkyl chain ligands available in the literature, calculations of the approximate ligand surface coverage in percent are performed (Table 5).[237,238] Z. Li et al. recently reported that a minimum surface coverage of 25% for Si-octyl on a 3.2 nm diameter silicon particle is needed to maintain solubility, as determined through CHNS elemental analysis. Using the aforementioned FTIR absorbance technique our 3.1 nm diameter Si-octyl functionalized SiQDs required a minimum (aka. critical) surface coverage of 36%, which is consistent with the results from Z. Li et al.[239] Measurements demonstrating TTA

2.4.2 – Ligand Saturation Effects:

The hypothesis of this subsection is that a gas-phase functionalization approach can provide control over alkyl ligand surface coverage on SiQDs, and that this in turn affects 9EA grafting and the UCQY. To test this, alkyl chains are grafted to 3.1 nm diameter SiQDs first in the gas phase. Then this partially functionalized SiQD undergoes thermal hydrosilylation in solution with 9VA to bind 9EA on the remaining unfunctionalized silicon surface sites. Thus, the surface density of alkyl chains installed in the gas phase allows for control of SiQD functionalization with

both ligands. To achieve this, the proportion of alkyl chains added to the reactor is controlled by varying the flow rate of hydrogen through a bubbler filled with the terminal alkene ligand. The hydrogen gas becomes saturated by the alkene within the bubbler, so higher flow rates correspond to greater amounts of the alkyl chain being deposited on the SiQD surface. In this study, 0, 2.5, and 10 sccm of hydrogen was flowed through a bubbler filled with 1-dodecene. Part of the sample is analysed with FTIR while the rest is further functionalized with 9EA to investigate the role of Si-dodecyl surface density on the UCQY. The FTIR spectra in Figure 45b suggest that the relative magnitudes of the CHx and SiHx stretching regions (2700-3050 cm^{-1} and 1900-2300 cm^{-1} respectively) in the Si-dodecyl samples can be varied.

Table 5: Absorption Cross sections at a given wavenumber.

Molecule	**Wavenumber (cm^{-1})**	**Absorbance Cross Section (cm^2/molecule)**	**Source**
Silylidyne (SiH)	2130	6.35E-19	[237]
Hexane (C_6H_{12})	2922	7.95E-19	Interpolated from Figure 46
Octane (C_8H_{16})	2922	1.30E-18	Interpolated from Figure 46
Dodecane ($C_{12}H_{24}$)	2922	2.31E-18	Interpolated from Figure 46

Using the peak absorption cross sections of the C-H bond (2922 cm^{-1}) from Klingbeil et al. for unbound alkyl groups pentane, heptane, and dodecane a fitting was made to interpolate the values for hexane and octane as shown in Figure 46a and Table 5.[238] The silylidyne molecule (Si-H) absorption cross section at 2130 cm^{-1} was then used as a proxy for all remaining surface bonds on the SiNC. A ratio of absorption amplitudes at the 2922 cm^{-1} and 2130 cm^{-1} peak positions can then be taken and sensitivity compensation via absorption cross section values are applied as shown in Equation 33. This estimates the surface coverage ratio between the alkyl and Si-H compounds and a ligand surface coverage estimate is then determined through Equation 34 and plotted.

$$R = \left(\frac{A_{\mathrm{SiH}}}{A_{\mathrm{CH}}}\right)\left(\frac{\sigma_{\mathrm{CH}}}{\sigma_{\mathrm{SiH}}}\right)$$

Equation 33: Absorption compensated ratio between ligand covered surface and hydrogen terminated silicon.

$$Surface\ Coverage\ \% = 100\left(\frac{R}{R+1}\right)$$

Equation 34: Estimated alkyne ligand surface coverage fraction.

In these equations R is the surface coverage ratio, A_{SiH} and A_{CH} are the experimental absorptions at 2130 cm^{-1} and 2922 cm^{-1} respectively, while σ_{SiH} and σ_{CH} are the

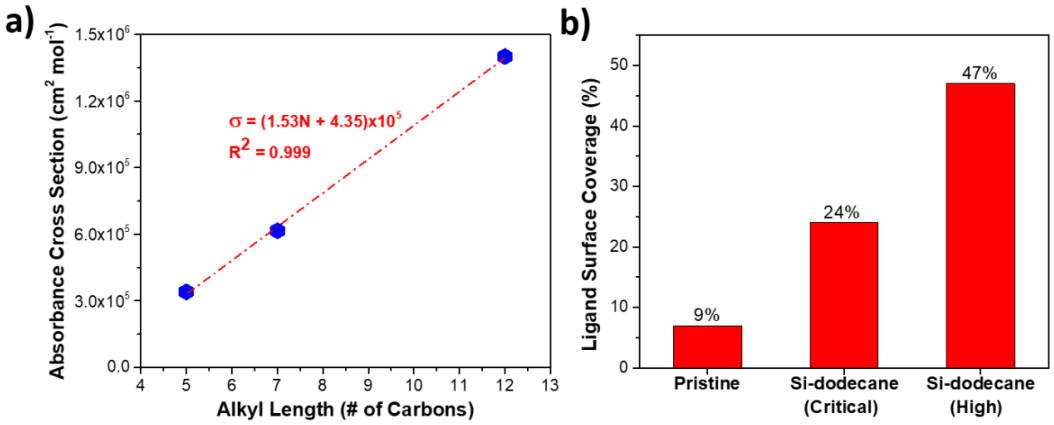

Figure 46: a) Fitting of the absorption cross section at 2922 cm^{-1} for alkyl groups with respect to carbon chain length and b) predicted ligand surface coverage using the silylidyne and dodecane absorption cross sections for samples produced with differing amounts of 1-dodecene flow.

absorption cross sections of the silylidyne and ligand chain at 2130 cm^{-1} and 2922 cm^{-1} respectively. It is worth noting that the literature sources for the absorption cross sections used for all species in this analysis were performed on unbound molecules. The resulting ligand surface coverages are plotted in Figure 46b and Figure 48a where the coverage for the "Pristine" sample used the dodecane absorption cross section.

After normalizing the FTIR data with respect to the absorption cross sections of the surface bound species the ligand surface coverages are shown to vary with bubbler flow rate, (Figure 45c). For the case of the "pristine sample" (0 sccm of hydrogen

through the bubbler) the CHx peaks present are likely a result of residual 1-dodecene adsorbed to the inner walls of the gas delivery lines. This SiQD sample without any stabilizing Si-dodecyl sediments out of solution and does not show any upconversion. Samples processed with a high flow of 1-dodecene show a reasonable UCQY of 4.99%. An intermediate flow rate of 1-dodecene is needed to maximize the upconversion efficiency at 17.17% as shown in Figure 45c. This confirms the hypothesis that a precise control of the relative concentrations of alkyl chains and transmitter molecule is needed to optimize optical activity. Note this 17.17% UCQY is the highest achieved with silicon QD light absorbers for photon upconversion. Next, is the comparison of the optical properties of SiQDs functionalized in-flight with alkyl chains of different lengths: 1-hexene, 1-octene, and 1-dodecene. With longer chains having larger London dispersion interactions, it is hypothesized that longer alkyl chains will require fewer ligands per SiQD to achieve solubility, thus leaving a greater surface area for attaching the transmitter ligands or further modification as illustrated in Figure 43a.

Upon finding the “critical”, or minimum amount of surface-bound linear hydrocarbons needed to attain SiQD solubility for 1-hexene and 1-octene, FTIR is used to compare the surface density for each alkyl chain. The FTIR data in Figure 47a indicates that the ratio of CHx with respect to SiHx peaks slightly decrease as the alkyl chain length increases. Calculation of the ligand surface coverage demonstrates that increased consumption of nanoparticle surface area by shorter

alkyl chains is vital for solubility, as shown in Figure 47b. To confirm this relation, the SiQD surface is saturated in these samples so as to occupy the remaining available surface sites with 9EA. Using absorption measurements, the average number of surface bound 9EA is determined as described in Section 2.1.6. This number correlates directly with the available surface area on the SiQD after gas phase alkyl functionalization, and inversely with alkyl chain surface coverage, as shown in Figure 47b and Figure 47c. This is to say, samples functionalized in-flight with the longer chain 1-dodecene require fewer surface-bound aliphatic chains to maintain solubility. Thus, these SiQDs have more available surface area permitting a higher number of 9EA groups per particle compared to SiQDs with shorter chains.

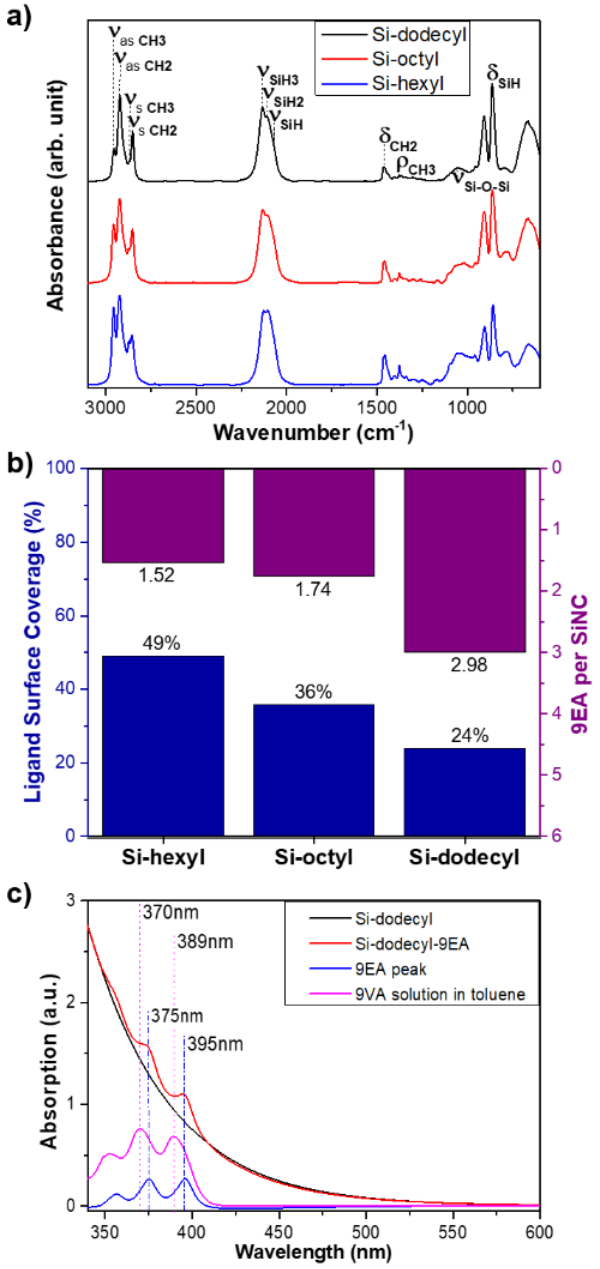

Figure 47: Prior to affixing the 9EA transmitter ligands to the SiQDs, the minimum amount of aliphatic ligands required to maintain solubility in toluene (critical loading) is investigated with 1-dodecene, 1-octene, or 1-hexene. a) Normalized FTIR scans of the partially functionalized SiQDs, which provide the b) Alkyl chain surface coverage on the SiQDs vs. the average number of surface-bound 9EA per SiQD after 9VA hydrosilylation. c) UV-Vis absorption spectra showing 9EA is bound to the SiQD surface.

2.4.3 – Size Effects:

Previous sections investigate the control of SiQD surface coverage while manipulating alkyl chain length for SiQDs of size ~3.1 nm. Semiconducting nanomaterial size influences bandgap and exciton energy.[132,142] As a result, it is theorized that both bandedge photoluminescence energy and the UCQY will be directly impacted by the sensitizer (SiNC) size. To investigate this, the absolute pressure in the low-temperature plasma reactor is varied between 0.7 and 1 Torr. The reactor pressure affects plasma characteristics which in turn affect particle size with higher pressures leading to larger SiNCs (see Section 1.1). Controlling the reactor pressure enables the average SiQD diameter to be shifted between 2.8 to 3.3 nm. These reported particle sizes are estimated from the peak bandedge PL wavelength using data from Wheeler et al. as XRD and TEM based measurements introduce error from oxide layer effects.[136] These SiQDs are partially functionalized with Si-dodecyl using identical mass flow rates of dodecene saturated hydrogen for consistency. The samples of partially functionalized C12|SiQDs with differing diameters then undergo the hydrosilylation with 9EA. As shown in Figure 48a, differing amounts of 9VA are used in the hydrosilylation process to control the surface density of 9EA to find the maximum UCQY of a sample (Table 6).

Table 6: Standard mixtures used for optimizing 9EA||SiQDs via in-solution thermal hydrosilylation.

	Si NC in Mesitylene (OD_{488} = 1.2)	**9VA in Mesitylene (1 mg/mL)**	**Mesitylene**	**Total volume**
Sample 1	200 µL	8 µL	1792 µL	2000 µL
Sample 2	200 µL	31 µL	1769 µL	2000 µL
Sample 3	200 µL	125 µL	1675 µL	2000 µL
Sample 4	200 µL	500 µL	1300 µL	2000 µL

Figure 48b shows the maximum UCQY occurs for the 3.1 nm diameter sample with a sharp drop off in as the particle diameter either increases or decreases. Additionally, bandedge PL appears to overtake upconversion only when the SiNC diameter is greater than the optimum. A UCQY of 17.17% is measured for the 3.1 nm diameter sample with a corresponding PL peak of 745 nm. The observed phenomenon that UCQY of SiQDs increase with size, then decreases after an optimal diameter can be explained by the balance between the driving force for triplet energy transfer from the SiNC to the surface 9EA and the QD exciton lifetime. As SiNCs increase in size, it is expected that the exciton lifetime increases due to the reduced confinement of a larger crystal volume, which in turn reduces exciton recombination probability. A longer QD donor lifetime promotes energy transfer to the 9EA acceptors.[141] However, the triplet exciton energy decreases as SiNC size increases leading to a smaller driving force for triplet transfer from the SiNC to the 9EA. Reduction of exciton energy due to increased SiNC size is a result of the dependence of a semiconducting material's energy gap and auger rate on its size, with smaller diameters correlating to higher energy gaps and a greater triplet transfer

driving force.[132] When exciton energy from the SiQD begins falling below the required energy levels of the 9EA, a smaller proportion of excitons will be able to achieve triplet transfer between the crystal and the transmitter ligand. A reduced population of excitons able to diffuse into the 9EA results in a smaller driving force experienced by larger SiQDs is detrimental to photon upconversion efficiency.[3,142] Thus, an optimal size is to be expected and is consistent with the observed results.

2.4.4 – Alkyl Chain Ligand:UCQY Relation:

A more detailed analysis of the fraction of the surface covered with various alkyl groups can hint at surface conditions that maximize UCQY. Using the bulk density of silicon, one can calculate that a 3.1 nm SiQD has ~780 total atoms, with between 204 and 290 of them being at the particle surface (see Surface Atom Calculations in Section 2.1). The much higher surface coverage of 1-hexyl groups

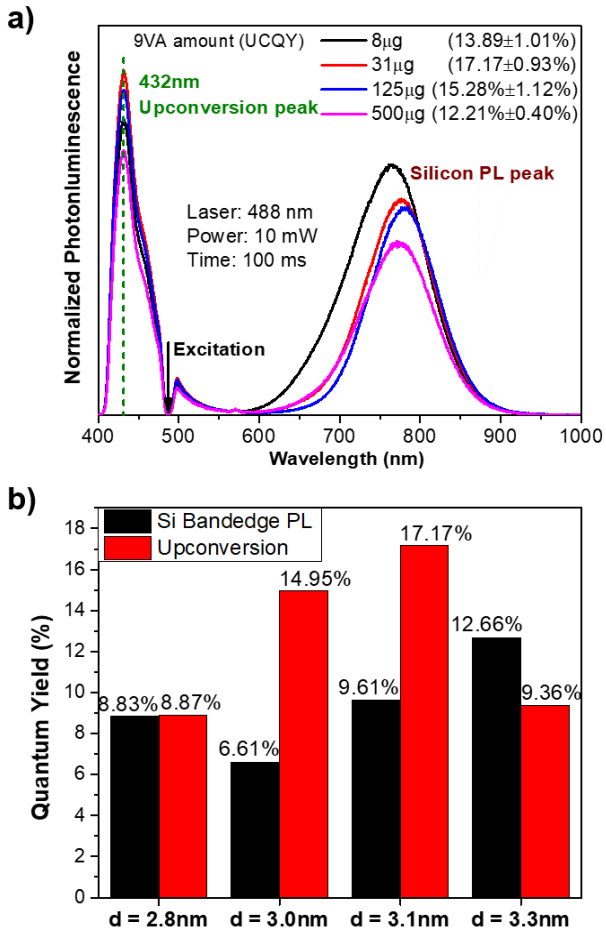

Figure 48: Photoluminescence (PL) of 488 nm irradiated, Si-dodecyl functionalized 3.1 nm diameter SiQDs with 745 nm PL maxima. These QDs have differing amounts of 9VA added during hydrosilylation to optimize the upconversion quantum yield (QY). (b) The bandedge PL QYs of SiQDs of varying diameter are compared to their optimized upconversion quantum yields. All measurements are performed in toluene at room temperature.

(49%) compared to Si-dodecyl groups (24%) is consistent with fewer surface sites available for the 9EA transmitter ligand for the case of Si-hexyl as shown in Figure 47b which is in turn consistent with a reduction in UCQY as shown in Figure 49a. Aggregating these observations, in Figure 49b it is shown that the ligand length does not appear to affect UCQY directly. This is demonstrated by comparing the Si-dodecyl sample with increased hydrogen flow rate through the bubbler so that the fraction of surface covered with Si-dodecyl (47%) is reasonably close to the fraction covered by Si-hexyl (49%). When 9VA is grafted onto the remaining surface sites of both, a very similar UCQY is measured between 12-carbon and 6-carbon long functionalization (4.99% for Si-dodecyl and 5.16% for Si-hexyl). It is not the length of the alkyl chain that limits the UCQY, but rather the availability of surface site for 9VA grafting.

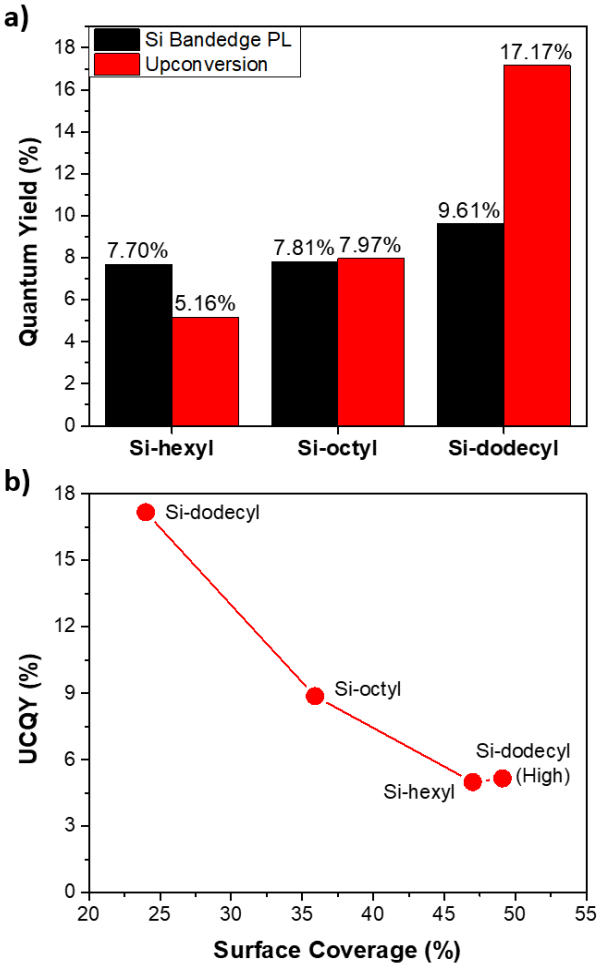

Figure 49: a) The bandedge photoluminescence and upconversion quantum yields for 3.1 nm diameter SiQDs functionalized with critical surface density of Si-hexyl, Si-octyl and Si-dodecyl, i.e. the minimum amount of aliphatic ligands required for colloidal stability. b) Comparison between ligand surface coverage and UCQY showing similar rates of surface coverage produce similar UCQY.

2.4.5 – Summary:

This in-flight gas-phase approach to surface modification allows for consistent and independent control over the type of ligand grafted onto SiQDs and its degree of surface coverage. The produced materials are readily soluble immediately after collection from the gas-phase reactor, simplifying any additional solution-based surface modification that is required to achieve the desired functionality. It is preferable to utilize longer alkyl chains (Si-dodecyl vs. 1-hexyl) to attain solubility with a low aliphatic ligand surface coverage (~24% vs. ~49%), as this allows the grafting of 9EA transmitter ligands to ensure efficient energy transfer with DPA and a resulting high UCQY (17.17% vs. 5.16%). The length of optoelectronically inactive ligands do not impact the upconversion process directly, but rather it affects the ability to further functionalize the surface with transmitter molecules. While this gas-phase partial functionalization approach specifically focuses on optical upconversion, the same functionalization strategy is likely desirable for other applications. For instance, hybrid organic-inorganic light emitting diodes, printed transistors or solar cells require building blocks with both good solubility for processability reasons and good electronic contact between the particles and the organic matrix for optimal functionality. The approach described here can be a route towards such materials.

Section 3: Battery Materials and Investigations

3.1 – Background on Lithium-Ion Batteries

3.1.1 – History of Batteries

Batteries are an old technology that has undergone multiple developments and iterations over the centuries. Whether you consider Benjamin Franklin's series of Leyden Jars in 1749 as a battery or a series of capacitors, chemical batteries (from now on referred to simply as "batteries") have been around for centuries. The chemical storage of electrical energy was first documented by Allessandro Volta in 1800 using a set of two metallic electrodes (Zinc and Copper) stacked alternatingly with a brine-soaked cloth between pairings, creating what is now known as a "voltaic pile".[240] In this case the copper reduced hydrogen ions acting as the cathode, the zinc dissolved in an oxidation reaction acting as the anode, and the brine-soaked cloth acted as an electrolyte-soaked separator. Since then, electrochemical batteries have followed a similar standard form with four primary components:

1. Anode – The "negative" electrode which has a comparatively low reduction potential for the ion being used within the electrochemical reaction.
2. Cathode – The positive electrode which has a comparatively high reduction potential for the ion being used within the electrochemical reaction.
3. Separator – A material keeping the two electrodes from directly reacting with each other.

4. Electrolyte – An ionically conductive material (liquid, gel, or solid) that enables positive charge motion through a cell.

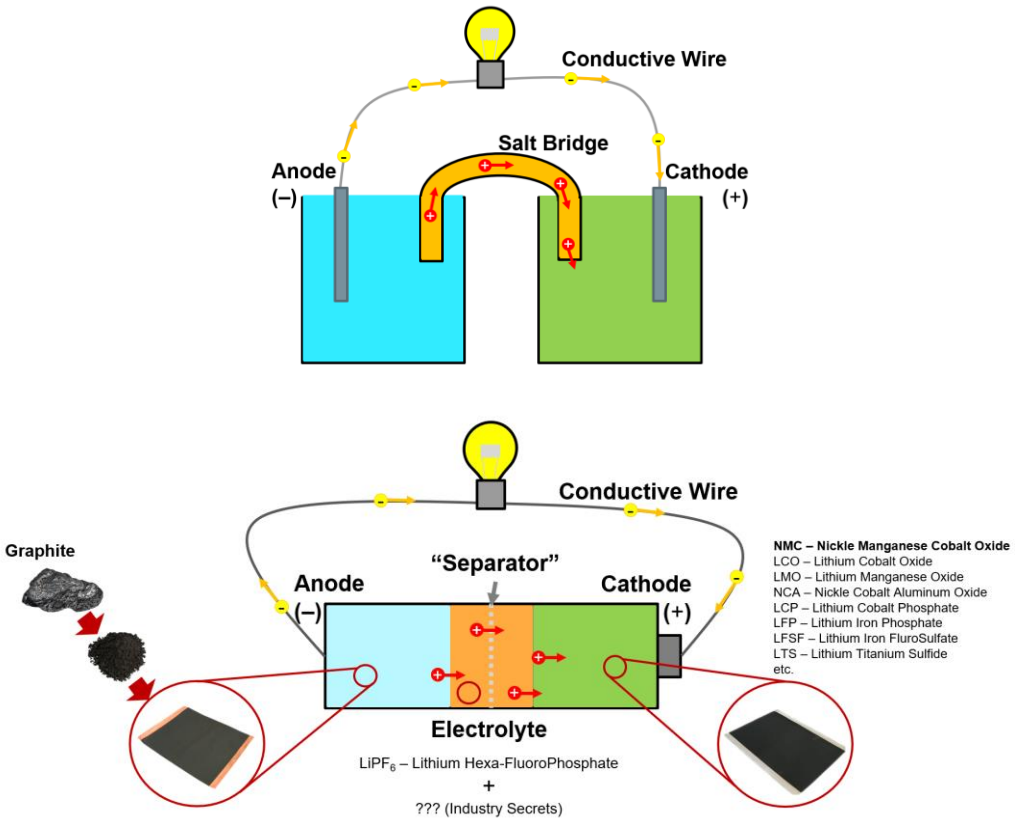

Figure 50: Electrochemical cell in a salt bridge configuration (top) and an illustrative cartoon demonstrating equivalencies in modern batteries (bottom).

These components are illustrated and compared to modern batteries within Figure 50. Batteries of this nature have evolved, but are defined by the concept that the ions stored in one electrode are more energetically favorable (reach a lower energy state) after migrating to the other electrode. The difference in reduction potential (termed electromotive force or "EMF") between the anode and cathode supplies an electrical potential measured in volts, however the inability of the electrolyte to efficiently conduct electrons prevents reactions from occurring until there is an electrical conduit between the two electrodes. When

connected, electrical current flows so that the reaction can take place at the cathode with ions moving from the anode to the cathode via the electrolyte.[240,241]

As battery chemistries have become more and more optimized to produce constant voltages and reliable sources of electricity over longer discharge times, it was discovered that some batteries could have a voltage applied to a discharged cell enabling a reverse in the chemical reactions that led to its discharge, effectively recharging the battery. This effectively split the concept of batteries into two sub-fields:

- "Primary" Batteries – Single use cells that upon discharging have exhausted one or both of the electrodes to the point where they cannot be regenerated.
- "Secondary" Batteries – Rechargeable electrochemical cells that can have all components restored to initial conditions.

Secondary batteries were first developed in 1859 by Gaston Planté in the form of lead-acid batteries, developing through the forms of Nickel-Cadmium (NiCad), Nickel-Iron, Silver-Zinc, and Silver-Cadmium before in 1980 a leap to lithium ions was made. Even in 1912 lithium was identified as a promising candidate for electrochemical batteries by G. N. Lewis,[240] but in 1980 the work of N. A. Godshall,[242] J. B. Goodenough,[243] and their respective labs made that a reality. Using Lithium Cobalt Oxide (LCO) as the cathode and pure lithium as the counter electrode, $LiBF_4$ acted as the electrolyte able to conduct lithium ions as the positive charge carriers. This made rechargeable batteries lighter, more efficient, removed the discharge "memory" that NiCad showed if not fully discharged, and revolutionized portable energy storage in a way that earned Goodenough, M.S. Whittingham, and A. Yoshio a joint Nobel Prize in Chemistry in 2019.[244] After

development the Lithium-Ion (Li-Ion) battery began commercialization by Sony in 1991 and has undergone several chemical changes. To minimize cost, improve safety, or maximize performance for a specific application, the cathode material has evolved from $LiCoO_2$, to $LiMn_2O_4$, to $LiFePO_4$ to a form of $Li(Ni_xMn_yCo_z)O_2$ commonly referred to as NMC-xyz (with xyz being the chemical ratios).[245,246] While this happened, developments in electrolyte chemistry were being made, diversifying in state from liquid electrolytes to polymers based on polyethylene oxide-lithium salts (PEO:Li) and now was evolving into solids in hopes of increasing thermal stability and overall safety. Initially lithium hexa-fluorophosphate ($LiPF_6$) in propylene carbonate and diethyl carbonate was developed by Sony, and $LiPF_6$ remains the primary active component of liquid electrolytes, though additives and solvents have changed.[246] The anodes development has been somewhat slower, initially switching from pure lithium to naturally mined flake graphite in the 1990s and has remained the dominant anode material due to its low cost and reliability.[246] This is not to say that graphite is the optimal material, indeed at 372 mAh/g it has a lower lithium capacity than a large number of materials (LTO, Ge, Sn, Li2O, etc.),[245,247] but until the problems of reliability, cost, and development of chemical side reactions in other materials are solved graphite is simply the best anode material available

3.1.2 – Why Silicon is Interesting:

Silicon was identified as a candidate for a next generation of Li-Ion battery anode materials as early as 1981.[248] This was due to its particularly high capacity for lithium, enabling each silicon atom to accommodate 4.4 Lithium ions in an alloying reaction giving

it a theoretical capacity of 4200 mAh/g as opposed to graphite's intercalation mechanism only allowing for a maximum of 1 Li^+ per 6 carbon atoms giving a theoretical 372 mAh/g.[247] An increase in anode capacity of over 11 times is naturally desirable, but silicon came with three primary drawbacks:[247,249]

1. Poor electrical conduction – Silicon is a semiconductor which will generally require some help to conduct electrons out.
2. Large volume expansion – Over a 360% volume expansion is experienced upon lithiation.
3. Solid Electrolyte Interphase (SEI) formation – Electrolyte, anode components, and silicon migrating out of the material form a semi-solid barrier on the surface of the silicon which can restrict ion transport, consume electrolyte, and generally reduce cell function.

Of the listed problems the poor electrical conduction of pure silicon can be overcome in a few ways, most simple being to increase surface area and coat the surface with an electrically conductive material. Carbon has been a favored coating method with carbon nanotubes and complex structures acting as supports for raw silicon, in addition to simply directly coating the silicon nanomaterials with an encapsulating layer of carbon.[245,247]

The next problem is the volume changes experienced during electrochemical cycling. H. Wu and Y. Cui noted that there are three primary detrimental effects from this cycling process:[249]

1. *Pulverization* – The stress fracturing of a crystal due to internal stresses from volume expansion.

2. *Electrode Collapse* – Active material separating from each other and the electrode substrate, preventing effective electrical cycling.
3. *Uncontrolled SEI Growth* – As the volume changes, the SEI cracks or separates exposing fresh anode to form new SEI with each cycle.

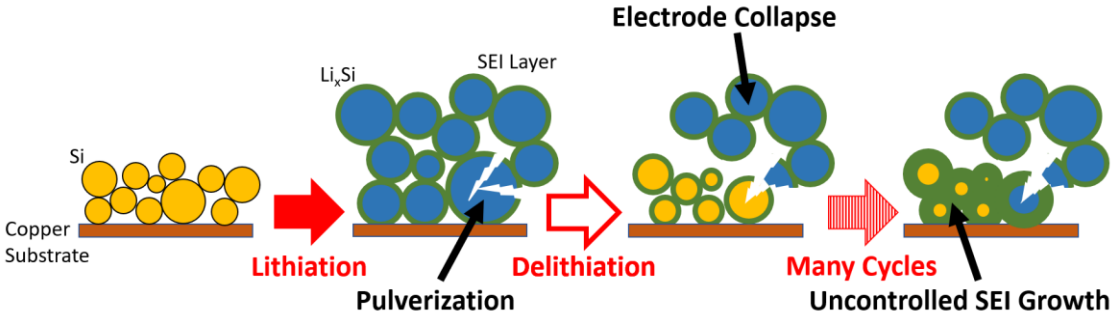

Figure 51: Illustration of pulverization, electrode collapse and uncontrolled SEI growth that happens due to silicon expansion during cycling.

These are illustrated in Figure 51 and can be combatted in with several potential solutions. The simplest of which is to reduce the size of the silicon material to < 150 nm prior to lithiation as that appears to be the pulverization limit.[112] Conductive or more flexible binders have also been put forward as a method of maintaining a functional electrode, in addition to intentionally creating void spaces for the silicon to expand into.[247,250] Finally, there is the problem of SEI formation and growth. As noted, volume changes appear to exacerbate this issue and due to the nature very nature of SEI it is a difficult problem to study, let alone solve. As opening a cell will change the expressed chemistries of an SEI due to pressure change alone and the organic nature of its components are problematic to accurately identify, this problem is much less understood than the others. What is known is that separate from changing the electrolyte, graphite appears to form a thinner SEI composed of differing components[251,252] and that silicon coated with graphite express

different SEI characteristics.[6] The problem needs more thorough study, but a potential solution seems to be hiding the silicon surface behind a less reactive layer which acts as the basis for the experiments of Section 3.4.

3.1.3 – Electrochemical Testing:

Charge/Discharge Cycling:

The most standard form of electrochemical testing is simple charge/discharge cell cycling, where the battery in question is brought from a charged to a discharged state and then back again while measuring the capacity and relevant properties. This can be done with either a constant voltage (CV) where a constant voltage is supplied by the potentiostat allowing for as much current as needed to flow into or out of the cell until it reaches the desired charged or discharged state, or more commonly with a constant current (CC) which will reduce/increase the cell's charge at a constant rate by maintaining a constant current and adjusting the applied potentiostat voltages. CV cycling will induce high currents initially, then nearing the end of a charge or discharge slow down dramatically which tends to apply uneven stresses during cycling, hence its limited adoption in research settings.[253] There are also calendar-life tests which simply monitor voltage over an extended period of time in order to estimate chemical stability, however these tests are significantly more rare in scientific literature and were not performed within this section.[254,255] These tests all utilize a potentiostat to supply the appropriate voltage to the cell connections in order to draw or push the appropriate current from the cell. Cycling using more extreme voltage ranges, for anodes cycling closer to 0 V while for cathodes or full-cells nominal cycling is

between 3.6-4.5 V tends to degrade battery material faster, as maximally removing or adding lithium ions to a material will generally maximize physical changes experienced by the anode and cathode.[253,256] Differing potentiostats were used in the studies within this paper with Arbin Instruments (Section 3.2), Neware (Section 3.3 and Section 1.4), and MACCOR (Section 3.4) all providing the same cycling instructions and achieving the same results. Cycling conditions were half-cell batteries operating at ~0.1 C C-rate as predicted by material's chemical composition.

Half-Cell vs. Full-Cell:

The terms "half-cell" and "full-cell" refer to the combination of electrodes within the battery. For Li-Ion batteries, a half-cell is what is used to test the maximum capacity or other properties of a material by using pure lithium as the second electrode (eg. anode testing would have the anode material with the counter electrode of pure lithium). This has the benefit of lithium ions population never being the limiting factor during cycling, which allows the anode being tested to discharge or charge to maximum effect. However, due to the simple chemistry of pure lithium being used as an electrode the cell will operate slightly differently, forming different compounds in the SEI and generally working better than would be expected with a more complicated counter-electrode. A full-cell is simply the term given to battery where neither electrode is pure lithium. For example, a standard commercially available full cell (as of writing) will contain a graphite on copper anode and NMC-622 on aluminum cathode. Now that more complex chemistries are being used, different compounds can be expected to form within the cell while operating. It is a

relatively common occurrence to have a material function well in half-cell, then demonstrate poor cycling performance in full-cell configuration. Sometimes this can be compensated by changing electrode chemistry (eg. switching NMC-622 for LCO), but these tests are generally less predictable. There is also the fact that full-cell testing no-longer has a large excess of available lithium, meaning that the anode capacity and cathode capacity need to be "balanced". In a perfect world this would mean the electrodes have equal capacities, but as SEI forms lithiated compounds and anodes/cathodes generally don't let go of all of their lithium, a larger capacity in the cathode (110-120% is what was aimed for during my experiments) is needed to maximize expressed cell capacity. It should be noted that these effects are expected to change if the anode is "pre-lithiated", has lithium already present within its active material, commonly done in a separate step where pure lithium is used similar to in a half-cell.

C-Rate:

This is the term denoting the discharge/charge rate for a battery. It is defined as 1 C being the testing conditions needed to fully discharge/charge a cell in 1 hour. Similarly, 0.1 C are the conditions needed to fully discharge/charge a cell in 10 hours. When testing in CC conditions a battery will have a predicted capacity that can be worked back from to determine what its 1 C value would be (eg. Capacity = 1000 mAh, 1 C = 1000 mA = 1 A as $\frac{\text{Capacity}}{\text{Time}} = \text{C}$). Using that value, it is possible to calculate the C-rate desired for testing (eg. 1 C = 1000 mA, then the desired 0.1 C = 100 mA). With this said, three things should be noted:

1. Without testing the material, a C-rate is only as good as the capacity prediction. For the purposes of these studies a spreadsheet was made to predict the capacity and included in the supplemental material file.
2. As a battery cycles and its capacity reduces, the effective C-rate increases. For example, if after 10 cycles the capacity of a cell drops from 1000 mAh to 900 mAh (because it is a terrible battery), then an initial 0.1 C of 100 mA will become an effective 0.111 C as the current is not updated during cycling.
3. C-rate changes the apparent material capacity. For larger materials that require more time for lithium ions to make their ways into the core (eg. 150 nm particles vs 10 nm particles), or low surface area geometries restricting lithium transport, a higher current will cause a backup of ions. This translates to higher C-rates causing the same material to appear as having a lower capacity. This is explored slightly further in Section 3.3.

The apparent capacity reducing effect of increasing C-rate can be clearly seen within the anodes in Figure 52. Due to these problems, some studies neglect to use C-rate as a metric, instead using a current value.[257] Nevertheless, this method is used throughout industry and literature as it can give a more intuitive idea of what a high discharge current for a cell is and what can be expected from it.

Coulombic Efficiency and Cycle Life Plots:

When reading battery papers, the term Coulombic Efficiency (CE) will come up a lot. Often times plots juxtaposing cycle life curves and CE curves will be presented which will naturally show the same transition profiles. The cycle life capacity curve is simply a plot of the cell capacity with respect to the times the cell has been charged or discharged. So, if a cell charges fully to 1.5 V and the potentiostat records 1000 mAh, the first charge point will be 1000 mAh. If that same cell then is discharged back down to 0.01 V, but the potentiostat only records 900 mAh to get it there, the first discharge point will read 900 mAh. For every full cycle an additional two points will be added, making up the charge and discharge capacities of cycle life plots. The coulombic efficiency is simply how much charge can be retrieved from the cell in percent, aka the difference between the charge and discharge capacities.[258] In the case described above we have 900 mAh discharged from a cell that was charged to 1000 mAh, which gives a 90% CE value. Clearly the cycle life and the CE curves are related, but the CE curve is a good metric of the rate of lost capacity over cycle life. The First-cycle Coulombic Efficiency (FCE) is also a method of estimating how much electrolyte is being consumed to form an SEI layer or other irreversible processes. In effect, the higher the FCE and CE the better.

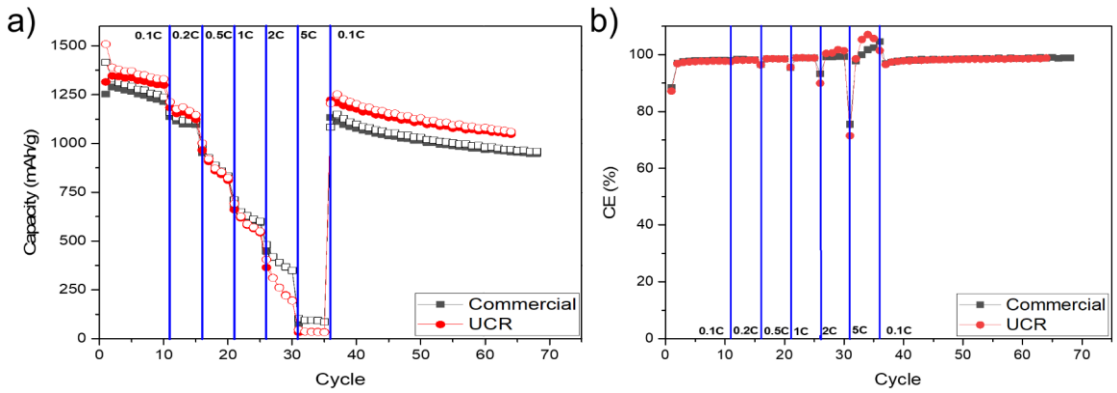

Figure 52: Example battery data comparing commercial silicon nanoparticles to silicon nanoparticles made at the University of California Riverside within the Mangolini lab. a) Cycle life testing with different C-rates demonstrating differing capacities and b) resulting coulombic efficiencies. Note that CE exceeds 100% during rapid cycling with reduced capacity, this is likely due to slower discharging ions working their way to the surface of materials enabling discharges of lithium ions present within the material bulk.

3.1.4 – Battery Construction:

Anode Forming:

It should be noted upfront that battery creation in lab scale facilities is exceedingly different from in commercial environments. The volumes used, mixing methods, coating procedures and even environments used for cell construction (industry employs dry-rooms while most labs utilize gloveboxes) are all very different. It is also worth noting that different research groups employ different methods for active material formation and coating, with some simply growing their materials directly on a conductive backplate while others attempt to replicate industry mixing and coating techniques. For the studies within this dissertation all anodes are produced by the following methods, which are intended to be more analogous to small (very small) batch industrial techniques.

Anode materials are prepared and collected separately from the anode substrate. For these tests a thin sheet of high purity copper foil is used as the anode substrate. Generally, the active material requires a form of glue or "binder" to hold it to the substrate and the other materials. The binder selected for these studies was carboxymethyl cellulose (CMC, MTI Supplier) dissolved in deionized water and mixed overnight (this replaces older toxic binders like N-methyl 2 Pyrrolidone and Polyvinylidene Fluoride mixtures).[??] Binder solution concentrations varied based on the particular study but was generally kept at or around 1% CMC. The active material was weighted out into appropriate ratios with the binder solution and other materials required for the given test (eg. carbon black to improve anode electrical conductivity, graphite to see how a material could be used as an additive to standard graphite electrodes, etc.). This solution would then be mixed in one of two ways:

1. If mixing just the active material and binder a mortar & pestle was implemented due to the limited ability of forming non-uniform regions.
2. If mixing the active material, binder, and a third component (eg. graphite), a high-sheer mixer is necessary to ensure equal dispersion of active materials. For these studies a Cole Palmer LabGEN 7 High-sheer mixer was used on settings 5-8 for 2-6 minutes (higher settings appeared to deteriorate the binder).

After mixing the slurry, the material is deposited on recently cleaned copper foil which is itself held on-top of a glass casting surface (like a super-flat clipboard). Depending on the desired thickness of the anode a "Dr. Blade" coater or a Meyer rod is used with the height

adjusted to the desired region, then the material is spread over the copper foil simply by dragging the Dr. Blade or Meyer rod over it. The described components can be seen below in Figure 53.

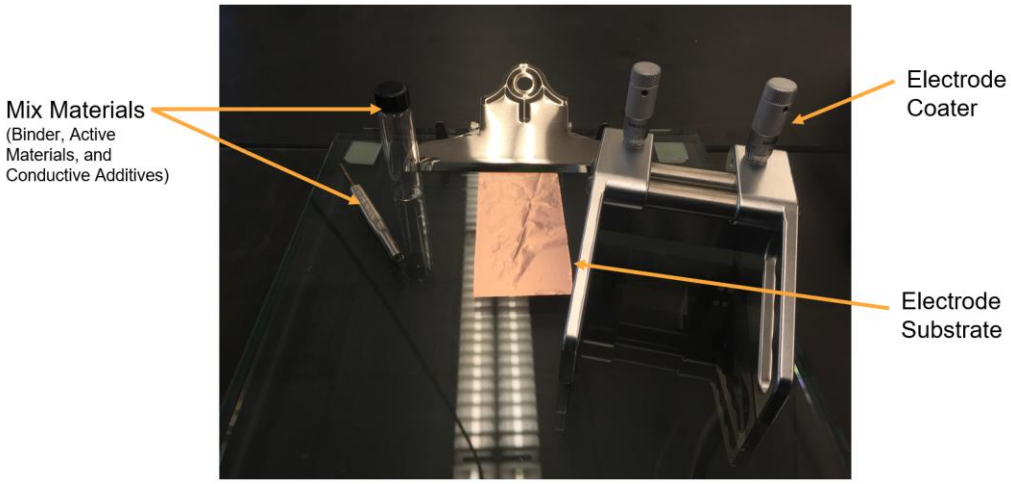

Figure 53: Slurry casting tools.

As water in lithium-ion batteries tends to be a bad thing, the anode dries on the casting surface until it can be moved into a vacuum furnace without altering the coating. The vacuum furnace is then brought into vacuum conditions (< -20 mmHg) and brought to a temperature between 90-110 ºC for a minimum of 12 hours. Upon cooling the vacuum oven can be opened and the anode (now dry) can be cut/punched into the desired shape. In this document anodes between 12.5-16 mm in diameter are punched out using either a hollow punch (like in leatherworking) or a specially built hand punch (similar to those used in arts and crafts). These disks are then transferred into the glovebox for cell assembly.

Cell Assembly:

As previously noted, the glovebox is typically used in research for cell assembly as it maintains an oxygen-free environment, but more importantly water free atmosphere. This dissertation only contains coin-cell (similar to batteries in a watch) data and thus will not go into the process of assembling pouch cells (similar to batteries in a phone or laptop) or other geometries. The coin cell (aka. "button cell") type used was a 2032 purchased from MTI. Each cell contains:

- Base – Stainless steel, complete with electrically insulating gasket to both isolate the electrodes and pressure seal the cell.
- The electrode being tested – made using the process described above.
- Electrolyte – Allowing for ion flow between the electrodes. Generally a 1:9 mixture of Fluoroethylene Carbonate (FEC) and a 1 M solution of Lithium Hexaflurophosphate ($LiPF_6$) in 1:1 v/v ethylene carbonate/diethyl carbonate.
- Separator – to prevent the electrodes from reacting directly with each other while allowing for lithium-ion flow (generally a 25um Trilayer polypropylene-polyethylene-polypropylene membrane).
- Counter electrode – Either pure lithium for half-cells or a commercial cathode for full cells.
- Spacer – Stainless-steel puck to fill the volume of the cell and ensure even pressure distribution on the electrodes.
- Spring – Stainless-steel wave spring to ensure electrical contact.
- Cap – Stainless-steel.

Examples of these components and the required equipment for closing and testing the cell can be seen in Figure 54. The cell is assembled in the order listed with the active materials facing each other while being separated by the separator (generally ~2 mm larger in diameter than the electrodes to prevent overlap). Electrolyte was added to be in surplus (>40 μL), meaning that upon closing the cell a small amount of excess electrolyte would be spilled out. In this way, electrolyte was never a limiting component within the cell enabling the active material to be investigated without convolving factors. After the cap was applied to the battery it was crimped in either an automated or manual cell crimper. Both simply have a stainless-steel mold that bends the cap edges to form a seal on the base gasket when sufficient pressure is applied. After sealing the cell, the outside of the battery is wiped down to remove excess electrolyte and subsequently put into electrochemical testing using the desired instrument. Standard testing conditions used in this document's studies are between 0.01-1.50 V at a C-rate of 0.1 C unless otherwise specified. A minimum of 12 hours "soak time" is given to each cell before testing so as to fully saturate the active material and separator with electrolyte before testing. Additionally, a 10 minute rest between discharging and charging was added in hopes of allowing for the ion distribution to reach an equilibrium within the material before reversing course.

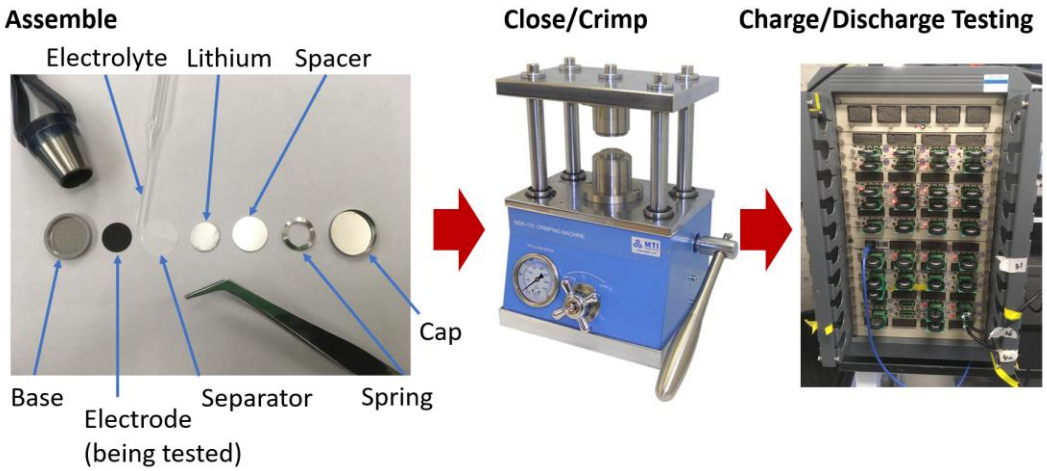

Figure 54: Cell assembly and electrochemical stages as (left) half-cell components needed for assembly, (center) coin-cell crimping tool, and c) Arbin potentiostat battery testing station.

3.2 – Core-Shell Graphitization Study[6]

As previously noted, silicon's use in anodes despite being highly desirable due to massively increased capacity compared to the standard anode (4200 mAh/g vs 372 mAh/g)[245] does face numerous problems preventing successful commercial implementation. Of these: poor electrical conductivity, thick Solid Electrolyte Interphase (SEI) layer, and large volume changes during cycling, much of these issues have been decently combated. For instance, the problem of large volume expansion upon lithiation can have its effects minimized through the use of silicon as nanostructures, as silicon nanomaterials encapsulated with a carbon coating has proven to be one of the more successful strategies.[78,247,259–261] The reason for nanoscale silicon implementation is to enable the volume expansion without the material pulverizing, though this alone is not enough to enable usable electrochemical performance.[78] Carbon encapsulation of the silicon has enhanced anode conductivity, helping to overcome the electrical conductivity issue while seeming to also provide an additional level of mechanical support to buffer against the volume expansion effects. Despite seeming fairly simple and having been studied through numerous architectures, nanoscale silicon nanoparticles coated with a layer of carbon lacks a thorough enough mechanistic understanding to enable rational engineering and material design. For instance, the influence of carbon-shell structure and whether graphite coatings perform differently to an amorphous carbon coating is still widely debated.[262–265] This study attempts to answer the question of how carbon shell

structure changes electrochemical performance, thus enabling a more mechanistic understanding that can lead to intentional material design for commercial applications.

To accomplish this, a new two-step Chemical Vapor Deposition (CVD) method of applying uniform carbon coatings and then graphitizing them has been developed. As CVD is cheap and compatible with a wide range of nanomaterials, it embodies a cost-effective approach for coating applications.[262,263,265,266] Naturally, the method's simplicity and compatibility with precursors as available as methane, acetylene, and toluene has led to CVD already being implemented at industrial scales.[266,267] Unfortunately using this method for growing low-surface-area graphitic carbon layers on silicon nanoparticles (SNPs) has proven challenging and has been extensively studied. These studies have led to the understanding that using carbon precursors at relatively low processing temperatures of 400-900 ºC will cause thermal cracking and the formation of amorphous carbon.[265,266,268] Using higher temperatures of 1000-1200 ºC will generally lead to the formation of silicon-carbide phases, which generally lower material capacity due to its poor lithiation capacity.[265,266,269] This has led to materials with amorphous carbon coatings being investigated more thoroughly, while two primary approaches have been used to attempt to study graphitized coatings: metal catalysts and mild oxidation agents. Metal catalysts have been shown to lower the temperature required for graphitic carbon growth,[270] while oxidation agents alter the carbon nucleation regime to grow conformal multi-layer graphene.[269] Both of these methods introduce problems as the metal catalysts need to be removed in order to not interfere with cycling tests, while the oxidation agent has a

tendency of forming thick oxide layers on the silicon which negatively impacts electrochemical performance via formation of lithium oxide when cycling.[262,269]

3.2.1 – Two-Step CVD for Graphitized Carbon-Shells:

This newly developed two-step CVD method has effectively split conformal carbon-shell formation from its graphitization, allowing for the study of chemically identical and structurally different carbon-coated particles. As noted above a relatively low temperature enables thermal cracking of carbonaceous precursors, however a pure atmosphere of a carbonaceous precursor at lower pressures and temperatures will be surface reaction limited and not mass transport limited, which produces conformal and uniform carbon coatings that get thicker with longer time exposures.[265] If carbon deposition and surface reaction induced heating have already occurred, high reactor temperatures will uniformly heat the material and enable graphitization of the carbon shell without migration of carbon into the SNP and the resulting formation of SiC. Thus, upon placing the SNP in an open-faced container (0.4 g of SNP in an alumina crucible) within a tube furnace evacuated of all air, the process is simply:

1. *Carbon Coating* – Flow acetylene (~36 sccm of C_2H_2) into the reactor while maintaining a pressure of 300-500 Torr (~0.5 atm) and a temperature of 650 ºC. Longer exposure times results in a thicker carbon shell, so timing was altered to control thickness with 30 minutes providing the samples analyzed in this study.

2. *Graphitization* – Evacuate the acetylene from the reactor and flow a small amount of argon (~20 sccm) through the reactor maintaining a pressure of ~30 Torr while increasing to a temperature of 1000 ºC. The graphitization process appears to happen relatively quickly, though for consistency this study used a 10 minute thermal soak time.

To accomplish this a simple 1-inch diameter quartz tube in a tube furnace was used, with gas inlets on one side and a vacuum pump on the other, with pressure being controlled manually through needle valves (opening the needle valve more allows for a higher rate of gas to be pulled into the pump). A cartoon of the process can be seen in Figure 55a while a picture can be seen in Figure 55b.

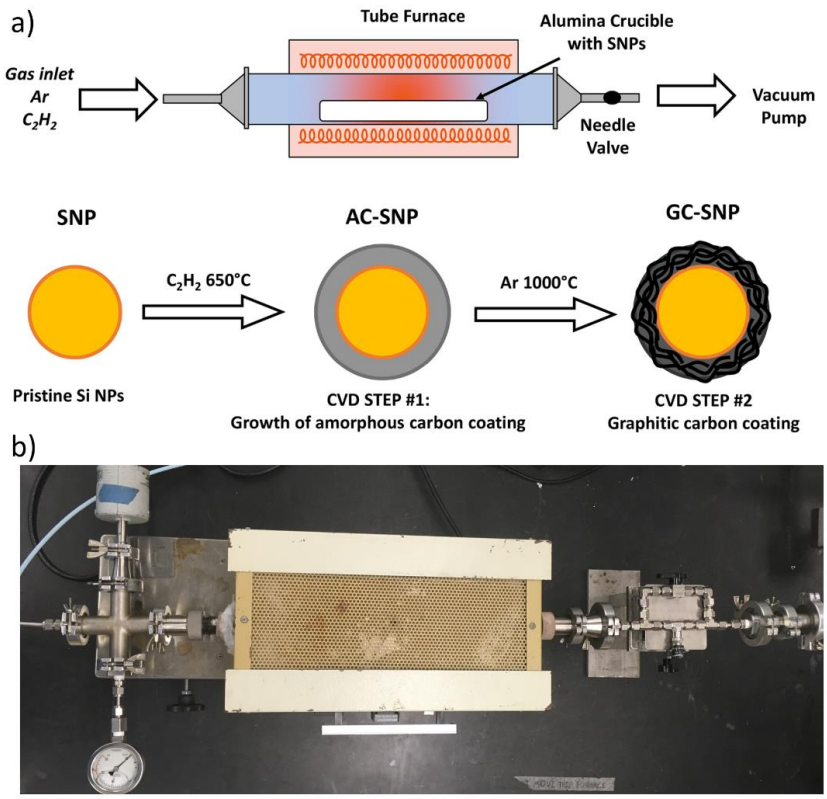

Figure 55: a) Cartoon scheme of the 2-step CVD process and b) image of the actual CVD system used.

As shown in Figure 55a, the study will begin with premade 50-100 nm silicon nanoparticles (SNP) sold by Nanostructured and Amorphous Materials, after undergoing step 1 and gaining an amorphous carbon-shell we will refer to the material as AC-SNP (Amorphous Carbon SNP), while material that has gone through step 2 will be termed GC-SNP (Graphitic Carbon SNP).

3.2.2 – Carbon-Coated Silicon Material Properties:

Transmission Electron Microscopy (TEM) images of AC-SNP and GC-SNP can be seen in Figure 57a and b respectively, taken using a Tecnai T12. These images clearly show

uniform carbon coverage over the encapsulated SNP with minimal surface roughness (no carbon spiking from the surface as seen with some methane precursors). Use of Brunauer-Emmett-Teller (BET) surface area analysis to quantify the surface area of material via nitrogen adsorption demonstrates in Figure 57f that the surface area expressed by all three sample states (SNP, AC-SNP, and GC-SNP) have no significant changes. There is a small reduction in the average coating thickness between the AC-SNP and GC-SNP samples from 7.7±2.8 nm to 7.1±2.1nm shown in the distributions of Figure 56a and b, with negligible differences in carbon content as seen through Energy Dispersive X-ray Spectroscopy (EDS) on a FEI Nova NanoSEM450 as shown in Figure 56c.

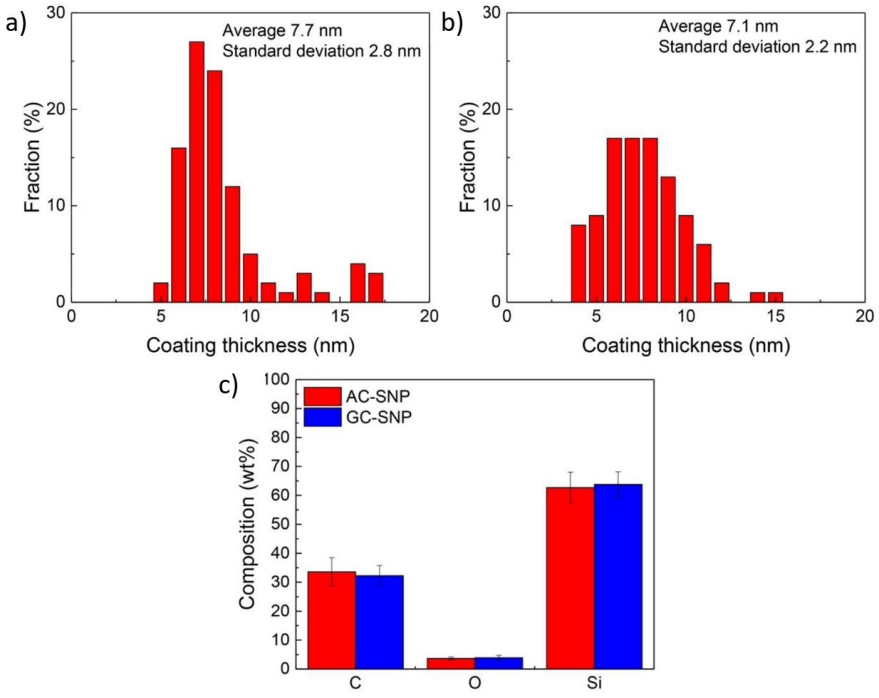

Figure 56: Carbon shell thickness measured via TEM of a) AC-SNP and b) GC-SNP. c) Chemical composition of the materials via EDS.

The altered shell thickness and more apparent graphitic fringing as seen by TEM indicates structural changes (likely graphitization) while the near constant chemical ratio via EDS has shown the high-temperature step 2 does not cause any major losses in carbon. Raman spectroscopy offers a clear method of quantifying the degree of graphitization of a material through comparing the peak ratios of a carbonaceous material's D and G peaks at ~1300 cm^{-1} and ~1600 cm^{-1} respectively.[55,271] In Figure 57c and d the AC-SNP and GC-SNP Raman spectra and peak fittings can be seen with data taken on a Horiba LabRam HR microscope equipped with a 532 nm laser and 1800 lines/mm grating. The peak at 520 cm^{-1} is the transverse optical (TO) mode of crystalline silicon, while the D and G peak ratios are clearly different for the two samples. The position of the G mode near 1600 cm^{-1} for both samples is higher with respect to typical literary values (1500-1520 cm^{-1}) which indicates the presence of nanoscale graphitic domains in both samples. However, when quantifying the peak ratio between the D and G peak for either sample as seen in Figure 57e, there is a clear difference shifting from 0.7 to 1.2 after undergoing step 2. Larger I_D/I_G values indicating greater nanoscale graphitization combined with the previously discussed TEM fringing is clear evidence of graphitization.[55,271]

A small shift in the ratio between the slope of the G peak baseline m/I_G from 0.15 to 0.1 was observed after step 2. According to Casiraghi et al. this change can allow for the estimation of hydrogen effusion from carbonaceous material, which in this case amounts to a 38% reduction in trapped hydrogen.[271] FTIR measurements were also performed on a Nicolet iS50 to check this conclusion and spectra show a weak CHx stretching mode at

3000 cm^{-1} for both samples, but GC-SNP appears to have a 35% lower proportional area upon normalization which also indicates a reduction in hydrogen upon graphitization.[272]

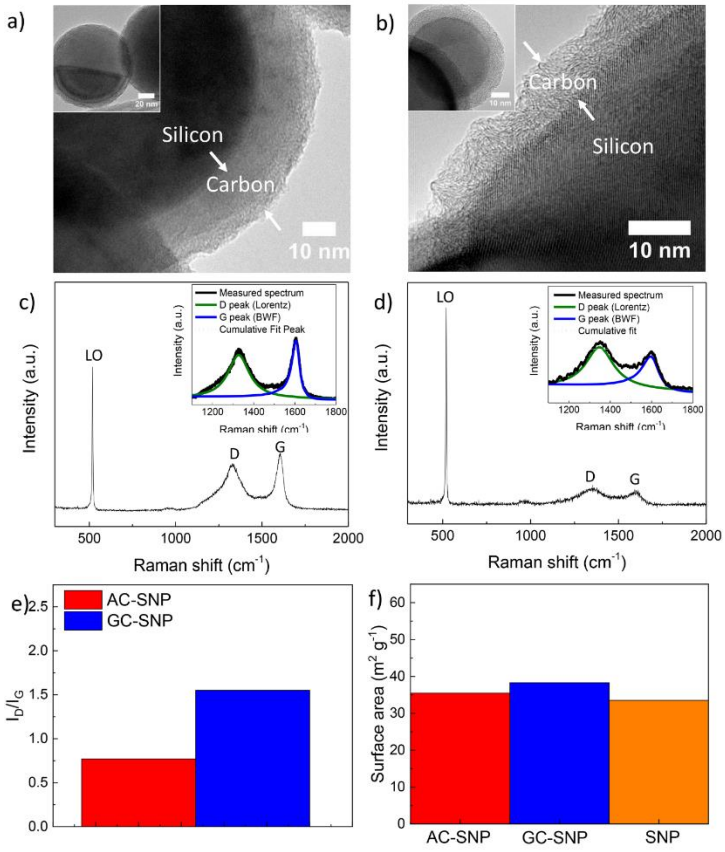

Figure 57: TEM images of a) AC-SNP and b) GC-SNP displaying the silicon core and highly uniform carbon shell for both samples, with graphitic fringing visible on the carbon shell in b). Raman spectra taken with 532 nm laser light in addition to D and G peak fittings for c) AC-SNP and d) GC-SNP. e) shows the I_D/I_G peak ratio for both AC-SNP and GC-SNP demonstrating a change, while f) shows BET analysis of all three SNP, AC-SNP, and GC-SNP samples.

The EDS data also shows a small oxygen content that can be attributed to a terminal SiO_2 layer on the SNP before they undergo the CVD treatment. It could be removed through use of hydrofluoric acid or another similar etching method, however the additional step would increase complexity and it was deemed that the shell effects would not interfere

significantly with the study. As there was no indication of SiC formation through Raman spectroscopy or other methods, an FEI Titan Themis 300 Scanning Transmission Electron Microscope (STEM) was used to see the structure of isolated AC-SNP and GC-SNP. Images of these scans can be seen in Figure 58 demonstrating a clear separation between the carbon-shell and the silicon-core. There is also a thin terminal oxide layer at the surface of the silicon as anticipated.

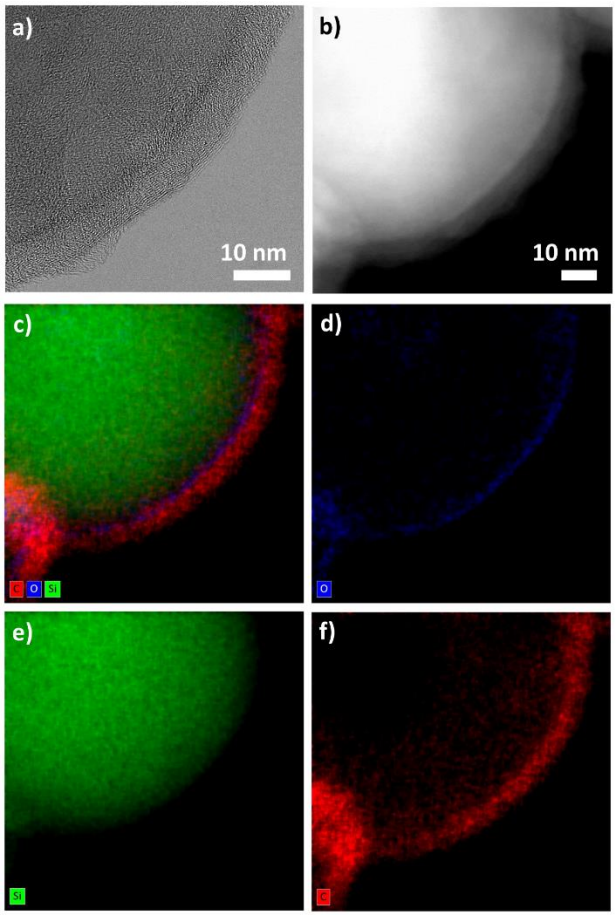

Figure 58: STEM images of GC-SNP in a) bright-field, b) dark-field, and c-f)STEM-EDS chemical highlighting.

3.2.3 – Carbon-Shell Silicon-Core Electrochemical Performance:

With the material synthesized and characterized, they need to be electrochemically tested to observe whether there is any difference between the structurally different and chemically identical materials. To do this half-cell deep-cycle testing was conducted on the materials, with each anode consisting of 85% active material (SNP, AC-SNP, or GC-SNP) and 15% Carboxymethyl Cellulose (CMC, Sigma Aldrich) by weight, with an areal loading of 0.48±0.08 mg/cm^2 on a thin copper base material. Cycling was conducted at a C-rate of 0.1 with a voltage range of 1.50 V to 0.01 V on an Arbin Instruments multichannel potentiostat, while the cell electrolyte consisted of 1:9 FEC:$LiPF_6$(1M in a 50:50 EC:DEC solution) by volume. As the silicon core material was the same for all three samples, the observed difference could be attributed directly to the presence and structure of the carbon-shell. In this way it can be observed in Figure 59a and b that the pure SNP sample was unable to successfully discharge, while both carbon-coated samples were able to cycle, clearly demonstrating the need for an electrically conductive coating. The AC-SNP shows a high initial capacity of 2200 mAh/g with a high First cycle Coulombic Efficiency (FCE) of 87%, while the GC-SNP has a slightly lower initial capacity of 1960 mAh/g and a similar FCE of around 88% putting both materials on par with high performing anodes in literature.[260] Differences between the materials become more apparent as cycling continues as the Coulombic Efficiency (CE) of the amorphous coated material proves unstable within the first 50 cycles and has its capacity drop to 34% of initial values within 100 cycles. In comparison the graphitic coated material rapidly increased in CE to values above 98% and retained near 71% of its initial capacity after 100 cycles.

Such a difference in cycling performance demonstrates a clear change in material response, so additional tests with Electro Impedance Spectroscopy (EIS) were carried out on a Gamry potentiostat from 10kHz-10mHz over the first 10 cycles to observe the cycling behavior. Using an equivalent circuit model to fit the Nyquist plots data on the Warburg element (W), the direct current resistance (R_{EL}), the SEI (R_{SEI}), and the charge transfer resistance from electrolyte to active material (R_{CT}) could be observed. The direct current resistance included the resistance between all of the half-cells contact points and was seen to be 6-7 Ω for all samples. The SEI resistance was found through semi-circle fitting the high-frequency region and demonstrated a clear 40% decrease in resistance (likely a thinner SEI layer) for the graphitic-carbon-shell as opposed to the amorphous-carbon-shell. Similarly, the charge transfer found through semi-circle fitting the mid-frequencies showed a 67% reduction in resistance when the carbon shell was graphitized, indicating the shell itself is more conductive for lithium ions as shown in Figure 59d. Analyzing the changes in R_{SEI} for both samples over the 10 cycles, the GC-SNP demonstrates a 1-4% variation while AC-SNP has a 1.7-11% variation, which shows a significant instability in SEI growth that would impact cycling stability as seen earlier and in literature.[257] When considering R_{CT} over these cycles, an increase of 30-40% is observed for both materials as also seen in studies by Guo et al. and attributed to uneven localized stress/strain distribution within the anode resulting in a loss of electrical contact.[257] This is unsurprising due to the identical silicon cores in all samples being expected to expand and contract in similar ways during cycling. Upon quantifying the size distribution of the SNPs used for this study via TEM (see Figure 59e) it becomes apparent that there is both a large size range (25-350 nm) and

a significant volumetric proportion that are above the 150 nm diameter expected to fracture upon lithiation.[78] These materials fracturing during lithiation would lead to the electrical disconnections and explain the R_{CT} observed, with a simple solution of reducing SNP populations above the 150 nm diameter.

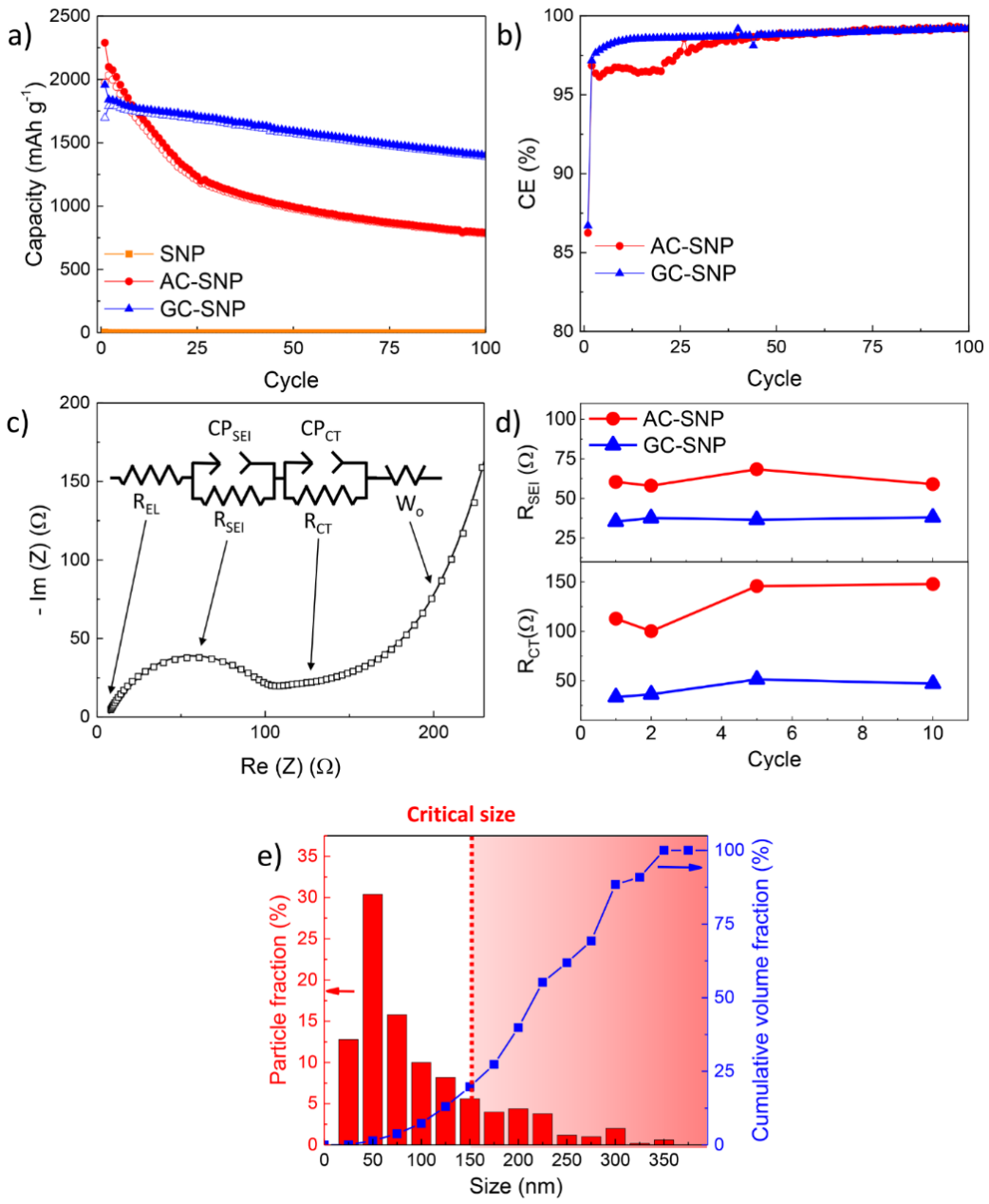

Figure 59: a) Charge/discharge curves and b) concurrent CE for SNP, AC-SNP, and GC-SNP in 85% active material 15% CMC binder configuration. c) shows an example EIS curve with the circuit fitting used to find the relevant variables including R_{SEI} and R_{CT} whose values over the first 10 cycles are plotted in d). TEM analysis of SNP size population provided e) a size distribution and cumulative volume fraction with material above the 150 nm lithiation fracture radius shaded in a red background.

To better understand the effects of the altered carbon-shell structure on lithiation, in-situ TEM lithiation experiments were performed using a Titan S 300 kV TEM and a Nanofactory Instruments probing/biasing system to supply -5.0 V to the SNPs when put in contact with a chunk of lithium. Physically observing lithium movement through the carbon layers has proven useful in understanding lithiation systems and can be seen in the AC-SNP and GC-SNP materials in Figure 60a-e and Figure 60f-g respectively, which summarizes videos (AC-SNP Video and GC-SNP Video).[6,273,274] Lithiation of amorphous-coated materials proved more difficult than the graphitic-coated material, taking longer than 480 seconds and even developing lithium metal on the surface before full lithiation was achieved. These effects and their absence in the GC-SNP sample indicate the amorphous coating is impeding the transport of Li^+ through the carbon and preventing the full reaction of the SNP material.[275] Conversely to the AC-SNP, the graphitic coating readily accommodated the lithium and appeared to expand during SNP lithiation more easily and without delaminating, suggesting graphitization accomplishes more than acting as a mere buffer in silicon swelling. These observed differences clearly show that selection of carbon layer properties can tailor anode material performance.

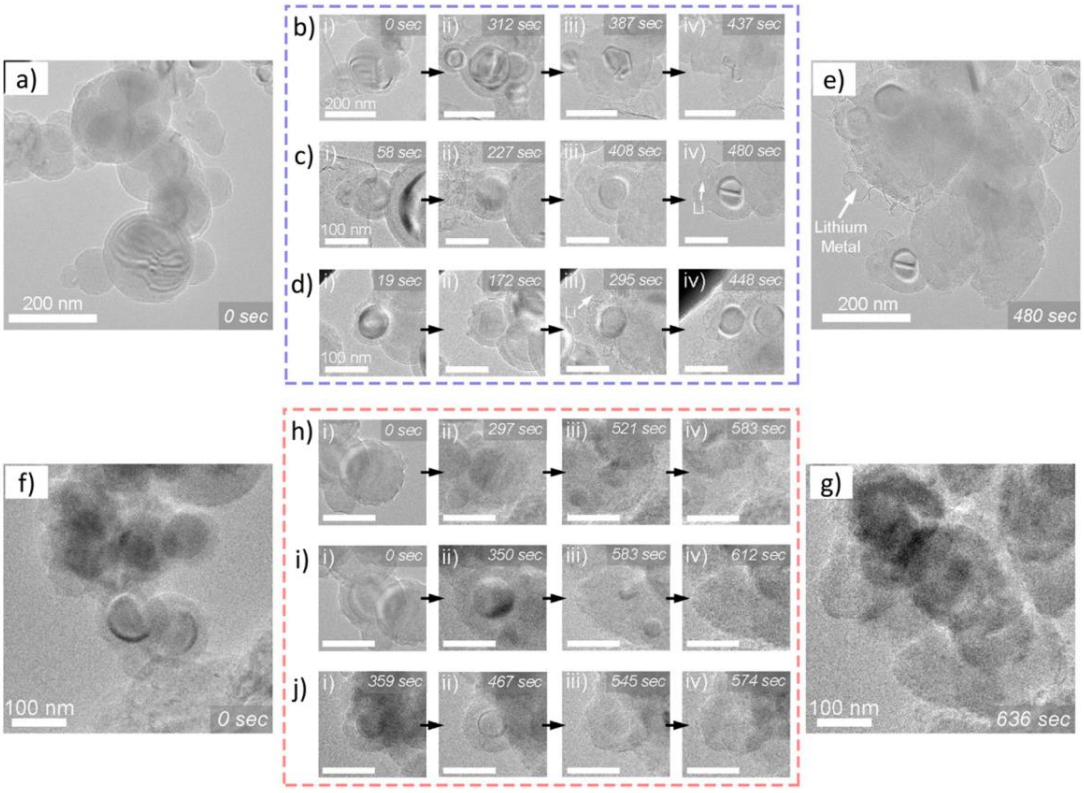

Figure 60: In-situ TEM of AC-SNP and GC-SNP lithiation. a) shows pristine AC-SNP while e) shows the same material after 480 seconds of lithiation. b-d) highlight the lithiation of specific particles with relevant timestamps. Similarly, f) shows pristine GC-SNP while g) shows the same material after 636 seconds of lithiation. h-j) highlight the lithiation of specific particles with relevant timestamps.

3.2.4 – Silicon as a Drop-In Additive:

As battery manufacturing facilities have already been developed and refitting would take extensive capitol, the most likely method that silicon will be implemented into a commercial lithium-ion battery would be as an additive. A drop in additive is the simple addition of a high-performance material to a standard manufacturing process. In this case, the SNP, AC-SNP, and GC-SNP materials will be added to a model of a standard graphite anode consisting of 90% natural flake graphite, 6% carbon black, and 4% CMC binder by weight. The additive will take the place of some of the graphite so that the new anode will

be composed of 10% SNP composite, 80% graphite, 6% carbon black, and 4% CMC by weight. Electrolyte composition and other half-cell testing conditions remain the same as previous testing (0.1 C from 1.50-0.01 V), while the anode loading is increased to 2.65±0.035 mg/cm^2 to better simulate more commercial loadings. Electrochemical performance of these cells is shown in Figure 61a and b demonstrating the graphite electrode achieved a 92% FEC with a reversible capacity of ~330 mAh/g and minimal capacity fade over 100 cycles. Meanwhile all three SNP based samples had significant increases in initial storage capacity, while all exhibiting very different capacity fade. The SNP was able to cycle in these circumstances with an initial capacity of 540 mAh/g and FCE of 89% because the electrical conductivity problem experienced earlier is compensated by the presence of carbon black and graphite, though unmitigated SEI growth and other functional problems result in a rapid capacity fade to 74% within 100 cycles. Both the AC-SNP and GC-SNP demonstrate similar cycling characteristics as seen in the active material half-cell testing before, with GC-SNP demonstrating greater cycling stability. Due to the lower proportional silicon content the AC-SNP and GC-SNP had 500 mAh/g and 520 mAh/g initial capacities, with FCEs of 88% and 90% respectively. They also experienced a capacity fade to 81% and 86% initial capacity over 100 cycles again demonstrating a clear difference in stability. In steady state the pure graphite anode had a CE of ~99.7% while all three additive samples had ~99.4% which can be attributed to the volume change effects and continual growth of SEI.[276]

Cyclic Voltammetry (CV) was also performed on these samples (see Figure 61c-e), illustrating the difference between pure graphite with one visible lithiation redox peak

(~0.12 V vs Li^+/Li) and one for delithiation (0.3-0.35 V vs Li^+/Li), compared to the GC-SNP which had a lithiation redox peak (~0.20 V vs Li^+/Li) and two for delithiation (0.38 V and 0.5 V vs Li^+/Li) as expected.[277,278] When CV testing the GC-SNP as an additive all of these peaks are convolved, showing that all active components of the anode are being utilized.

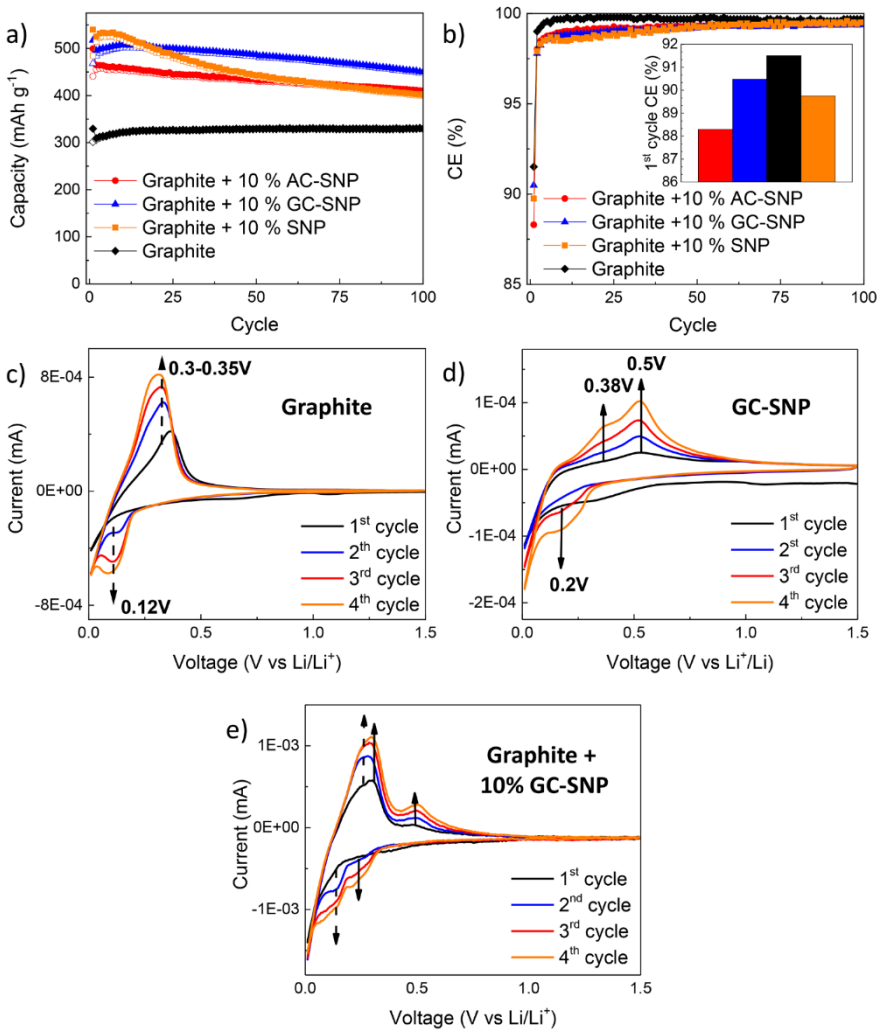

Figure 61: a) Charge/discharge curves and b) CE of a graphite control anode and 10% wt. drop in additives of SNP, AC-SNP, and GC-SNP in a graphite anode mixture. c-e) Show CV curves of the graphite anode, the GC-SNP anode, and the GC-SNP being used as a 10% wt. drop in additive, displaying characteristics of both active components.

3.2.5 – Summary:

This study has developed a 2-step CVD process for depositing conformal graphitic carbon-shells on silicon nanomaterials, decoupling the shell deposition step from the graphitization step and thus enabling a mechanistic study on chemically identical and structurally different silicon-carbon composites. The scalable CVD method has demonstrated that it can produce a graphitic carbon shell without forming electrochemically obstructive silicon carbide while still enabling the separate tuning of carbon-shell thickness and degree of graphitization. Electrochemical testing of amorphous-carbon and graphitic-carbon shelled silicon nanoparticles showed a clear difference in cycling stability and overall performance with graphitic outperforming amorphous carbon shells. This seems to be due to graphite not only improving electrical conductivity, but also lithium-ion transport into the silicon and reducing SEI development. Simple use as a drop-in additive to standard lithium-ion battery anode chemistries has also been demonstrated, indicating a path for a scalable easy-to-implement additive for commercial product improvement.

3.3 – Silicon Synthesis Methods and Commercial Material Effects[7]

As alluded to in previous sections, the use of differing silicon geometries with differing chemical impurities can cause significant alterations in a material's electrochemical performance. This section will be investigating these physical and chemical differences and their resulting effects through the use of both available data within published literature and data personally collected about these phenomena that were not openly investigated as of yet. This subsection will also be explaining the available methods of current large-scale material production used in commercial synthesis of silicon nanoparticles, then comparing their outputs to construct a wholistic picture of what benefits and drawbacks can be anticipated from a given production method. There are seemingly countless methods of producing silicon of varying geometries, purities, and sizes. However, as many of these methods produce materials more suited to use in quantum-dots or in quantities that would not satisfy the material demands of a single commercial battery, this section will focus on affordable high-yield methods of material production similar to those available for direct purchase from material/chemical distributors. For clarity these production methods will be broken into categories relating to the overarching method in which the material is synthesized, starting now with the simplest:

3.3.1 – Mechanical Synthesis:

Ball Milling:

The majority of papers published on silicon being ball-milled for battery purposes are of silicon or a silicon alloy being milled together with a secondary material and/or a binder as a method of mechanical alloying,[279,280] however ball-milling can also be a standalone method of silicon nanoparticle production[281–284] and the method's use in both cased should be viewed through the cumulative effects this approach has. Ball-milling is the process in which a material or multiple materials are typically placed within an inert jar-like container of a greater hardness than the material being milled, with a set of relatively high-strength beads (common materials ranging from stainless steel to tungsten carbide and sizes commonly ranging from tens of millimeters to hundreds of microns). These containers are then rotated in a way that will induce the beads to grind on the materials within the ball mill so as to break them down or instigate alloying with the amount of energy input (E_m) during the process being generally governed by the equation $E_m = \left(\frac{P_{net}}{m}\right) \cdot t$ where m is the mass of the material being ground, t is the grinding time, and P_{net} is the net power input by the particular grinding method.[284] For mixing and alloying purposes lower energy ball milling can be used, however for the production of nanoparticles from a larger grained feedstock, a faster more powerful version of the process known as "high-energy ball milling" is required. Within this category are nutating mills, stirred media mills, planetary mills, and mills simply marketed as "high energy ball mills",[284,285] where planetary mills are seemingly the most versatile and popular among research labs. Due to the high energy nature of this process, heat production is often a

complication, requiring cooling breaks during processing or an internal cooling system to prevent the fusing of particles, reacting of components, or simply the degradation of the device.[286] By name it cannot be determined if the material container's atmosphere has been evacuated and/or filled with an inert gas or left in air, though for many "wet" experiments a fluid such as ethanol is added to allow for efficient cooling and particle separation.[284] After being subjected to this kind of mechanical working, the material is generally under a higher lattice strain[283] and often contains chemical impurities resulting from the deterioration container and milling beads.[284] Also notable is the fact that this method produces asymmetric particles, so despite being noted as having an average given diameter, the output will be more flake-like in geometry with the diameter being ascribed as an approximation of a BET or laser diffraction analysis result.[283,284] This implies that in one or two directions it is likely that the length of the average particle will be significantly larger or smaller than the stated diameter. Another thing to be aware of with this technique is that the average size ignores the generally large size distribution produced by this technique. Different machines have been designed to minimize this distribution with limited success, though it has become apparent that use of progressively smaller beads tend to output a smaller average particle size.[284] There are additional variations on this technique such as "cryomilling" where liquid nitrogen is used to control the grinding temperature, "mixer milling" which is lower energy and often used to homogenize biological samples, and "drum milling" which is used for processing large quantities of materials. Even though this process is relatively simple, the high-energy nature of its implementation coupled with

high-energy systems typically being small in size, limits its implementation at industrial scales for nanomaterials by cost as of writing.[284]

3.3.2 – Reactive Synthesis:

Of the categories being described within this section, chemical synthesis is typically employed to create more porous structures or complex geometries as well as tends to display limited potential for scaling. For many publications chemical synthesis of pure silicon nanoparticles tends to focus on quantum dots and other applications with lower required yields and significantly lower particle sizes than those of desired by the battery industry. As this review is focused more broadly on pure silicon nanoparticle production with less emphasis on nanorod or precision nanostructures the following will focus on the different strategies being employed for high-yield methods of production for simpler or less precise geometries.

Magnesiothermic

This is the process of utilizing the reduction of silica with magnesium to bypass the temperature limitations of melting silica or silicon to achieve a pure material, while also gaining the benefit of maintaining a desired metastructure. Simply put, a desired geometry of silica can be easily manufactured or purified from nature such as with rice husks, then after being placed in a furnace with magnesium and brought to a temperature often above magnesium's melting point (640 ºC) and below silicon's melting point (1414 ºC), the

gaseous magnesium vapors or liquid magnesium will diffuse into the silica and reduce it while maintaining the metastructure through the following reaction:[287–292]

$$SiO_2 + 2Mg \rightarrow Si + 2MgO$$

Equation 35: Magnesiothermic reduction of silica example reaction.

Even in temperatures below the melting point of magnesium this reaction can still take place as the vapor pressure of magnesium at 428 ºC is still 1 Pa[292] and experiments are typically done in partial vacuum or under an inert gas to maximize the desired reaction. The magnesia can then be etched away through the use of HCl, thus avoiding use of HF and leaving behind a porous nanostructure of pure silicon. It should be noted that the pore size, overall mass-yield, and crystal size are impacted by the temperature the reaction takes place under and the molar ratio between the magnesium and silica. Larger yields and larger crystals tended to be produced at higher temperatures (950 ºC vs 750 ºC) if an excess of magnesium was present (ratio greater than 2:1 of Mg to SiO_2).[292] This is due to an increased reaction rate removing partially reacted magnesium:

$$SiO_2 + Mg_2Si \rightarrow 2Si + 2MgO$$

Equation 36: Removal of partially reacted magnesium in magnesiothermic reduction.

In addition to a reduction in the formation of Mg_2SiO_4 which is also problematic to remove.[289–292] This heat would also come at the cost of mild structural deformation due to the heat partially melting the material. The process is also sensitive to temperature ramp rate, insufficient reaction times, and material ratios.[287,292] Despite this, magnesiothermic production of silicon has the benefit of both relative simplicity and easily producing a

desired porous geometry which lends itself to use in research applications. The use of reagents and pure magnesium does produce a cost limitation when upscaling, but due to this technique's rising prevalence in lab-produced porous silicon nanoparticles we believed that it was worth mentioning briefly and pointing out that well-made reviews can also be found on the topic.[292]

3.3.3 – Plasma Synthesis:

Plasma synthesis has now become one of the standard methods of pure silicon production, though plasma itself is a broad category. As the fourth state of matter, plasma is defined by its large composition of ions and electrons as a high-energy gas-like state. This can be achieved by heating the gas directly, however as electromagnetic radiation can induce movement of charged particles like ions and free electrons, strong electromagnetic fields can cause an "avalanche" where one charged particle amasses enough energy to ionize a neutral atom upon collision which grows the ion density and produces a plasma. Depending on the method of powering the plasma and the frequency of the applied electric field, the ions and neutral atoms can either achieve significant motion becoming close to the temperature of the electrons, a phenomenon termed a "thermal plasma". Conversely the frequency may be too fast for these heavier particles to gain momentum before the direction of the electric field changes, which keeps the gas relatively cool in comparison to the free electrons and has been termed a "non-thermal plasma". This distinction is worth making as the mechanisms for SNP production in either of these conditions differs dramatically and though they may both be termed "plasma processing" they are most definitely

different. With that noted, both methods get particle surface temperatures well above their material melting points without the use of combustion and without having material physically contact the containment vessel, thus preventing any unwanted oxidization or unintended reactions.

Inductive Plasma Jet:

This is an example of a thermal plasma method of SNP production. The method relies on a phenomenon known as spheroidization, which is when a room-temperature solid is superheated into a gaseous state and then cooled so that the material coalesces and condenses into spherical particles, growing until they deplete the available material or reach a temperature too low to continue growth.[293] Both in research and commercial applications spheroidization is accomplished through the use of an inductive plasma jet, where the plasma is maintained by feeding an inert gas (often argon with hydrogen added for thermal conductivity) into the jet nozzle which is then emits the high-velocity gas into an inductively coupled plasma (ICP). Tekna produces commercial nozzles for this process powered between 15 kW and 200 kW,[293–295] but in general the ICP generator consists of a coil around the region of interest, then applying an alternating current through the coil which induces an alternating magnetic field at the center of the coil. If this region is occupied by a conductive material it will heat up which is the means of induction heating in metals, and when the region is occupied by a gas it will heat to the point of becoming a plasma. This maintains a superheated region that when fed a material carried will vaporize it and carry it with the gas flow of the jet. Materials fed into this process are typically

already milled to a small size and carried into the reactor with the gas flow. To prevent overheating the coil it is often liquid cooled, while a ceramic tube is often placed as a barrier between the coils and the region of interest.[294,295] After vaporization the gaseous material comes into contact with a cold inert gas which promotes condensation, causing uniform particle nucleation and growth until the plume has cooled past the point where particles fuse. Size of the produced particles can be tuned by altering the rate of cooling using gasses of different temperature, thermal conductivities, or speeds.[293] Similarly, even dispersion of the feedstock into the plasma region allows for the narrowing of the particle size distribution as equal time in the plasma allows for equal heating and reduces partially vaporized feedstock from instigating uneven nucleation and growth upon reaching the cooling stage. As of 2017 this method is capable of producing average particle sizes between 20 nm and 200 nm in the way described according to Tekna.[295] However, Liu et. all have pushed this method further by using micron sized feedstock and repeating the inductive plasma jet process with a 15 kW plasma jet, achieving average sizes as low as 15 nm.[293] Adding to this technique, Kambara et al. uses an inductive RF torch and metallurgical grade silicon powder for a precursor to form the nanomaterial as described, but adds methane to the outer region's gas stream in order to form a conformal carbon coating (though this technique does result in the formation of some silicon carbide).[296] An example schematic of this production method can be seen in Figure 62.

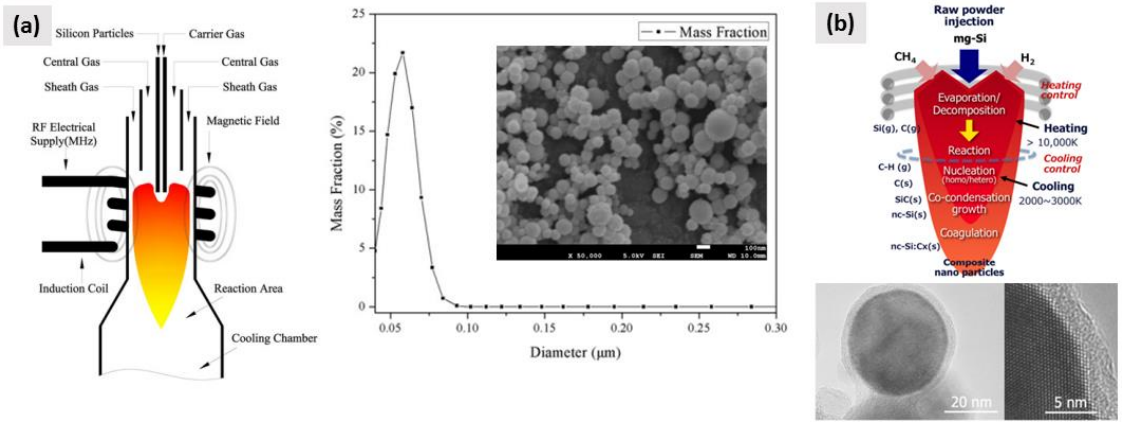

Figure 62: a) Thermal inductively coupled plasma reactor schematic for conversion of silicon microparticles to silicon nanoparticles with TEM images and size distribution of the resulting materials. b) Schematic of a similar silicon nanoparticle synthesis system with additional carbon-coating abilities also with output material TEM. Reproduced with permission from [296,297] in [7].

Capacitive Plasma:

Synthesis reactors for this method utilize a form of non-thermal plasmas, typically powering their electrodes by radio-frequencies power generators in the in the ISM bands (electromagnetic bandwidths without noise limiting legislation for Industrial Scientific and Medical uses). As described above, the electrodes for this system are supplied with an oscillating voltage which is separated from ground by insulative containment for a region filled with a gaseous precursor mixture, usually consisting of argon mixed with silane or another silicon-based gas as illustrated in Figure 12.[67,298,299] The strong oscillating electric field causes the free electrons within the precursor mixture to accelerate to a speed that can instigate the electrical avalanche while the ions and heavier particles' inertia prevent the accumulation of kinetic energy thus maintaining a low temperature relative to the hot

electrons (300 ºK vs 11000 ºK).[67] Particle growth follows a process that can be broken into three steps:

1. Charged molecules and chemistries missing one of the external bonds quickly react to form dimers which randomly collide, picking up mass and nucleating the particle for further growth.
2. At this point the nucleated particles are too small to maintain a charge and they begin to coagulate with each other until reaching a point where they begin to develop plasma sheath effects which produce a negative average charge.
3. At this point the particles repel each other and grow primarily from chemical reactions with the remaining precursor as a form of chemical vapor deposition (CVD).[67,298] As this process occurs under vacuum and builds the particle from precursor with no preferred direction, this method tends to produce extremely high purity spherical silicon nanoparticles with chemical impurities occurring after production.

Despite its benefits and relative simplicity this method is fundamentally limited in the size of the spherical particles it can produce, with changes in pressure and production conditions limiting the maximum average size to around 10 nm regardless of precursor.[178,300,301] Fortunately, due to the small size of these particles in-flight sintering has proven to be a reliable method of increasing average particle size. This method produces a branched structure which varies greatly in length, however the width of these branches is tightly controlled and tunable by the temperature and pressure of the reactor system allowing for average diameters up to 50 nm.[265]

3.3.4 – Thermal Synthesis:

Pyrolysis:

This process takes a number of forms to arrive at the same general synthesizing mechanism. Pyrolysis itself is the thermally instigated decomposition of a gas so that a change in chemistry occurs, in the cases that relate to this section that implies the precursor gas decomposes to form silicon nanoparticles through nucleation and CVD. Methods of thermally decomposing the gas vary by the precursor and the desired output ranging from flame pyrolysis, to laser pyrolysis (see Figure 63), to simple furnace pyrolysis (see Figure 64). Flame pyrolysis is the injection of a precursor material into an oxidizing flame (often fueled by an oxygen/natural gas mixture) to instigate the formation of particles, with their size and crystallinity controlled by the pressure gradient and precursor injection rate[302,303]. Despite being an efficient material production method, flame pyrolysis exclusively produces oxidized materials which require additional processing to be useful so this method holds little potential in battery material development. Laser pyrolysis typically flows a mixture of a precursor gas (often silane) in an inert gas (often argon) and expose the flow to a region of high-intensity laser light at a wavelength that strongly interacts with the gas. For silane and silicon production this usually implies the use of an infrared CO_2 laser with a wavelength near 10.6 μm to achieve pyrolysis due to the absorbance spectra of the typical precursors (silane and trichlorosilane).[304–307] The simplest incarnation of pyrolysis is use of a tube furnace to cause the thermal decomposition of the precursor gas and thus the formation of nanoparticles. To accomplish this at any scale the residence time

within the heated region needs to be substantial enough to adequately heat the precursor gas. For Wiggers et. al that meant 5.3 cm/second to 6.7 cm/second of flow velocity for an average time of 2.4 seconds to 3 seconds within the heated region.[308] Synthesized particle size with this method can be controlled through gas composition ratios, pressure, and residence time, though there is no indication on production yield efficiency from any of the listed publications. For all of the listed pyrolysis methods the output particles contain branched structure similar if not identical to that of the in-flight sintering described in the capacitive plasma section. Laser pyrolysis unlike the other pyrolysis methods seems to produce a combination of branched particles and spherical particles though papers seldom acknowledge the branched nature of some of the materials. Particle size is often estimated through BET by simplifying the geometry to a sphere, though branch diameters can range from 15 nm as produced via laser pyrolysis, to 100 nm as produced by furnace pyrolysis with their estimated spherical equivalents being 18.7 nm and 270 nm respectively.[306,308] As non-oxidative methods are typically done in partial vacuum or inert environments, they generally produce high purity crystalline chemistries, though amorphous particles are also theoretically possible.

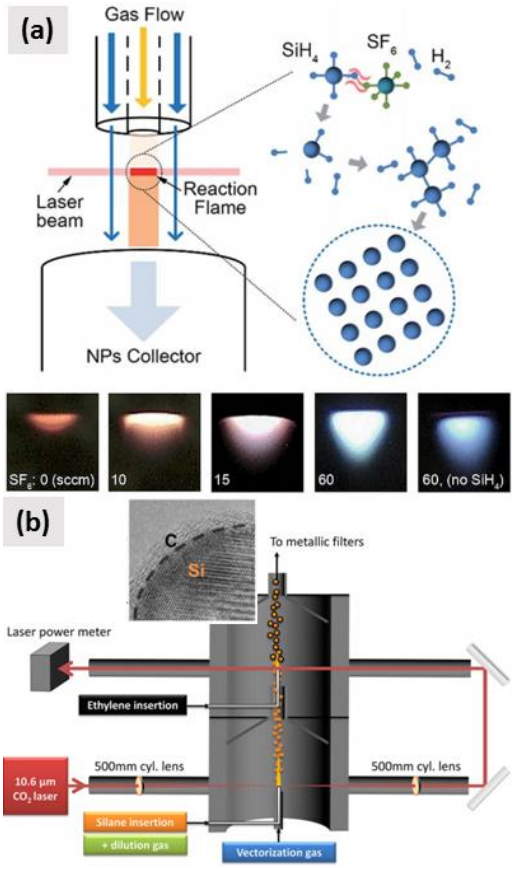

Figure 63: a) Silane-laser pyrolysis process using SF_6 as a photosensitizer to react SiH_4 and b) a two-step laser pyrolysis system for silicon nanoparticle production and carbon-shell application. Reproduced with permission from [306,309] in [7].

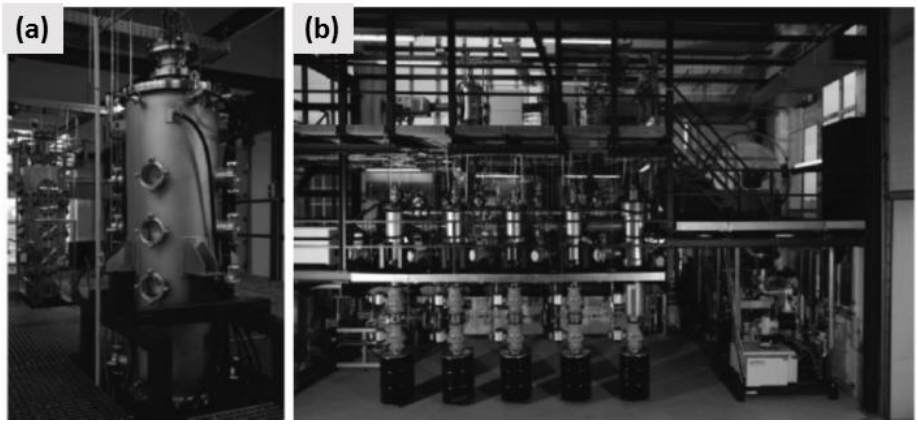

Figure 64: Photographs of a) pilot-scale hot-walled reactor and b) the related plant. Reproduced with permission from [310] in [7].

Laser Ablation:

Comparatively uncommon to laser pyrolysis and other methods of nanoparticle synthesis, laser ablation produces nanoscale spheroids that tend to form clusters through the use of pulsed-laser induced ablation. This is typically done by scanning across a polished silicon surface with a pulsed laser which will temporarily ablate the area in focus, creating a plasmatic plume that re-condenses into nanoparticles. The ablation can also be carried out in vacuum, air, or in solution with particle collection either being done through the removal of colloidally suspended particles or procuring nanoparticles that fell back to the substrate surface. Variables that control the output particles are: pulse-width, central wavelength, pulse-energy, and fluid/gaseous surrounding conditions. Pulse-width of an impinging beam can vary from the nanosecond to the femtosecond regime[311] with "long" pulses in the nanosecond regime being comparable to the timescales of silicon's thermal relaxation rate and will thus induce a form of local heating.[312] Use of shorter pulses are thus able to avoid thermal complications sometimes being referred to as nonthermal, in addition to a reduced interference between the laser and the evaporated material.[312] Often to maximize the energy absorption the pulse's central wavelength is selected to be an easily absorbed frequency for the material (generally near 800 nm), while the pulse energy itself is generally maximized by the system being used (often a Ti:sapphire laser at around 1 mJ per pulse).[312–316] The resulting particles from this process are relatively monodisperse as R. Intartaglia et al has shown with by varying the pulse energy to change the average size from 2.5 nm to 60 nm with a standard deviation roughly half the particle size for all conditions.[312] Finally, the purity of the nanoparticles will be directly related to the purity

of the substrate and the surroundings during the ablation process producing trace amounts of silicon carbide and silica with ethanol and deionized water respectively.[312,313] It may be worth noting that after investigating individual retailers or re-sellers of silicon nanoparticles such as: Tekna, Sigma-Aldrich, Nanostructured and Amorphous Materials (NanoAmor), etc. as well as the patents that they held in an attempt to determine commercially standard methods of particle production: Inductive Plasma Jets, Thermal Pyrolysis, and Laser Pyrolysis seem to be the most common modes of production. Though most companies simply did not have patented techniques of SNP production or list their method of production.

3.3.5 – Effects of Size and Purity:

It has been noted that there appears to be a critical diameter of ~150 nm whereupon pure silicon is unable to maintain structural stability when lithiating, resulting in fracture and general loss of material usability.[317] The methods of silicon nanomaterial production described above have been applied to electrochemical applications and demonstrated in multiple ways that is critical dimension for inducing pulverization and fracture needs to be met in all dimensions, so plasma synthesized materials such as Alvarez-Barragan et al. or structurally reduced material like that of Entwistle et al. are able to surpass 150 nm in size through 2 dimensions while maintaining cycling stability.[265,292]

This is not to say that there is no effect from altering dimensions beneath the critical diameter, as increased surface area permits faster lithium-ion transport and appears to enable faster charging and discharging.[318,319] Unfortunately, silicon is air reactive which

implies the development of a terminal oxide layer which consumes a greater and greater proportion of the total material with poorly cycling nano silicates instead of crystalline silicon.[320] Work done by Zhu et al. using commercial powders with average three average diameters beneath the critical 150 nm mark, electrochemically tested and demonstrated reduced initial capacity of smaller materials as well as the reduced stability of larger materials in addition to a stratification of discharge stability where smaller materials perform better as anticipated.[319]

It is worth noting that these results are dependent upon the accuracy and monodisperse nature of materials produced and sold under the banner of "100 nm average diameter". This can generally be assumed to be an exaggeration as monodisperse materials are exceedingly difficult to manufacture as demonstrated in the previous subsections, but also marketed materials have a clear size distribution as noted by Nava et al.[6] This raised the question of how materials with identical marketing descriptions compare in electrochemical cycling and in chemically for that matter. As shown in Figure 65, the oxygen content and performance for four such materials vary dramatically (note: materials shown were coated in ~7 nm of conformal graphite coating using the method described by Nava et al. to test electrochemical performance).

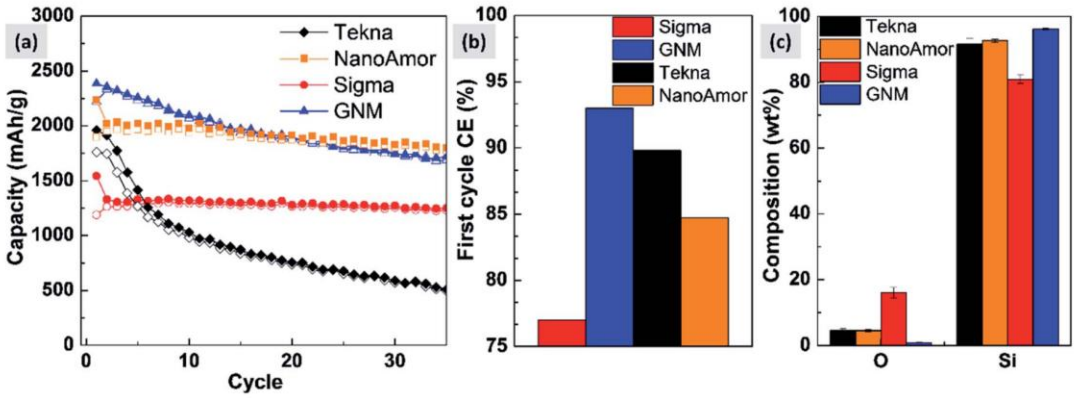

Figure 65: Comparison of a) cycling performance, b) first cycle coulombic efficiency, and c) chemical content via EDS of four identically marketed "100 nm Silicon Nanopowders" from Sigma Aldrich (Sigma), Nanostructured and Amorphous Materials (NanoAmor), Tekna, and GetNanoMaterials (GNM).[7]

The marked difference between material composition and performance makes logical sense on its own, as higher oxygen containing Sigma would contain more silicates which would reduce capacity as observed. However further analysis of the materials which were all marketed as 100 nm in diameter demonstrates unexpected differences in size distribution as well (see Figure 66). GNM demonstrates both the highest degree of purity, but their "100 nm material" is actually closer to 200 nm which both explains the increased purity due to less surface area to oxidize and the constant rapid decrease in capacity as the materials fracture. Tekna despite being of similar purity to NanoAmor performed significantly worse, which can be explained by the large size distribution where 400 nm particles that will fracture, despite being infrequent still make up the majority of the mass fraction and thus active material content. These few larger particles explain the rapid initial decline in capacity.

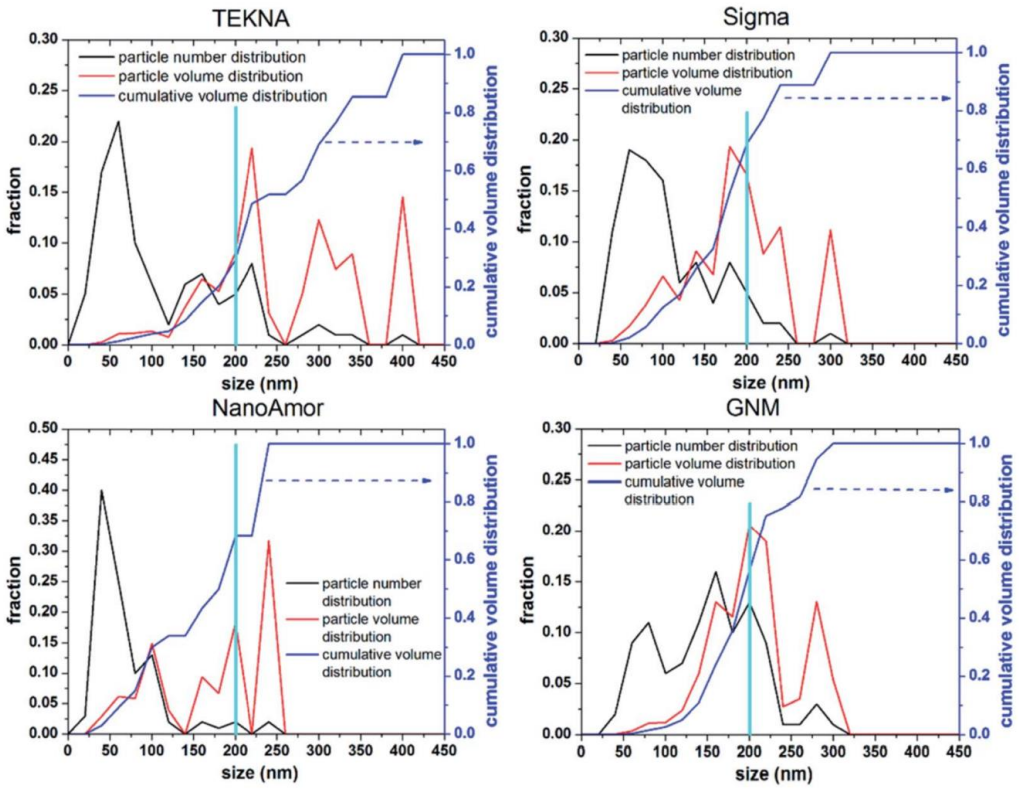

Figure 66: Size distribution and resultant volume distributions for "100 nm silicon" materials from multiple suppliers (Tekna, Sigma Aldrich, Nanostructured and Amorphous Materials, GetNanoMaterials).[7]

Even using the same method of production, slight changes in process parameter have demonstrated large changes in output material size. For instance, using a capacitive plasma for material production with no post synthesis annealing will produce spherical materials of an average diameter dependent on the reactor pressure (see Section 1.3). The addition of a furnace will instigate sintering of these materials inducing rapid growth and development of the branched structure described by Alvarez-Barragan et al.[265] While increasing the furnace temperature is a fairly benign action that doesn't influence the mass yield of the material, that alone can drastically increase the average "branch" diameter observed to >10 times the original particle radius as shown in Figure 67.

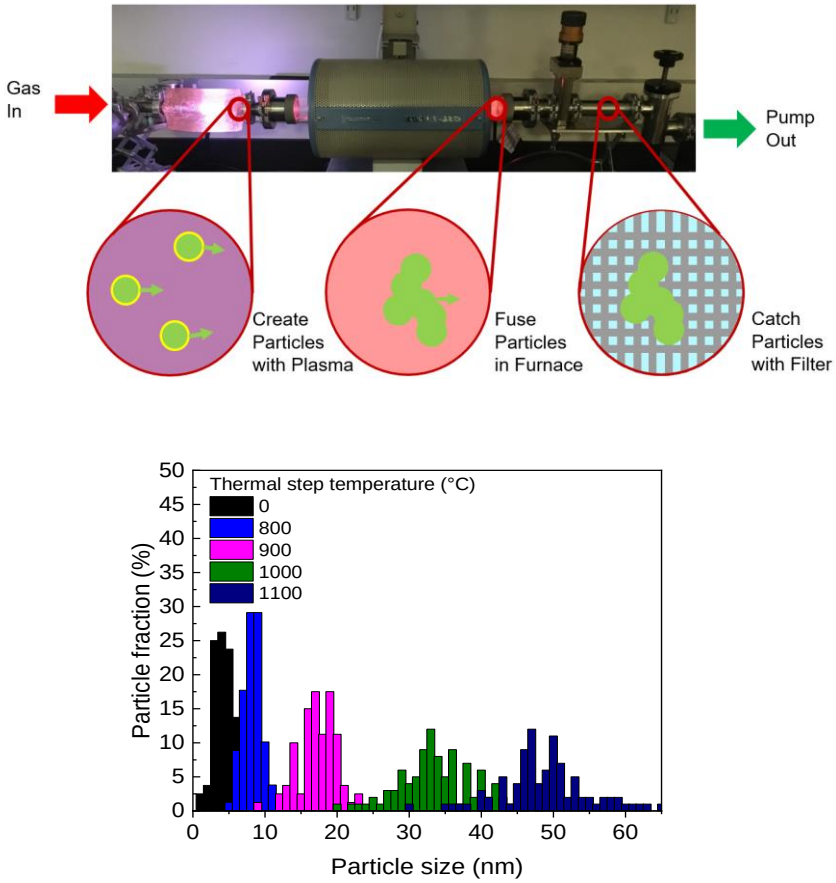

Figure 67: Non-thermal capacitive plasma and sintering induced growth of branch structures system cartoon (top) and branch size-distribution to annealing temperature relation (bottom).

3.3.6 – Summary:

This subsection acted as an introduction to the methods involved in synthesizing the most common and promising silicon nanomaterials for lithium-ion battery applications. These methods ranged from: classical ball milling, to reactive chemical formation, to laser ablation, and the more recently dominant plasma synthesis methods. Even within the category of plasma synthesis there is a substantial variety between the smaller more monodisperse particles formed via capacitive non-thermal plasmas with gaseous

precursors to the larger more rapid production of inductive thermal plasmas that use solid precursor materials. Naturally the differences in structure have effects on electrochemical cycling with it becoming apparent that the 150 nm fracture diameter observed by Liu et al. in their 2012 publication is only valid for materials that restrict expansion in multiple directions. Finally, it is noted that even materials marketed with the same description for differing companies will have substantially different chemistries and physical structures that can lead to massive inconsistencies in observed effects between studies with otherwise identical experiments. More detailed observations and wider topics are described in *Critical barriers to the large-scale commercialization of silicon containing batteries*. This both contains the above section and describes in greater detail that standardized electrochemical testing procedures should be instated to enable a fair and usable comparison of materials. Areal loadings greatly impact observed material capacity and stability with referenced publications ranging from commercially viable loadings to negligible films in order to obtain impressive, but scientifically useless results. Similarly, cycling conditions had varying upper and lower voltage boundaries undergoing differing charge/discharge rates, all of which greatly impact performance and stability. The main takeaways of this section being that different production methods produce different materials that may be marketed in the same way, which makes investigation of the physical and chemical properties of the materials being tested necessary for accurate and usable publications.

3.4 – Anode Material Surface Chemistry Effects on SEI

3.4.1 – Intro to SEI:

The Solid Electrolyte Interphase (SEI) is a fairly enigmatic topic within battery science. Before the production and adoption of the Li-Ion battery the working assumption for cells using sodium or lithium was that direct electron transfer from the electrode to lithium cations in solution would not be a rate-limiting factor.[321] Upon discovering a passivating layer on pure lithium anodes it was immediately predicted that it would interfere with cycle life and needed to be removed to maximize cell life.[322] The observed passivating layer was termed the SEI due to the fact that it consisted of insoluble and partially soluble products of electrolyte reduction, making it not quite a solid and not quite a liquid. In effect the SEI acts as a solid electrolyte which also had a high electrical resistivity, both enabling effective electron transfer and adding to internal cell resistance acting as a necessary evil. Desirable SEI chemistries appear to be highly cation permeable, thin, high-strength, flexible, insoluble, and stable for both thermal and electrical gradients.[322] Unfortunately SEI thickness for all anode chemistries appears to increase with cycling and for high volume changing materials like silicon, quickly becomes untenable.[322]

Formation of the SEI begins when the electrolyte contacts an anode material and continues as a negative potential is applied. The competition between reduction reactions is dependent on both the electrolyte and in theory the catalytic properties of the electrode surface, producing inorganic compounds like LiF, LiCl, and Li_2O as well as organic compounds like Li_2CO_3. For carbon-based anodes the surface catalytic properties are

thought to be related to everything from chemical imperfections to the crystallographic plane. Regardless, the first cycle of Li-Ion batteries consumes electrolyte to create the SEI in an irreversible capacity loss leading to the observably lower FCE. Reduction potential of lithium is more negative than most solvated-electron systems, which reduce both solvent molecules and anions. However, in the case of more stable solvents electrons are able to diffuse through the electrolyte into the cathode causing the cell to self-discharge, demonstrating a clear electrochemical need for SEI. As a result, electrolytes are designed to contain SEI precursors with high standard electrode potential and additives are put into the standard $LiPF_6$ to optimize function through intentional SEI formation.[323] This quickly becomes a complicated field in itself as everything from the active electrode material to the voltages forming the SEI (0.5-1.7 V vs. reference lithium appears to be the active range)[324] to the time it takes to form the SEI has a role on its development. The general description of SEI form is as a polycrystalline material,[325] with ion transfer occurring through mobile-point defects/grain boundaries.[326] It has been estimated that SEI thicknesses of ≥1 nm would be enough to prevent electron tunneling and the aforementioned self-discharge.[327]

Carbon Anode SEI:

Standard carbonaceous or graphitic anodes are expected to experience non-uniformities in SEI formation due to the non-uniformities in their structure. It has been shown that irreversible reactions predominantly occur on edge planes and activated carbon.[322] The generally understood aim to maximize cell performance is to produce

insoluble denser compounds more akin to Li_2CO_3 than ROLi (where R is an alkyl group). Studies on porosity and SEI growth found through BET that higher surface area materials tend to develop more SEI and induce a greater initial consumption of electrolyte.[328] As a result, the technique of burning off excessive surface areas to reduce electrolyte formation has been adopted and proven relatively successful.[329] The presence of oxygen species on graphite also appears to increase reduction potential and induce SEI formation prior to lithiation.[251] It has been demonstrated in graphite that the unbound fringes experiencing the greatest volume changes (the non-basal regions) grow a thicker SEI, implying both additional reactions due to the geometry and due to the regional stresses.[330]

Silicon Anode SEI:

Silicon and carbon anodes are said to have a similar initial intercalation of lithium as much of the intercalation of lithium into the alloy is meant to take place after electrolyte reduction into SEI. Small amounts of lithium are thought to be added at voltages above 1 V on the lithium scale prior to SEI formation. Silicon nanostructures tend to have an advantage of short lithium diffusion distances and as mentioned before, maintaining diameter beneath 150 nm is essential to prevent the material itself from pulverizing, implying multiple benefits to small complex geometries.[317,331] Upon SEI fracture (often an effect of expansion) new anode surface is exposed and is again able to catalyze the development of SEI. Oddly enough, it is also theorized that the contraction phase during delithiation causes the SEI to bunch up and become more porous, also allowing for formation of additional SEI.[322] This extensive SEI growth mechanism is illustrated in

Figure 68 and has been shown to induce such capacity losses that it has been mistaken for the material loss via pulverization.[332] As mentioned, excessive SEI development increases internal cell resistance and in the case of silicon due to its large volumetric changes continuously deteriorates the cell performance with the consumption of electrolyte and increasing cell resistance. Initial cycling is thought to produce predominantly Li_2CO_3 and LiF species,[332] however it is worth noting that in all ex-situ cases there is a pressure and equilibrium chemistry change associated cell disassembly. Experiments seem to show that some additives like FEC to the standard $LiPF_6$ solution are able to repress the formation of porous SEI layers, which is attributed to (in part) the formation of more complex Li_xSiO_y species that create a more homogeneous and denser initial SEI.[333]

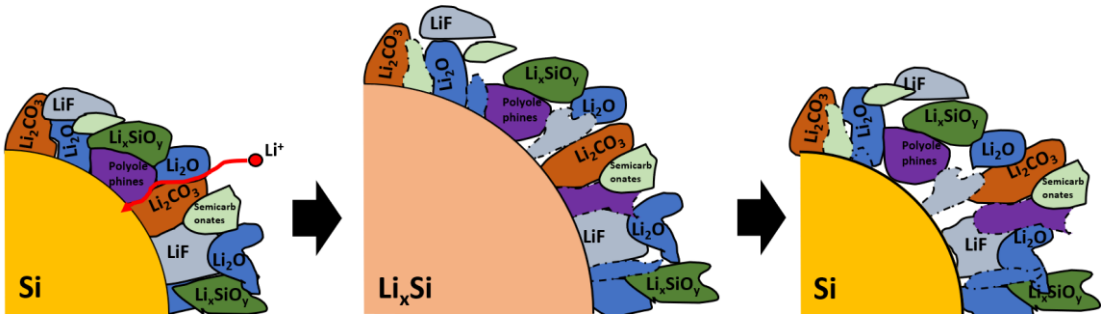

Figure 68: Illustration of the cyclical formation of additional SEI species due to volumetric expansion and contraction.

3.4.2 – Carbon Shell Effects on SEI:

Many of the efforts to control SEI development that have been mentioned thus far have been done by altering the electrolyte chemistry. However, as noted in Section 3.2 there appeared to be a decrease in SEI resistance simply by changing the surface material

structure. Using the coating technique described in Section 3.2 a variety of coatings have been prepared on both commercial Nanostructured and Amorphous materials and lab-grown silicon nanospheres (synthesized using the pulsing method described in Section 1.4) for the purposes of testing whether the surface chemistry and structure influences SEI development. Something worth keeping in mind during this investigation is the value of in-situ measurements as the deconstruction of a cell is destructive by its very nature. The pressure and regional chemical equilibriums will be disrupted, while at the same time many studies tend to "wash" their anodes to remove electrolyte. This process of washing/rinsing even if performed quickly will inevitably alter the SEI as it introduces new chemicals and likely dissolves soluble SEI components. Within this study, when referring to "washed" anodes the process in which they are prepared is by cycling them at the described conditions, then disassembling the cell within an argon filled glovebox and dropping the anode in a vial of Dimethyl Carbonate (DMC) for ~60 seconds before removal. The reason for doing this will become apparent when discussing Raman fluorescence and the changing signals observed during FTIR spectroscopy as the anodes dried.

Materials:

The materials prepared for this study fall into two silicon core size ranges described as:

- "*100 nm*" – Referring to commercially purchased 100 nm Nanostructured and Amorphous Materials

- "*20 nm*" – Referring to silicon nanoparticles that were produced using the methods described in Section 1.4 at conditions of 100 sccm silane precursor mixture, 100 W of power supplied so as to expose the material to 3 pulses of a 50% duty cycle, in a 1 inch diameter reactor held at an operating pressure of 4 Torr.

These materials were characterized through TEM to obtain their actual size distributions which can be seen in Figure 69. For these conditions it is clear that despite the average particle volume being near the described values, both populations have a median diameter lower than the stated size. There is also a non-negligible population of >150 nm particles within the Nanostructured and Amorphous Materials batch that will likely impact cycling performance.

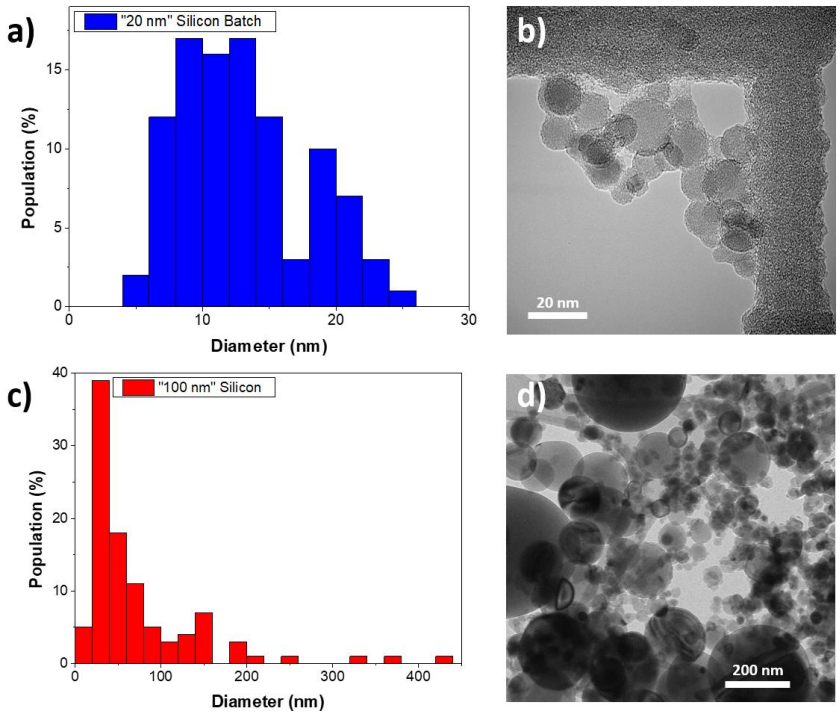

Figure 69: Size distribution and TEM of a-b) "20 nm" lab-synthesized material and c-d) commercially purchased Nanostructured and Amorphous "100 nm" material.

These silicon materials underwent the two-step CVD process described in Section 3.2 to attain multiple different carbon coating thicknesses, with a couple only undergoing the amorphous carbon coating step in hopes of observing a change in SEI based solely on shell crystallinity. The notation used to describe these materials is simply the carbon content by weight in percent as determined by EDS measurements, followed by the coating structure and in parenthesis the described particle size. If the material is uncoated it will just be referred to as silicon.

Electrochemical Testing:

Anode composition was made to be 8% CMC and 92% active material by weight, with a loading between 0.36-0.55 mg/cm^2 for all samples. The electrolyte used was 1.2 M

$LiPF_6$ in an EC:EMC (3:7 w/w) solution, diluted to have 3% FEC by weight (Note: additional tests using the standard 10% FEC did not alter the cycling results in any measurable way). The material cycling conditions used were based upon an initial rate test, where it was determined "formation cycling", low current for the first few cycles to develop a dense and thin SEI, would be performed at C/10 for 5 cycles from 0.01-1.50 V. Following that, additional cycling would be performed at C/5. This produced the results shown in Figure 70, which seem to demonstrate for the 100 nm materials an optimal shell coating of 21% Graphite, equating to a ~8.5 nm shell thickness. It is theorized that thicker carbon coatings are restricting material expansion and interfering with the lithiation process, while thinner layers do not provide the required physical and electrical support for stable cycling. In the case of the 20 nm materials, thicker coatings are associated with more stable cycling and lower initial capacity, with the 72% Graphite (20nm) sample achieving a stabilized >99% CE. It should be noted that the shell thickness jumps from 3.4 nm to 10.8 nm between the 36% Graphite (20 nm) and 72% Graphite (20 nm) samples, making the thickest sample the closest to the 8.5 nm optimal thickness seen in the 100 nm materials.

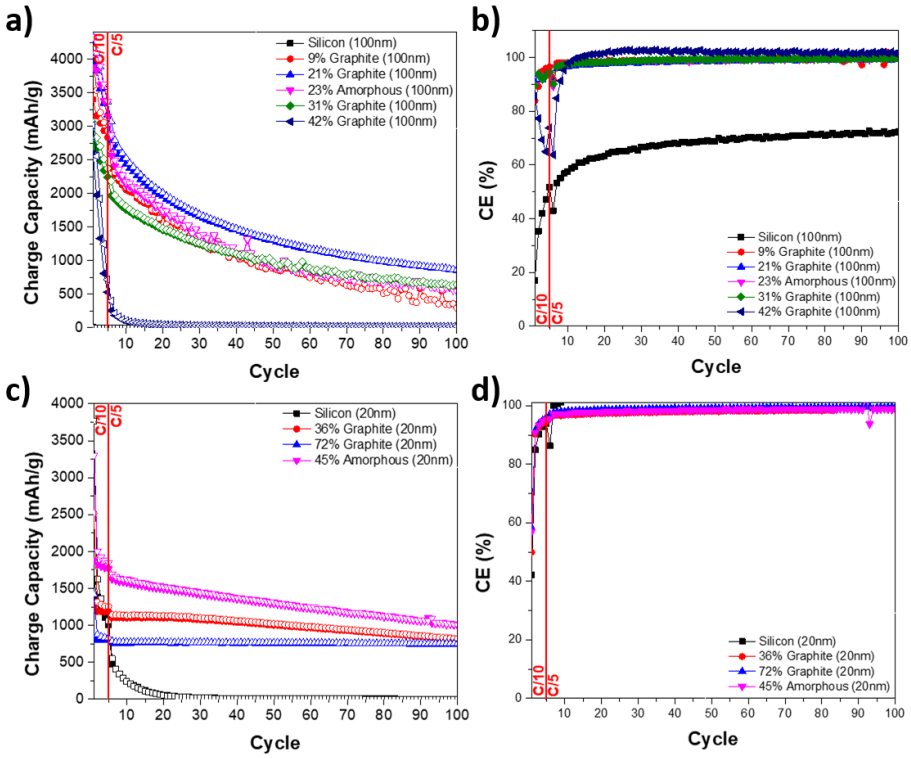

Figure 70: Electrochemical cycling data silicon nanoparticles with varying coating thicknesses and structures of a-b) commercial particles sold as 100 nm in average diameter, and c-d) 20 nm lab-made silicon nanoparticles.

Ex-situ Chemical Analysis:

The intention of this study was not to create an optimized battery, but instead understand the influence of surface chemistry on SEI development. As such, initial tests were performed on FTIR ex-situ to determine the regions of interest in an anode if an operando FTIR technique was implemented as in Tremolet de Villers et al.[334] To do this the 100 nm materials underwent the 5 formation cycles and were disassembled upon the final delithiation. These anodes were then scanned on a Bruker Alpha Compact FT-IR spectrometer with a diamond ATR in an argon filled glovebox while "wet", which is to

say that the electrolyte still soaked the surface. As it dried additional scans were taken, showing a high degree of vaporization until finally the fully dried anodes were scanned as shown in Figure 71. The continuously changing nature of the FTIR signal implies that the ex-situ method would not be reliable without first washing the anode into a more stable state. As mentioned before, the washing process will likely interfere with not only the residual electrolyte, but also the SEI making any post washing data only part of the story.

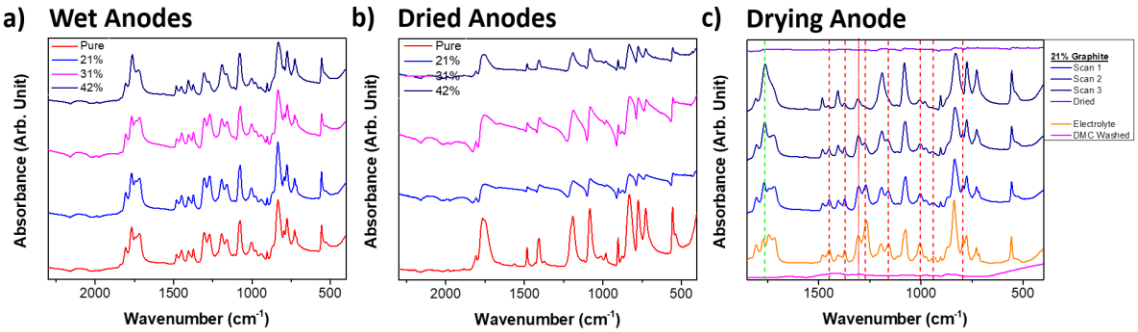

Figure 71: FTIR data of 100 nm commercial silicon with differing carbon-coating thicknesses after 5 charge/discharge cycles at 0.1 C to develop an SEI, with scans taken while a) still coated in electrolyte, b) after the electrolyte had dried, and c) while the electrolyte was drying (green dashed line indicates relative signal increase with time with red line indicating decrease).

Another batch of formed 100 nm anodes were removed from their cells and then washed in DMC. FTIR scans were then taken and normalized using the magnitude between 1073 cm^{-1} valley and the 1173 cm^{-1} Si-O-Si peak, as the Si-O-Si species should be predominantly at the barrier of the silicon nanoparticles oxide layer which would be uniform throughout the samples. Apart from the uncoated sample there was very minor variation between all conditions, implying that the SEI either washed away with the DMC or that any differences in the SEI are not chemical, but structural in nature (eg. thicker grains of different arrangement). To further understand the observed signal, the components of the cycled

anode were scanned separately. In this way any new peaks observed would correlate to an SEI species. These peaks were then marked measured and recorded showing minor shifts and the added presence of peaks at 1493 cm^{-1} and 1652 cm^{-1} which likely correspond to carbon-hydrogen symmetric deformation and carbon-carbon double bond stretching which could be the formation of expected ROLi compounds.[322,335] More specifically 1652 cm^{1} when taken with the 990 and 871 cm^{-1} peaks indicates an R-CH=CH_2 species.[335] Unfortunately, as shown in Figure 72b, the electrolyte signal is noisy and has numerous species that could interfere with any operando scan of the material. This region of electrolyte interference allows for work with potential cathode materials, but is problematic for silicon or carbon-based composites.

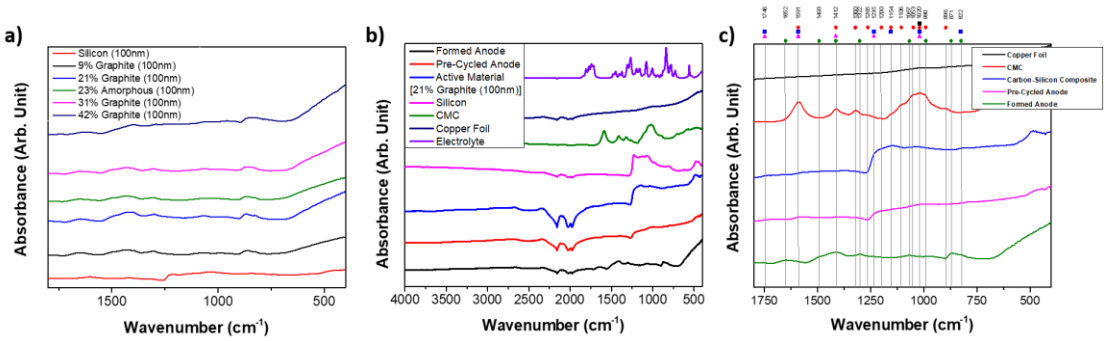

Figure 72: a) FTIR spectra of washed anodes composed of 100 nm silicon particles with varying coating thicknesses and structures, with peak magnitudes normalized to the Si-O-Si peak at 1073 cm^{-1} relative to a low at 1173 cm^{-1}. Using this normalization minimal differences are observed between the samples. b) Cycled anode FTIR spectra compared to its constituent parts and c) peak location noting.

In hopes of detecting additional chemical species from increased surface area 20 nm materials were prepared for X-ray Photoelectron Spectroscopy (XPS) testing. The materials tested included uncycled anodes, formation cycled anodes where the electrolyte was allowed to dry, and formation cycled anodes washed with DMC. Again, it was found

that any changes between signals were minor and seen only through peak magnitude and not position (see Figure 73). Samples with dried electrolyte proved to be inconsistent due to the comparatively uncontrolled amounts of electrolyte remaining from the cell disassembly process.

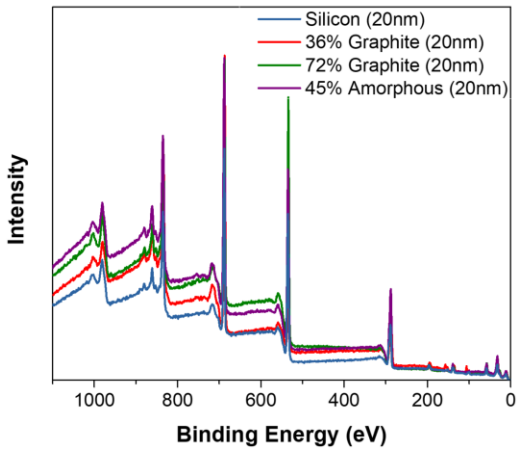

Figure 73: Comparison of XPS anode signals for DMC washed 20 nm silicon-based anodes.

In-Situ Raman:

Using Silicon (20 nm) and 36% Graphite (20 nm) as active anode materials, in-situ Raman spectroscopy measurements were taken. The cells consisted of a standard 2032 coin-cell with a hole punched in the base that was then closed using a thin sapphire window to enable measurements. The electrode itself was actually a copper mesh with a 0.71-0.84 mg/cm^2 coating, facing towards the window, allowing for both ion transfer through the mesh and material monitoring through the window. Raman measurements were taken with a Horiba XploRA Plus with 532 nm laser light that was set up to accommodate electrochemical testing using a Bio-Logic SAS SP-300. Prior to testing an estimate of the

capacity was made through using standard cycling procedures on mesh electrodes and comparing the data. Maintaining the formation cycling of C/10 for 5 cycles the anodes were tested. Thicker electrodes were also tested, however fluorescent signals drowned out any usable data. Within Figure 74e it is clear to see an increase in fluorescence as time progresses, however it is unclear what the absolute cause of the fluorescence is. Scans of highly-fluorescent materials appear to be indistinguishable from regions of pure electrolyte, so fluorescence could be an effect of electrolyte seeping into the region of focus or it could be that compounds in both the electrolyte and the SEI fluoresce. During ex-situ measurements of anodes that had undergone formation cycling, washed anodes did not display fluorescence while anodes with dried electrolyte did, again implying that surface chemistries are altered upon washing the electrode. Comparing the cycling and magnitude of Raman signals, both materials demonstrate signal peaks when delithiated, however there is a much clearer pattern in the 36% Graphite (20 nm) sample despite the increasing background fluorescence. Peak and valley spectra for the 36% Graphite (20 nm) anode at delithiated and lithiated states respectively show the increasing curved background signal in addition to the continued presence of the D and G peaks (1330 and 1600 respectively)[1], though only in the delithiated state. These features can all be found in Figure 74. Not much in the way of specific electrolyte chemistries can be said due to the lack of clear peaks. However, the cyclic signal peaking indicates that the SEI could be dissociating during

lithiation or merely spreading apart, while the background fluorescence indicates a degree of continuous growth.

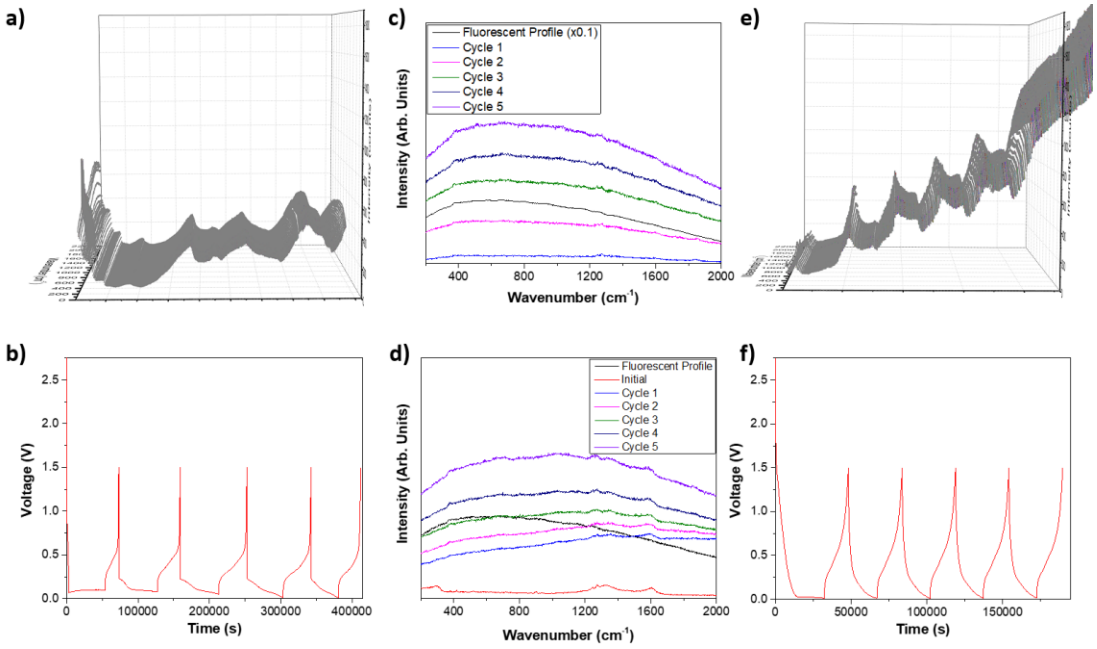

Figure 74: Comparison of in-situ Raman spectra and the associated charge/discharge curves for a-b) 20 nm uncoated silicon and e-f) 36% Graphite (20 nm). Spectra for the 36% Graphite (20 nm) particles are highlighted at the c) fully charged state and d) fully discharged state, illustrating the growing fluorescent signal and constant changing nature of the spectra.

3.4.3 – Carbon Shell Lithiation:

When performing in-situ Raman measurements on a 31% Graphite (100 nm) sample the voltage range was reduced to 0.05-1.50 V (as opposed to 0.01-1.50 V used in standard testing). Lithium penetration of the silicon oxide layer appears as a dip and is generally seen within this material charge/discharge curve at ~0.4 V (see Figure 74b) and in this case did not occur, leaving all measured capacity to be attributed to the carbon shell itself. This capacity contributes only an estimated 4.6% of the overall material capacity,

which though comparatively minor is nearing the maximum predicted value of 4.7% of the material capacity (assuming SiO_2 contributions are negligible). Raman spectra demonstrated the deformation of the D and G peaks indicating the expansion of the graphite shell from lithium intercalation as with larger flake graphite. These findings can be seen in Figure 75 and clearly show the silicon peak at 470 cm^{-1} does not shift, broaden, or shrink as would be expected upon lithiation,[336] while the D and G peaks become more equal during lithiation and then become less equal upon delithiation. The pairs of peaks around 900 cm^{-1} and 1250 cm^{-1} can be ascribed to the sapphire window the measurements were performed through, while the bump ~1400 cm^{-1} between the D and G peaks is likely Lithium Ethylene Dicarbonate (LEDC) and can be expected to shift during cycling.[337]

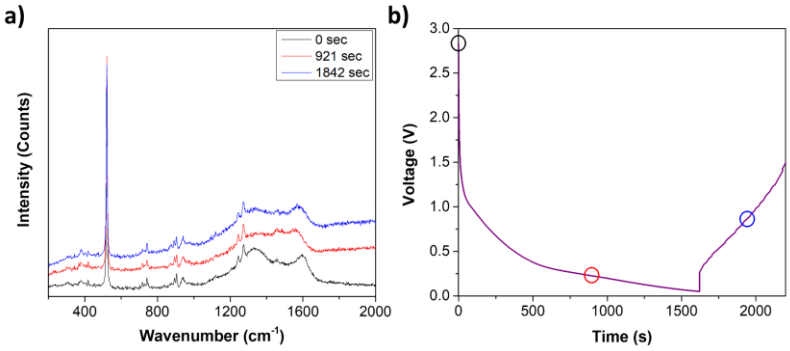

Figure 75: a) Stratified in-situ Raman spectra during lithiation and delithiation of the graphite shell and b) the charge/discharge curve with relevant times marked, illustrating the deformation of the carbon via the shifting D and G peak ratios in the Raman spectra.

Confirmation of the graphite shell expansion was performed through the use of XRD as there is a graphite signal at ~25.5 degrees.[338] To maximize the observation through ex-situ measurements higher surface area materials (20 nm anode materials) were tested. Unsurprisingly, the material with the highest proportion of graphite, 72% Graphite (20 nm), showed the strongest graphite signal and was used to observe the deformation of the

graphitic planes. This was done by discharging one anode, and performing a full discharge/charge cycle on another, then washing both with DMC. These materials were then scanned in air and showed a clear shift in the graphite peak upon lithiation from ~25.0 degrees to ~23.5 degrees, which is similar to what is seen by Y. Reynier et al. with pure graphite at the micron scale.[338] The slight difference between peak position can likely be ascribed to the difference in material scale. Upon delithiation the shift was effectively restored to its original state. Additionally, the crystalline silicon peaks at 28.4 degrees (111), 47.4 degrees (220), and 56.0 degrees (311) became amorphous and broad 30.8 degrees while highly lithiated silicon appeared in sharp peaks around 21.0, 21.6, 25.0 and 40 degrees which have also been observed by S. Iwamura et al.[339] These effects can be seen in Figure 76 a and b, while TEM of the 72% Graphite (20 nm) can be seen in Figure 76c.

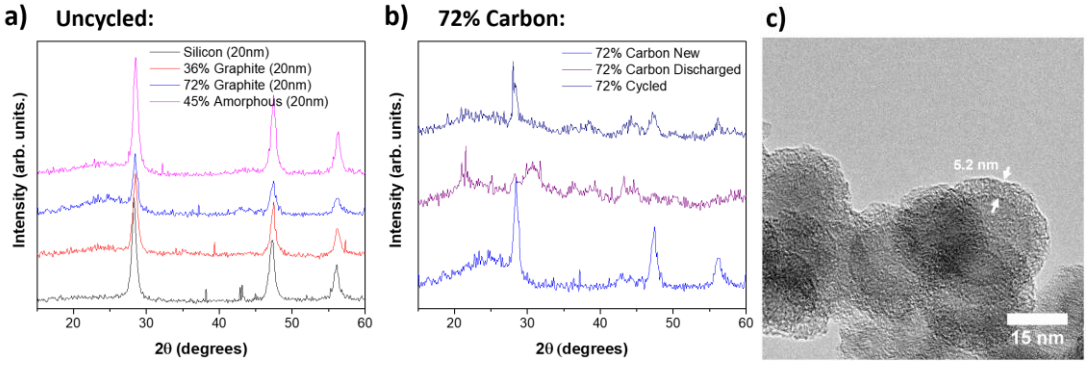

Figure 76: a) XRD scan of uncycled anodes with active material of 20 nm silicon containing differing shell thicknesses and structures. Using the sample with the strongest graphite signal at 25 degrees a comparison of b) XRD spectra of DMC washed anodes after a discharge and charge cycle and c) TEM images of the 72% Graphite (20 nm) material scanned.

As a final interesting point, it appears that the silicon partially re-crystallizes after delithiating as it regains its distinctive (111), (220), and (311) peaks. The carbon shells

around silicon nanomaterials were generally viewed as a method of enhancing charging and more recently mediating SEI growth, but this data demonstrates that even thin shells of low surface area graphite coatings have an observable direct impact on overall material capacity.

3.4.4 – Summary:

Using the techniques developed in section 1.4 for silicon synthesis and section 3.2 for carbon-coating a series of silicon-core carbon shelled materials were made with varying shell thicknesses and degrees of graphitization. These materials were electrochemically tested and using 5 cycles at C/10 as the standard SEI forming conditions underwent a series of ex-situ analysis demonstrating the complications of constantly changing electrolyte chemistries for wet samples, the overpowering dried electrolyte chemistries for dried samples, and the apparent loss of SEI components in DMC washed samples. Combination of in-situ and ex-situ Raman measurements suggest that SEI species could potentially be fluorescent, though more work is needed to make any conclusive statements. Finally, clear observations of graphite coatings lithiating and delithiating during electrochemical cycling were made on both in-situ Raman and with XRD spectroscopy. This shows that not only is a graphitic carbon shell beneficial for electrochemical stabilization, but it also contributes to the overall material capacity.

Section 4: Mask Decontamination and Energetic Materials

4.1 – Facemask Decontamination via Plasma-Produced Forced Ozone Convection[8]

The COVID-19 crisis has taken a significant toll on human life and the global economy since its start in early 2020. Healthcare professionals have been particularly vulnerable because of the unprecedented shortage of Facepiece Respirators (FPRs), which act as fundamental tools to protect the medical staff treating the coronavirus patients. In addition, many FPRs are designed to be disposable single-use devices, creating an issue related to the generation of large quantities of non-biodegradable waste. In this contribution, a plasma-based decontamination technique designed to circumvent the shortages of FPRs and alleviate the environmental problems posed by waste generation is demonstrated. The system utilizes a Dielectric Barrier Discharge (DBD) to generate ozone and feed it through the fibers of the FPRs. The flow-through configuration is different than canonical ozone-based sterilization methods, in which the equipment is placed in a sealed ozone-containing enclosure without any flow through the mask polymer fibers. This study demonstrates the rapid decontamination of surgical masks using *Escherichia coli* (*E. coli*) and *Vesicular Stomatitis Virus* (VSV) as model pathogens, with the flow-through configuration providing a drastic reduction in sterilization time compared to the canonical approach. It also demonstrates that there is no deterioration in mask structure or filtration efficiency resulting from sterilization. Finally, this decontamination approach can be implemented using readily available tools, such as a plastic box, a glass tube, few 3D printed components, and the high-voltage power supply from a plasma globe toy. The

prototype assembled for this study is portable and affordable, with effectiveness comparable to that of larger and more expensive equipment.

4.1.1 – Motivation and Method:

In the beginning of 2020, COVID-19 rapidly emerged as a global pandemic that has resulted in hundreds of thousands of deaths. Unprepared for this crisis, healthcare professionals experienced a shortage of disposable Personal Protective Equipment (PPE); in particular Facepiece Respirators (FPRs), such as designated N95 masks in the US and the FFP3 respirators in Europe. These respirators are fundamental tools that protect medical personnel caring for COVID-19 patients. Their designations are earned by the ability to filter out 95% and 99% of particulate matter at or above 0.3 microns in size,[340] the scale of an average virion. The response to this disease has been severely compromised by the lack of adequate PPE. Disruptions to the PPE global supply chain have led to month-long delivery times and massive price increases, leaving doctors and nurses unprotected. As manufacturers are called upon to meet demand, healthcare providers have improvised with less effective substitutes.[341] While, based on manufacturer recommendations, the FPRs are single-use PPE and the US Centers for Disease Control and Prevention (CDC) does not formally recommend their decontamination and re-use, it is acknowledged that in these times of scarcity, decontamination might be considered as a good "practical" solution.[342] The development of standardized approaches to decontaminate fibers, restore filtering electrostatic charge, and in general re-use FPRs is necessary to mitigate impact on both humans and the environment due to their future increased use, as the World Health

Organization estimated that a 40% increase of the global PPE supplies will be needed.[343] Existing sterilization methods have been proposed and even adopted in some capacity, though each method appears to have a set of drawbacks or caveats. For example, methods such as autoclaving (steam treatment) and liquid hydrogen peroxide (H_2O_2) saturation tend to deform or destroy the mask.[344,345] Similarly, use of UV irradiation has problems with standardization (wavelength, intensity, etc.) and the pathogen protecting effect of shadows.[344] One promising technique is use of gaseous disinfectant species with current work focusing on H_2O_2 vapor as it has been proven to work, though it is costly and not a particularly rapid process.[344] Meanwhile, plasma reactors operating in air generate significant amounts of reactive gaseous species such as ozone (O_3) and H_2O_2 with minimal heating.[346]

Ozone (O_3) is an allotropic form of oxygen with proven pan-viricidal and bactericidal capabilities. It is already widely employed on an industrial scale for wastewater treatment.[347] Its method of sterilization is due to the limited stability of O_3 (half-life of 22 minutes in room temperature), whereby after a collision it is likely to cause oxidation an organic material with the emission of an O_2 molecule.[345,348] Notably, O_3 has been reported as effective in de-activating other members of the coronavirus family[349,350] and the bacteriophage MS2,[348] a virus previously shown to be more resistant to UV-based disinfection with respect to coronaviruses.[351] Additionally, O_3 can be directly produced from air (e.g. via plasmas or irradiation with UV light) and reconverted into non-hazardous O_2 with the aid of catalytic converters.[350] Therefore, unlike other compounds, O_3 can be readily manufactured with cost-effective approaches at the point-of-use. As a gaseous

sterilization agent, it is a particularly promising option for disinfecting poorly accessible spaces within porous materials, such as FRPs. While both consumer-grade and large-scale O_3 sterilization devices are widely available for deodorizing and sanitizing both rooms and objects, the design of these systems is not optimized for the disinfection of FPRs. In consumer grade O_3 sterilization devices objects are loaded into a sterilization chamber which is then sealed and flooded with O_3. O_3 passively diffuses into the objects and may slowly enter the porous media of an FPR.[348]

This study introduces an efficient and low-cost O_3 disinfection approach specifically designed for FPRs. Compressed air is fed into a cylindrical atmospheric pressure Dielectric Barrier Discharge (DBD) plasma that rapidly produces O_3. The ozone-rich gas flow is then forced through the porous media of the FPR, which is directly connected to the plasma reactor. This method uses a low temperature plasma to produce O_3, thus avoiding thermal degradation of FPRs as the output gas is near room temperature. The efficacy of this method is compared to the canonical method by quantifying the decontamination effectiveness of surgical masks saturated with either *E. coli* or *Vesicular Stomatitis Virus*. These pathogens were chosen due to their safety, availability, and ease of use. Observations on the structure and filtration efficiency of masks post processing are also taken to understand whether this method of sterilization is non-destructive. Finally, this approach is shown to be readily adapted as a low-cost solution by using the power supply of a widely available commercial plasma globe toy, a few 3D printed parts, some steel mesh, and a plastic box, to construct a portable low-power system capable of attaining similar disinfection efficiencies.

4.1.2 – DBD Plasma Reactor for FPR Decontamination:

Figure 77 shows the DBD reactor used for the mask sterilization experiments. The system comprises a quartz tube (10 mm outer diameter; quartz wall thickness 1 mm), an outer copper electrode connected to a DC power supply (Trek High Voltage Amplifier 10/40A/HS connected to a signal generator; 10 kHz sinusoidal wave with amplitude between 1 kV and 10 kV) and a 6 mm stainless steel tube as a grounded electrode. Compressed air is flown through the system at constant rate of 10 slm controlled by a King Instruments flowmeter. The waveform of the discharge voltage V was measured from the output of the power supply while the waveform of the discharge charge Q was recorded using a 20 nF capacitor, serially connected to the grounded electrode. Both V and Q were recorded using a digital oscilloscope (Tektronix AFG320).

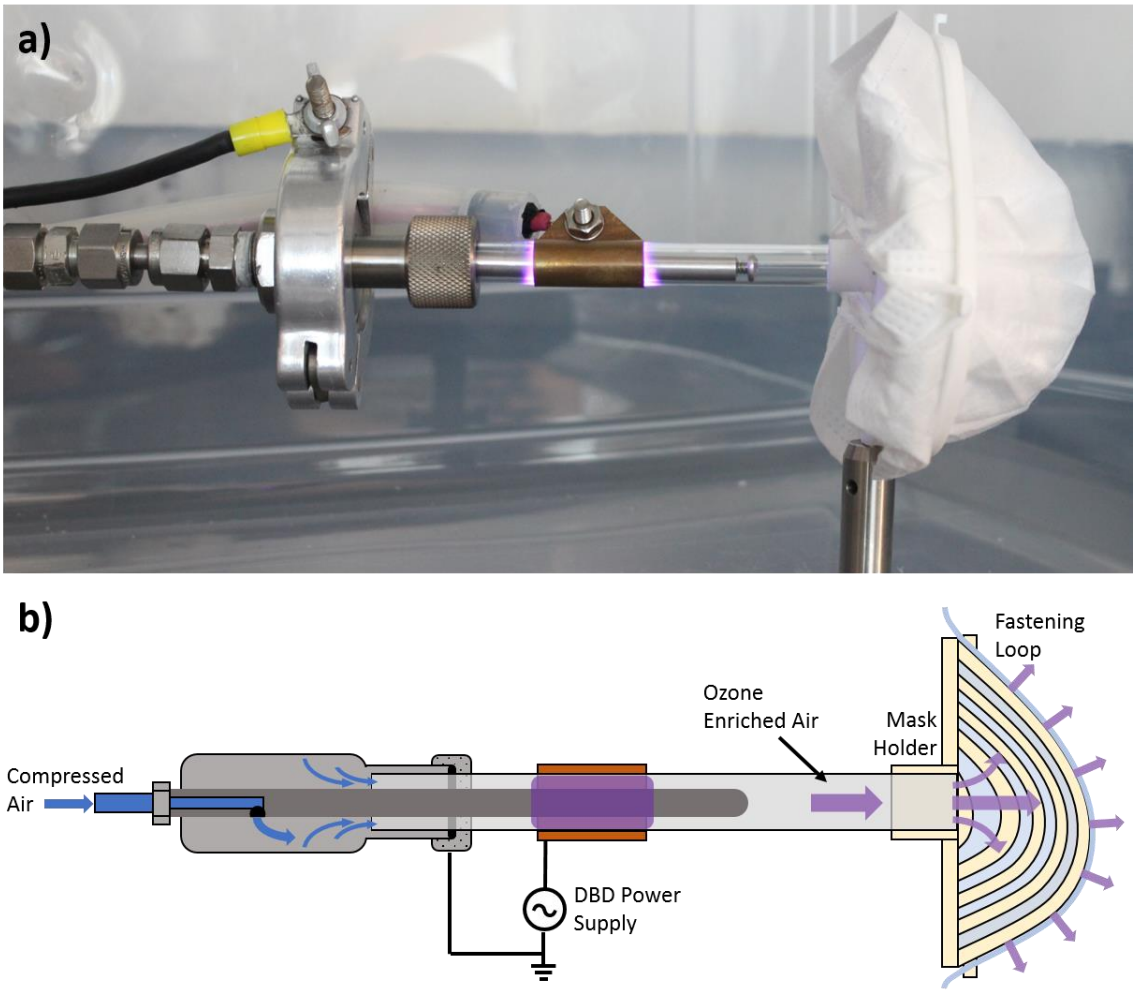

Figure 77: (a) Picture and (b) schematic of the DBD reactor used in the mask sterilization experiments.

4.1.3 – Low-Cost Plasma Reactor for FPR Disinfection:

The power supply from a $25 plasma globe toy (in these experiments a 6-inch Theefun plasma globe) can be used to drive a low-temperature plasma in air to evolve O_3. This is due to the flyback transformer and the timer circuit within the system that produces low-current and high-voltage (1 kV to 6 kV) sawtooth or ramp output signals near or at a frequency of 30 kHz. In order to take advantage of this system, the electrode geometry was

modified so that a steel mesh inside the reactor was powered and the external electrode (now consisting of metallic HVAC tape to further lower material costs) was grounded.

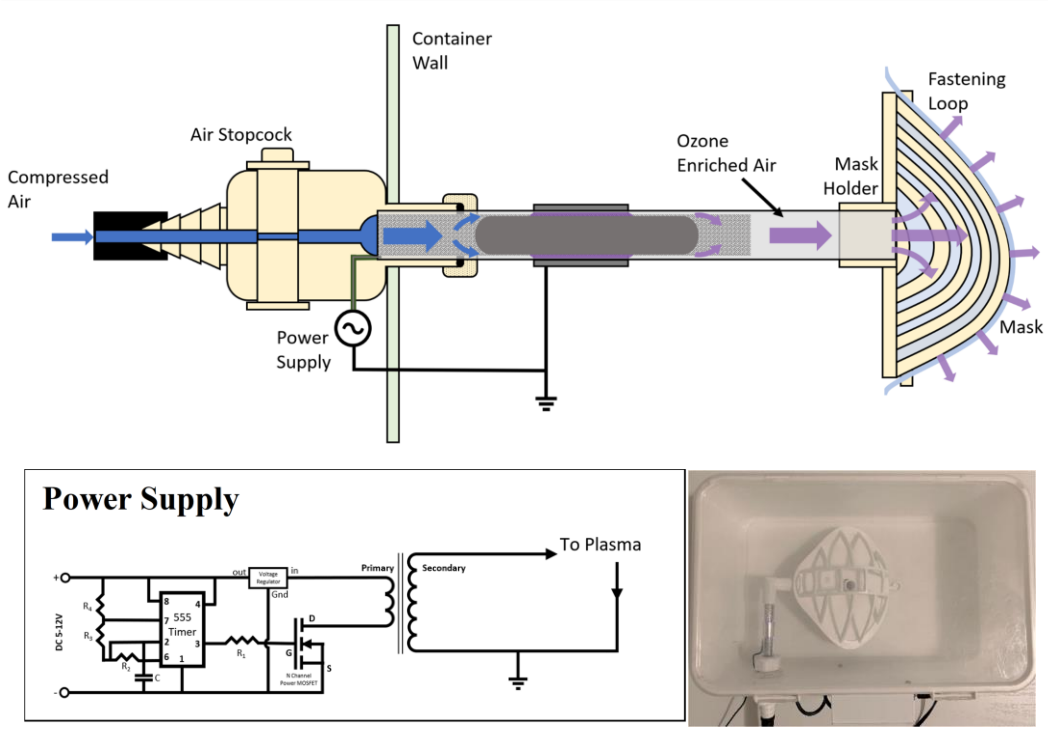

Figure 78: Schematic of cost-effective plasma reactor build by using a commercial toy plasma-ball (top), its simplified circuit diagram (bottom left), and a picture of the system (bottom right).

Additional material was placed within the mesh acting as a flow control, forcing all compressed air to pass through the plasma region. Additionally, a mask holder was 3D printed to direct plasma flow through the mask and minimize leakage. Figure 78 displays this system via a schematic, a picture, and the concurrent circuit diagram. For a more direct comparison between the original and the low-cost system, the same flowmeter was used in both systems, however if implemented the simple 3D-printed stopcock design is able to

effectively act as an imprecise flowmeter. Analysis of the electrical output characteristics of this system was performed in the same way as for the system outlined in section 2.1.

4.1.4 – Gas Composition and Characterization:

The power dissipated in the DBD discharge was characterized following the procedure described by W. Liu et al.[352] Chemical composition of the gas at the outlet of the plasma discharge was measured via an FTIR spectrometer positioned orthogonally to the plasma stream as shown in Figure 79. The reactor was located to one side of a stainless-steel cross connector (KF 25) and, perpendicular to the gas flow, an IR source (Newport 80007) was placed in front of a KBr window. The transmitted light through the gas path was collected after another KBr window by a FTIR spectrometer (Nicolet iS50) (from 800 to 4000 cm^{-1}; 50 cumulative averages). Absorption spectra were measured as a function of voltage discharge from 0 to 10 kV. For each applied voltage, a background was acquired before striking the plasma and subtracted.

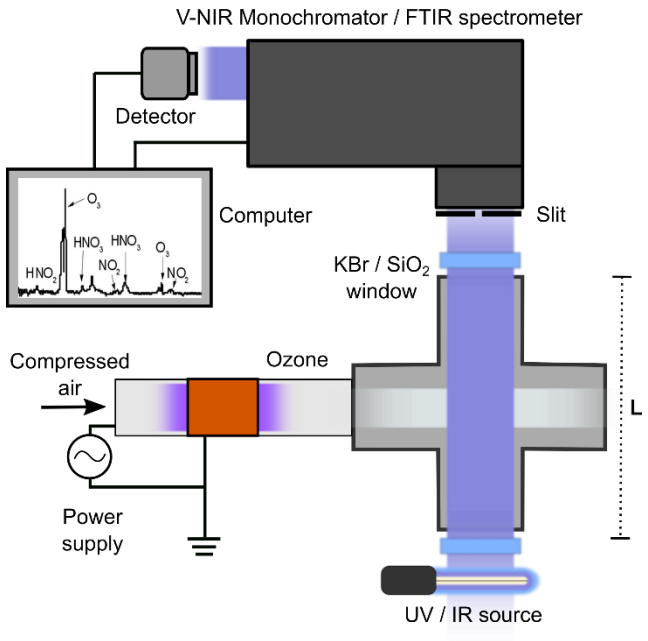

Figure 79: The same system was used to characterize the chemical composition (FTIR spectrometer and IR source) and the ozone concentration (V-INR monochromator and UV lamp) after the plasma discharge.

The concentration of ozone after the plasma discharge was carried out by means of UV absorption spectrum with the same configuration used for the chemical composition measurements (see schematic Figure 3). However, a standard UV lamp (Analytik Jen Pen-Ray 90001201) and V-NR spectrometer (Acton Spectra Pro, Princeton Instruments), connected to a CCD camera, substituted the IR source and the FTIR spectrometer, respectively. The KBr windows were also replaced by SiO_2 ones to minimize UV light absorption before and after the gas optical path.

The signal intensity at λ = 253 nm, where the peak of the ozone absorption cross section is located,[353] was captured by a CCD camera for different discharge voltages from 0 to 10 kV. In addition, the same signal intensity was recorded at different times (from 0 minutes to 64 minutes in steps accordingly to the disinfection times) to study the stability

of the ozone production. These measurements were used to calculate the ozone concentration by Equation 37.[354]

$$C_{oz}[g/m^3] = -\frac{10^6 m_{oz}}{\sigma L N} \ln\left(\frac{I_{oz}}{I_0}\right)$$

Equation 37: Absorption based ozone concentration calculation.

Where I_{oz} and I_o are the intensity of the signal with and without the presence of ozone respectively, L is the distance in cm of the light path inside the gas (in this case 10.5 cm), σ is the absorption cross section of ozone at approximately 12×10^{-18} cm^2, m_{oz} is the atomic mass of ozone and N is the Avogadro's number.[355] For consistency with common presentation of ozone concentration as parts per million (ppm), Equation 1 was multiplied by $10^6 \frac{RT}{m_{air}}$, where R is the ideal gas constant, T is the temperature and m_{air} is the atomic mass of air. These ozone measurements were then confirmed to within 40 ppm through use of FTIR measurements and the method outlined by Petruci et al.[356]

4.1.5 – Quantifying Decontamination Efficacy:

Bacterial Decontamination Efficacy:

All assays were performed using *E. coli* β10 cells transformed and selected for ampicillin resistance and constitutive expression of super-folding green fluorescent protein (sfGFP). For each biological replicate, 50 mL of LB media (1% tryptone, 0.5% yeast extract and 1% NaCl) were grown to saturation overnight at 37˚C with agitation. Surgical masks were inoculated with 200 µL of culture that were spread on defined 1" x 1"

hydrophobic (blue side) regions using sterile scoopulas. Masks were allowed to dry for 60 minutes prior to decontamination.

Inoculated segments were excised from masks using sterile scalpels and placed in sterile 50 mL conical tubes. Masks were suspended in 10 mL sterile water and agitated via pulse vortex for 10 seconds. Cells were extracted from masks via centrifugation at 2147 g (4,000 RPM) for 10 minutes. Pelleted cells were resuspended in solution via pulse vortex for 10 seconds. LB agar plates containing 100 μg/mL ampicillin were inoculated using 200 μL of resuspended cellular solution. Each mask was used to inoculate three agar plates as technical triplicates. Agar plates were incubated at 37˚C for 16 hours before green fluorescence imaging using a ChemiDoc MP imaging system (Bio-Rad Laboratories, Hercules, CA).

Sterilization kinetics were modelled as the percent of colony forming units (CFUs) relative to control values. Control masks were placed on the mask holder with the device powered off for 16, 32, or 64 minutes, while treated masks underwent the same time increment testing with the device powered on. CFUs were counted from fluorescent images using custom MATLAB scripts (MATLAB 2019b; MathWorks, Natick, MA). Control CFUs were calculated as the mean of three biological replicates, and time point measurements are presented as the percent control CFU. Decontamination was modelled as the sum of two exponential decays fit by non-linear least-squares regression in R. Confidence intervals were calculated using a parametric bootstrap with 5,000 sample draws.

Efficacies for different sterilization configurations were determined by comparing CFUs on surgical masks after 32 minutes of sterilization. These configurations included passive sterilization (O_3 flooded box), flow-through DBD, and low-cost flow-through DBD. Negative controls were performed by leaving inoculated masks in the passive O_3 reactor in the absence of O_3 for the prescribed amount of time.

A similar experiment was performed using the low-cost flow-through DBD system to decontaminate surgical masks, KN95 FPRs, and cloth facemasks for 32 minutes. This experiment allowed for the observation of decontamination efficacies on different mask types. Negative controls were treated identically to their treated counterparts but were not exposed to O_3.

Viral Decontamination Efficacy:

Vesicular Stomatitis Virus (VSV), SARS, and COVID-19 are all enveloped, single strand RNA viruses of approximately the same size (60-200 nm)[357,358] and possess comparable viabilities with alternate sterilization methods.[359,360] VSV was chosen as a functional surrogate to COVID-19 for these similarities, researcher safety concerns, and rapid experimental completion.[344] For our experiments, VSV was replication deficient and expressed Green Fluorescent Protein (VSVΔG*/GFP-G). This allowed for high throughput monitoring of infectivity using flow cytometry to calculate the percentage of cells expressing GFP.

The day prior to face mask inoculation 10,000 BHK cell per well in 50 μL were seeded in flat-bottomed 96 well plates. On the day of inoculation, 200 μL of VSVΔG*G-

GFP stock (9×10^7 IU/mL in D10 media) was spread on defined 1" × 1" hydrophobic (blue side) regions of a face mask using sterile scoopulas. Masks were allowed to dry for 60 minutes followed by designated plasma treatment. Inoculated segments were excised from masks using sterile scalpels and placed in sterile 50 mL conical tubes containing 5 mL D10. The mask segment was soaked and mixed for 5 minutes. 100 μL of media from the conical tube was then add to a well of BHK cells (performed in triplicate). The following day, BHK cells were assessed for GFP positive cells using flow cytometry. Briefly, cells were trypsinized, washed with PBS, then resuspended and analyzed using MACSQuant. Titer (TU, transducing units) was calculated according to Equation 38:

$$TU = \left(P\frac{N}{100\,V}\right)TV$$

Equation 38: Transducing units calculation for E. coli quantification.

where P = % GFP+ cells, N = number of cells at time of transduction = 20000, V = volume of dilution added to each well = 0.1 mL, and TV = total volume = 5 mL. TU was zeroed using negative control values. Using the low cost DBD system the same exposure protocol was used for the viral testing as was implemented for the E. coli. Namely, control samples at 16, 32, and 64 minutes, undergoing attachment to the facemask holder without activating the device, while treated facemasks underwent the same process with the device on.

Mask Sterilization and Assessment of Structural Integrity:

Initial observations on the sterilization process' effect on overall structural integrity of the fibers of a medical mask was performed with an optical microscope. A medical mask was analyzed with an optical microscope before and after 64 minutes of ozone treatment

(the mask was marked in its center with a sharpie enabling to perform the analysis in a fixed position on the surface of the mask). After observing for alterations in mask structure the question of whether mask filtration efficiency was altered becomes dominant. To test this, Nelson Labs LLC, a 3rd party contractor, was used to perform Sodium Chloride Aerosol Test to determine filtration efficiency on three sets of identical KN95 masks, with each set consisting of masks that had undergone: 30 minute treatment, 60 minute treatment, 120 minute treatment, and an untreated control. This filtration test is the industrial standard and is performed by generating neutralized polydisperse aerosol particles of NaCl and passing them through the facemask in question. Efficiency is then found by comparing the measured concentration of salt against the challenge concentration, while additional measurements of airflow resistance is also taken. It should be noted that this method provides limited insight into which particle size in the polydisperse aerosol maximizes mask permeability.

4.1.6 – Results and Discussion:

To determine dissipated power within the DBD discharge, the applied voltage V was measured directly from the output of the power supply, while the current flowing through the electrodes was estimated by measuring the charge Q accumulated on a 20 nF measuring capacitor C_M serially connected to the grounded electrode. The Lissajous figure of the DBD discharge was obtained by plotting the measured Q-V characteristics (see Figure 80a) and the power dissipated in the discharge was estimated from its area S and discharge frequency f using Equation 39 (see Figure 80b).[352]

$$Power\ (W) = f\ C_M S$$

Equation 39: Power consumption via Lissajous figure calculation

The reactor starts coupling a measurable amount of power around 4 kV, linearly increasing with the applied voltage above this threshold (see Figure 80b). Fourier Transform Infrared Spectroscopic (FTIR) analysis of the gas produced by the DBD discharge corresponds with the appearance of the typical features of ozone (1055 cm^{-1}, 1030 cm^{-1}, 2098 cm^{-1}, and 2121 cm^{-1}) with voltages near and above 4 kV (see Figure 80c).[361] In air fed DBDs O_3 production is initiated in the plasma phase by the electron impact dissociation of O_2 into atomic O (see Equation 40). O quickly reacts with O_2 molecules to form O_3 via three-body collision (see Equation 41, being M a third-body collision partner).[362,363]

$$O_2 + e \rightarrow O + O + e$$

Equation 40: Dissociation of O_2 via electron collision.

$$O + O_2 + M \rightarrow O_3 + M$$

Equation 41: Ozone formation via third-body collision.

Other smaller contributions corresponding to N_xO_y species, such as N_2O_5 (1250 cm^{-1} and 1720 cm^{-1}) and NO_2 (1600 cm^{-1} and 1627 cm^{-1}), are observed in the spectra.[361] It is worth mentioning that these compounds as well as H_2O_2, and reactive molecular radicals are also sterilizing agents produced through the electrical breakdown of air. However, the reactors described in this work do not permit contact of plasma and the facemask which restricts active sterilization being done by longer lived reactive molecules such as O_3. Finally, a sharp feature around 1360 cm^{-1} was found to be an artifact, attributed to the O_3-

induced oxidation of the KBr windows. To demonstrate this, a series of FTIR over few minutes after switching off the plasma were conducted (Figure 80d). While the ozone contribution disappears over time, it is observed that peak around 1360 cm^{-1} remained unchanged and is hence not related to any gaseous species produced by the plasma discharge.

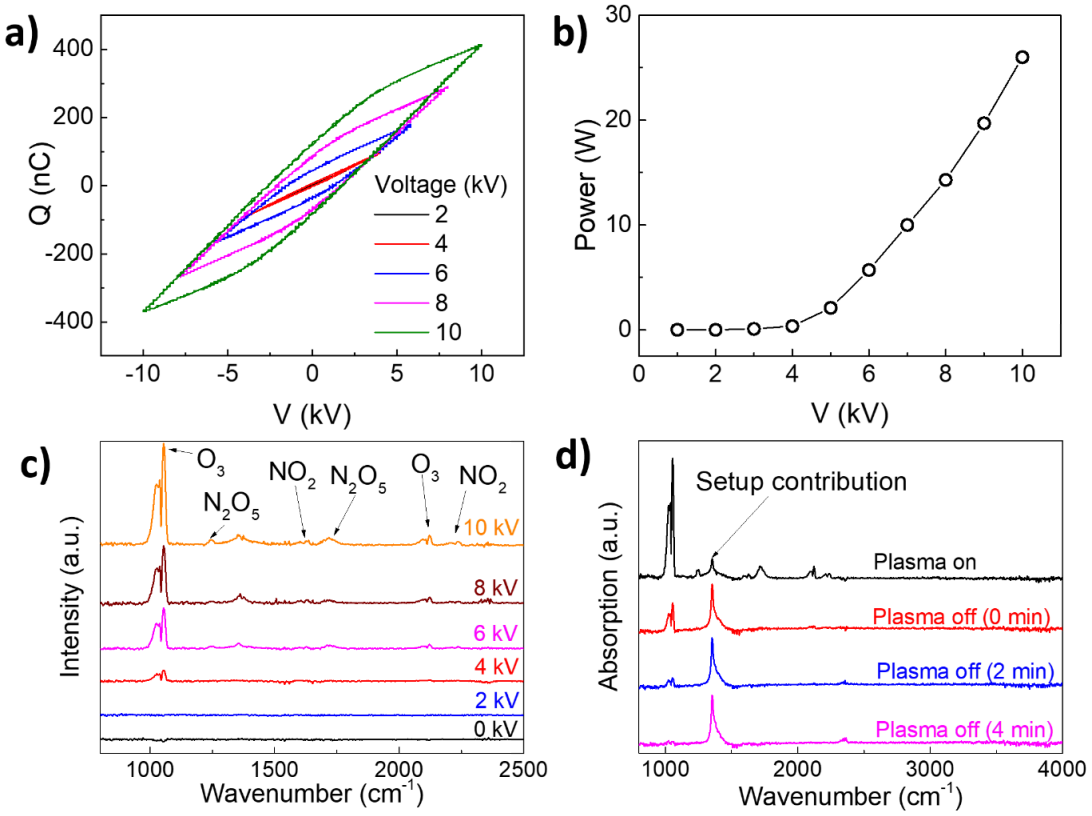

Figure 80: (a) Lissajous Figure as a function of applied voltage, (b) coupled power and (c) FTIR measured downstream of the reactor as a function of applied voltage. (d) FTIR measurement downstream of the plasma reactor in plasm-on condition, right after switching off the plasma, after 2 minutes and after 4 minutes.

The concentration of O_3 produced by the DBD discharge as a function of the applied voltage was measured via UV absorption spectroscopy, as described previously in section 2.3. In the first set of experiments the plasma was ignited at a given voltage and

allowed to stabilize for 4 minutes before acquiring the measurement. Figure 81a shows a linear increase of the gas concentration above 4 kV, reaching a maximum of 750 ppm approximately at 9 kV and slowly decreasing above this voltage. This effect has been detailed in the work of S. Yagi et al. on air-fed DBD discharges.[361] As the power consumption of the discharge increases, the ozone production shows a correspondent gradual increase, reaches a maximum and then begins decreasing. This effect is likely due to the production of NO_x in the plasma discharge that generates catalytic cycles of O_3 destruction (see Equation 42 and Equation 43).

$$O + NO_2 \rightarrow NO + O_2$$

Equation 42: Production of NO via oxygen radicals.

$$NO + O_3 \rightarrow NO_2 + O_2$$

Equation 43: Destruction of ozone via NO.

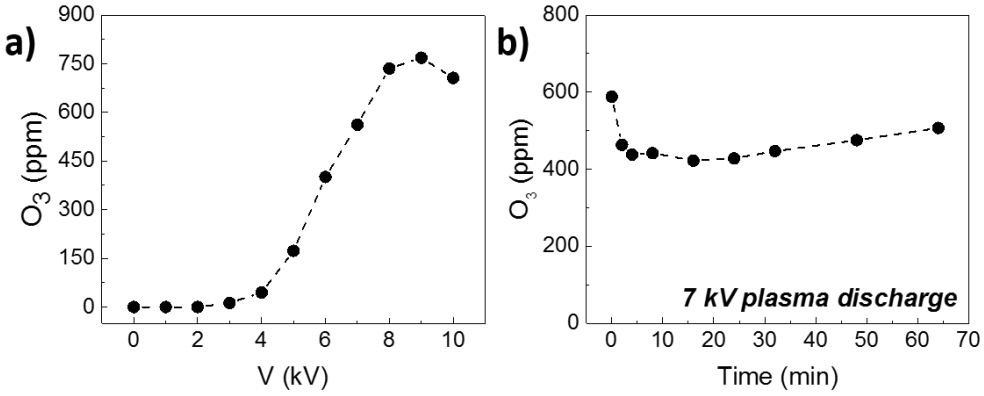

Figure 81: (a) Ozone concentration as a function of DBD plasma discharge voltage. (b) Ozone concentration as a function of time (maximum disinfection time) for 7 kV applied voltage.

For the following sterilization experiments with the DBD system, the applied voltage was held at 7 kV as increasing plasma instability was observed above this value. The ozone concentration was sampled over a period of 64 minutes at 7 kV, to study the overall stability of the DBD production process. As depicted in Figure 81b, after roughly 4 min, the quantity of produced O_3 slightly decreases in the first minutes, likely because of the heating of the tube section on which the plasma impinges, but then remains quite stable. On average, the ozone production over 64 minutes is around 453±27 ppm.

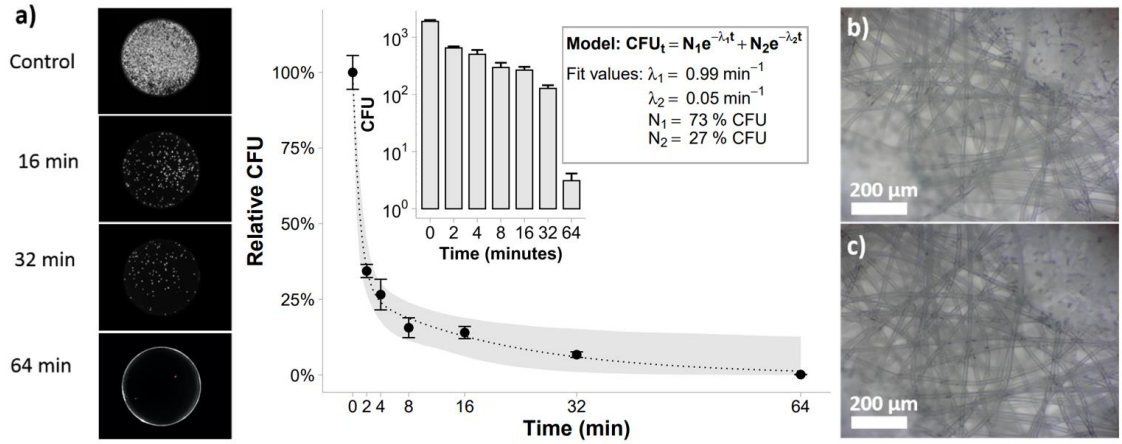

Figure 82: Bacterial sterilization of surgical masks over time. (a) Fluorescent images of colony growth on agar after varying decontamination times are portrayed on the left. The image at 64 minutes (bottom) is overexposed as only a single colony was observed (red). In the scatter plot, each point represents the mean and S.E.M. from three technical replicates that were normalized by their respective control's mean CFU (mean of control's CFU was $10^{3.42}$). Relative CFU were modelled as the sum of two exponential decays. The gray ribbon represents a 95% confidence interval calculated using a parametric bootstrap. After 64 minutes, a $10^{2.78}$ reduction in CFU is observed as illustrated in the inlayed plot. (b) Optical microscope image of mask before decontamination. (c) Optical microscope image of mask after 64 minutes of O_3 sterilization. Major discrepancies in strand formation were not observed.

The sterilization effectiveness was determined using *E. coli* incubated surgical masks (Figure 82). Between 100,000 and 200,000 CFUs were routinely recovered from

control masks. CFUs decreased with increasing exposure time. Notably, the change in CFUs exhibits a biphasic behavior that could be modelled as the sum of two exponential curves. This implies two populations: a fast-dying population with a decay constant λ_1 (see Figure 82a) of 0.99 minutes^{-1} and a mean lifetime of approximately 1 minute, and a slow-dying population with a decay constant λ_2 (see Figure 82a) of 0.05 minutes^{-1} and a mean lifetime of approximately 20 minutes. Across all experiments, a 3:1 ratio (N_1:N_2, see Figure 82a) between fast and slow-dying populations is seen, possibly the slow-dying population has reduced ozone exposure due to fouling from the saturated bacterial culture. This set of experiments indicated that most bacteria are quickly killed over the first few minutes of the disinfection process, and a bacterial reduction greater than three orders of magnitude is achieved within 64 minutes (Figure 82a). Finally, an analysis of the morphology of the medical mask before and after the sterilization process was performed to assess any possible structural damage induced by the O_3 treatment (Figure 82b-c). There was no observable variation of the fiber structure upon sterilization, consistent with the near room temperature operating conditions this method utilizes.

After verifying the effectiveness of the O_3 based decontamination in removing bacteria from surgical masks, characteristics of the low-cost version was tested. The power supply feeds the discharge electrode with a sawtooth signal with frequency equal to roughly 30 kHz and a peak-to-peak amplitude of 5.6 kV, corresponding to a discharge power of 2 W (Figure 83a and Figure 83b). Surprisingly, in this configuration an extremely stable O_3 production with average concentration was observed, in the order of 1000 ppm (Figure 83c-d).

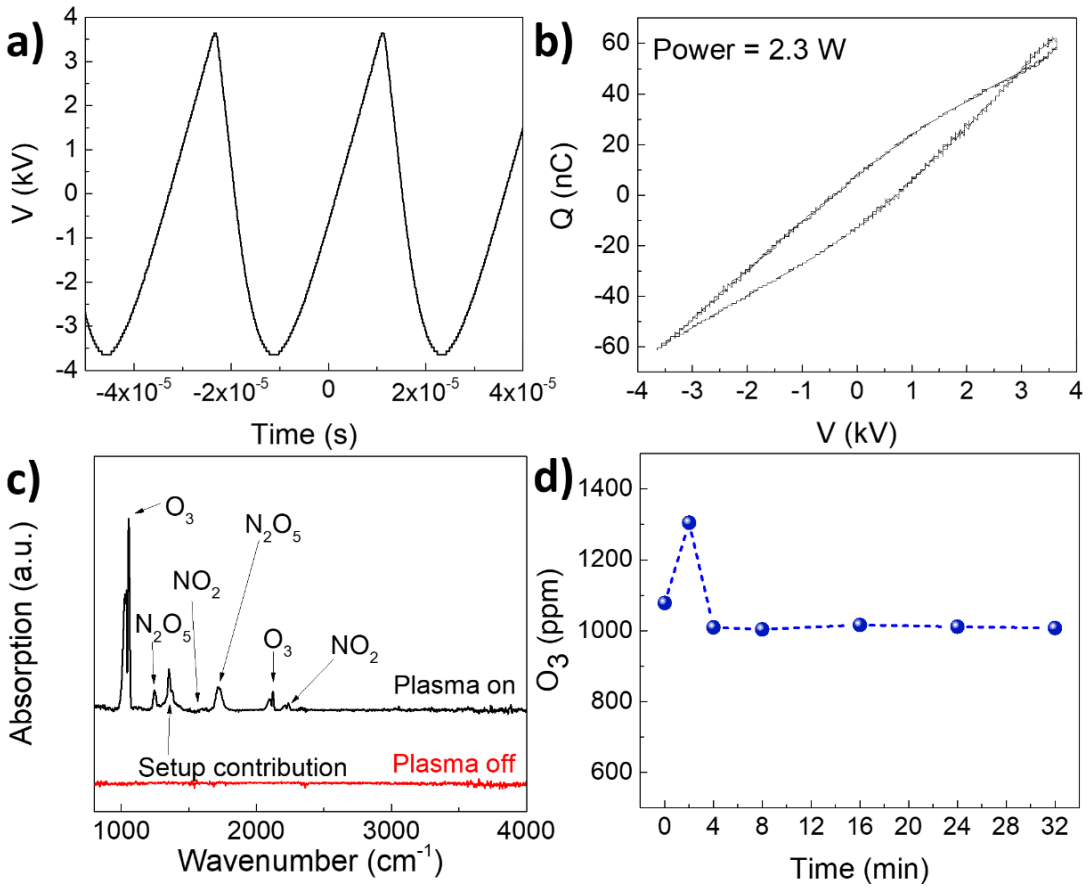

Figure 83: (a) Voltage signal produced by the power supply of the plasma globe. (b) Lissajous Figure of the plasma globe reactor. (c) FTIR analysis of the gas composition produced by the Plasma Globe Reactor and (d) corresponding O_3 concentration produced by the plasma globe reactor as a function of time. An average of 1010 ± 5 ppm along the stability period (4 to 32 minutes).

Finally, the sterilization efficacy of the low cost DBD device was measured for 32 minutes treatment time and compared with the one of the DBD and the more widespread configuration where masks are simply placed in a box that is then flooded with O_3 and left to soak (for this case the mask was simply unplugged from the mask holder and placed in the closed 72 L plastic box containing the plasma reactor; the DBD was operated at 7 kV with compressed air flow rate of 10 slm). A corresponding 429% improvement is seen in

the sterilization efficacy with respect to the standard configuration. Results are summarized in Figure 84**.**

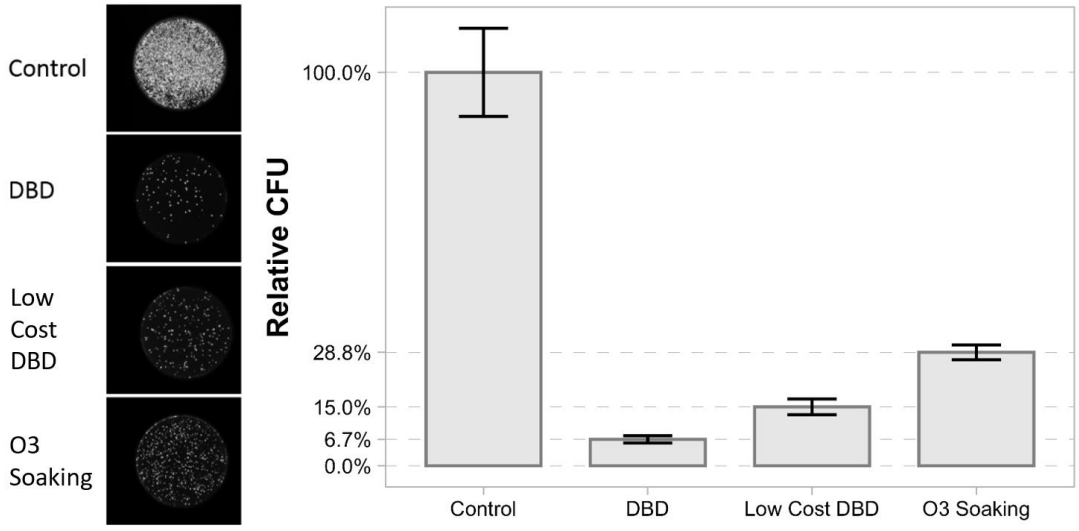

Figure 84: Sterilization efficacy using different sterilization configurations. The left inset shows fluorescent images of colony growth on agar after 32 minutes of sterilization using different configurations. Right graph shows CFU values of different configurations relative to the negative control.

These results provide conclusive evidence that the forced ozone disinfectant method is effective on bacterial pathogens, does not induce structural damage to mask fibers, and can be implemented into a portable configuration using low-cost components. Next, the sterilization efficacy of this scheme is confirmed on a viral pathogen physically comparable to those prompting the use of facemasks (eg. SARS, MERS, COVID-19). For this, VSV with GFP was used and analyzed via flow cytometry. Utilizing the low-cost sterilization setup, sterilization is performed on the same masks for the same time intervals as done with the *E. coli* described in section 2.5. Similarly to the *E. coli*, this test regress on VSV population over time using a two population exponential decay model. Similarly to *E. coli*, it is observed that approximately 68% of the population dies quickly with a 3

second half-life and the remainder die slowly with a near 100 second half-life. Also similar to *E. coli*, sterilization for 64 minutes resulted in a pathogen reduction of greater than two orders of magnitude (shown in Figure 85a).

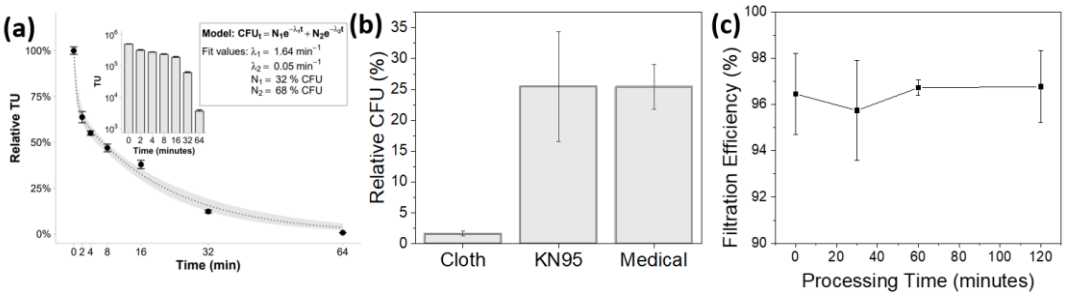

Figure 85: VSV sterilization results (a) VSV sterilization of surgical masks over time. Each point represents the mean and S.E.M. from three biological replicates that were normalized by the control's mean TU (mean of control TU was $10^{5.68}$). Relative TU were modelled as the sum of two exponential decays. The gray ribbon represents a 95% confidence interval calculated using a parametric bootstrap. After 64 minutes, a $10^{2.13}$ reduction in TU is observed as illustrated in the inlayed plot. (b) Sterilization efficacy after 30 minutes using low-cost sterilization system on different mask types. (c) Filtration efficiency of KN95 masks as a function of sterilization time. No significant change in filtration was observed.

Next, this method is shown to be both functional and non-destructive for different mask types. To accomplish this, a side-by-side comparison between medical masks, thick cotton masks, and KN95 masks was performed using the same pathogen and processing conditions as for the *E. coli* time trial, performed with the low-cost sterilization system. Each mask was sterilized for 30 minutes and upon processing has shown the more absorbent masks to have sterilized more rapidly (see Figure 85b). This is likely a result of the cotton fibers having a lower surface tension allowing the viral load to cover more area and as a result be more accessible to the ozone as it flowed through the mask. Finally, this technology does not adversely affect the filtration efficiency of the masks. To test this a series of KN95 masks were exposed to the ozone-rich air stream produced via low-

temperature plasma then underwent blind 3rd party NaCl filtration testing at Nelson Labs. The obtained results show no impact on mask filtration efficiency, as shown in Figure 85c, with the filtration efficiency exceeding the KN95 standard of 95% for all the sterilization durations.

4.1.7 – Summary:

Ozone decontamination of facepiece respirators using this system can be dramatically improved through careful design of the reactor configurations. Specifically, a flow-through configuration where the ozone is passed directly through the porous fiber structure of the mask demonstrated superior sterilization kinetics with respect to the standard approach of an ozone chamber. This method has proven effective against both viral and bacterial pathogens causing a reduction of active pathogens by a minimum of two orders of magnitude within the first hour of processing. Treatment has also proven to be non-destructive to the mask's physical structure and does not reduce filtration efficiency over time. Finally, this method has been demonstrated to be effective when reconstructed for use as a portable single mask sterilization device using low-cost commercially available components (a plasma ball toy, a plastic box, a quartz tube, some steel mesh, HVAC tape, and a few 3D printed parts).

Final Conclusions:

This dissertation has presented work with the central theme of analyzing and utilizing non-thermal plasmas and the silicon nanomaterials it was used to create. By no means is this all of the work that was done during the Ph.D. process or even wholly inclusive of the materials published, but this document does provide a summary of the primary efforts made during the degree and introductions to relevant concepts in hope of being a useful reference for those continuing these lines of research.

Within section 1 the key concepts behind plasmas, non-thermal plasmas, and potential surface interactions were introduced, leading into work done on non-thermal plasma-induced surface-heating measurements. These measurements were taken by developing a new form of in-situ Raman thermometry that continuously subtracts the plasma glow interference through chopping the laser light, while at the same time making use of a custom reactor to impinge plasma onto a heated substrate held in vacuum. This demonstrated that non-thermal plasmas were indeed performing non-convective surface heating, providing a uniform increase in temperature regardless of the initial substrate temperature. Heating effects were confirmed through simulation, while altering gas composition altered both surface-heating and surface-etching as adding hydrogen reduced temperature effects while increasing etching. Following that study was a brief introduction to material synthesis within non-thermal plasmas and an introduction to the standard silicon production setup used throughout this dissertation. This naturally led into a study analyzing the size increase effects of silicon synthesis using plasma discontinuities (pulsing the

plasma). Studying the size effects of pressure changes and different pulse rates showed that increases in pressure do increase material diameter until the plasma becomes filamentary (less glow-like, more lightning-like), while pulsing the plasma only a couple of times while the precursor flows through the reactor can more than triple the diameter without changing the reactor pressure or gas composition. A zero-dimensional simulation was then made (see Appendix A) which modeled particle growth and charging after the steady state size was attained. Despite demonstrating a clear reaction to pulsing, the predicted effect was not large enough to match the experiment and has evidently become the basis for work by other research groups.

Section 2 introduced the use of silicon nanocrystals in quantum dots (QDs), initially explaining the science of QDs, photoluminescence, photon upconversion, and the systems used to create and measure the material, before introducing the studies carried out with it. These studies began with the measuring and modeling exciton flow and balance between transmitter ligand and the silicon nanocrystal sensitizer, demonstrating the sensitivity of the energy transition between the components and providing a framework for designing photon upconverting hybrid inorganic-organic QD systems. The unfortunate limitation of these QD systems is their sensitivity to oxygen, which quenches exciton transfer and alters the silicon core chemistry. The next study tests methods of air-stabilization through use of multiple ligand lengths, inducing polymers, changing the fluid the QDs were suspended in, and finally putting all of the learnings together demonstrating that micelles using oily oxygen resistive materials in concert with polymerizing long-chain ligands enables upconversion signals in an oxygen rich environment that lasts for days instead of minutes.

The process of preparing these materials is time intensive and though promising for multiple applications, unless high quality QDs could be produced with an optimized surface chemistry rapidly the research would have limited use. With this in mind, a method of in-flight plasma-induced partial functionalization of the silicon QDs was implemented, controlling the amount of transmitter ligands by restricting the surface availability through the alkyl-chain ligands that enable solubility. As a result, a more rapid process was developed that demonstrated maximizing transmitter ligand to alkyl chain ligand surface coverage of the silicon QD maximizes upconversion, with this method even setting the upconversion record for this type of hybrid quantum dot material at the time of publishing.

Moving from upconverting light with plasma produced silicon quantum dots to powering lights though silicon-based batteries, section 3 increases the size of the plasma produced silicon nanocrystals to study next generation lithium-ion battery anode materials. Silicon was identified as a candidate for the next evolution of lithium-ion battery anodes almost as soon as lithium-ion batteries were put into production. However, silicon unless beneath 150 nm would fracture under the stress of lithiation and even when small enough to avoid that fate, problems of electrical conductivity and uncontrolled solid electrolyte interphase (SEI) growth prevent adoption. An introduction to the topic is again provided to clarify any initial questions, while also explaining the method of cell construction and electrochemical testing implemented. To overcome the issue of conductivity layers of carbon coating silicon structures have been regularly implemented under the assumption that degree of graphitization would make little to no difference. A method to test this assumption was developed as a two-step carbon coating and graphitizing process which

demonstrated not only was there an observable difference in cycling performance, but also an apparent reduction in SEI growth as well as increased structural strength and lithiation rate capacity via in-situ TEM of the lithiation process. As carbon-coating structure matters, the next part of the carbon-coated silicon nanoparticle anode generally assumed to provide the same performance was the silicon core. Through both literature review and lab-experiments it was shown that different silicon production methods produce different silicon structures with differing oxygen contents and size distributions, which of course perform differently as anode materials even if the material label is the same. From the coating study the apparent resistance of the SEI layer developing on the active material surface decreased with graphitization. This led to the question of whether SEI growth is influenced by material surface chemistry, which in-turn led to measurements of differently coated materials through in-situ Raman and ex-situ FTIR. These ex-situ measurements appear to show a reduction in SEI signal through FTIR while XPS data was less clear. Fluorescence during in-situ Raman restricted what could be learned, however deformation in the graphite shell during lithiation was observed occurring separately of the silicon, implying the carbon-shell itself contributes directly to the material's charge capacity.

The systems above have demonstrated non-thermal plasma's utility in nanomaterial synthesis, while unfortunately requiring costly systems and expensive precursor gasses to be used. However, utilizing non-thermal plasmas for real-world applications does not require costly equipment as demonstrated by the final study. Production of ozone and other reactive gasses for the purposes of sterilization is not a new concept, but limited effort has been spent on decontamination of facepiece respirators (FPRs) with this technique. Forcing

air through a dielectric barrier discharge plasma formed ozone and NOx compounds that proved capable of decontaminating FPRs quickly and effectively. After measuring the output ozone and optimizing the discharge conditions, the process was adapted to an extremely low-cost system (~$25) and demonstrated to quickly decontaminate masks with K95 ratings without impacting the filtering efficiency.

Hopefully this dissertation has shown the versatility of non-thermal plasmas while exposing how there is much more to learn about them and do with them. Work expanding on these studies will continue. As silicon QDs evolve into even more efficient optoelectronic materials that can operate in real-world conditions and become faster to produce it is likely that they will be introduced commercially. Similarly, silicon nanomaterials are already being implemented into batteries and these learnings will likely evolve to increase cell quality (even during these studies we patented the techniques and built our own company to improve commercial batteries). Plasma as a method of medical treatment or sterilization, though currently expensive can be made affordable with the principles demonstrated here. In conclusion, non-thermal plasmas have a profound amount of untapped potential applications while maintain a mystery allowing for extensive fundamental mechanistic studies. This field of science and its engineering applications will in all likelihood continue to evolve and change our lives as it has been doing for nearly a century.

Bibliography:

1. Berrospe-Rodriguez, C. *et al.* Interaction between a Low-Temperature Plasma and Graphene: An in situ Raman Thermometry Study. *Phys. Rev. Appl.* **15**, 1 (2021).

2. Schwan, J., Wagner, B., Kim, M. & Mangolini, L. Controlled growth of silicon particles via plasma pulsing and their application as battery material. *J. Phys. D. Appl. Phys.* **55**, 094002 (2022).

3. Huang, T. *et al.* Bidirectional triplet exciton transfer between silicon nanocrystals and perylene. *Chem. Sci.* **12**, 6737–6746 (2021).

4. Xia, P., Schwan, J., Dugger, T. W., Mangolini, L. & Tang, M. L. Air-Stable Silicon Nanocrystal-Based Photon Upconversion. *Adv. Opt. Mater.* **9**, 1–6 (2021).

5. Schwan, J., Wang, K., Tang, M. L. & Mangolini, L. Gas-phase grafting for the multifunctinoal surface modification of silicon quantum dots. *Nanoscale* (2022) doi:10.1039/d2nr04902c.

6. Nava, G., Schwan, J., Boebinger, M. G., McDowell, M. T. & Mangolini, L. Silicon-Core-Carbon-Shell Nanoparticles for Lithium-Ion Batteries: Rational Comparison between Amorphous and Graphitic Carbon Coatings. *Nano Lett.* **19**, 7236–7245 (2019).

7. Schwan, J., Nava, G. & Mangolini, L. Critical barriers to the large scale commercialization of silicon-containing batteries. *Nanoscale Adv.* **2**, 4368–4389 (2020).

8. Schwan, J. *et al.* Efficient facemask decontamination via forced ozone convection. *Sci. Rep.* **11**, 1–11 (2021).

9. Britannica, T. E. of E. Plasma Summary. *Encyclopedia Britannica* https://www.britannica.com/summary/plasma-state-of-matter (2003).

10. Laroussi, M. Plasma Medicine : A Brief Introduction. *Plasma* **1**, 47–60 (2018).

11. Chen, F. F. *Introduction to Plasma Physics and Controlled Fusion*. *Introduction to Plasma Physics and Controlled Fusion* (Plenum Press, 1974). doi:10.1007/978-3-319-22309-4.

12. Lilley, B. S., Potter, S. & Kelley, M. C. Plasma. *Encyclopedia Britannica* https://www.britannica.com/science/plasma-state-of-matter (2022).

13. Hariharan, S. J., Vigneshwar, M., Selvamani, S. T. & Shanmugam, K. Optimizing the Plasma Arc Welding Process Parameters to Attain the Minimum Corrosion Rate in the AISI 409M grade Ferritic Stainless Steel Autogenous Joints. *Mater. Today Proc.* **16**, 1259–1270 (2019).

14. Townsend, M. A. Electronics of the Fluorescent Lamp. *IEEE* **61**, (1942).

15. Poulsen, R. G. Plasma etching in integrated circuit manufacture — A review. **14**, 266–274 (1977).

16. Weber, L. F. History of the Plasma Display Panel. *IEEE Trans. Plasma Sci.* **34**, 268–278 (2006).

17. Meyer, R. X. A space-charge-sheath electric thruster - Meyer.pdf. *AIAA J.* **5**, 2057–2059 (1967).

18. Matveev, I. B., Serbin, S. I. & Washchilenko, N. V. Plasma-Assisted Treatment of Sewage Sludge. *IEEE Trans. Plasma Sci.* **44**, 3023–3027 (2016).

19. Adamovich, I. *et al.* The 2017 Plasma Roadmap : Low temperature The 2017 Plasma Roadmap : Low temperature plasma science and technology. *J. Phys. D. Appl. Phys.* **50**, (2017).

20. Lieberman, M. A. & Lichtenberg, A. J. *Principles of Plasma Discharges and Materials Processing*. (John Wiley & Sons, 2005).

21. Gibbon, P. Introduction to Plasma Physics. *Proc. CAS-CERN Accel. Sch. Plasma Wake Accel.* **001**, (2016).

22. Mangolini, L. & Kortshagen, U. Selective nanoparticle heating: Another form of nonequilibrium in dusty plasmas. *Phys. Rev. E - Stat. Nonlinear, Soft Matter Phys.* **79**, 1–8 (2009).

23. Lopez, T. & Mangolini, L. On the nucleation and crystallization of nanoparticles in continuous-flow nonthermal plasma reactors. *J. Vac. Sci. Technol. B* **32**, 061802 (2014).

24. Bonizzoni, G. & Vassallo, E. Plasma physics and technology; industrial applications. *Vacuum* **64**, 327–336 (2002).

25. Colonna, G. & Kustova, E. Editorial : Thermal and Non-Thermal Plasmas at Atmospheric Pressure. *Front. Phys.* **10**, 10–12 (2022).

26. Union, I. T. *ARTICLE 1 Terms and definitions*. (2009).

27. Lafleur, T., Schulze, J. & Donko, Z. Plasma-surface interactions. *Plasma Sources Sci. Technol.* **28**, (2019).

28. Adam, J. Review of Tokamak plasma heating by wave damping in the ion cyclotron range of frequency. *Plasma Phys. Control. Fusion* **29**, 443–472 (1987).

29. Walton, S. G. *et al.* Plasma-surface interactions in atmospheric pressure plasmas: In situ measurements of electron heating in materials. *J. Appl. Phys.* **124**, (2018).

30. Graves, D. B. & Humbird, D. Surface chemistry associated with plasma etching processes. *Appl. Surf. Sci.* **192**, 72–87 (2002).

31. Chiao, M. *Encyclopedia of Microfluidics and Nanofluidics*. *Encyclopedia of Microfluidics and Nanofluidics* (2015). doi:10.1007/978-1-4614-5491-5.

32. Lieberman, M. A. & Lichtenberg, A. J. *Principles of Plasma Discharges and Materials*. (John Wiley & Sons, 1994).

33. Lee, C. G. N., Kanarik, K. J. & Gottscho, R. A. The grand challenges of plasma etching: A manufacturing perspective. *J. Phys. D. Appl. Phys.* **47**, (2014).

34. Schwan, J., Wang, X., Hsu, H. W., Grün, E. & Horányi, M. The charge state of electrostatically transported dust on regolith surfaces. *Geophys. Res. Lett.* **44**, 3059–3065 (2017).

35. Oehrlein, G. S. & Lee, Y. H. Reactive ion etching related Si surface residues and subsurface damage: Their relationship to fundamental etching mechanisms. *J. Vac. Sci. Technol. A Vacuum, Surfaces, Film.* **5**, 1585–1594 (1987).

36. Coburn, J. W. Role of ions in reactive ion etching. *J. Vac. Sci. Technol. A Vacuum, Surfaces, Film.* **12**, 1417–1424 (1994).

37. Gasvoda, R. J., Zhang, Z., Wang, S., Hudson, E. A. & Agarwal, S. Etch selectivity during plasma-assisted etching of SiO 2 and SiN x : Transitioning from reactive ion etching to atomic layer etching . *J. Vac. Sci. Technol. A* **38**, 050803 (2020).

38. Rai, V. R., Vandalon, V. & Agarwal, S. Surface reaction mechanisms during ozone and oxygen plasma assisted atomic layer deposition of aluminum oxide. *Langmuir* **26**, 13732–13735 (2010).

39. Kwon, O. S. *et al.* Dual-color emissive upconversion nanocapsules for differential cancer bioimaging in vivo. *ACS Nano* **10**, 1512–1521 (2016).

40. Nozaki, T., Muto, N., Kado, S. & Okazaki, K. Dissociation of vibrationally excited methane on Ni catalyst: Part 1. Application to methane steam reforming. *Catal. Today* **89**, 57–65 (2004).

41. Kim, H. M., Sun, H. H., Belharouak, I., Manthiram, A. & Sun, Y. K. An Alternative Approach to Enhance the Performance of High Sulfur-Loading Electrodes for Li-S Batteries. *ACS Energy Lett.* **1**, 136–141 (2016).

42. Liu, T. *et al.* Direct, Transfer-Free Growth of Large-Area Hexagonal Boron Nitride Films by Plasma-Enhanced Chemical Film Conversion (PECFC) of Printable, Solution-Processed Ammonia Borane. *ACS Appl. Mater. Interfaces* **10**, 43936–43945 (2018).

43. Nan, H., Zhou, R., Gu, X., Xiao, S. & Ostrikov, K. K. Recent advances in plasma modification of 2D transition metal dichalcogenides. *Nanoscale* **11**, 19202–19213 (2019).

44. Liu, T. *et al.* Plasma-Induced Fabrication and Straining of MoS2 Films for the Hydrogen Evolution Reaction. *ACS Appl. Energy Mater.* **2**, 5162–5170 (2019).

45. Childres, I., Jauregui, L. A., Tian, J. & Chen, Y. P. Effect of oxygen plasma etching on graphene studied using Raman spectroscopy and electronic transport measurements. *New J. Phys.* **13**, (2011).

46. Coleman, D., Lopez, T., Yasar-Inceoglu, O. & Mangolini, L. Hollow silicon carbide nanoparticles from a non-thermal plasma process. *J. Appl. Phys.* **117**, (2015).

47. Exarhos, S., Alvarez-Barragan, A., Aytan, E., Balandin, A. A. & Mangolini, L. Plasmonic Core-Shell Zirconium Nitride-Silicon Oxynitride Nanoparticles. *ACS Energy Lett.* **3**, 2349–2356 (2018).

48. Swinkels, G. H. P. M., Kersten, H., Deutsch, H. & Kroesen, G. M. W. Microcalorimetry of dust particles in a radio-frequency plasma. *J. Appl. Phys.* **88**, 1747–1755 (2000).

49. Maurer, H., Basner, R. & Kersten, H. Measuring the temperature of microparticles in plasmas. *Rev. Sci. Instrum.* **79**, (2008).

50. Lopez, T. & Mangolini, L. In situ monitoring of hydrogen desorption from silicon nanoparticles dispersed in a nonthermal plasma . *J. Vac. Sci. Technol. B, Nanotechnol. Microelectron. Mater. Process. Meas. Phenom.* **34**, 041206 (2016).

51. Chávez-Ángel, E. *et al.* Reduction of the thermal conductivity in free-standing silicon nano-membranes investigated by non-invasive Raman thermometry. *APL Mater.* **2**, (2014).

52. Beechem, T., Christensen, A., Graham, S. & Green, D. Micro-Raman thermometry in the presence of complex stresses in GaN devices. *J. Appl. Phys.* **103**, (2008).

53. Li, X. *et al.* Large-area synthesis of high-quality and uniform graphene films on copper foils. *Science (80-.).* **324**, 1312–1314 (2009).

54. Li, X. *et al.* Graphene films with large domain size by a two-step chemical vapor deposition process. *Nano Lett.* **10**, 4328–4334 (2010).

55. Ferrari, A. C. & Robertson, J. Interpretation of Raman spectra of disordered and amorphous carbon. *Phys. Rev. B* **61**, 14095–14107 (2000).

56. Lieber, C. M. *et al.* Electronic transition energy (formula presented) for an isolated (formula presented) single-wall carbon nanotube obtained by anti-Stokes/Stokes resonant Raman intensity ratio. *Phys. Rev. B - Condens. Matter Mater. Phys.* **63**, 6–9 (2001).

57. Peng, H. *et al.* Substrate Doping Effect and Unusually Large Angle van Hove Singularity Evolution in Twisted Bi- and Multilayer Graphene. *Adv. Mater.* **29**, 1–7 (2017).

58. Godyak, V. A. & Piejak, R. B. In situ simultaneous radio frequency discharge power measurements. *J. Vac. Sci. Technol. A* **8**, 3833–3837 (1990).

59. Bellani, S. *et al.* 'ion sliding' on graphene: A novel concept to boost supercapacitor performance. *Nanoscale Horizons* **4**, 1077–1091 (2019).

60. López-Polín, G. *et al.* Increasing the elastic modulus of graphene by controlled defect creation. *Nat. Phys.* **11**, 26–31 (2015).

61. Xie, L., Jiao, L. & Dai, H. Selective etching of graphene edges by hydrogen plasma. *J. Am. Chem. Soc.* **132**, 14751–14753 (2010).

62. Mattox, D. M. Plasmas and Plasma Enhanced CVD. in *The Foundations of Vacuum Coating Technology* 61–86 (2018). doi:10.1016/b978-0-12-813084-1.00003-0.

63. Hedlund, C., Blom, H. -O. & Berg, S. Microloading effect in reactive ion etching. *J. Vac. Sci. Technol. A Vacuum, Surfaces, Film.* **12**, 1962–1965 (1994).

64. Kushner, M. J. A model for the discharge kinetics and plasma chemistry during plasma enhanced chemical vapor deposition of amorphous silicon. *J. Appl. Phys.* **63**, 2532–2551 (1988).

65. *Thin Film Processes II*. (Academic Press, 1991). doi:10.1016/B978-0-08-052421-4.50021-6.

66. Girshick, S. L. Particle nucleation and growth in thermal plasmas. *Plasma Sources Sci. Technol.* **3**, 388–394 (1994).

67. Kortshagen, U. R. *et al.* Nonthermal plasma synthesis of nanocrystals: Fundamental principles, materials, and applications. *Chem. Rev.* **116**, 11061–11127 (2016).

68. Boufendi, L. & Bouchoule, A. Particle nucleation and growth in a low-pressure argon-silane discharge. *Plasma Sources Sci. Technol.* **3**, 262–267 (1994).

69. Perrin, J., Bbhm, C., Etemadi, R. & Lloret, A. Possible routes for cluster growth and particle formation in RF silane discharges. *Plasma Sources Sci. Technol.* **3**, 252–261 (1994).

70. Ravi, L. & Girshick, S. L. Coagulation of nanoparticles in a plasma. *Phys. Rev. E - Stat. Nonlinear, Soft Matter Phys.* **79**, 1–9 (2009).

71. Xiong, Z. *et al.* Particle trapping, size-filtering, and focusing in the nonthermal plasma synthesis of sub-10 nanometer particles. *J. Phys. D. Appl. Phys.* **55**, (2022).

72. Lanham, S. J., Polito, J., Xiong, Z., Kortshagen, U. R. & Kushner, M. J. Pulsed power to control growth of silicon nanoparticles in low temperature flowing plasmas. *J. Appl. Phys.* **132**, (2022).

73. Pickard, D. S. & Leung, K.-N. Matching Network for RF Plasma Source. (2007).

74. Mariotti, D. & Sankaran, R. M. Microplasmas for nanomaterials synthesis. *J. Phys. D. Appl. Phys.* **43**, (2010).

75. Chan, C. K. *et al.* High-performance lithium battery anodes using silicon nanowires. *Nat. Nanotechnol.* **3**, 31–35 (2008).

76. Magasinski, A. *et al.* High-performance lithium-ion anodes using a hierarchical bottom-up approach. *Nat. Mater.* **9**, 353–358 (2010).

77. Yan, Z. & Guo, J. High-performance silicon-carbon anode material via aerosol spray drying and magnesiothermic reduction. *Nano Energy* **63**, 103845 (2019).

78. Liu, X. H. *et al.* Size-dependent fracture of silicon nanoparticles during lithiation. *ACS Nano* **6**, 1522–1531 (2012).

79. Husmann, E., Thimsen, E. & Chen, X. Particle charge distributions in the effluent of a flow-through atmospheric pressure low temperature plasma. *Plasma Sources Sci. Technol.* **30**, (2021).

80. Chen, X. & Hogan, C. J. Nanoparticle dynamics in the spatial afterglows of nonthermal plasma synthesis reactors. *Chem. Eng. J.* **411**, 128383 (2021).

81. Alexandrov, A. L., Schweigert, I. V. & Ariskin, D. A. Kinetic simulations of argon dusty plasma afterglow including metastable atom kinetics. *J. Exp. Theor. Phys.* **116**, 663–672 (2013).

82. Coudel, L., Samarian, A. A., Mikikian, M. & Boufendi, L. Influence of the ambipolar-to-free diffusion transition on dust particle charge in a complex plasma afterglow. *Phys. Plasmas* **15**, (2008).

83. Denysenko, I. *et al.* A global model for the afterglow of pure argon and of argon with negatively charged dust particles. *J. Phys. D. Appl. Phys.* **44**, (2011).

84. Denysenko, I. B., Azarenkov, N. A., Ostrikov, K. & Yu, M. Y. Electron energy probability function in the temporal afterglow of a dusty plasma. *Phys. Plasmas* **25**, (2018).

85. Denysenko, I. B., Stefanović, I., Azarenkov, N. A. & Burmaka, G. P. Effect of secondary emission on the argon plasma afterglow with large dust density. *Phys. Plasmas* **22**, (2015).

86. Stefanovi´, I., Sadeghi, N. & Winter, J. The influence of C2H2 and dust formation on the time dependence of metastable argon density in pulsed plasmas. *J. Phys. D. Appl. Phys.* **43**, (2010).

87. Henriksen, G. L., Amine, K., Liu, J. & Nelson, P. A. *Materials Cost Evaluation Report for High-Power Li-Ion HEV Batteries, Report number ANL-03/5*. *ARGONNE NATIONAL LABORATORY online* vol. 1 http://www.ipd.anl.gov/anlpubs/2003/01/45346.pdf (2002).

88. Vemury, S., Janzen, C. & Pratsinis, S. E. Coagulation of symmetric and asymmetric bipolar aerosols. *J. Aerosol Sci.* **28**, 599–611 (1997).

89. Kortshagen, U. R. & Bhandarkar, U. Modeling of particulate coagulation in low pressure plasmas. *Phys. Rev. E* **60**, 887–898 (1999).

90. Allen, J. E. Probe theory - the orbital motion approach. *Phys. Scr.* **45**, 497–503 (1992).

91. Mott-Smith, H. M. & Langmuir, I. The theory of collectors in gaseous discharges. *Phys. Rev.* **28**, 727–763 (1926).

92. Allen, J. E., Annaratone, B. M. & De Angelis, U. On the orbital motion limited theory for a small body at floating potential in a Maxwellian plasma. *J. Plasma Phys.* **63**, 299–309 (2000).

93. Gatti, M. & Kortshagen, U. Analytical model of particle charging in plasmas over a wide range of collisionality. *Phys. Rev. E - Stat. Nonlinear, Soft Matter Phys.* **78**, 1–6 (2008).

94. McAfee, K. B., Sipler, D. & Edelson, D. Mobilities and reactions of ions in Argon. *Phys. Rev.* **160**, 130–135 (1967).

95. Bogaerts, A. & Gijbels, R. Effects of adding hydrogen to an argon glow discharge: overview of relevant processes and some qualitative explanations. *J. Anal. At. Spectrom.* **15**, 441–449 (2000).

96. Videnović, I. R., Konjevic, N. & Kuraica, M. M. Spectroscopic investigations of a cathode fall region of the Grimm-type glow discharge. *Spectrochim. Acta - Part B At. Spectrosc.* **51**, 1707–1731 (1996).

97. Gerber, R. A. & Gerardo, J. B. Ambipolar-to-free diffusion: The temporal behavior of the electrons and ions. *Phys. Rev. A* **7**, 781–790 (1973).

98. Stefanović, I. *et al.* Secondary electron emission of carbonaceous dust particles. *Phys. Rev. E - Stat. Nonlinear, Soft Matter Phys.* **74**, 1–11 (2006).

99. Le Picard, R. & Girshick, S. L. The effect of single-particle charge limits on charge distributions in dusty plasmas. *J. Phys. D. Appl. Phys.* **49**, (2016).

100. Bronold, F. X., Deutsch, H. & Fehske, H. Physisorption kinetics of electrons at plasma boundaries. *Eur. Phys. J. D* **54**, 519–544 (2009).

101. Hogan, C. J. & Mora, J. F. de la. Tandem ion mobility-mass spectrometry (IMS-MS) study of ion evaporation from ionic liquid-acetonitrile nanodrops. *Phys. Chem. Chem. Phys.* **11**, 7759 (2009).

102. Kramer, N. J., Anthony, R. J., Mamunuru, M., Aydil, E. S. & Kortshagen, U. R. Plasma-induced crystallization of silicon nanoparticles. *J. Phys. D. Appl. Phys.* **47**, (2014).

103. Hawa, T. & Zachariah, M. R. Coalescence kinetics of bare and hydrogen-coated silicon nanoparticles: A molecular dynamics study. *Phys. Rev. B - Condens. Matter Mater. Phys.* **71**, 1–12 (2005).

104. Zachariah, M. R. & Carrier, M. J. Molecular dynamics computation of gas-phase nanoparticle sintering: A comparison with phenomenological models. *J. Aerosol Sci.* **30**, 1139–1151 (1999).

105. Friedlander, S. K. & Wu, M. K. Linear rate law for the decay of the excess surface area of a coalescing solid particle. *Phys. Rev. B* **49**, 3622–3624 (1994).

106. Ornes, S. Quantum dots. *PNAS* **113**, 2796–2797 (2016).

107. Ekimov, A. I., Efros, A. L. & Onushcenko, A. A. QUANTUM SIZE EFFECT IN SEMICONDUCTOR MICROCRYSTALS. *Solid State Commun.* **56**, 921–924 (1985).

108. Rossetti, R., Nakahara, S. & Brus, L. E. Quantum size effects in the redox potentials , resonance Raman spectra , and electronic spectra of CdS crystallites in aqueous solution. *J. Chem. Phys.* **79**, (1983).

109. Efros, A. L. & Efros, A. L. Interband absorption of light in a semiconductor sphere. *Fiz. Tekh. Poluprovodn* **16**, 1209–1214 (1982).

110. Reed, M. A., Bate, R. T. & Bradshaw, K. Spatial quantization in GaAs–AlGaAs multiple quantum dots. *J. Vac. Sci. Technol. B Microelectron. Process. Phenom.* **358**, 79–82 (1993).

111. Huo, M. *et al.* Upconversion Nanoparticles Hybridized Cyanobacterial Cells for Near-Infrared Mediated Photosynthesis and Enhanced Photodynamic Therapy. *Adv. Funct. Mater.* **31**, 1–10 (2021).

112. Wang, C., Thompson, R. L., Ohodnicki, P., Baltrus, J. & Matranga, C. Size-dependent photocatalytic reduction of CO2 with PbS quantum dot sensitized TiO2 heterostructured photocatalysts. *J. Mater. Chem.* **21**, 13452–13457 (2011).

113. Aroutiounian, V., Petrosyan, S., Khachatryan, A. & Touryan, K. Quantum dot solar cells. *J. Appl. Phys.* **89**, 2268–2271 (2001).

114. Qasaimeh, Q., Zhou, W.-D., Bhattacharya, P., Huffaker, D. & Deppe, D. G. Monolithically integrated low-power phototranceiver incorporating InGaAs/GaAs quantum-dot microcavity LED and modulated barrier photodiode. *Electron. Lett.* **36**, (2000).

115. Moon, H., Lee, C., Lee, W., Kim, J. & Chae, H. Stability of Quantum Dots, Quantum Dot Films, and Quantum Dot Light-Emitting Diodes for Display Applications. *Adv. Mater.* **31**, (2019).

116. Culcer, D., Cywiński, Ł., Li, Q., Hu, X. & Das Sarma, S. Quantum dot spin qubits in silicon: Multivalley physics. *Phys. Rev. B - Condens. Matter Mater. Phys.* **82**, (2010).

117. Halsted, R. E., Lorenz, M. R. & Segall, B. BAND EDGE EMISSION PROPERTIES OF CdTe*. *J. Phys. Chem. Solids* **22**, 109–116 (1961).

118. Singh-Rachford, T. N. & Castellano, F. N. Photon upconversion based on sensitized triplet-triplet annihilation. *Coord. Chem. Rev.* **254**, 2560–2573 (2010).

119. Lee, S. W., Mao, C., Flynn, C. E. & Belcher, A. M. Ordering of quantum dots, using genetically engineered viruses. *Science (80-.).* **296**, 892–895 (2002).

120. Nozik, A. J. & Mićić, O. I. Colloidal quantum dots of III-V semiconductors. *MRS Bull.* **23**, 24–30 (1998).

121. Mangolini, L., Thimsen, E. & Kortshagen, U. High-Yeild Plasma Synthesis of Luminescent Silicon Nanocrystals. *Nano Lett.* **5**, 655–659 (2005).

122. Maximov, I. *et al.* Fabrication of quantum dot structures using aerosol deposition and plasma etching techniques. *J. Vac. Sci. Technol. A Vacuum, Surfaces, Film.* **11**, 748–753 (1993).

123. Napierska, D., Thomassen, L. C. J., Lison, D., Martens, J. A. & Hoet, P. H. The nanosilica hazard: Another variable entity. *Part. Fibre Toxicol.* **7**, 39 (2010).

124. Lu, H. *et al.* Transforming energy using quantum dots. *Energy Environ. Sci.* **13**, 1347–1376 (2020).

125. Huang, Y., Singh, K. J., Liu, A. & Lin, C. Advances in Quantum-Dot-Based Displays. *Nanomaterials* **10**, 1327 (2020).

126. Jia, T. *et al.* Highly efficient BODIPY-doped upconversion nanoparticles for deep-red luminescence bioimagingin vivo. *Chem. Commun.* **57**, 1518–1521 (2021).

127. Liang, X., Fan, J., Zhao, Y. & Jin, R. Synthesis of NaYF4:Yb,Er upconversion nanoparticle-based optomagnetic multifunctional composite for drug delivery system. *J. Rare Earths* **39**, 579–586 (2021).

128. Chen, X., Zhang, Y., Zhang, X., Zhang, Z. & Zhang, Y. Rationally designed upconversion nanoparticles for NIR light-controlled lysosomal escape and nucleus-based photodynamic therapy. *Microchim. Acta* **188**, (2021).

129. Zhai, Y. *et al.* Near infrared neuromorphic computing via upconversion-mediated optogenetics. *Nano Energy* **67**, 104262 (2020).

130. Chen, S. *et al.* Near-infrared deep brain stimulation via upconversion nanoparticle–mediated optogenetics. *Science (80-.).* **359**, 679–684 (2018).

131. Cassidy, J. & Zamkov, M. Nanoshell quantum dots: Quantum confinement beyond the exciton Bohr radius. *J. Chem. Phys.* **152**, (2020).

132. Robel, I., Gresback, R., Kortshagen, U., Schaller, R. D. & Klimov, V. I. Universal size-dependent trend in auger recombination in direct-gap and indirect-gap semiconductor nanocrystals. *Phys. Rev. Lett.* **102**, 1–4 (2009).

133. Cullis, A. G. & Canham, L. T. Visible light emission due to quantum size effects in highly porous crystalline silicon. *Nature* **353**, 335–338 (1991).

134. Kovalev, D., Heckler, H., Polisski, G. & Koch, F. Optical Properties of Si Nanocrystals. *Phys. Status Solidi b* **215**, 871–932 (1999).

135. Barbagiovanni, E. G., Lockwood, D. J., Simpson, P. J. & Goncharova, L. V. Quantum confinement in Si and Ge nanostructures. *J. Appl. Phys.* **111**, (2012).

136. Wheeler, L. M. *et al.* Silyl Radical Abstraction in the Functionalization of Plasma-Synthesized Silicon Nanocrystals. *Chem. Mater.* **27**, 6869–6878 (2015).

137. Huang, Z. *et al.* Hybrid Molecule-Nanocrystal Photon Upconversion Across the Visible and Near-Infrared. *Nano Lett.* **15**, 5552–5557 (2015).

138. Weissleder, R. *et al.* Near-Infrared Optogenetic Genome Engineering Based on Photon-Upconversion Hydrogels. *Nano Lett.* **10**, 865–873 (2016).

139. Huang, Z. *et al.* PbS/CdS Core–Shell Quantum Dots Suppress Charge Transfer and Enhance Triplet Transfer. *Angew. Chemie - Int. Ed.* **56**, 16583–16587 (2017).

140. Gray, V. *et al.* CdS/ZnS core-shell nanocrystal photosensitizers for visible to UV upconversion. *Chem. Sci.* **8**, 5488–5496 (2017).

141. Mahboub, M., Huang, Z. & Tang, M. L. Efficient Infrared-to-Visible Upconversion with Subsolar Irradiance. *Nano Lett.* **16**, 7169–7175 (2016).

142. Jurbergs, D., Rogojina, E., Mangolini, L. & Kortshagen, U. Silicon nanocrystals with ensemble quantum yields exceeding 60%. *Appl. Phys. Lett.* **88**, (2006).

143. Montalti, M., Credi, A., Prodi, L. & Gandolfi, M. T. *Handbook of Photochemistry*. *Handbook of Third Edition* (2006).

144. Evans, D. F. 257. Perturbation of singlet-triplet transitions of aromatic molecules by oxygen under pressure. *J. Chem. Soc.* 1351–1357 (1957) doi:https://doi.org/10.1039/JR9570001351.

145. Xia, P. *et al.* Achieving spin-triplet exciton transfer between silicon and molecular acceptors for photon upconversion. *Nat. Chem.* **12**, 137–144 (2020).

146. Forziati, A. F., Camin, D. L. & Rossini, F. D. Density, refractive index, boiling point, and vapor pressure of eight monoolefin (1-alkene), six pentadiene, and two cyclomonoolefin hydrocarbons. *J. Res. Natl. Bur. Stand. (1934).* **45**, 406 (1950).

147. Carroll, G. M., Limpens, R. & Neale, N. R. Tuning Confinement in Colloidal Silicon Nanocrystals with Saturated Surface Ligands. *Nano Lett.* **18**, 3118–3124 (2018).

148. Moreels, I. *et al.* Composition and size-dependent extinction coefficient of colloidal PbSe quantum dots. *Chem. Mater.* **19**, 6101–6106 (2007).

149. Garakyaraghi, S. & Castellano, F. N. Nanocrystals for Triplet Sensitization: Molecular Behavior from Quantum-Confined Materials. *Inorg. Chem.* **57**, 2351–2359 (2018).

150. Huang, Z. & Tang, M. L. Designing Transmitter Ligands That Mediate Energy Transfer between Semiconductor Nanocrystals and Molecules. *J. Am. Chem. Soc.* **139**, 9412–9418 (2017).

151. Yanai, N. & Kimizuka, N. New Triplet Sensitization Routes for Photon Upconversion: Thermally Activated Delayed Fluorescence Molecules, Inorganic Nanocrystals, and Singlet-to-Triplet Absorption. *Acc. Chem. Res.* **50**, 2487–2495 (2017).

152. Mongin, C., Garakyaraghi, S., Razgoniaeva, N., Zamkov, M. & Castellano, F. N. Direct observation of triplet energy transfer from semiconductor nanocrystals. *Science (80-.).* **351**, 369–372 (2016).

153. Wu, M. *et al.* Solid-state infrared-to-visible upconversion sensitized by colloidal nanocrystals. *Nat. Photonics* **10**, 31–34 (2016).

154. Okumura, K., Mase, K., Yanai, N. & Kimizuka, N. Employing Core-Shell Quantum Dots as Triplet Sensitizers for Photon Upconversion. *Chem. - A Eur. J.* **22**, 7721–7726 (2016).

155. Nienhaus, L. *et al.* Speed Limit for Triplet-Exciton Transfer in Solid-State PbS Nanocrystal-Sensitized Photon Upconversion. *ACS Nano* **11**, 7848–7857 (2017).

156. Tayebjee, M. J. Y., McCamey, D. R. & Schmidt, T. W. Beyond shockley-queisser: Molecular approaches to high-efficiency photovoltaics. *J. Phys. Chem. Lett.* **6**, 2367–2378 (2015).

157. Lin, X. *et al.* Core-Shell-Shell Upconversion Nanoparticles with Enhanced Emission for Wireless Optogenetic Inhibition. *Nano Lett.* **18**, 948–956 (2018).

158. Kumar, B., Murali, A., Mattan, I. & Giri, S. Near-Infrared-Triggered Photodynamic, Photothermal, and on Demand Chemotherapy by Multifunctional Upconversion Nanocomposite. *J. Phys. Chem. B* **123**, 3738–3755 (2019).

159. Zhou, J., Liu, Q., Feng, W., Sun, Y. & Li, F. Upconversion luminescent materials: Advances and applications. *Chem. Rev.* **115**, 395–465 (2015).

160. Weissleder, R. News and views: A clearer vision for in vivo imaging. *Nat. Biotechnol.* **19**, 316–317 (2001).

161. Piland, G. B., Huang, Z., Lee Tang, M. & Bardeen, C. J. Dynamics of Energy Transfer from CdSe Nanocrystals to Triplet States of Anthracene Ligand Molecules. *J. Phys. Chem. C* **120**, 5883–5889 (2016).

162. Mahboub, M., Maghsoudiganjeh, H., Pham, A. M., Huang, Z. & Tang, M. L. Triplet Energy Transfer from PbS(Se) Nanocrystals to Rubrene: the Relationship between the Upconversion Quantum Yield and Size. *Adv. Funct. Mater.* **26**, 6091–6097 (2016).

163. Lewis, N. S. Research opportunities to advance solar energy utilization. *Science (80-.).* **351**, (2016).

164. Dexter, D. L. Two ideas on energy transfer phenomena: Ion-pair effects involving the OH stretching mode, and sensitization of photovoltaic cells. *J. Lumin.* **18**–**19**, 779–784 (1979).

165. Hanna, M. C. & Nozik, A. J. Solar conversion efficiency of photovoltaic and photoelectrolysis cells with carrier multiplication absorbers. *J. Appl. Phys.* **100**, (2006).

166. Macqueen, R. W. *et al.* Crystalline silicon solar cells with tetracene interlayers: The path to silicon-singlet fission heterojunction devices. *Mater. Horizons* **5**, 1065–1075 (2018).

167. Niederhausen, J. *et al.* Energy-level alignment tuning at tetracene/c-Si interfaces. *J. Phys. Chem. C* **124**, 27867–27881 (2020).

168. Ehrler, B., Musselman, K. P., Böhm, M. L., Friend, R. H. & Greenham, N. C. Hybrid pentacene/a-silicon solar cells utilizing multiple carrier generation via singlet exciton fission. *Appl. Phys. Lett.* **101**, 1–4 (2012).

169. Congreve, D. N. *et al.* External Quantum Efficiency Above 100% in a Singlet-Exciton-Fission-Based Organic Photovoltatic Cell. 334–338 (2013).

170. Einzinger, M. *et al.* Sensitization of silicon by singlet exciton fission in tetracene. *Nature* **571**, 90–94 (2019).

171. Rao, A. & Friend, R. H. Harnessing singlet exciton fission to Break the Shockley-Queisser Limit. *Nat. Rev. Mater.* **2**, (2017).

172. Futscher, M. H., Rao, A. & Ehrler, B. The Potential of Singlet Fission Photon Multipliers as an Alternative to Silicon-Based Tandem Solar Cells. *ACS Energy Lett.* **3**, 2587–2592 (2018).

173. Jean, J., Brown, P. R., Jaffe, R. L., Buonassisi, T. & Bulović, V. Pathways for solar photovoltaics. *Energy Environ. Sci.* **8**, 1200–1219 (2015).

174. Kroupa, D. M. *et al.* Control of Energy Flow Dynamics between Tetracene Ligands and PbS Quantum Dots by Size Tuning and Ligand Coverage. *Nano Lett.* **18**, 865–873 (2018).

175. Gray, V. *et al.* Direct vs Delayed Triplet Energy Transfer from Organic Semiconductors to Quantum Dots and Implications for Luminescent Harvesting of Triplet Excitons. *ACS Nano* **14**, 4224–4234 (2020).

176. Mongin, C., Moroz, P., Zamkov, M. & Castellano, F. N. Thermally activated delayed photoluminescence from pyrenyl-functionalized CdSe quantum dots. *Nat. Chem.* **10**, 225–230 (2018).

177. Fallon, K. J. *et al.* Molecular Engineering of Chromophores to Enable Triplet-Triplet Annihilation Upconversion. *J. Am. Chem. Soc.* **142**, 19917–19925 (2020).

178. Mangolini, L., Thimsen, E. & Kortshagen, U. High-yield plasma synthesis of luminescent silicon nanocrystals. *Nano Lett.* **5**, 655–659 (2005).

179. Birks, B. J. B. & Slifkin, M. A. Drug Supplies During the American Revolution. *Nature* **191**, 761–761 (1961).

180. Clarke, R. H. & Hochstrasser, R. M. Location and assignment of the lowest triplet state of perylene. *J. Mol. Spectrosc.* **32**, 309–319 (1969).

181. Albrecht, W. G., Michel-Beyerle, M. E. & Yakhot, V. Exciton fission in excimer forming crystal. Dynamics of an excimer build-up in α-perylene. *Chem. Phys.* **35**, 193–200 (1978).

182. Giri, G., Prodhan, S., Pati, Y. A. & Ramasesha, S. A Model Exact Study of the Properties of Low-Lying Electronic States of Perylene and Substituted Perylenes. *J. Phys. Chem. A* **122**, 8650–8658 (2018).

183. Beard, M. C. *et al.* Multiple exciton generation in silicon nanocrystals. *Opt. InfoBase Conf. Pap.* **4**, 4–10 (2007).

184. Limpens, R., Pach, G. F. & Neale, N. R. Nonthermal Plasma-Synthesized Phosphorus-Boron co-Doped Si Nanocrystals: A New Approach to Nontoxic NIR-Emitters. *Chem. Mater.* **31**, 4426–4435 (2019).

185. Trinh, M. T., Limpens, R. & Gregorkiewicz, T. Experimental investigations and modeling of Auger recombination in silicon nanocrystals. *J. Phys. Chem. C* **117**, 5963–5968 (2013).

186. Stolle, C. J., Lu, X., Yu, Y., Schaller, R. D. & Korgel, B. A. Efficient Carrier Multiplication in Colloidal Silicon Nanorods. *Nano Lett.* **17**, 5580–5586 (2017).

187. Utterback, J. K. *et al.* Competition between electron transfer, trapping, and recombination in Cds nanorod-hydrogenase complexes. *Phys. Chem. Chem. Phys.* **17**, 5538–5542 (2015).

188. Porter, G. & Windsor, M. W. The triplet state in fluid media. *Proc. R. Soc. London* 238–258 (1955).

189. Ye, C., Gray, V., Mårtensson, J. & Börjesson, K. Annihilation Versus Excimer Formation by the Triplet Pair in Triplet-Triplet Annihilation Photon Upconversion. *J. Am. Chem. Soc.* **141**, 9578–9584 (2019).

190. Lee, B. G. *et al.* Quasi-Direct Optical Transitions in Silicon Nanocrystals with Intensity Exceeding the Bulk. *Nano Lett.* **16**, 1583–1589 (2016).

191. Luo, X. *et al.* Triplet Energy Transfer from CsPbBr3 Nanocrystals Enabled by Quantum Confinement. *J. Am. Chem. Soc.* **141**, 4186–4190 (2019).

192. Berkelbach, T. C., Hybertsen, M. S. & Reichman, D. R. Microscopic theory of singlet exciton fission. I. General formulation. *J. Chem. Phys.* **138**, (2013).

193. Reich, K. V. & Shklovskii, B. I. Exciton Transfer in Array of Epitaxially Connected Nanocrystals. *ACS Nano* **10**, 10267–10274 (2016).

194. Peyton Cline, R. & Eaves, J. D. Surface-trapped hole diffusion in CdS and CdSe: The superexchange mechanism. *J. Phys. Chem. C* **124**, 28244–28251 (2020).

195. Singh-Rachford, T. N. & Castellano, F. N. Triplet sensitized red-to-blue photon upconversion. *J. Phys. Chem. Lett.* **1**, 195–200 (2010).

196. Parker, C. A. & Joyce, T. A. Formation efficiency and energy of the perylene triplet. *Chem. Commun.* 108–109 (1966) doi:10.1039/C1966000108b.

197. Ho, S. K., Siegel, S. & Schwarz, H. A. Pulse radiolysis of polystyrene. *J. Phys. Chem.* **71**, 4527–4533 (1967).

198. Miller, A. & Abrahams, E. Impurity conduction at low concentrations. *Phys. Rev.* **120**, 745–755 (1960).

199. Köhler, A. & Bässler, H. What controls triplet exciton transfer in organic semiconductors? *J. Mater. Chem.* **21**, 4003–4011 (2011).

200. Jackson, G., Livingston, R. & Pugh, A. C. Experimental Study of the Triplet State of Anthracene in Fluid Solutions. *Trans. Faraday Soc.* 1635–1639 (1960).

201. Dempster, D. N., Morrow, T. & Quinn, M. F. Extinction coefficients for triplet-triplet absorption in ethanol solutions of anthracene, naphthalene, 2,5-diphenyloxazole, 7-diethylamino- 4-methyl coumarin and 4-methyl-7-amino-carbostyril. *J. Photochem.* **2**, 329–341 (1973).

202. Monguzzi, A., Tubino, R., Hoseinkhani, S., Campione, M. & Meinardi, F. Low power, non-coherent sensitized photon up-conversion: Modelling and perspectives. *Phys. Chem. Chem. Phys.* **14**, 4322–4332 (2012).

203. Haefele, A., Blumhoff, J., Khnayzer, R. S. & Castellano, F. N. Getting to the (Square) root of the problem: How to make noncoherent pumped upconversion linear. *J. Phys. Chem. Lett.* **3**, 299–303 (2012).

204. Mcglynn, S. P., Padhye, M. R. & Kasha, M. Lowest triplet levels of the polyacenes. *J. Chem. Phys.* **23**, 593–594 (1955).

205. Burgdorff, C., Kircher, T. & Löhmannsröben, H. G. Photophysical properties of tetracene derivatives in solution. *Spectrochim. Acta Part A Mol. Spectrosc.* **44**, 1137–1141 (1988).

206. Tomkiewicz, Y., Groff, R. P. & Avakian, P. Spectroscopic approach to energetics of exciton fission and fusion in tetracene crystals. *J. Chem. Phys.* **54**, 4504–4507 (1971).

207. Huang, Z. *et al.* ZnS Shells Enhance Triplet Energy Transfer from CdSe Nanocrystals for Photon Upconversion. *ACS Photonics* **5**, 3089–3096 (2018).

208. Mase, K., Okumura, K., Yanai, N. & Kimizuka, N. Triplet sensitization by perovskite nanocrystals for photon upconversion. *Chem. Commun.* **53**, 8261–8264 (2017).

209. Kim, J. H. & Kim, J. H. Triple-Emulsion microcapsules for highly efficient multispectral upconversion in the aqueous phase. *ACS Photonics* **2**, 633–638 (2015).

210. Kim, J. H., Deng, F., Castellano, F. N. & Kim, J. H. Red-to-Blue/Cyan/Green Upconverting Microcapsules for Aqueous- and Dry-Phase Color Tuning and Magnetic Sorting. *ACS Photonics* **1**, 382–388 (2014).

211. Hisamitsu, S. *et al.* Visible-to-UV Photon Upconversion in Nanostructured Chromophoric Ionic Liquids. *ChemistryOpen* **9**, 14–17 (2020).

212. Duan, P., Yanai, N., Nagatomi, H. & Kimizuka, N. Photon upconversion in supramolecular gel matrixes: Spontaneous accumulation of light-harvesting donor-acceptor arrays in nanofibers and acquired air stability. *J. Am. Chem. Soc.* **137**, 1887–1894 (2015).

213. Liu, Q. *et al.* A general strategy for biocompatible, high-effective upconversion nanocapsules based on triplet-triplet annihilation. *J. Am. Chem. Soc.* **135**, 5029–5037 (2013).

214. Marsico, F. *et al.* Hyperbranched unsaturated polyphosphates as a protective matrix for long-term photon upconversion in air. *J. Am. Chem. Soc.* **136**, 11057–11064 (2014).

215. Xia, P. *et al.* On the efficacy of anthracene isomers for triplet transmission from CdSe nanocrystals. *Chem. Commun.* **53**, 1241–1244 (2017).

216. Askes, S. H. C. & Bonnet, S. Solving the oxygen sensitivity of sensitized photon upconversion in life science applications. *Nat. Rev. Chem.* **2**, 437–452 (2018).

217. Dhaene, E., Billet, J., Bennett, E., Van Driessche, I. & De Roo, J. The Trouble with ODE: Polymerization during Nanocrystal Synthesis. *Nano Lett.* **19**, 7411–7417 (2019).

218. Askes, S. H. C. *et al.* Imaging Upconverting Polymersomes in Cancer Cells: Biocompatible Antioxidants Brighten Triplet–Triplet Annihilation Upconversion. *Small* **12**, 5579–5590 (2016).

219. Kawashima, Y. *et al.* Visible-to-UV photon upconversion in air-saturated water by multicomponent co-assembly. *Mol. Syst. Des. Eng.* **5**, 792–796 (2020).

220. Ogawa, T., Yanai, N., Monguzzi, A. & Kimizuka, N. Highly Efficient Photon Upconversion in Self-Assembled Light-Harvesting Molecular Systems. *Sci. Rep.* **5**, 1–9 (2015).

221. Kouno, H., Sasaki, Y., Yanai, N. & Kimizuka, N. Supramolecular Crowding Can Avoid Oxygen Quenching of Photon Upconversion in Water. *Chem. - A Eur. J.* **25**, 6124–6130 (2019).

222. Schumpe, A. & Lühring, P. Oxygen Diffusivities in Organic Liquids at 293.2 K. *J. Chem. Eng. Data* **35**, 24–25 (1990).

223. Ware, W. R. Oxygen quenching of fluorescence in solution: An experimental study of the diffusion process. *J. Phys. Chem.* **66**, 455–458 (1962).

224. Serrano, L., Silva, J. A. & Farelo, F. Densities and Viscosities of Binary and Ternary Liquid Systems Containing Xylenes. *J. Chem. Eng. Data* **35**, 288–291 (1990).

225. Sanchez-Vicente, Y. *et al.* Viscosities of Liquid Hexadecane at Temperatures between 323 K and 673 K and Pressures up to 4 MPa Measured Using a Dual-Capillary Viscometer. *J. Chem. Eng. Data* **64**, 706–712 (2019).

226. Ju, L. -K & Ho, C. S. Oxygen diffusion coefficient and solubility in n-hexadecane. *Biotechnol. Bioeng.* **34**, 1221–1224 (1989).

227. Caudwell, D. R., Trusler, J. P. M., Vesovic, V. & Wakeham, W. A. The viscosity and density of n-dodecane and n-octadecane at pressures up to 200 MPa and temperatures up to 473 K. *Int. J. Thermophys.* **25**, 1339–1352 (2004).

228. Pratas, M. J. *et al.* Densities and viscosities of minority fatty acid methyl and ethyl esters present in biodiesel. *J. Chem. Eng. Data* **56**, 2175–2180 (2011).

229. Morita, M., Ohmi, T., Hasegawa, E., Kawakami, M. & Ohwada, M. Growth of native oxide on a silicon surface. *J. Appl. Phys.* **68**, 1272–1281 (1990).

230. Kohno, Y. *et al.* Kinetic study of quenching reaction of singlet oxygen and scavenging reaction of free radical by squalene in n-butanol. *Biochim. Biophys. Acta (BBA)/Lipids Lipid Metab.* **1256**, 52–56 (1995).

231. Greer, A. Christopher Foote's Discovery of the Role of Singlet Oxygen [1O2 (1Deltag)] in Photosensitized Oxidation Reactions. *Acc. Chem. Res.* **39**, 797–804 (2006).

232. Chan, H. W. S. Photo-sensitized oxidation of unsaturated fatty acid methyl esters. The identification of different pathways. *J. Am. Oil Chem. Soc.* **54**, 100–104 (1977).

233. Danielyan, L. *et al.* Survival, neuron-like differentiation and functionality of mesenchymal stem cells in neurotoxic environment: The critical role of erythropoietin. *Cell Death Differ.* **16**, 1599–1614 (2009).

234. McKeown, S. R. Defining normoxia, physoxia and hypoxia in tumours - Implications for treatment response. *Br. J. Radiol.* **87**, 1–12 (2014).

235. Mangolini, L. & Kortshagen, U. Plasma-assisted synthesis of silicon nanocrystal inks. *Adv. Mater.* **19**, 2513–2519 (2007).

236. Anthony, R. J., Cheng, K. Y., Holman, Z. C., Holmes, R. J. & Kortshagen, U. R. An all-gas-phase approach for the fabrication of silicon nanocrystal light-emitting devices. *Nano Lett.* **12**, 2822–2825 (2012).

237. Gupta, P., Colvin, V. L., Brand, J. L. & George, S. M. Desorption kinetics of hydrogen from silicon surfaces using transmission FTIR. *AIP Conf. Proc.* **167**, 50–59 (1998).

238. Klingbeil, A. E., Jeffries, J. B. & Hanson, R. K. Temperature-dependent mid-IR absorption spectra of gaseous hydrocarbons. *J. Quant. Spectrosc. Radiat. Transf.* **107**, 407–420 (2007).

239. Li, Z. & Kortshagen, U. R. Aerosol-phase synthesis and processing of luminescent silicon nanocrystals. *Chem. Mater.* **31**, 8451–8458 (2019).

240. Sarma, D. D. & Shukla, A. K. Building better batteries: A travel back in time. *ACS Energy Lett.* **3**, 2841–2845 (2018).

241. *Electrochemical power sources Primary & Secondary Batteries*. (Peter Peregrinus LTD, 1980).

242. Godshall, N. A., Raistrick, I. D. & Huggins, R. A. THERMODYNAMIC INVESTIGATIONS OF TERNARY LITHIUM-TRANSITION METAL-OXYGEN CATHODE MATERIALS. *Mater. Res. Bull.* **15**, 561–570 (1980).

243. Mizushima, K., Jones, P. C., Wiseman, P. J. & Goodenough, J. B. LixCoO2 (0<x<1): A NEW CATHODE MATERIAL FOR BATTERIES OF HIGH ENERGY DENSITY. *Mater. Res. Bull.* **15**, 783–789 (1980).

244. The Nobel Prize in Chemistry 2019. *The Royal Swedish Academy of Sciences* (2019).

245. Nitta, N., Wu, F., Lee, J. T. & Yushin, G. Li-ion battery materials: Present and future. *Mater. Today* **18**, 252–264 (2015).

246. Reddy, M. V., Mauger, A., Julien, C. M., Paoletta, A. & Zaghib, K. Brief History of Early Lithium-Battery Development. *Materials (Basel).* **13**, (2020).

247. Zuo, X., Zhu, J., Müller-Buschbaum, P. & Cheng, Y. J. Silicon based lithium-ion battery anodes: A chronicle perspective review. *Nano Energy* **31**, 113–143 (2017).

248. Boukamp, B. A., Lesh, G. C. & Huggins, R. A. All-Solid Lithium Electrodes with Mixed - Conductor Matrix. *J. Electrochem. Soc.* **128**, 725–729 (1981).

249. Wu, H. & Cui, Y. Designing nanostructured Si anodes for high energy lithium ion batteries. *Nano Today* **7**, 414–429 (2012).

250. Zhu, W. *et al.* Progress of Binder Structures in Silicon-Based Anodes for Advanced Lithium-Ion Batteries : A Mini Review. *Front. Chem.* **9**, 1–11 (2021).

251. Jin, S. *et al.* The state of understanding of the lithium-ion-battery graphite solid electrolyte interphase (SEI) and its relationship to formation cycling *. *Carbon N. Y.* **105**, 52–76 (2016).

252. Kim, J., Chae, O. B. & Lucht, B. L. Perspective — Structure and Stability of the Solid Electrolyte Interphase on Silicon Anodes of Lithium-ion Batteries. *J. Electrochem. Soc.* **168**, (2021).

253. Stübler, T., Lahyani, A. & Zayoud, A. A. Lithium-ion battery modeling using CC–CV and impedance spectroscopy characterizations. *SN Appl. Sci.* **2**, 1–8 (2020).

254. Fares, R. L. & Webber, M. E. What are the tradeoffs between battery energy storage cycle life and calendar life in the energy arbitrage application? *J. Energy Storage* **16**, 37–45 (2018).

255. Lu, W., Zhang, L., Qin, Y. & Jansen, A. Calendar and Cycle Life of Lithium-Ion Batteries Containing Silicon Monoxide Anode. *J. Electrochem. Soc.* **165**, A2179–A2183 (2018).

256. Louli, A. J. *et al.* Optimizing Cycling Conditions for Anode-Free Lithium Metal Cells. *J. Electrochem. Soc.* **168**, 020515 (2021).

257. Guo, J., Sun, A., Chen, X., Wang, C. & Manivannan, A. Electrochimica Acta Cyclability study of silicon – carbon composite anodes for lithium-ion batteries using electrochemical impedance spectroscopy. *Electrochim. Acta* **56**, 3981–3987 (2011).

258. Wang, S. *et al. Lithium-ion battery characteristics and applications*. *Battery System Modeling* (2021). doi:10.1016/b978-0-323-90472-8.00003-2.

259. Feng, K. *et al.* Silicon-Based Anodes for Lithium-Ion Batteries : From Fundamentals to Practical Applications. *Small* **14**, (2018).

260. Luo, F. *et al.* Review — Nano-Silicon / Carbon Composite Anode Materials Towards Practical Application for Next Generation Li-Ion Batteries. *J. Electrochem. Soc.* **162**, A2509–A2528 (2015).

261. Mcdowell, M. T., Lee, S. W., Nix, W. D. & Cui, Y. 25th Anniversary Article : Understanding the Lithiation of Silicon and Other Alloying Anodes for Lithium-Ion Batteries. *Adv. Mater.* **25**, 4966–4985 (2013).

262. Bachmatiuk, A. *et al.* Silicon carbide-free graphene growth on silicon for lithium-ion battery with high volumetric energy density. *Nat. Commun.* 1–8 (2015) doi:10.1038/ncomms8393.

263. Shi, L. *et al.* Vertical Graphene Growth on SiO Microparticles for Stable Lithium Ion Battery Anodes. *Nano Lett.* **17**, 3681–3687 (2017).

264. Greco, E. *et al.* Few-layer graphene improves silicon performance in Li-ion battery anodes †. *J. Mater. Chem. A* **5**, 19306–19315 (2017).

265. Alvarez Barragan, A., Nava, G., Wagner, N. J. & Mangolini, L. Silicon-carbon composites for lithium-ion batteries: A comparative study of different carbon deposition approaches. *J. Vac. Sci. Technol. B, Nanotechnol. Microelectron. Mater. Process. Meas. Phenom.* **36**, 011402 (2018).

266. Yu, J. *et al.* Uniform Carbon Coating on Silicon Nanoparticles by Dynamic CVD Process for Electrochemical Lithium Storage. *Ind. Eng. Chem. Res.* **53**, 12697–12704 (2014).

267. Bensebaa, F. *Nanoparticle Technologies: From Lab to Market*. (Elsevier Science, 2012). doi:10.1016/B978-0-12-369550-5.00001-X.

268. Liu, N. *et al.* A pomegranate-inspired nanoscale design for large-volume-change lithium battery anodes. *Nat. Nanotechnol.* **9**, 187–192 (2014).

269. Son, I. H., Park, J. H., Kwon, S., Choi, J. W. & Rümmeli, M. H. Graphene Coating of Silicon Nanoparticles with CO2-Enhanced Chemical Vapor Deposition. *Small* **12**, 658–667 (2016).

270. Li, Y. *et al.* Growth of conformal graphene cages on micrometre-sized silicon particles as stable battery anodes. *Nat. Energy* **1**, (2016).

271. Casiraghi, C., Ferrari, A. C. & Robertson, J. Raman spectroscopy of hydrogenated amorphous carbons. *Phys. Rev. B* 1–14 (2005) doi:10.1103/PhysRevB.72.085401.

272. Buijnsters, J. G. *et al.* Hydrogen quantification in hydrogenated amorphous carbon films by infrared , Raman , and x-ray absorption near edge spectroscopies. *J. Appl. Phys.* **105**, (2009).

273. Boebinger, M. G. *et al.* Avoiding Fracture in a Conversion Battery Material through Reaction with Larger Ions Avoiding Fracture in a Conversion Battery Material through Reaction with Larger Ions. *Joule* **2**, 1783–1799 (2018).

274. Boebinger, M. G. *et al.* Distinct nanoscale reaction pathways in a sulfide material for sodium and lithium batteries. *J. Mater. Chem. A* **5**, 11701–11709 (2017).

275. Mcdowell, M. T., Ryu, I., Lee, S. W., Wang, C. & Nix, W. D. Studying the Kinetics of Crystalline Silicon Nanoparticle Lithiation with In Situ Transmission Electron Microscopy. *Adv. Mater.* **24**, 6034–6041 (2012).

276. Wu, H. *et al.* Stable cycling of double-walled silicon nanotube battery anodes through solid – electrolyte interphase control. *Nat. Nanotechnol.* **7**, (2012).

277. Zhong, L., Beaudette, C., Guo, J., Bozhilov, K. & Mangolini, L. Tin nanoparticles as an effective conductive additive in silicon anodes. *Sci. Rep.* (2016) doi:10.1038/srep30952.

278. Licht, B. K., Homeyer, F., Bösebeck, K., Binnewies, M. & Heitjans, P. Synthesis and Electrochemical Behavior of Nanostructured Copper Particles on Graphite for Application in Lithium Ion Batteries. *De Gruyter* **229**, 1415–1427 (2015).

279. Chen, X. *et al.* Conductive rigid skeleton supported silicon as high-performance Li-Ion battery anodes. *Nano Lett.* **12**, 4124–4130 (2012).

280. Chartrel, T. *et al.* Revisiting and improving the preparation of silicon-based electrodes for lithium-ion batteries: ball milling impact on poly(acrylic acid) polymer binders. *Mater. Chem. Front.* **3**, 881–891 (2019).

281. Zhu, B. *et al.* Scalable Production of Si Nanoparticles Directly from Low Grade Sources for Lithium-Ion Battery Anode. *Nano Lett.* **15**, 5750–5754 (2015).

282. Shen, C. *et al.* Hierarchical Carbon-Coated Ball-Milled Silicon: Synthesis and Applications in Free-Standing Electrodes and High-Voltage Full Lithium-Ion Batteries. *ACS Nano* **12**, 6280–6291 (2018).

283. Gauthier, M. *et al.* A low-cost and high performance ball-milled Si-based negative electrode for high-energy Li-ion batteries. *Energy Environ. Sci.* **6**, 2145–2155 (2013).

284. Nilssen, B. E. & Kleiv, R. A. Silicon Powder Properties Produced in a Planetary Ball Mill as a Function of Grinding Time, Grinding Bead Size and Rotational Speed. *Silicon* 21–23 (2020) doi:10.1007/s12633-019-00340-0.

285. Hui, L. Planetary High-energy Ball Mill - Li Patent.pdf. 9 (2000).

286. Fuduka, T., Hidaka, K., Mizutani, T., Nishida, M. & Kohira, Y. (12) United States Patent. vol. 1 (2001).

287. Martell, S. A. *et al.* High Surface Area Mesoporous Silicon Nanoparticles Prepared via Two-Step Magnesiothermic Reduction for Stoichiometric CO2 to CH3OH Conversion. *ACS Appl. Nano Mater.* **2**, 5713–5719 (2019).

288. Luo, W. *et al.* Efficient fabrication of nanoporous Si and Si/Ge enabled by a heat scavenger in magnesiothermic reactions. *Sci. Rep.* **3**, 1–7 (2013).

289. Kim, K. H. *et al.* Complete magnesiothermic reduction reaction of vertically aligned mesoporous silica channels to form pure silicon nanoparticles. *Sci. Rep.* **5**, 1–7 (2015).

290. Yang, Z. *et al.* Nanoporous silicon spheres preparation via a controllable magnesiothermic reduction as anode for Li-ion batteries. *Electrochim. Acta* **329**, 1–10 (2020).

291. Darghouth, A., Aouida, S. & Bessais, B. High Purity Porous Silicon Powder Synthesis by Magnesiothermic Reduction of Tunisian Silica Sand. *Silicon* (2020) doi:10.1007/s12633-020-00433-1.

292. Entwistle, J., Rennie, A. & Patwardhan, S. A review of magnesiothermic reduction of silica to porous silicon for lithium-ion battery applications and beyond. *J. Mater. Chem. A* **6**, 18344–18356 (2018).

293. Liu, W. *et al.* Silicon Nanoparticles Preparation by Induction Plasma Technology for Li-ion Batteries Anode Material. (2019).

294. Specification, E. P. Ep 1 433 366 b1 (12). vol. 1 1–12 (2011).

295. Dolbec, R., Systems, T. P. & Guerfi, A. Silicon nanopowder synthesis by inductively coupled plasma as anode for high-energy Li-ion batteries: Arrays, Functional Materials, and Industrial Nanosilicon. in *Silicon Nanomaterials Sourcebook* (ed. Sattler, K. D.) 463–482 (CRC Press, 2017). doi:10.1201/9781315153551-24.

296. Kambara, M. *et al.* Nano-composite Si particle formation by plasma spraying for negative electrode of Li ion batteries. *J. Appl. Phys.* **115**, (2014).

297. He, J. *et al.* Simulation and experimental observation of silicon particles' vaporization in RF thermal plasma reactor for preparing Si nano-powder. *Powder Technol.* **313**, 27–35 (2017).

298. Mangolini, L. Synthesis, properties, and applications of silicon nanocrystals. *J. Vac. Sci. Technol. B, Nanotechnol. Microelectron. Mater. Process. Meas. Phenom.* **31**, 020801 (2013).

299. Mangolini, L. Monitoring non-thermal plasma processes for nanoparticle synthesis. *J. Phys. D. Appl. Phys.* **50**, (2017).

300. Ding, Y. *et al.* A parametric study of non-thermal plasma synthesis of silicon nanoparticles from a chlorinated precursor. *J. Phys. D. Appl. Phys.* **47**, (2014).

301. Lopez, T. & Mangolini, L. Low activation energy for the crystallization of amorphous silicon nanoparticles. *Nanoscale* **6**, 1286–1294 (2014).

302. Mädler, L., Kammler, H. K., Mueller, R. & Pratsinis, S. E. Controlled synthesis of nanostructured particles by flame spray pyrolysis. *J. Aerosol Sci.* **33**, 369–389 (2002).

303. Mueller, R., Mädler, L. & Pratsinis, S. E. Nanoparticle synthesis at high production rates by flame spray pyrolysis. *Chem. Eng. Sci.* **58**, 1969–1976 (2003).

304. Lacour, F. *et al.* Laser pyrolysis synthesis and characterization of luminescent silicon nanocrystals. *Phys. E Low-Dimensional Syst. Nanostructures* **38**, 11–15 (2007).

305. Sublemontier, O., Lacour, F., Leconte, Y., Herlin-Boime, N. & Reynaud, C. CO2 laser-driven pyrolysis synthesis of silicon nanocrystals and applications. *J. Alloys Compd.* **483**, 499–502 (2009).

306. Kim, S. *et al.* High-yield synthesis of single-crystal silicon nanoparticles as anode materials of lithium ion batteries via photosensitizer-assisted laser pyrolysis. *J. Mater. Chem. A* **2**, 18070–18075 (2014).

307. Li, X., He, Y. & Swihart, M. T. Surface functionalization of silicon nanoparticles produced by laser-driven pyrolysis of silane followed by HF-HNO 3 Etching. *Langmuir* **20**, 4720–4727 (2004).

308. Wiggers, H., Starke, R. & Roth, P. Silicon particle formation by pyrolysis of silane in a hot wall gasphase reactor. *Chem. Eng. Technol.* **24**, 261–264 (2001).

309. Sourice, J. *et al.* One-step synthesis of Si@C nanoparticles by laser pyrolysis: High-capacity anode material for lithium-ion batteries. *ACS Appl. Mater. Interfaces* **7**, 6637–6644 (2015).

310. Kessler, V. *et al.* Thermoelectric properties of nanocrystalline silicon from a scaled-up synthesis plant. *Adv. Eng. Mater.* **15**, 379–385 (2013).

311. Patrone, L. *et al.* Photoluminescence of silicon nanoclusters with reduced size dispersion produced by laser ablation. *J. Appl. Phys.* **87**, 3829–3837 (2000).

312. Intartaglia, R. *et al.* Optical properties of femtosecond laser-synthesized silicon nanoparticles in deionized water. *J. Phys. Chem. C* **115**, 5102–5107 (2011).

313. Kuzmin, P. G. *et al.* Silicon nanoparticles produced by femtosecond laser ablation in ethanol: Size control, structural characterization, and optical properties. *J. Phys. Chem. C* **114**, 15266–15273 (2010).

314. Luo, X. *et al.* SiOx Nanodandelion by Laser Ablation for Anode of Lithium-Ion Battery. *Small* **11**, 6009–6012 (2015).

315. Yoshida, T., Takeyama, S., Yamada, Y. & Mutoh, K. Nanometer-sized silicon crystallites prepared by excimer laser ablation in constant pressure inert gas. *Appl. Phys. Lett.* **68**, 1772–1774 (1996).

316. Amoruso, S. *et al.* Generation of silicon nanoparticles via femtosecond laser ablation in vacuum. *Appl. Phys. Lett.* **84**, 4502–4504 (2004).

317. Liu, X. H. *et al.* Size-Dependent Fracture of Silicon Nanoparticles During Lithiation. *ACS Nano* 1522–1531 (2012) doi:10.1021/nn204476h.

318. Aghajamali, M. *et al.* Size and Surface Effects of Silicon Nanocrystals in Graphene Aerogel Composite Anodes for Lithium Ion Batteries. *Chem. Mater.* **30**, 7782–7792 (2018).

319. Zhu, G., Wang, Y., Yang, S., Qu, Q. & Zheng, H. Correlation between the physical parameters and the electrochemical performance of a silicon anode in lithium-ion batteries. *J. Mater.* **5**, 164–175 (2019).

320. Carroll, G. M. *et al.* SiO2 is wasted space in single-nanometer-scale silicon nanoparticle-based composite anodes for Li-ion electrochemical energy storage. *ACS Appl. Energy Mater.* **3**, 10993–11001 (2020).

321. Peled, E. The Electrochemical Behavior of Alkali and Alkaline Earth Metals in Nonaqueous Battery Systems—The Solid Electrolyte Interphase Model. *J. Electrochem. Soc.* **126**, 2047–2051 (1979).

322. Peled, E. & Menkin, S. Review—SEI: Past, Present and Future. *J. Electrochem. Soc.* **164**, A1703–A1719 (2017).

323. Kanamura, K., Shiraishi, S. & Takehara, Z. Electrochemical Deposition of Very Smooth Lithium Using Nonaqueous Electrolytes Containing HF. *J. Electrochem. Soc.* **143**, 2187–2197 (1996).

324. Peled, E., Golodnitsky, D., Menachem, C. & Bar-Tow, D. An Advanced Tool for the Selection of Electrolyte Components for Rechargeable Lithium Batteries. *J. Electrochem. Soc.* **145**, 3482–3486 (1998).

325. Funabiki, A., Inaba, M., Abe, T. & Ogumi, Z. Stage Transformation of Lithium-Graphite Intercalation Compounds Caused by Electrochemical Lithium Intercalation. *J. Electrochem. Soc.* **146**, 2443–2448 (1999).

326. Jurgen O. Besenhard (Ed.). *Handbook of Battery Materials*. (Wiley, 1998).

327. Soto, F. A., Ma, Y., Martinez De La Hoz, J. M., Seminario, J. M. & Balbuena, P. B. Formation and Growth Mechanisms of Solid-Electrolyte Interphase Layers in Rechargeable Batteries. *Chem. Mater.* **27**, 7990–8000 (2015).

328. Joho, F. *et al.* Relation between surface properties, pore structure and first-cycle charge loss of graphite as negative electrode in lithium-ion batteries. *J. Power Sources* **97**–**98**, 78–82 (2001).

329. Béguin, F. *et al.* Correlation of the irreversible lithium capacity with the active surface area of modified carbons. *Carbon N. Y.* **43**, 2160–2167 (2005).

330. Tsubouchi, S. *et al.* Spectroscopic Characterization of Surface Films Formed on Edge Plane Graphite in Ethylene Carbonate-Based Electrolytes Containing Film-Forming Additives. *J. Electrochem. Soc.* **159**, A1786–A1790 (2012).

331. Deshpande, R., Cheng, Y. T. & Verbrugge, M. W. Modeling diffusion-induced stress in nanowire electrode structures. *J. Power Sources* **195**, 5081–5088 (2010).

332. Chan, C. K., Ruffo, R., Hong, S. S. & Cui, Y. Surface chemistry and morphology of the solid electrolyte interphase on silicon nanowire lithium-ion battery anodes. *J. Power Sources* **189**, 1132–1140 (2009).

333. Sina, M. *et al.* Direct Visualization of the Solid Electrolyte Interphase and Its Effects on Silicon Electrochemical Performance. *Adv. Mater. Interfaces* **3**, 1–10 (2016).

334. Tremolet de Villers, B. J., Bak, S. M., Yang, J. & Han, S. D. In Situ ATR-FTIR Study of the Cathode–Electrolyte Interphase: Electrolyte Solution Structure, Transition Metal Redox, and Surface Layer Evolution. *Batter. Supercaps* **4**, 778–784 (2021).

335. Larkin, P. *IR and Raman spectroscopy*. *Infrared and Raman Spectroscopy* (2011).

336. Ha, Y. *et al.* Probing the Evolution of Surface Chemistry at the Silicon-Electrolyte Interphase via in Situ Surface-Enhanced Raman Spectroscopy. *J. Phys. Chem. Lett.* **11**, 286–291 (2020).

337. Nanda, J. *et al.* Unraveling the Nanoscale Heterogeneity of Solid Electrolyte Interphase Using Tip-Enhanced Raman Spectroscopy. *Joule* **3**, 2001–2019 (2019).

338. Reynier, Y., Yazami, R. & Fultz, B. XRD evidence of macroscopic composition inhomogeneities in the graphite-lithium electrode. *J. Power Sources* **165**, 616–619 (2007).

339. Iwamura, S. *et al.* Li-Rich Li-Si Alloy As A Lithium-Containing Negative Electrode Material Towards High Energy Lithium-Ion Batteries. *Sci. Rep.* **5**, 25–27 (2015).

340. Health, C. for D. and R. N95 Respirators and Surgical Masks. *FDA* (2020).

341. Konda, A. *et al.* Aerosol Filtration Efficiency of Common Fabrics Used in Respiratory Cloth Masks. *ACS Nano* **14**, 6339–6347 (2020).

342. CDC. Implementing Filtering Facepiece Respirator (FFR) Reuse, Including Reuse after Decontamination, When There Are Known Shortages of N95 Respirators. (2020).

343. Setiyani, M. S. Emergencies Coronavirus Press Conference - 03 March 2020. *WHO - Audio* 1–9 (2020).

344. Kumar, A. *et al.* Decontamination of N95 masks for re-use employing 7 widely available sterilization methods. *PLoS One* **15**, 1–16 (2020).

345. Rutala, W. A. & Weber, D. J. Guideline for Disinfection and Sterilization in Healthcare Facilities, 2008 (Update: May 2019). *CDC* (2019) doi:10.1016/j.idc.2021.04.004.

346. Herron, J. T. & Green, D. S. Chemical kinetics database and predictive schemes for nonthermal humid air plasma chemistry. Part II. Neutral species reactions. *Plasma Chem. Plasma Process.* **21**, 459–481 (2001).

347. María Neftalí Rojas-Valencia, . Research on Ozone Application as Disinfectant and Action Mechanisms on Wastewater Microorganisms Research on ozone application as disinfectant and action mechanisms on wastewater microorganisms. *Sci. against Microb. Pathog. Commun. Curr. Res. Technol. Adv.* 236–271 (2014).

348. Tseng, C. C. & Li, C. S. Ozone for inactivation of aerosolized bacteriophages. *Aerosol Sci. Technol.* **40**, 683–689 (2006).

349. Dennis, R., Cashion, A. & Hubbard, D. Durability of Disposable N95 Mask Material When Exposed to Improvised Ozone Gas Disinfection. *J. Sci. Med.* **2**, 1–23 (2020).

350. Hudson, J. B., Sharma, M. & Vimalanathan, S. Development of a practical method for using ozone gas as a virus decontaminating agent. *Ozone Sci. Eng.* **31**, 216–223 (2009).

351. Walker, C. M. & Ko, G. Effect of ultraviolet germicidal irradiation on viral aerosols. *Environ. Sci. Technol.* **41**, 5460–5465 (2007).

352. Liu, W., Sun, G., Li, C. & Zhang, R. A study of the glow discharge characteristics of contact electrodes at atmospheric pressure in air. *Phys. Plasmas* **21**, (2014).

353. Bass, A. M. & Paur, R. J. The Ultraviolet Cross-Sections of Ozone: I The Measurements. in *Atmospheric Ozone* 606–607 (Springer US, 1985). doi:https://doi.org/10.1007/978-94-009-5313-0_120.

354. Jodpimai, S., Piriyawong, V., Limsuwan, P. Ozone Concentration Measurement in the Range of 0- 200 Go3/M3 By Using Ultra Violet Light Emitting Diode At Wavelength 280 Nm. *Int. J. Adv. Sci. Eng. Technol.* **3**, 74–77 (2015).

355. Hodges, J. T. *et al.* Recommendation of a consensus value of the ozone absorption cross-section at 253.65 nm based on a literature review. *Metrologia* **56**, (2019).

356. Da Silveira Petruci, J. F. *et al.* Real-time monitoring of ozone in air using substrate-integrated hollow waveguide mid-infrared sensors. *Sci. Rep.* **3**, 1–5 (2013).

357. Miller, S. E. & Brealey, J. K. *Electron microscopy of SARS-CoV-2: a challenging task*. *The Lancet* vol. 98 (2020).

358. Akpinar, F. & Yin, J. Characterization of vesicular stomatitis virus populations by tunable resistive pulse sensing. *J. Virol. Methods* **218**, 71–76 (2015).

359. Lai, M. Y. Y., Cheng, P. K. C. & Lim, W. W. L. Survival of severe acute respiratory syndrome coronavirus. *Clin. Infect. Dis.* **41**, 67–71 (2005).

360. Zimmer, B., Summermatter, K. & Zimmer, G. Stability and inactivation of vesicular stomatitis virus, a prototype rhabdovirus. *Vet. Microbiol.* **162**, 78–84 (2013).

361. Al-Abduly, A. & Christensen, P. An in situ and downstream study of non-thermal plasma chemistry in an air fed dielectric barrier discharge (DBD). *Plasma Sources Sci. Technol.* **24**, (2015).

362. Zhang, X., Lee, B. J., Im, H. G. & Cha, M. S. Ozone Production with Dielectric Barrier Discharge: Effects of Power Source and Humidity. *IEEE Trans. Plasma Sci.* **44**, 2288–2296 (2016).

363. Yagi, S. & Tanaka, M. Mechanism of ozone generation in air-fed ozonisers. *J. Phys. D. Appl. Phys.* **12**, 1509–1520 (1979).

Appendixes:

Appendix A: Pulsed Plasma Modeling Code (Python)

```
"""
Project:        Pulsing Plasma (Kortshagen Method on Steroids)
Version:        1
Date:           26 June 2021
Author:         Joseph Schwan
"""

#   Import the required libraries
import math
import numpy as np
import matplotlib.pyplot as plt
import imageio as ii
import os
import time

#   Time the program runtime
start_time = time.time()
```

```
#########################################################################
######

'''Directories and Files'''

if not os.path.exists('Pulsing Plasma'):          # Create file for data to save in
    os.makedirs('Pulsing Plasma')

if not os.path.exists('Pulsing Plasma/Pulse'):     # Create file for steady state data to save
in
    os.makedirs('Pulsing Plasma/Pulse')

if not os.path.exists('Pulsing Plasma/PulseOff'):   # Create file for afterglw data to save in
    os.makedirs('Pulsing Plasma/PulseOff')

if not os.path.exists('Pulsing Plasma/Neutral'):   # Create file for afterglw data to save in
    os.makedirs('Pulsing Plasma/Neutral')

'''Constants and Variables'''

q_i = 1.60217662*10**(-19)            # Ion charge [C]
q_e = -1.60217662*10**(-19)           # Electron charge [C]
```

```
m_i = 3*1.67377*10**(-27)             # Ion mass (H3) [kg]

m_e = 9.10938*10**(-31)               # Electron mass [kg]

k_b = 1.38064852*10**(-23)            # Boltzmann constant [J K-1]

epsilon_0 = 8.8541878128*10**(-12)    # Vacuum permitivity [F m-1]

pi = math.pi                          # Pi (16 digits)

T_i = 300                             # Ion temperature [K]

k_boltz = 8.617333262145*10**(-5)   # Boltzmann constant [eV K-1]

alp = 1.22                 # A constant that exists for some reason []

TorrPa = 133.322           # Torr to Pa conversion factor [Pa/Torr]

sigma_i = 1*10**(-19)      # Ion collision cross section [m2]

mu_i = 0.104               # Ion mobility for 4.69E-6[m] mean free path. [m2 V-1 s-1]


rho_p = 2.33*10**3         # Particle material density [particles kg m-3]

mph = 30*10**(-6)          # Particle mass per hour [kg hr-1]

mps = mph/60/60            # Particle mass per second [kg s-1]

L_tube = 0.101             # Reactor length [m]

D_tube = 0.021             # Internal diameter of reactor [m]

FR = 100                   # Flow rate [sccm]

plasmaT_e = 4              # Maximum electron temperature [eV]

T_e = plasmaT_e/k_boltz    # Electron temperature [K]

R_p = 4*10**(-9)           # 4 Torr steadystate particle diameter [m]
```

```
minR = 4*10**(-9)          # Minimum particle radius [m]
maxR = 15*10**(-9)         # Maximum particle radius [m]
minVol = 4/3*math.pi*minR**3     # Minimum particle volume [m3]
maxVol = 4/3*math.pi*maxR**3     # Maximum particle volume [m3]
volBins = int(np.ceil((maxR**3)/(minR**3))) # Number of discrete volume bins using
minimum particle volume as 1 unit []
v = np.linspace(minVol, maxVol, volBins)    # Particle volume [m3]
r = (3/(4*pi)*v)**(1/3)     # Create radius array analagous to volume array [m]

minCharge = -10           # Create charge bounds
maxCharge = 5
chargeBins = maxCharge - minCharge + 1  # Number of discrete charge bins []
chargeRange = np.linspace(minCharge, maxCharge, chargeBins) # Set up charge array

dt = 10*10**(-8)                    # Time steps [s]
DT = dt
hiTime = 300*10**(-8)                # End time for stability plot [s]

'''Static Numbers and Martricies'''

"Residence Time Math"
P = 4                               # Reactor pressure [Torr]
```

```
RV = L_tube/3*math.pi*D_tube**2          # Reactor volume [m3]
VFR = FR*(1/(P*0.0013)*(300/273.15))/60/1000000   # Corrected flow rate [m3 s-1]
RT = RV/VFR                              # Residence time in reactor [s]

"Steady State Particle Density"
PR = mps/rho_p/(4/3*math.pi*R_p**3)     # Particle production rate by a constant plasma
[particles s-1]
PD = PR/VFR                              # Particle density [particles m-3]

"Initiate Charge/Size Profile"
n_kvInit = np.zeros([chargeBins,volBins], dtype=float)
n_kvInit[-minCharge,0] = PD

n_i = 3*100*10**(15)             # Define initial ion density [m-3]

"Making Q"
y = (3/(4*pi))**(1/3)
R_s = np.zeros([volBins,volBins], dtype=float)

i = 0
while i < volBins:
    R_s[i,:] = y*(v[:]**(1/3) + v[i]**(1/3))
```

```
    i += 1


z = q_i**2/(4*pi*epsilon_0*k_b*T_i*R_s)
Q = np.zeros([chargeBins,chargeBins,volBins,volBins], dtype=float)


i = 0
while i < chargeBins:


    j = 0
    while j < chargeBins:


        kk = chargeRange[i]*chargeRange[j]
        if kk <= 0:
            Q[i,j,:,:] = 1 - kk*z
        else:


            q = 0
            while q < volBins:


                p = 0
                while p < volBins:
                    Q[i,j,q,p] = math.exp(-kk*z[q,p])
```

```
                p += 1


            q += 1


        j += 1


    i += 1


"Making Neutral beta"
x = (3/(4*pi))**(1/6)*(6*k_b*T_i/rho_p)**(0.5)
beta_n = np.zeros([volBins, volBins], dtype=float)


i = 0
while i < volBins:
    beta_n[i,:] = x*(1/v[:] + 1/v[i])**(0.5)*(v[:]**(1/3) + v[i]**(1/3))**2
    i += 1


#########################################################################
######
def On(n_kv, n_i, dt, tStop):
    """Pulse"""
```

```
    with ii.get_writer('Pulsing Plasma/Pulse/ChargeSizeDist.gif', mode='I') as writer:  # Create .gif to show charge evolution

        '''Charge Distribution'''

        "Setup Constants"
        a_e = q_e**2/(4*pi*epsilon_0*k_b*T_e)
        a_i = q_i**2/(4*pi*epsilon_0*k_b*T_i)
        b_i = a_i*2*alp*(P*TorrPa)*sigma_i
        w_i = 4*pi*(k_b*T_i/(2*pi*m_i))**(0.5)
        w_e = 4*pi*(k_b*T_e/(2*pi*m_e))**(0.5)
        nu_e = np.zeros([chargeBins,volBins], dtype=float)
        nu_i = np.zeros([chargeBins,volBins], dtype=float)
        timeBins = int(np.ceil(tStop/dt))

        "Initiate Arrays"
        b = np.zeros([chargeBins], dtype=float)
        dF = np.zeros([chargeBins,volBins], dtype=float)
        F = np.zeros([chargeBins,volBins], dtype=float)
        beta = np.zeros([chargeBins,chargeBins,volBins,volBins], dtype=float)
        n_eArray = np.zeros(timeBins, dtype=float)
        dn_Array = np.zeros(timeBins, dtype=float)
```

```
n_total = np.zeros(timeBins, dtype=float)
vol_total = np.zeros(timeBins, dtype=float)
charge_total = np.zeros(timeBins, dtype=float)

tt = 0
while tt < timeBins:
    "Calculate Ion and Electron Densities"
    i = 0
    while i < chargeBins:
        b[i] = sum(n_kv[i,:])
        i += 1

    n_i = n_i                          # Ion density from paper [m-3]
    n_e = n_i + sum(b*chargeRange)         # Electron density [m-3]
    n_eArray[tt] = n_e                 # Keep track of electron density [m-3]

    "Populate Collision Frequency Matricies"
    i = 0
    while i < chargeBins:

        j = 0
        while j < volBins:
```

```
            nu_i[i,j] = w_i*r[j]**2*n_i*math.exp(-b_i*chargeRange[i]/r[j])*((1-
a_i*chargeRange[i]/r[j]) +
(8*b_i*alp**2*a_i**2/(27*k_b*T_i))*chargeRange[i]**3/r[j]**2) +
(q_i*mu_i/epsilon_0)*n_i*chargeRange[i]*(1 -
(1+(2*b_i*chargeRange[i]/(3*k_b*T_i))*math.exp(-b_i*chargeRange[i]/r[j])))

            if chargeRange[i] >= 0:
                nu_e[i,:] = w_e*r[:]**2*n_e*(1 + a_e*chargeRange[i]/r[:])
            else:
                nu_e[i,j] = w_e*r[j]**2*n_e*math.exp(a_e*chargeRange[i]/r[j])

            j += 1

        i += 1

    "Evaluate Change in Charge Profile"
    i = 0
    while i < volBins:

        j = 0
        while j < chargeBins:
```

```
            if j == 0:
                dF[j,i] = nu_e[j+1,i]*F[j+1,i] - (nu_e[j,i] + nu_i[j,i])*F[j,i]
            elif j == (chargeBins-1):
                dF[j,i] = (nu_e[j,i] + nu_i[j,i])*F[j,i] + nu_i[j-1,i]*F[j-1,i]
            else:
                dF[j,i] = nu_e[j+1,i]*F[j+1,i] - (nu_e[j,i] + nu_i[j,i])*F[j,i] + nu_i[j-
1,i]*F[j-1,i]

            j += 1

        i += 1

    F = F + dF*dt               # Apply change to particle charge population
    F = n_kv/np.sum(n_kv)       # Normalize F with respect to total particle density
    n_kv = np.sum(n_kv)*F

    "Evaluate Change in Size Profile"
    i = 0
    while i < volBins:

        j = 0
```

```
    while j < chargeBins:

        k = 0
        while k < chargeBins:
            beta[k,j,i,:] = Q[k,j,i,:]*F[k,i]*F[j,:]*beta_n[i,:]
            k += 1

        j += 1

    i += 1

dn = np.zeros([chargeBins,volBins], dtype=float)

i = 0
while i < volBins:

    j = 0
    while j < volBins:

        k = 0
        while k < chargeBins:
```

```
            p = 0
            while p < chargeBins:
                dn[k,i] = dn[k,i] - beta[k,p,i,j]*n_kv[k,i]*n_kv[p,j]

                if ((j < i) and (k-p-minCharge < chargeBins) and (k-p-minCharge > -1)):
                    dn[k,i] = dn[k,i] + 0.5*beta[k-p-minCharge,p,i-j-1,j]*n_kv[k-p-
minCharge,i-j-1]*n_kv[p,j]

                p += 1

            k += 1

        j += 1

    i += 1

dn_Array[tt] = np.sum(dn)
n_kv = n_kv + dn*dt
n_total[tt] = np.sum(n_kv)

i = 0
while i < volBins:
```

```
            vol_total[tt] = vol_total[tt] + sum(n_kv[:,i])*v[i]
            i += 1


        plt.figure()                    # Plot n_pk as a 2D representation
        plt.imshow(n_kv, extent=[v[0],v[-1],chargeRange[-1],chargeRange[0]],
aspect='auto')
        plt.title('Particle Characteristics')
        plt.xlabel('Particle Volume ($m^{-3}$)')
        plt.ylabel('Particle Charge ($q_{e}$)')
        plt.text(v[-5], chargeRange[-3], 'Time = ' + "{0:.3g}".format(tt*dt),
horizontalalignment='left', verticalalignment='center')
        plt.colorbar()
        plt.savefig('Pulsing Plasma/Pulse/nkv.png', dpi = 400)
        plt.close()

        image = ii.imread('Pulsing Plasma/Pulse/nkv.png')          # Put graph at end of
F.gif
        writer.append_data(image)

        if dn_Array[tt]/PD > -0.01:
            break
```

```
    tt += 1


g = np.linspace(0,tStop,timeBins)
plt.figure()                    # Plot the evolution of n_e
plt.plot(g, n_eArray)
plt.xlim([0,tt*dt])
plt.title('Evolution of n_e')
plt.xlabel('Time (s)')
plt.ylabel('n_e ($m^{-3}$)')
plt.savefig('Pulsing Plasma/Pulse/ne.png', dpi = 400)
plt.close()

plt.figure()                    # Plot the evolution of n_e
plt.plot(g, dn_Array)
plt.xlim([0,tt*dt])
plt.title('Evolution of dn')
plt.xlabel('Time (s)')
plt.ylabel('dn/dt')
plt.savefig('Pulsing Plasma/Pulse/dn.png', dpi = 400)
plt.close()

plt.figure()                    # Plot the evolution of total particle population
```

```
        plt.plot(g, n_total)
        plt.xlim([0,tt*dt])
        plt.title('Evolution of Total Particle Population')
        plt.xlabel('Time (s)')
        plt.ylabel('Particle Count')
        plt.savefig('Pulsing Plasma/Pulse/nTotal.png', dpi = 400)
        plt.close()

        plt.figure()                        # Plot the evolution of total particle population
        plt.plot(g, vol_total)
        plt.xlim([0,tt*dt])
        plt.title('Afterglow: Total Particle Volume')
        plt.xlabel('Time (s)')
        plt.ylabel('Total Particle Volume ($m^{-3}$)')
        plt.savefig('Pulsing Plasma/Pulse/volTotal.png', dpi = 400)
        plt.close()

    return dn_Array, n_eArray, n_e, n_kv, nu_i, nu_e

##########################################################################
######
```

```
def Off(n_kv, n_i, n_e, T_e, dt, tStop):
    """Afterglow"""

    with ii.get_writer('Pulsing Plasma/PulseOff/ChargeSizeDist.gif', mode='I') as writer:  # Create .gif to show charge evolution

        "Setup Constants"
        nu_eb = np.zeros(chargeBins, dtype=float)
        nu_ib = np.zeros(chargeBins, dtype=float)
        a_i = q_i**2/(4*pi*epsilon_0*k_b*T_i)
        b_i = a_i*2*alp*(P*TorrPa)*sigma_i
        w_i = 4*pi*(k_b*T_i/(2*pi*m_i))**(0.5)
        timeBins = int(np.ceil(tStop/dt))

        "Initiate Arrays"
        b = np.zeros([chargeBins], dtype=float)
        dF = np.zeros([chargeBins,volBins], dtype=float)
        F = np.zeros([chargeBins,volBins], dtype=float)
        beta = np.zeros([chargeBins,chargeBins,volBins,volBins], dtype=float)
        n_eArray = np.zeros(timeBins, dtype=float)
        n_eArray[0] = n_e
        n_iArray = np.zeros(timeBins, dtype=float)
```

```
n_iArray[0] = n_i

dn_Array = np.zeros(timeBins, dtype=float)

T_eArray = np.zeros(timeBins, dtype=float)

T_eArray[0] = T_e

nu_e = np.zeros([chargeBins,volBins], dtype=float)

nu_i = np.zeros([chargeBins,volBins], dtype=float)

nu_eArray = np.zeros([chargeBins,volBins,timeBins], dtype=float)

nu_iArray = np.zeros([chargeBins,volBins,timeBins], dtype=float)

n_total = np.zeros(timeBins, dtype=float)

vol_total = np.zeros(timeBins, dtype=float)

charge_total = np.zeros(timeBins, dtype=float)


tt = 0

while tt < timeBins:


    a_e = q_e**2/(4*pi*epsilon_0*k_b*T_eArray[tt])

    w_e = 4*pi*(k_b*T_eArray[tt]/(2*pi*m_e))**(0.5)


    "Populate Collision Frequency Matricies"

    i = 0

    while i < chargeBins:
```

```
        j = 0
        while j < volBins:

            nu_i[i,j] = w_i*r[j]**2*n_i*math.exp(-b_i*chargeRange[i]/r[j])*((1-
a_i*chargeRange[i]/r[j]) +
(8*b_i*alp**2*a_i**2/(27*k_b*T_i))*chargeRange[i]**3/r[j]**2) +
(q_i*mu_i/epsilon_0)*n_i*chargeRange[i]*(1 -
(1+(2*b_i*chargeRange[i]/(3*k_b*T_i))*math.exp(-b_i*chargeRange[i]/r[j])))

            if chargeRange[i] >= 0:
                nu_e[i,:] = w_e*r[:]**2*n_e*(1 + a_e*chargeRange[i]/r[:])
            else:
                nu_e[i,j] = w_e*r[j]**2*n_e*math.exp(a_e*chargeRange[i]/r[j])

            j += 1

        i += 1

    nu_eArray[:,:,tt] = nu_e
    nu_iArray[:,:,tt] = nu_i

    "Evaluate Change in Charge Profile"
```

```
F = n_kv/np.sum(n_kv)          # Normalize F with respect to total particle density

i = 0
while i < volBins:

   j = 0
   while j < chargeBins:

      if j == 0:
         dF[j,i] = nu_e[j+1,i]*F[j+1,i] - (nu_e[j,i] + nu_i[j,i])*F[j,i]
      elif j == (chargeBins-1):
         dF[j,i] = (nu_e[j,i] + nu_i[j,i])*F[j,i] + nu_i[j-1,i]*F[j-1,i]
      else:
         dF[j,i] = nu_e[j+1,i]*F[j+1,i] - (nu_e[j,i] + nu_i[j,i])*F[j,i] + nu_i[j-
1,i]*F[j-1,i]

      j += 1

   i += 1

F = F + dF*dt                  # Apply change to particle charge population
n_kv = np.sum(n_kv)*F
```

```
"Evaluate Change in Size Profile"
F = n_kv/np.sum(n_kv)          # Normalize F with respect to total particle density

i = 0
while i < volBins:

   j = 0
   while j < chargeBins:

      k = 0
      while k < chargeBins:
         beta[k,j,i,:] = Q[k,j,i,:]*F[k,i]*F[j,:]*beta_n[i,:]
         k += 1

      j += 1

   i +=1

dn = np.zeros([chargeBins,volBins], dtype=float)

i = 0
```

```
while i < volBins:

    j = 0
    while j < volBins:

        k = 0
        while k < chargeBins:

            p = 0
            while p < chargeBins:
                dn[k,i] = dn[k,i] - beta[k,p,i,j]*n_kv[k,i]*n_kv[p,j]

                if ((j < i) and (k-p-minCharge < chargeBins) and (k-p-minCharge > -1)):
                    dn[k,i] = dn[k,i] + 0.5*beta[k-p-minCharge,p,i-j-1,j]*n_kv[k-p-
minCharge,i-j-1]*n_kv[p,j]

                p += 1

            k += 1

        j += 1
```

```
    i += 1

dn_Array[tt] = np.sum(dn)
n_kv = n_kv + dn*dt
n_total[tt] = np.sum(n_kv)

i = 0
while i < volBins:
    vol_total[tt] = vol_total[tt] + sum(n_kv[:,i])*v[i]
    i += 1

i = 0
while i < chargeBins:
    charge_total[tt] = charge_total[tt] + sum(n_kv[i,:])*chargeRange[i]
    i += 1
charge_total[tt] = charge_total[tt] + n_i + n_e

if tt == 1:
    n_kv1 = n_kv

if tt % 10 == 0:
    plt.figure()                    # Plot n_pk as a 2D representation
```

```
            plt.imshow(n_kv, extent=[v[0],v[-1],chargeRange[-1],chargeRange[0]],
aspect='auto')
            plt.title('Afterglow: Particle Characteristics')
            plt.xlabel('Particle Volume ($m^{-3}$)')
            plt.ylabel('Particle Charge ($q_{e}$)')
            plt.text(v[-5], chargeRange[-3], 'Time = ' + "{0:.3g}".format(tt*dt),
horizontalalignment='left', verticalalignment='center')
            plt.colorbar()
            plt.savefig('Pulsing Plasma/PulseOff/nkv.png', dpi = 400)
            plt.close()

            image = ii.imread('Pulsing Plasma/PulseOff/nkv.png')          # Put graph at end
of F.gif
            writer.append_data(image)

        tt += 1

        if tt == timeBins:
            break

        "Calculate Ion and Electron Densities"
        i = 0
```

```
    while i < chargeBins:
        b[i] = sum(n_kv[i,:])
        nu_ib[i] = sum(nu_i[i,:])
        nu_eb[i] = sum(nu_e[i,:])
        i += 1

    n_i = n_i - dt*sum(nu_ib*b)          # Ion density from paper [m-3]
    n_e = n_e - dt*sum(nu_eb*b)          # Electron density [m-3]
    n_iArray[tt] = n_i                   # Keep track of ion density [m-3]
    n_eArray[tt] = n_e                   # Keep track of electron density [m-3]

    "Update T_e"
    if tt > 0:
        T_e = T_e*(2/3 + n_eArray[tt]/(3*n_eArray[tt-1]))
    if T_e < 300:
        T_e = 300
    T_eArray[tt] = T_e

g = np.linspace(0,tStop,timeBins)
plt.figure()                             # Plot the evolution of n_e
plt.plot(g, n_eArray)
plt.xlim([0,tt*dt])
```

```
plt.title('Afterglow: Evolution of $n_{e}$')
plt.xlabel('Time (s)')
plt.ylabel('$n_{e}$ ($m^{-3}$)')
plt.savefig('Pulsing Plasma/PulseOff/ne.png', dpi = 400)
plt.close()

plt.figure()                    # Plot the evolution of n_i
plt.plot(g, n_iArray)
plt.xlim([0,tt*dt])
plt.title('Afterglow: Evolution of $n_{i}$')
plt.xlabel('Time (s)')
plt.ylabel('$n_{i}$ ($m^{-3}$)')
plt.savefig('Pulsing Plasma/PulseOff/ni.png', dpi = 400)
plt.close()

plt.figure()                    # Plot the evolution of T_e
plt.plot(g, T_eArray)
plt.xlim([0,tt*dt])
plt.title('Afterglow: Evolution of $T_{e}$')
plt.xlabel('Time (s)')
plt.ylabel('$T_{e}$ ($m^{-3}$)')
plt.savefig('Pulsing Plasma/PulseOff/Te.png', dpi = 400)
```

```
plt.close()


plt.figure()                    # Plot the evolution of dn
plt.plot(g, dn_Array)
plt.xlim([0,tt*dt])
plt.title('Afterglow: Evolution of dn')
plt.xlabel('Time (s)')
plt.ylabel('dn/dt')
plt.savefig('Pulsing Plasma/PulseOff/dn.png', dpi = 400)
plt.close()


plt.figure()                    # Plot the evolution of total particle population
plt.plot(g, n_total)
plt.xlim([0,tt*dt])
plt.title('Afterglow: Evolution of Total Particle Population')
plt.xlabel('Time (s)')
plt.ylabel('Particle Count')
plt.savefig('Pulsing Plasma/PulseOff/nTotal.png', dpi = 400)
plt.close()


plt.figure()                    # Plot the evolution of total particle population
plt.plot(g, vol_total)
```

```
        plt.xlim([0,tt*dt])
        plt.title('Afterglow: Evolution of Total Particle Volume')
        plt.xlabel('Time (s)')
        plt.ylabel('Total Particle Volume ($m^{-3}$)')
        plt.savefig('Pulsing Plasma/PulseOff/volTotal.png', dpi = 400)
        plt.close()

        plt.figure()                        # Plot the evolution of total particle population
        plt.plot(g, charge_total)
        plt.xlim([0,tt*dt])
        plt.title('Afterglow: Evolution of Total Plasma Charge')
        plt.xlabel('Time (s)')
        plt.ylabel('Plasma Charge $(\frac{e}{m^{3}})$')
        plt.savefig('Pulsing Plasma/PulseOff/chargeTotal.png', dpi = 400)
        plt.close()

    return dn_Array, n_eArray, n_iArray, n_kv, T_eArray, n_kv1, nu_eArray, nu_iArray

#########################################################################
######
def Coag(n_kv, dt, tStop):
    """Afterglow"""
```

```
    vol_lol = 0.0
    i = 0
    while i < volBins:
        vol_lol = vol_lol + sum(n_kv[:,i])*v[i]
        i += 1

    with ii.get_writer('Pulsing Plasma/Neutral/ChargeSizeDist.gif', mode='I') as writer:  # Create .gif to show charge evolution

        "Setup Constants"
        timeBins = int(np.ceil(tStop/dt))

        "Initiate Arrays"
        dn_Array = np.zeros(timeBins, dtype=float)
        n_total = np.zeros(timeBins, dtype=float)
        vol_total = np.zeros(timeBins, dtype=float)

        tt = 0
        while tt < timeBins:

            dn = np.zeros([chargeBins,volBins], dtype=float)
```

```
i = 0
while i < volBins:

  j = 0
  while j < volBins:

    k = 0
    while k < chargeBins:

      p = 0
      while p < chargeBins:
        dn[k,i] = dn[k,i] - beta_n[i,j]*n_kv[k,i]*n_kv[p,j]

        if ((j < i) and (k-p-minCharge < chargeBins) and (k-p-minCharge > -1)):
          dn[k,i] = dn[k,i] + 0.5*beta_n[i-j-1,j]*n_kv[k-p-minCharge,i-j-
1]*n_kv[p,j]

        p += 1

      k += 1
```

```
            j += 1


        i += 1


    dn_Array[tt] = np.sum(dn)
    n_kv = n_kv + dn*dt
    n_total[tt] = np.sum(n_kv)


    i = 0
    while i < volBins:
        vol_total[tt] = vol_total[tt] + sum(n_kv[:,i])*v[i]
        i += 1


    if tt % 10 == 0:
        plt.figure()                    # Plot n_pk as a 2D representation
        plt.imshow(n_kv, extent=[v[0],v[-1],chargeRange[-1],chargeRange[0]],
aspect='auto')
        plt.title('Neutral: Particle Characteristics')
        plt.xlabel('Particle Volume ($m^{-3}$)')
        plt.ylabel('Particle Charge ($q_{e}$)')
        plt.text(v[-5], chargeRange[-3], 'Time = ' + "{0:.3g}".format(tt*dt),
horizontalalignment='left', verticalalignment='center')
```

```
            plt.colorbar()
            plt.savefig('Pulsing Plasma/Neutral/nkv.png', dpi = 400)
            plt.close()

            image = ii.imread('Pulsing Plasma/Neutral/nkv.png')          # Put graph at end
of F.gif
            writer.append_data(image)

        tt += 1

    g = np.linspace(0,tStop,timeBins)
    plt.figure()                            # Plot the evolution of dn
    plt.plot(g, dn_Array)
    plt.xlim([0,tt*dt])
    plt.title('Neutral: Evolution of dn')
    plt.xlabel('Time (s)')
    plt.ylabel('dn/dt')
    plt.savefig('Pulsing Plasma/Neutral/dn.png', dpi = 400)
    plt.close()

    plt.figure()                            # Plot the evolution of total particle population
    plt.plot(g, n_total)
```

```
        plt.xlim([0,tt*dt])
        plt.title('Evolution of Total Particle Population')
        plt.xlabel('Time (s)')
        plt.ylabel('Particle Count')
        plt.savefig('Pulsing Plasma/Neutral/nTotal.png', dpi = 400)
        plt.close()

        plt.figure()                    # Plot the evolution of total particle population
        plt.plot(g, vol_total)
        plt.xlim([0,tt*dt])
        plt.title('Neutral: Total Particle Volume')
        plt.xlabel('Time (s)')
        plt.ylabel('Total Particle Volume ($m^{-3}$)')
        plt.savefig('Pulsing Plasma/Neutral/volTotal.png', dpi = 400)
        plt.close()

    return dn_Array, n_kv

#########################################################################
######

'''Run the Program'''
```

```
dn_ArrayOn, n_eArrayOn, n_e, n_kvOn, nu_iOn, nu_eOn = On(n_kvInit, n_i, dt,
hiTime)

extraHighTime = 1*10**(-5)
extraDt = 10*10**(-8)

dn_ArrayOff, n_eArrayOff, n_iArrayOff, n_kvOff, T_eArrayOff, n_kv1, nu_eArray,
nu_iArray = Off(n_kvOn, n_i, n_e, T_e, dt, extraHighTime)

# dn_ArrayNeutral, n_kvNeutral = Coag(n_kvInit, extraDt, extraHighTime)

runTime = time.time() - start_time
print("--- %s seconds ---" % (runTime))
```